

**Head-disk Interface Study for Heat Assisted Magnetic Recording (HAMR) and  
Plasmonic Nanolithography for Patterned Media**

by

Shaomin Xiong

A dissertation submitted in partial satisfaction of the

requirements of the degree of

Doctor of Philosophy

in

Engineering - Mechanical Engineering

in the

Graduate Division

of the

University of California, Berkeley

Committee in charge:

Professor David B. Bogy, Co-Chair

Professor Xiang Zhang, Co-Chair

Professor David Attwood

Professor Roberto Horowitz





Fall 2014

**Head-disk Interface Study for Heat Assisted Magnetic Recording (HAMR) and  
Plasmonic Nanolithography for Patterned Media**

Copyright 2014

Shaomin Xiong

The dissertation of Shaomin Xiong, titled Head-disk Interface Study for Heat Assisted Magnetic Recording (HAMR) and Plasmonic Nanolithography for Patterned Media, is approved:

Chair		Date	<u>October 1, 2014</u>
Co-Chair		Date	<u>Oct 3, 2014</u>
		Date	<u>19 August 2014</u>
		Date	<u>10/6/14</u>

University of California, Berkeley

## Abstract

Head-disk interface study for Heat Assisted Magnetic Recording (HAMR) and Plasmonic Nanolithography for Patterned Media

by

Shaomin Xiong

Doctor of Philosophy in Engineering - Mechanical Engineering  
University of California, Berkeley

Professor David B. Bogy, Co-Chair  
Professor Xiang Zhang, Co-Chair

The magnetic storage areal density keeps increasing every year, and magnetic recording-based hard disk drives provide a very cheap and effective solution to the ever increasing demand for data storage. Heat assisted magnetic recording (HAMR) and bit patterned media have been proposed to increase the magnetic storage density beyond 1 Tb/in<sup>2</sup>.

In HAMR systems, high magnetic anisotropy materials are recommended to break the superparamagnetic limit for further scaling down the size of magnetic bits. However, the current magnetic transducers are not able to generate strong enough field to switch the magnetic orientations of the high magnetic anisotropy material so the data writing is not able to be achieved. So thermal heating has to be applied to reduce the coercivity for the magnetic writing. To provide the heating, a laser is focused using a near field transducer (NFT) to locally heat a  $\sim(25 \text{ nm})^2$  spot on the magnetic disk to the Curie temperature, which is  $\sim 400 \text{ C}-600 \text{ }^\circ\text{C}$ , to assist in the data writing process. But this high temperature working condition is a great challenge for the traditional head-disk interface (HDI). The disk lubricant can be depleted by evaporation or decomposition. The protective carbon overcoat can be graphitized or oxidized. The surface quality, such as its roughness, can be changed as well. The NFT structure is also vulnerable to degradation under the large number of thermal load cycles. The changes of the HDI under the thermal conditions could significantly reduce the robustness and reliability of the HAMR products.

In bit patterned media systems, instead of using the continuous magnetic granular material, physically isolated magnetic islands are used to store data. The size of the magnetic islands should be about or less than 25 nm in order to achieve the storage areal density beyond 1 Tb/in<sup>2</sup>. However, the manufacture of the patterned media disks is a

great challenge for the current optical lithography technology. Alternative lithography solutions, such as nanoimprint, plasmonic nanolithography, could be potential candidates for the fabrication of patterned disks.

This dissertation focuses mainly on: (1) an experimental study of the HDI under HAMR conditions (2) exploration of a plasmonic nanolithography technology.

In this work, an experimental HAMR testbed (named “Cal stage”) is developed to study different aspects of HAMR systems, including the tribological head-disk interface and heat transfer in the head-disk gap. A temperature calibration method based on magnetization decay is proposed to obtain the relationship between the laser power input and temperature increase on the disk. Furthermore, lubricant depletion tests under various laser heating conditions are performed. The effects of laser heating repetitions, laser power and disk speeds on lubricant depletion are discussed. Lubricant depletion under the optical focused laser beam heating and the NFT heating are compared, revealing that thermal gradient plays an important role for lubricant depletion. Lubricant reflow behavior under various conditions is also studied, and a power law dependency of lubricant depletion on laser heating repetitions is obtained from the experimental results. A conductive-AFM system is developed to measure the electrical properties of thin carbon films. The conductivity or resistivity is a good parameter for characterizing the sp<sup>2</sup>/sp<sup>3</sup> components of the carbon films. Different heating modes are applied to study the degradation of the carbon films, including temperature-controlled electric heater heating, focused laser beam heating and NFT heating. It is revealed that the temperature and heating duration significantly affect the degradation of the carbon films. Surface reflectivity and roughness are changed under certain heating conditions. The failure of the NFT structure during slider flying is investigated using our in-house fabricated sliders. In order to extend the lifetime of the NFT, a two-stage heating scheme is proposed and a numerical simulation has verified the feasibility of this new scheme. The heat dissipated around the NFT structure causes a thermal protrusion. There is a chance for contact to occur between the protrusion and disk which can result in a failure of the NFT. A design method to combine both TFC protrusion and laser induced NFT protrusion is proposed to reduce the fly-height modulation and chance of head-disk contact.

Finally, an integrated plasmonic nanolithography machine is introduced to fabricate the master template for patterned disks. The plasmonic nanolithography machine uses a flying slider with a plasmonic lens to expose the thermal resist on a spinning wafer. The system design, optimization and integration have been performed over the past few years. Several sub-systems of the plasmonic nanolithography machine, such as the radial and circumferential direction position control, high speed pattern generation, are presented in this work. The lithography results are shown as well.

## Acknowledgements

First of all, I would like to thank my two advisers, Professor David Bogy and Professor Xiang Zhang, for guiding and supporting me through my five years of Ph.D study at Cal. I am grateful to them for their continuous encouragement and support in exploring the facts, unknowns and application of science and technology. I also appreciate their valuable advice and help for my professional development. Their philosophy of lab management at both macro and microscales also impressed me. I believe what I have learned from them is very critical for my future career. It is my great honor and fortune to have them as my advisors and mentors.

I would also like to express my appreciation to Professor David Attwood and Professor Roberto Horowitz for their valuable contributions and feedback to my dissertation and my qualify exam.

I would like to thank my colleagues in CML. I have really enjoyed the free atmosphere to discuss and learn from each other with different backgrounds in CML. It has been a great pleasure to work with them: Nan Liu, Sripathi Vangipuram Canchi, Rahul Rai, Jinglin Zheng, Joanna Bechtel, Liping Li, Yung-kan Chen, Alejandro Rodriguez, Soroush Sarabi, Haoyu Wu, Yuan Ma, Dolf Mardan, Jia Zhao, Yuliang Liu and Dequan Shi. Life sharing with them makes my study in CML a wonderful experience. Discussions with Yung-kan Chen and Alejandro always provide me chances to think from different aspects in my research. Dr. Budaev's information in heat transfer also inspired and helped me to jump to a new field: heat transfer at nano-scales. I also would like to sincerely thank Dolf Mardan for helping me with the computers and other hardware. Haoyu Wu, Mingyi Zheng and Xing Zhang helped a lot in my fifth year and sped up the progress of some of our projects significantly.

Members from the control groups and material group in CML contributed a lot to my work at Cal. I would like to extend special thanks to Na Wang for her expertise in material science and Fu Zhang for his expertise in system control. Their knowledge and continued help was important to some of the studies in this dissertation. Jun Xie from Professor Komvopoulos' group, Minghui Zheng and Liting Sun from Professor Tomizuka's group, and Erhan Keikha from Professor Horowitz' group also provide their help and cooperation.

Colleagues from SINAM, including XLab at Cal, MCL at UCLA and MCP at UNCC, also provided me with the chance to expand my knowledge of different fields. I would like to express my great thanks to them: Yuan Wang, Liang Pan, Erick Ulin-Avila, Jeongmin Kim, Zijing Wong and Hanyu Zhu from Xlab, Yenchang from MCL, Mohamed E. Saad and Kang Ni from UNCC. I started my FPGA experience from Erick,

learned optics from Jeongmin, microfabrication from Zijing Wong and real-time control from Yenchu. It has been a wonderful experience to work with them.

Life in Berkeley is wonderful with my friends: Meng Wang, Yang Deng, Xuance Zhou, Sherry Shao, Hongwei Li, Chenghao Wu, Yang Zhao, Peng Zhou and Angelina Zhou. They make my life easy and sweet.

I have been mainly dealing with laser technology in my graduate study at Cal, as seen from this dissertation. I am always self-motivated and proud that what I have done here fits with the motto of Cal: "Let there be light". Laser is a special light, and I could "let research be laser". But I want to say special thanks to Miss Yao for her reminder and encouragement that we should also "let life be light".

Finally, I should give my thanks to my parents and sister for their unconditional love and support throughout my life in Berkeley.

This work is supported by the Computer Mechanics Laboratory at the University of California, Berkeley, The Center for Scalable and Integrated Nano Manufacturing (SINAM) and Advanced Storage Technology Consortium (ASTC).

## Table of Contents

Table of Contents.....	iii
List of Figures.....	vi
List of Tables.....	xv
List of Abbreviations.....	xvi
<b>Chapter 1: Introduction.....</b>	<b>1</b>
1.1 Technology Developments for HDDs.....	1
1.2 New approaches.....	7
1.3 Motivation.....	11
1.4 Objective.....	16
<b>Chapter 2 Temperature calibration based on magnetization decay for perpendicular media.....</b>	<b>18</b>
2.1 Introduction.....	18
2.2 Numerical model for the magnetic thermal decay.....	19
2.3 Experimental procedure.....	21
2.4 Experimental results and discussion.....	23
2.5 Numerical modeling.....	25
2.6 Summary.....	28
<b>Chapter 3 HAMR stage development.....</b>	<b>30</b>
3.1 Cal stage for the tribological study of the HDI for HAMR.....	30
3.1.1 Spindle system.....	30
3.1.2 Optics.....	31
3.1.3 Laser focusing servo system.....	37
3.1.4 Linear stage.....	43
3.1.5 User graphic interface.....	44
3.2 Cal stage for the study of heat transfer in the HDI.....	44
3.3 Summary.....	48
<b>Chapter 4 Lubricant changes under laser heating.....</b>	<b>49</b>
4.1 Introduction.....	49



4.2 Experimental condition and process.....	52
4.2.1 Free laser beam heating mode.....	52
4.2.2 NFT heating mode.....	54
4.3 Lubricant study under free laser beam heating.....	55
4.3.1 Image processing of OSA scans.....	55
4.3.2 Lubricant reflow.....	56
4.3.2 Lubricant depletion under heating by the free laser beam.....	61
4.4. Lubricant depletion under NFT heating.....	67
4.5 Summary.....	68
<b>Chapter 5 Degradation of carbon overcoat under laser heating.....</b>	<b>70</b>
5.1 Introduction.....	70
5.2 Conductive AFM measurement of carbon films.....	74
5.3 Experimental conditions and procedures for thermal annealing.....	78
5.3.1 Temperature controlled heating by a temperature controlled electric heater.....	78
5.3.2 Free laser beam heating procedure.....	78
5.3.3 NFT exposure procedure.....	79
5.4 Experimental results and discussion.....	80
5.4.1 Carbon film degradation after thermal annealing using the electric heater.....	80
5.4.2 Surface reflectivity change under the free laser beam heating conditions.....	81
5.4.3 Surface topography.....	82
5.4 Carbon overcoat degradation under NFT heating.....	85
5.5 Summary.....	86
<b>Chapter 6 Failure of the NFT under HAMR conditions.....</b>	<b>88</b>
6.1 Introduction.....	88
6.2 Experimental study for NFT failure.....	93
6.3 Dual-stage heating scheme.....	97
6.3.1 Modeling.....	98

6.3.2 Results and discussion.....	101
6.4 Summary.....	106
<b>Chapter 7 Fly-height modulation for a two protrusion (TFC-NFT) HAMR slider.....</b>	<b>107</b>
7.1 Introduction.....	107
7.2 2-DOF numerical model.....	109
7.3. Dual protrusion design and discussion.....	112
7.4 Summary.....	116
<b>Chapter 8 Plasmonic nanolithography system for patterned media.....</b>	<b>117</b>
8.1 Introduction of plasmonic nanolithography.....	118
8.2 Machine configuration.....	120
8.2.1 Optical system.....	121
8.2.2 Linear stage for radial positioning.....	123
8.2.3 Magnetic encoder for circumferential positioning.....	125
8.2.4 Pattern generator.....	126
8.2.5 Central control unit (CCU).....	127
8.3 Magnetic Rotary Encoder.....	127
8.3.1 Introduction.....	127
8.3.2 System configuration.....	128
8.3.3 FPGA based servo system for track following.....	130
8.3.4. Servo and encoder writing and reading.....	135
8.3.5. Track following controller and its implementation.....	137
8.3.6 Digitized encoder and timing jitter.....	141
8.4 Pattern generator.....	143
8.5 Summary.....	147
<b>Chapter 9 Conclusions and Future Work.....</b>	<b>149</b>
9.1 Conclusion.....	149
9.2 Future work.....	151
<b>Bibliography.....</b>	<b>154</b>

## List of Figures

Figure 1. 1 Areal density increase curves for HDD and flash SSD in the past decades [3].....	1
Figure 1. 2 Cost for per GB for HDD and flash SSD in the past two decades [3].2	
Figure 1. 3 IBM RAMAC 350 Magnetic Disk Drive, 1956 [4].....	2
Figure 1. 4 Structure of “Winchester” HDD [5].....	3
Figure 1. 5 Small integrated HDD (ST-506) in a PC.....	3
Figure 1. 6 Structure of the modern HDD and microscope image of the air bearing surface.....	4
Figure 1. 7 Longitudinal recording diagram (top).....	5
Figure 1. 8 MFM image of the LMR disk (left) and servo zone of the PMR disk (right).....	5
Figure 1. 9 Trend of head media spacing (HMS) as areal density. Green: Actual HDD data, Red:Earlier predictions [14].....	6
Figure 1. 10 Sketch-up of TFC technology for slider [17].....	6
Figure 1. 11 Magnetic trilemma for the PMR technology.....	7
Figure 1. 12 Concept of HAMR.....	9
Figure 1. 13 Comparison of conventional PMR continuous granular media with BPM [30].....	10
Figure 1. 14 Comparison of antenna coupling to continuous and bit patterned media. a, Top view of disk surface absorption profile on continuous medium. Peak value = 1.4. b, Top view of disk absorption profile on bit-patterned medium. Peak value = 16.5. c, Side view of a. Peak value = 2.8 (in notch). d, Side view of b. Peak value = 7.9 (in island). Scale bar, 50 nm (a–d). The colour scale in b applies to a, and the colour scale in d applies to c [26].....	10
Figure 1. 15 Schematic drawing of the HDI for a PMR drive (figures are not to scale).....	11
Figure 1. 16 Schematic drawing of HDI for HAMR systems.....	12
Figure 1. 17 multiple physical couplings among light, heat, mechanical deformation and magnetics inside the HDI of HAMR systems.....	14

Figure 1. 18 DRAM and MPU Metal Level Potential Solutions for ITRS.....	16
Figure 2. 1 Temperature dependency of the magnetic properties.....	21
Figure 2. 2 Schematic plot of the experimental setup for HAMR study.....	22
Figure 2. 3 Schematic plot of MFM.....	22
Figure 2. 4 A typical MFM image of the magnetic media after laser exposure...	23
Figure 2. 5 Topography of the perpendicular recording media after laser exposure at different power densities. (a) 26.0 mW/ $\mu\text{m}^2$ ; (b) 32.5 mW/ $\mu\text{m}^2$ ; (c) 39.0 mW/ $\mu\text{m}^2$ ; (d) 66.3 mW/ $\mu\text{m}^2$ . From image a to d, the scan size is 5 by 5 $\mu\text{m}$ and the scale bar is 1 $\mu\text{m}$ . The down-track direction is horizontal.....	24
Figure 2. 6 MFM images of the perpendicular recording media after laser exposure at different power densities. (a) 26.0 mW/ $\mu\text{m}^2$ ; (b) 32.5 mW/ $\mu\text{m}^2$ ; (c) 39.0 mW/ $\mu\text{m}^2$ ; (d) 66.3 mW/ $\mu\text{m}^2$ . From image a to d, the scan size is 5 by 5 $\mu\text{m}$ and the scale bar is 1 $\mu\text{m}$ . The down-track direction is horizontal.....	24
Figure 2. 7 Normalized magnetization along the down-track direction as a function of radial (off-track) displacement for different power exposure. (a) 26.0 mW/ $\mu\text{m}^2$ ; (b) 32.5 mW/ $\mu\text{m}^2$ ; (c) 39.0 mW/ $\mu\text{m}^2$ ; (d) 66.3 mW/ $\mu\text{m}^2$ .....	25
Figure 2. 8 Schematic plot (top) and mesh (bottom) of the 3D FEM model of the thermal behavior simulation for the free laser beam laser heating.....	26
Figure 2. 9 The temperature distribution at the laser power density of 39.0 mW/ $\mu\text{m}^2$ from the numerical analysis.....	27
Figure 2. 10 The temperature history (left) and magnetization decay history (right) for the 3 nodes at different locations when the laser passed at a power density of 39.0 mW/ $\mu\text{m}^2$ .....	28
Figure 2. 11 Thermally erased magnetic track width due to the laser heating.....	28
Figure 3. 1 Schematic design of the Cal stage for tribological study of the HDI in HAMR.....	30
Figure 3. 2 Laser light modulation and synchronization with the spindle index.	31
Figure 3. 3 Delay of the laser emission with respect to the modulation signal....	32
Figure 3. 4 Optical beam path of the Cal stage.....	33
Figure 3. 5 Reflected image of the laser focused spot captured by a CCD camera	34

Figure 3. 6 Intensity profiles of the focused laser beam along the down-track (left) and cross-track (right) directions.....	34
Figure 3. 7 Homemade slider with an NFT; (left) Optical microscope image of a homemade air bearing surface; (right) zoomed NFT structure and alignment structure on the trailing edge.....	35
Figure 3. 8 AFM topography of the NFT and alignment mark on the homemade slider surface.....	35
Figure 3. 9 Reflected image of the NFT structure after alignment captured by a CCD camera.....	36
Figure 3. 10 Optical intensity distribution at a plane 10 nm away from the NFT.....	36
Figure 3. 11 Intensity profile of the transmitted light at a plane 10 nm away from the NFT along the down-track (top) and cross-track (bottom) directions.....	37
Figure 3. 12 Beam profile along radial direction when the laser was on and out of focus.....	38
Figure 3. 13 Disk vertical run-out profiles at three different radii for a 3.5 inch disk.....	39
Figure 3. 14 Repetitive disk run-out measurements for a 2.5 inch disk at a fixed radius.....	39
Figure 3. 15 Transfer function of the bender with objective lens attached.....	40
Figure 3. 16 Bender's response to different amplitudes of the driving voltage....	40
Figure 3. 17 A vertical run-out profile for a 3.5 inch disk.....	41
Figure 3. 18 Reflected images of laser focus spots when the focus servo system was on and off.....	42
Figure 3. 19 Schematic plot of the relative motion of the linear stage relatively to the disk surface.....	43
Figure 3. 20 Measured variation of the gap as the linear stage moves radially and the disk was stationary.....	43
Figure 3. 21 Schematic of a contact sensor embedded into head structure [50]..	44
Figure 3. 22 Schematic design of the testbed for study of heat transfer inside the HAMR HDI.....	45
Figure 3. 23 Close up view of the Cal stage integrating a function of an ECS....	45

Figure 3. 24 Laser alignment to the magnetic transducer and ECS. (left) Optical image of the magnetic transducer captured by the optical microscope; (right) reflected image of the magnetic transducer captured by the CCD camera.....	46
Figure 3. 25 An acoustic emission sensor is attached to the base of a HGA holder	47
Figure 3. 26 A typical signal from the ECS, TFC and AE sensor in the experiment	47
Figure 4. 1 Schematic drawing of HDI for HAMR systems.....	49
Figure 4. 2 Schematics of lubricant main-chain and end-group progression [52]	50
Figure 4. 3 Schematic drawing of the experimental procedure for the free laser beam heating.....	53
Figure 4. 4 Schematic drawing of NFT heating.....	55
Figure 4. 5 A typical raw OSA Q-phase image of an exposed band.....	55
Figure 4. 6 Final OSA Q-phase image after removing the run-out curvature and background.....	56
Figure 4. 7 OSA Q-phase image of an exposed track at different time periods when the laser power was 192.5 mW, the spindle speed was 1500 RPM and heating repetition was 50.....	57
Figure 4. 8 Lubricant depletion profiles of the exposed track at different times. The laser power was 192.5 mW, the spindle speed was 1500 RPM and repetition number was 50.....	57
Figure 4. 9 Real lubricant depletion depths vs. time after disk was heated after 50 repetitions. The laser power was 192.5 mW and the spindle speed was 1500 RPM...	58
Figure 4. 10 Lubricant depletion depth as time elapses after the tracks were heated at different repetitions. The laser power was 192.5 mW and the spindle speed was 1500 RPM.....	58
Figure 4. 11 Normalized lubricant depletion depth during the reflow process after the disk was initially heated for the different repetitions. The laser power was 192.5 mW and spindle speed was 1500 RPM.....	59
Figure 4. 12 Normalized lubricant depletion depth during the reflow process after the initial heating at various heating conditions.....	60
Figure 4. 13 Lubricant depletion after the disk was heated at different power levels and spindle speeds. (a) all of the tracks were exposed by 50 repetitions (b) all the tracks were exposed by 100 repetitions.....	61

Figure 4. 14 Initial lubricant depletion profile from OSA Q-phase image captured 0 minute (Figure 4. 6). The laser power for all seven tracks was 192.5 mW and spindle speed was 1500 RPM. Repetition was 1000, 500, 100, 50, 10, 5, 1 for the seven tracks from left to right.....	62
Figure 4. 15 Lubricant depletion at 0 minute vs. number of repetition when laser power was 192.5 mW and spindle speed was 1500 RPM.....	62
Figure 4. 16 Lubricant depletion vs. repetition under different heating conditions.....	63
Figure 4. 17 A heating point source on a semi-infinite moving workpiece at speed of v.....	64
Figure 4. 18 Temperature contours of point source heating .....	65
Figure 4. 19 Sketched trends of temperature and magnitude of thermal gradient at P1 with respect to disk speed and laser power.....	67
Figure 4. 20 (a) Q-phase image of lubricant depletion after NFT heating (b) surface reflectivity change due to lubricant depletion after NFT heating.....	68
Figure 5. 1 Sp <sup>3</sup> and sp <sup>2</sup> carbon hybridization in diamond like carbon overcoat .....	71
Figure 5. 2 (a) Schematic drawing of C-AFM system for conductivity measurement; .....	74
Figure 5. 3 (a) Topography of sample 1 (3.6 nm carbon film) (b) Current map of sample 1.....	75
Figure 5. 4 RMS value of the perpendicular resistance and surface roughness for a-C films with different thickness.....	76
Figure 5. 5 Average resistivity and sp <sup>3</sup> fraction for different thickness samples.....	76
Figure 5. 6 (a) Topography of the PMR disk after laser exposure.....	77
Figure 5. 7 Schematic diagram of a temperature control setup.....	78
Figure 5. 8 OSA p-sp image of the carbon disks after thermal annealing.....	80
Figure 5. 9 Surface topography of carbon film after thermally annealing at different temperatures. The color bar for all 3 plots is -3 nm to 3 nm.....	81
Figure 5. 10 Surface RMS roughness of the carbon film after thermally annealing at different temperatures by a temperature controlled electric heater.....	81
Figure 5. 11 P-sp images of the exposed tracks at different laser power densities.....	82

Figure 5. 12 Surface reflectivity profiles of the tracks after exposure at various repetitions at a power density of $29.0 \text{ mW}/\mu\text{m}^2$ .....	82
Figure 5. 13 Surface topography for 6 tracks exposed at different conditions. The scale bar in all the figures are $1 \mu\text{m}$ .....	84
Figure 5. 14 Surface deformation of the tracks exposed at $29.0 \text{ mW}/\mu\text{m}^2$ under different repetitions.....	85
Figure 5. 15 OSA p-sp scan of the disk after the NFT heating for different repetitions. ....	86
Figure 6. 1 Integrated recording head schematic from HGST. [26].....	90
Figure 6. 2 A schematic diagram of an HAMR recording system [29].....	90
Figure 6. 3 Diagram of the NFT and planar solid immersion mirror (PSIM) for the HAMR system from Seagate. [25].....	91
Figure 6. 4 (a) NFT array on the left rail of the air bearing surface. (b) Different laser power values on different NFTs (power unit: mW) (c) SEM image of the NFT design, scale bar is $0.5 \mu\text{m}$ .....	93
Figure 6. 5 Schematic diagram of the far field transmission measurement setup.....	94
Figure 6. 6 Optical images of the NFTs after laser exposure at different powers. (a) NFT without any exposure; (b) NFT after $35 \text{ mW}$ exposure; (c) NFT after $43 \text{ mW}$ exposure; (d) NFT after $70 \text{ mW}$ exposure.....	95
Figure 6. 7 Far field transmission of the NFT after laser exposure. (Left) Transmission of the unexposed NFT; (right) Transmission of the NFT after $43 \text{ mW}$ exposure;.....	95
Figure 6. 8 Topography of the NFT structure after different laser exposure conditions. (a) NFT without any exposure; (b) NFT after $35 \text{ mW}$ exposure; (c) NFT after $43 \text{ mW}$ exposure; (d) NFT after $70 \text{ mW}$ exposure. Scale bar is $1 \mu\text{m}$ for all plots. The outer ring in all plots is not part of the NFT structure, but was used for laser alignment in the experiments.....	96
Figure 6. 9 Topography change of the blank metal film of the slider surface after different laser exposure conditions.....	97
Figure 6. 10 Concept and model of the two-stage heating.....	99
Figure 6. 11 Schematic drawing (left) and mesh (right) of the 3D FEM thermal model for disks multi-layers.....	100



Figure 6. 12 A typical thermal profile on the media surface under the two heating stages.....	101
Figure 6. 13 Dependence of the laser radius ( $R_a$ ) on the size of waveguide.....	102
Figure 6. 14 FWHM of the temperature distribution in the waveguide heating stage by different laser radii ( $R_{spot}$ ).....	102
Figure 6. 15 Ratio of the background temperature $T^*$ and peak temperature $T_{p1}$ under different $R_{spot}$ in the waveguide heating stage.....	103
Figure 6. 16 The down-track thermal profile in the two stage heating scheme and single NFT heating scheme.....	104
Figure 6. 17 Switching field $H_k$ distribution on the disk surface for the two-stage heating scheme and single NFT heating scheme.....	104
Figure 6. 18 (a) 3D FEM thermal model for the NFT metal layer; (b) Deformation of the NFT under laser heating.....	105
Figure 7. 1 Energy flow in a HAMR drive [119].....	108
Figure 7. 2 (a) ABS design; (b) 2-DOF mass-spring model.....	110
Figure 7.3 The impulse response of the slider and its spectrum. a. Response to the force excitation; b. Spectrum of a; c. Response to the torque excitation; d. Spectrum of c.....	111
Figure 7. 4 Feedback control loop for the ABS with two thermal protrusions..	112
Figure 7. 5 Dual protrusions design. (a) Location of the dual protrusion on the rear pad; (b) geometry of TFC (left bigger one) and laser-induced protrusion (right smaller one).....	112
Figure 7. 6 Air lift force under the two protrusions, (a) laser-induced protrusion; (b) TFC protrusion.....	113
Figure 7. 7 FHM due to the disk waviness when different number of protrusions is applied. The FHM of the single laser -induced protrusion case and TFC protrusion are offset by 1 nm and 0.5 nm, the waviness is offset by -1 nm for a better view.....	114
Figure 7. 8 FHM induced by the external disturbance when different number of protrusions are applied. (a) Force disturbance; (b) FHM.....	114
Figure 7. 9 Normalized FHM vs. height of the TFC protrusion by CML dynamic simulator when the dual protrusion separation is 33 $\mu\text{m}$ .....	115

Figure 7. 10 Normalized FHM for different dual protrusion separation and TFC protrusion height. The stars indicate slider and disk contact.....	116
Figure 8. 1 Fabrication process for bit patterned media [128].....	118
Figure 8. 2 DRAM and MPU Metal Level Potential Solutions for ITRS.....	119
Figure 8. 3 Integrated plasmonic nanolithography machine (a) brief schematic (b) real system.....	120
Figure 8. 4 Laser modulation by an EOM. The input and output were both 80 MHz. ....	121
Figure 8. 5 Structure of the optical head.....	122
Figure 8. 6 Flexure to assist laser beam alignment to the NFT (a) schematic design of the flexure; (b) photo of the flexure.....	122
Figure 8. 7 Oblique view of the ABS. The topography is scaled up by a factor of 200 for better illustration.....	123
Figure 8. 8 3D design (a) and photo of the linear stage.....	123
Figure 8. 9 Stage positioning error when the stage was moved at different speeds: (a) the stage was stationary; (b) the stage was moved at 5 $\mu\text{m/s}$ ; (c) the stage was moved at 33 $\mu\text{m/s}$ .....	125
Figure 8. 10 (a) User designed pattern: a “CAL” logo; (b) a binary matrix of the “CAL” logo, used for pattern generator.....	126
Figure 8. 11 Operation process flow chart for the plasmonic nanolithography machine.....	127
Figure 8. 12 Schematic block diagram of the magnetic encoder system for the plasmonic nanolithography machine.....	128
Figure 8. 13 (a) MFM image of two magnetic encoder tracks, the scale bar is 1 $\mu\text{m}$ .....	129
Figure 8. 14 Servo scheme for the magnetic encoder system (a) interleaved structure of dual-frequency servo sector and encoder sector (b) Process sequence of the servo and encoder counter.....	130
Figure 8. 15 Servo systems in the HDDs showing a typical conventional servo sector; magnetic readback signal of the conventional servo bursts when the head has different offsets from the track center; proposed dual frequency servo bursts; spectrum of the readback signal for dual frequency servo bursts.....	132

Figure 8. 16 Configuration of the FPGA based servo system for HDDs.....	133
Figure 8. 17 (a) Schematic plot of the FPGA; (b) Timing diagram for the decoding process; (c) Delay measurements for the decoding process.....	135
Figure 8. 18 Measured readback signal of the written tracks (a) Readback signal of the interleaved servo, blank and encoder sectors, (b) readback signal of the servo sector, (c) frequency spectrum of the servo sector readback (d) readback signal of the blank zone, (e) readback signal of the encoder sector (f) frequency spectrum of the encoder sector readback.....	136
Figure 8. 19 Relationship between PES and the displacement.....	137
Figure 8. 20 Frequency response and identified model of the piezo stage with head cartridge.....	138
Figure 8. 21 Schematic diagram of the HDD servo controller based on the FPGA. (a) real-time control system structure; (b) combination of PID and repetitive controller in the Labview FPGA.....	139
Figure 8. 22 Sensitivity function of the servo system.....	140
Figure 8. 23 (a) PES history when the controller is switched on and off; (b) spectrum of PES.....	140
Figure 8. 24 Analog readback signal from the magnetic encoder and digitized signal from the FPGA.....	141
Figure 8. 25 Histogram of the period variation of the magnetic encoder.....	142
Figure 8. 26 Time uncertainty of the magnetic encoder and optical encoder in 6 revolutions' readback.....	142
Figure 8. 27 Schematic drawing of a pattern generator array based on a FPGA card.....	144
Figure 8. 28 The flow chart of a finite state machine in the FPGA.....	145
Figure 8. 29 Simulated pattern output from Modelsim.....	145
Figure 8. 30 Measured pattern output and magnetic encoder by a high speed DAQ.....	146
Figure 8. 31 Optical microscope image of the "CAL" logo written by lithography machine for the demonstration of pattern generator.....	147

## List of Tables

Table 1. 1 Length and time scales in HDI for HAMR.....	15
Table 2. 1 Laser power levels and densities for exposure on the aluminum substrate PMR disk.....	22
Table 4. 1 Experimental conditions for free laser beam exposure.....	54
Table 4. 2 Values of parameters A and b for the lubricant depletion model (4.2)	64
Table 5. 1 Free laser beam heating conditions for the a-C films.....	79
Table 5. 2 Exposed tracks under different free laser beam heating conditions....	83
Table 6. 1 Thermal properties of 4 layers in the HAMR media [72].....	100
Table 6. 2 Maximum temperature, mechanical stress and deformation for two-stage heating and single NFT heating.....	105
Table 8. 1 Size of a magnetic bit/island and track with respect to areal density [38] .....	119

## List of Abbreviations

ABS: Air Bearing Surface  
A-C: Amorphous Carbon  
AFM: Atomic Force Microscopy  
AlTiC: Al<sub>2</sub>O<sub>3</sub>-TiC ceramic  
AU: Arbitrary Unit  
BPM: Bit Patterned Media  
C-AFM: Conductive-AFM  
CLK: Clock  
CPR: Count per Revolution  
DLC: Diamond like Carbon  
DOF: Degree Of Freedom  
FEM: Finite Element Method  
FFT: Fast Fourier Transform  
FH: Fly-height  
FHM: Fly-height modulation  
FPGA: Field Programmable Gate Array  
GB: Gigabyte  
GMR: Giant Magneto-Resistive  
HAMR: Heat-Assisted Magnetic Recording  
HDD: Hard Disk Drives  
HDI: Head Disk Interface  
LMR: Longitudinal Magnetic Recording  
MB: Megabytes  
MFM: Magnetic Force Microscopy  
NFT: Near-Field Transducer  
PFPE: Perfluoropolyether  
PMR: Perpendicular Magnetic Recording  
RAMAC: Random Access Method of Accounting and Control  
RPM: Revolution per Minute  
R/W: Reading/Writing  
TB: Terabyte  
Tb: Terabit  
TFC: Thermal Fly-height Control

## Chapter 1: Introduction

The volume of data generated per day has increased exponentially in recent decades. As of 2013, an estimated four zettabytes ( $2^{18}$ ) of data were created [1]. Easy access to Internet devices, mass storage and computers drive the explosion of data. Mass data storage devices, such as solid state, magnetic, and optical storage for digital electronic systems, provide major non-volatile storage and rapid access to data. As a result, there is an ever increasing capacity requirement for those mass data storage systems. Among those mass data storage systems, magnetic recording-based hard disk drives (HDDs) play the largest and most critical role in mass data storage because of their high capacity and low cost [2].

This introductory chapter provides an overview of the hard disk drive technology developments that are pushing storage capacities in future products. Next, the two main approaches for the next generation HDDs, heat assisted magnetic recording (HAMR) and bit patterned media (BPM) are introduced. Finally, the motivation and objectives of this dissertation are given.

### 1.1 Technology Developments for HDDs

A continuous goal for HDDs is to increase the storage areal density without raising the cost significantly. In the past two decades, magnetic storage areal density has increased at a rate of more than 25% per year, as shown in Figure 1. 1 [3]. As the areal density increases, the cost for storing data continues to drop (Figure 1. 2). Compared to solid state drives (SSDs), HDDs still provide a larger capacity for a lower price. Currently, the cost per gigabyte of data for HDDs is about 1/10 of that for SSDs.

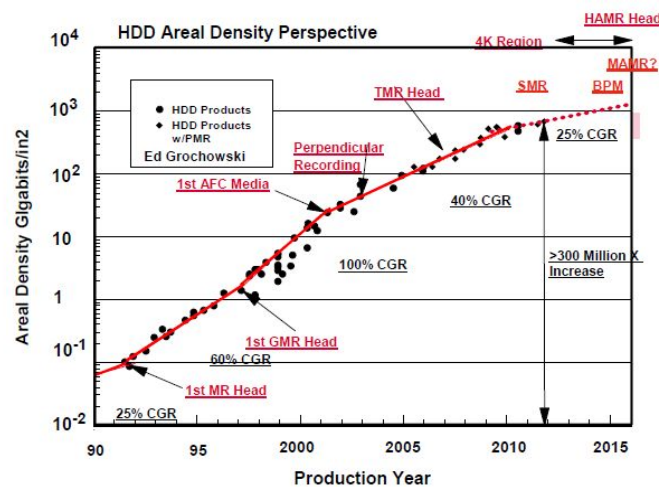


Figure 1. 1 Areal density increase curves for HDD and flash SSD in the past decades [3]

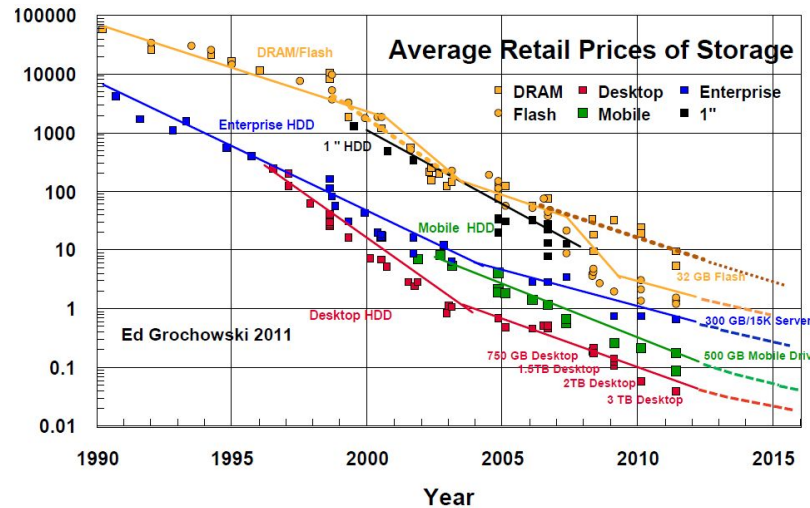


Figure 1. 2 Cost for per GB for HDD and flash SSD in the past two decades [3].

Technical innovations contribute to the continuing increase of areal density and cost reduction for HDDs. The innovative story of HDDs started 58 years ago with the invention of the 5 MB expensive and giant IBM disk. Currently, a 3.5 inch HDD provides a total storage capacity of 5 TB with a price lower than \$100.

The first HDD, RAMAC (random access method of accounting and control), was introduced in 1956 for the IBM 305 computer [4]. The RAMAC's cabinet was 60 inches long, 68 inches high and 29 inches wide. The data was stored in fifty 24-inch disks with a total storage capacity of about 5 MB (Figure 1. 3). The pressurized air was used to control the spacing between the head and disk, and it took a room full of compressors to supply the air needed to float the flying sliders to keep them from contacting the rotating disk surface. The cost of the RAMAC unit was about \$ 57,000.

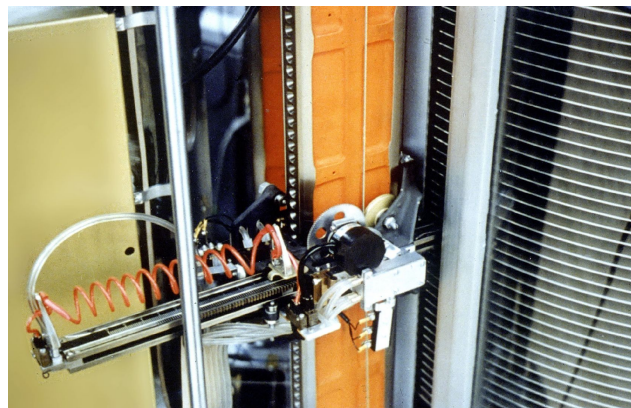


Figure 1. 3 IBM RAMAC 350 Magnetic Disk Drive, 1956 [4]

In 1973, IBM introduced the IBM 3340 "Winchester" disk drive [5], the first significant commercial use of low mass and low load heads with lubricated platters, as shown in Figure 1. 4. The IBM 3340 drive featured a small read/write head that flew

closer to the disk surface. The air gap was 18 millionths of an inch. The disk size was about 14-inches. The IBM 3340 drive had an areal density at about 1.7 Mb/in<sup>2</sup>. The “Winchester” drive had almost all the same major functional parts as the modern HDDs.

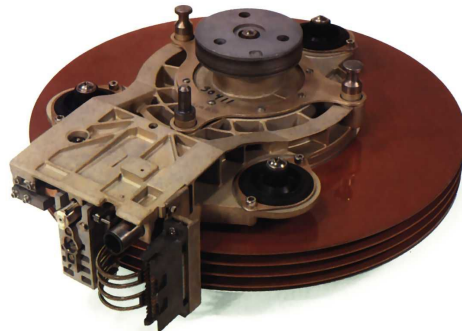
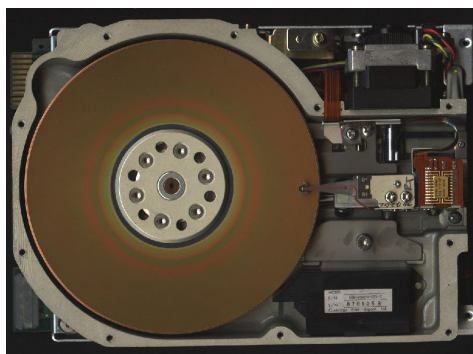
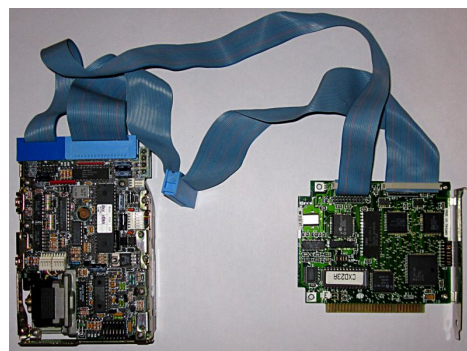


Figure 1. 4 Structure of “Winchester” HDD [5]

Small HDDs based on magnetic recording storage first appeared in 1980 when Seagate designed and announced a 5 MB hard disk ST-506 in a 5 1/4 inch form factor, as shown in Figure 1. 5 [6]. One of the main advantages of this HDD was that it could be integrated into the body of a personal computer. The ST-506 could be connected to a computer system through a disk controller.



(a) ST-506 hard disk drive



(b) controller interface

Figure 1. 5 Small integrated HDD (ST-506) in a PC

Modern HDDs have a similar internal structure design as the “Winchester” HDD. The major parts are shown in Figure 1. 6. The HDD is mainly composed of a few magnetic disks on a spinning spindle, an actuator arm with several flexible suspensions, one flying head for every face of each disk attached to the suspension, and some electronic boards for the signal processing and communication with a computer. The magnetic transducer with magnetic reading and writing parts are carried by the flying heads. Figure 1. 6b shows a typical head with the air bearing surface and magnetic transducer.



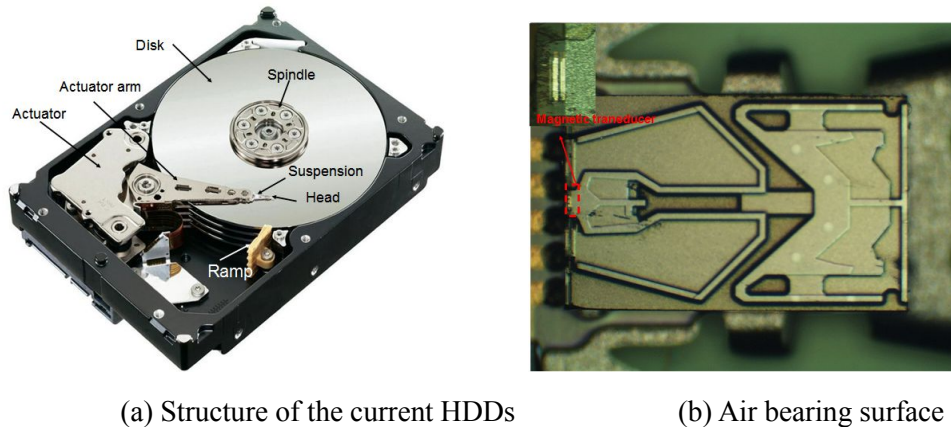


Figure 1. 6 Structure of the modern HDD and microscope image of the air bearing surface

In the past few decades, great effort has been made to improve the performance and storage density of HDDs. One fundamental requirement to increase the storage areal density is to reduce the size of a magnetic bit so more data can be stored on a fixed area disk. However, shrinking a magnetic bit brings other changes for the HDDs. For example, to get stable and strong enough readback signals with an acceptable signal to noise ratio (SNR), the gap between the head and disk should be reduced, or the gain of the magnetic readback sensor should be enhanced. The position of the head should be controlled more precisely because the track width is also reduced.

In 1989, the giant magneto-resistance (GMR) sensor was announced, which provided a huge improvement of the performance of the magnetic reader. With a GMR reader, the field sensing effect was far superior to the conventional MR head so that the readback signal was much stronger. The first head with a GMR sensor was introduced for HDDs in the late 90s [7]. The implementation of a GMR in a HDD enabled greatly increased storage densities in the next few decades.

The data (user information) in a HDD is recorded to the disk and retrieved from the magnetic orientation of magnetic bits. There are two basic directions of the magnetic orientations: in-plane and out-of plane of the disk, which are referred to as longitudinal magnetic recording (LMR) and perpendicular magnetic recording (PMR), as shown in Figure 1. 7 [8]. Figure 1. 8 top and bottom shows a magnetic image of the magnetic bits from a LMR and PMR disk, respectively. The magnetic image was obtained by a magnetic force microscopy (MFM).

LMR dominated in HDDs for several years and successfully extended the areal density to about  $100 \text{ Gb/in}^2$ . PMR was first proposed to have advantages over LMR in 1970s by Shun-ichi Iwasak [9, 10]. But it was not commercially implemented until 2005. The LMR was replaced by the PMR because there was a thermal stability limit of the LMR at an areal density of about  $100 \text{ Gb/in}^2$  [11, 12, 13].

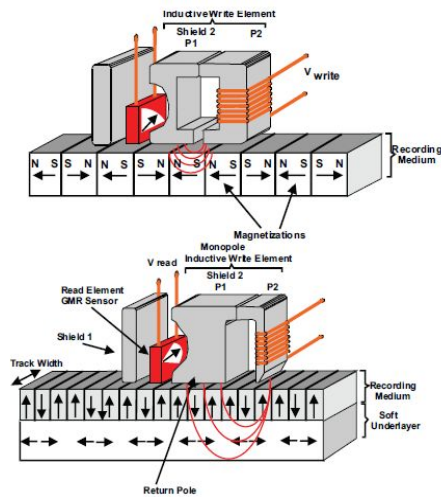


Figure 1. 7 Longitudinal recording diagram (top)  
and perpendicular recording diagram (bottom) [8]

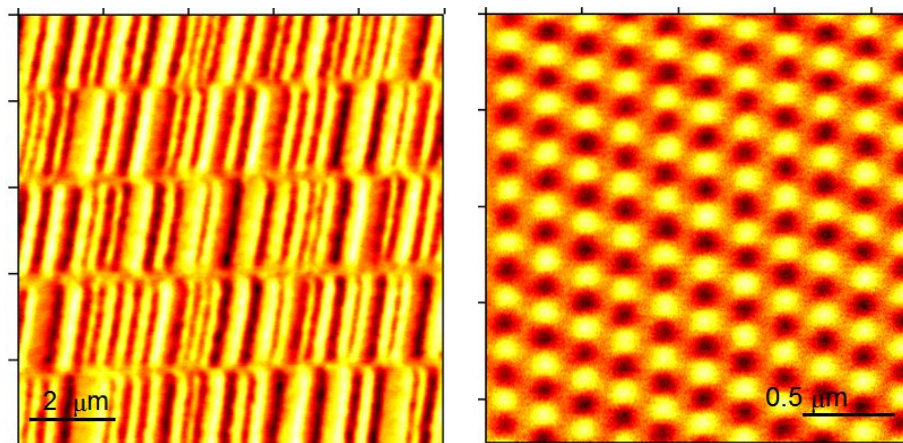


Figure 1. 8 MFM image of the LMR disk (left) and servo zone of the PMR disk (right)

As the storage areal density increased, the head to media spacing (HMS) between the slider and the recording disk has been reduced from microns to a few nanometers in order to get a strong readback signal and small error rate. Figure 1. 9 shows the HMS trend as the areal density increases [14]. Some novel air bearing designs have been proposed. With those new designs, the head can fly lower than 10 nm. However, at a gap of several nanometers, the intermolecular force starts to affect the stability of the slider's flying status [15].

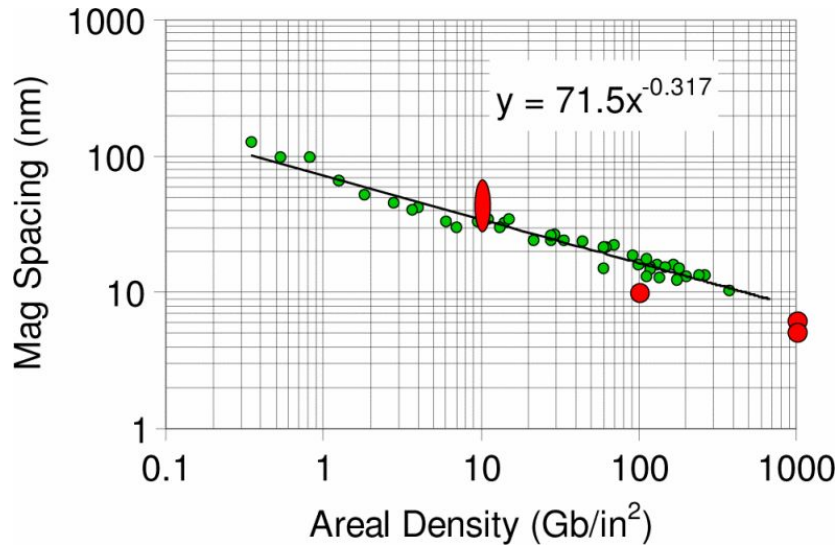


Figure 1. 9 Trend of head media spacing (HMS) as areal density. Green: Actual HDD data, Red:Earlier predictions [14]

In 2007, a new technology called thermal fly-height control (TFC) [16, 17] was introduced to HDDs to reduce the fly-height without losing the fly stability, as shown in the sketched drawing (Figure 1. 10). An electric heater is integrated into the head body at the location close to the magnetic reader and writer. When electrical power is applied to the heater, its temperature increases, and thermal expansion of the material close to it occurs. Due to the mismatch of the coefficients of thermal expansion of the heater material and head material, a local thermal protrusion is generated. This thermal protrusion is about tens of microns wide and several nanometers high towards the disk surface. The dimension of the local protrusion can be adjusted by the power input to the heater. The magnetic transducer is at or very near the tip of the protrusion, and so it is closer to the disk surface compared to other surface areas on the slider. The gap between the magnetic transducer and disk is reduced while a large portion of the head body is still relatively far away from the disk. The minimum fly-height can be reduced to less than 5 nm with the TFC technology while the slider still flies stably [18, 19].

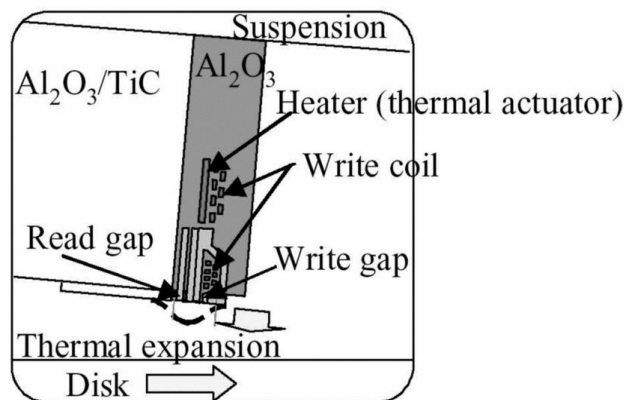


Figure 1. 10 Sketch-up of TFC technology for slider [17]

## 1.2 New approaches

In the past few years, PMR has successfully increased the areal density of magnetic recording by shrinking the size of the magnetic bits and magnetic grains. Current PMR drives reach a maximum areal density of about 800 Gb/in<sup>2</sup>. However, as the storage density is increased beyond 1 Tb/in<sup>2</sup>, there is a trilemma that prevents the further scale up for PMR technology, as illuminated in Figure 1. 11.

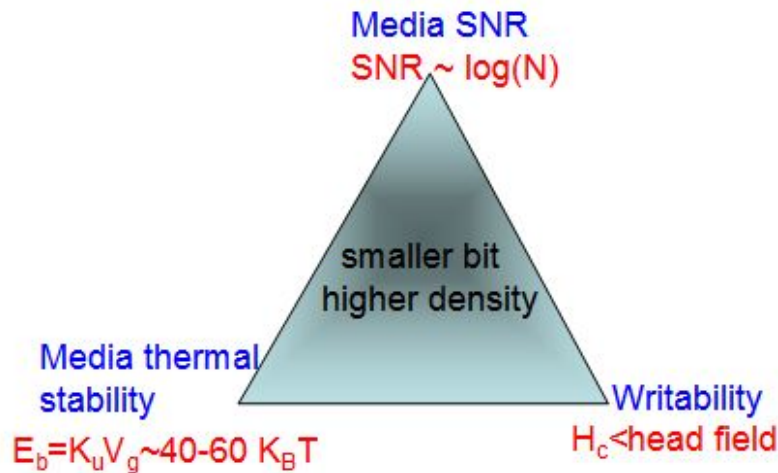


Figure 1. 11 Magnetic trilemma for the PMR technology

Billions of bits are stored on a magnetic disk. As the storage density increases, the size of each magnetic bit must shrink without degrading other performances (e.g. the reading, writing and storage stability). For a continuous granular magnetic media, each magnetic grain has random easy axis orientation. One magnetic bit is composed of some number of highly packed magnetic grains. The magnetic orientation for one bit is determined by the overall orientations of all of the magnetic grains in this bit. The SNR for magnetic recording is approximately given by the equation 1.1 [20]. For the continuous perpendicular magnetic media, the number of grains in one bit should be almost a constant in order to get an acceptable SNR. There is not much margin to reduce the size of the bit by cutting the number of magnetic grains. Therefore, using finer magnetic grains is the preferred option for reducing the size of a magnetic bit for the continuous magnetic media.

$$SNR \propto 10 \log(N) \text{ dB} \quad (1.1)$$

A finer grain has a smaller volume. However, the volume of a magnetic grain affects its thermal stability [21], as shown in equation 1.2. Here,  $P$  is the switching probability of a magnetic grain under thermal activation.  $E_b$  is the energy barrier to switch the orientation of a magnetic grain.  $E_b$  approximately equals  $K_u V$ , where  $K_u$  is the magnetic anisotropy, and  $V$  is the volume of a grain.  $K_b$  is the Boltzmann constant, and  $T$  is the

absolute temperature.  $K_u V / k_B T$  normally, must be larger than 40 to maintain adequate thermal stability of the magnetic bits for several years at room temperature [21].

$$P \propto e^{-E_b / k_B T} = e^{-K_u V / k_B T} \quad (1.2)$$

It can be seen from equation 1.2 that the magnetic switching probability is inversely proportional to the energy barrier of the grain. At higher temperatures, the orientation of a magnetic grain is easier to switch. At room temperature, the thermally stable recording for 5 years requires that  $K_u V$  be larger than  $40 k_B T$ . However, as the volume of a magnetic grain is reduced for a higher areal density,  $K_u V$  is no longer larger than  $40 k_B T$  if  $K_u$  is not raised. In this situation, magnetic storage is not thermally stable at room temperature because the orientation of the magnetic grain fluctuates randomly under thermal activation, known as superparamagnetism. So  $K_u$  should be raised to make the magnetic grain thermally stable. A magnetic material with higher anisotropy is recommended to reach magnetic thermal stability.

The higher anisotropy means that the material has higher magnetic coercivity. A material candidate, the  $L_{10}$ -FePt based magnetic thin film [22] has a magnetic coercivity greater than 1.5 Tesla. The magnetic writer needs to generate a switching field with a magnitude more than 3 Tesla to switch the magnetic grains. As indicated by equation 1.3, a higher switching field is needed if the anisotropy of the material is higher [23].

$$H_k = \frac{2K_u}{M_s} \quad (1.3)$$

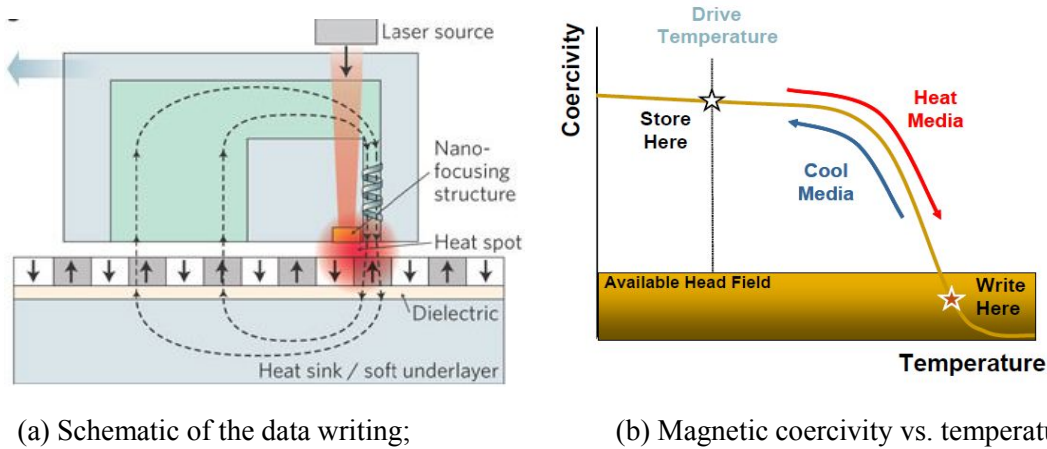
It is challenging to generate such a strong magnetic switching field with current magnetic transducers. The high-density perpendicular writing field is limited to about 2 Tesla for current PMR technology [24]. What is more, as the size of the writer shrinks to write smaller magnetic bits, the magnetic writing field will further decrease. So data writing is more difficult to achieve if a magnetic material with higher anisotropy is used as the storage layer.

This trilemma among the thermal stability, SNR and writability for PMR essentially blocks the further scaling up of the areal density for present HDDs. However, a few approaches have been recently proposed to break the trilemma.

Among those approaches, heat assisted magnetic recording (HAMR) [25, 26] and bit patterned media (BPM) [27, 28] are proposed to extend the areal density to over 1 Tb/in<sup>2</sup>. HAMR uses high anisotropy materials to break the superparamagnetism limits and introduces a new writing method to reach writability. BPM breaks the limits of the grain number in a bit while still withholding an acceptable SNR.

In HAMR systems, as the name implies, thermal heating is employed during the data writing. The temperature of a high anisotropy recording medium is locally elevated

to facilitate the writing process by significantly reducing the required magnetic switching field. Then, the temperature drops abruptly to room temperature, and the magnetic information is frozen in a stable state. As shown in Figure 1. 12, a laser is placed in front of the magnetic writer. The writing is performed after the local temperature of the disk is raised to near the Curie point of the magnetic material. At the Curie point, the coercivity drops to almost zero, and the orientation of the magnetic grain can be easily switched. In order to avoid the data erasure to the adjacent tracks or bits, the size of the heating spot should be close to the size of a magnetic bit.



(a) Schematic of the data writing;

(b) Magnetic coercivity vs. temperature [29]

Figure 1. 12 Concept of HAMR.

Equation 1.4 shows the relationship between the effective writing field gradient and thermal gradient. It indicates that increasing the thermal gradient can equivalently increase the effective writing field gradient. A larger writing field gradient benefits the maximum down-track recording density in a given medium. Meanwhile, a high cross-track gradient also helps to reduce the adjacent track erasure effects. So HAMR scales more favorably than the conventional PMR for higher areal density recording: higher anisotropy for more thermal stability and higher effective field gradient for better writing performance [29]

$$\frac{dH_{write}}{dx} = \frac{dH_k}{dT} \frac{dT}{dx} \quad (1.4)$$

Quite different from the HAMR technology, BPM technology mainly breaks the limits of the SNR for a continuous granular material. The transition noise for continuous granular films, originating from irregularities or jaggedness in the magnetization transitions, mainly depends on the boundaries between the magnetic bits. Instead of using continuous films, BPM prefers discrete magnetic islands to store the information as shown in Figure 1. 13 [30]. The grains within each patterned island are coupled so that the entire island behaves as a single magnetic domain. By physically separating the magnetic islands, transition noise is eliminated because there is no transition boundary between the two islands. The SNR for the BPM does not need to follow equation 1.1. The

number of grains in a magnetic island in BPM can be much less than that in the traditional PMR. So the volume of the magnetic grains in the BPM can be increased thus it is thermally stable.

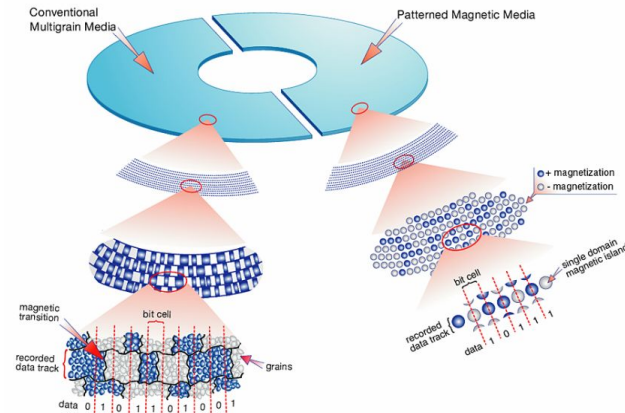


Figure 1. 13 Comparison of conventional PMR continuous granular media with BPM [30]

Those approaches can be combined together to further increase the areal density. As demonstrated in reference [26], HAMR can work on a patterned media as well. The combination of BPM and HAMR provides even more benefits for data writing. The total power absorption by an island of BPM is four times larger than that of a flat continuous media, as shown in Figure 1. 14. It has been said that heat assisted writing on the patterned media has the capability to extend the areal density to 100 Tb/in<sup>2</sup> [31]

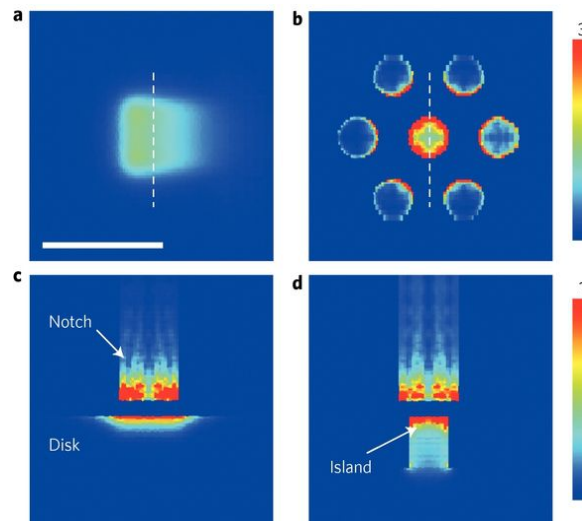


Figure 1. 14 Comparison of antenna coupling to continuous and bit patterned media. a, Top view of disk surface absorption profile on continuous medium. Peak value = 1.4. b, Top view of disk absorption profile on bit-patterned medium. Peak value = 16.5. c, Side view of a. Peak value = 2.8 (in notch). d, Side view of b. Peak value = 7.9 (in island). Scale bar, 50 nm (a–d). The colour scale in b applies to a, and the colour scale in d applies to c [26].

### 1.3 Motivation

Current HDDs rely on a floating slider that flies above the recording disk without contacts. The slider, the disk and the air gap between the slider and disk compose the head-disk interface (HDI). There are several functional layers on both the disk and slider to make the HDI reliable, as shown in Figure 1. 15.

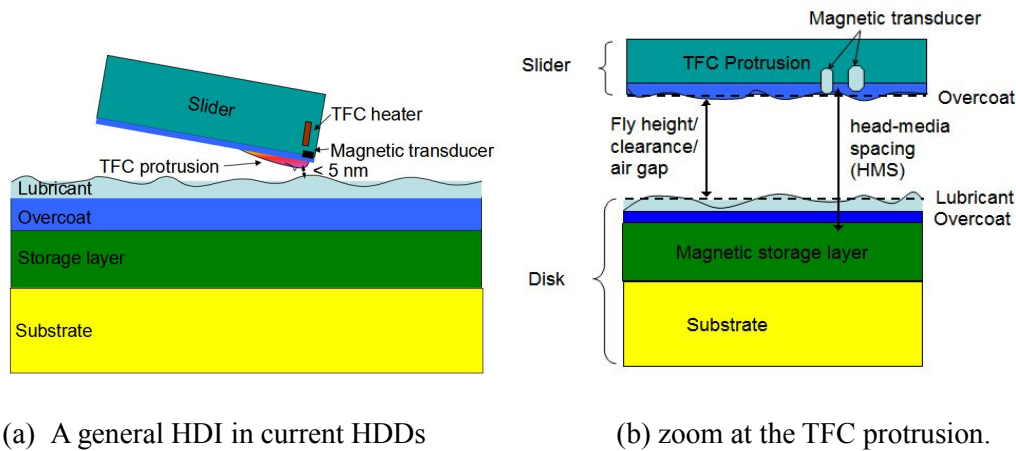


Figure 1. 15 Schematic drawing of the HDI for a PMR drive (figures are not to scale).

The top surface of a disk is a perfluoropolyether (PFPE) lubricant layer, including bonded and mobile parts, with a total thickness of about 1 to 2 nm. Lubricants like Z-Dol or Z-Tetraol are currently used in HDDs to reduce the friction and wear during head-disk contacts [32]. It can also reduce the surface energy, thus reducing the intermolecular forces between the head and disk. The mobile part of the lubricant allows the lubricant to recover if some change happens at high air pressures or after contact.

The layer below the lubricant is a diamond like carbon (DLC) overcoat, which is about 2 to 4 nm thick [33]. The DLC overcoat can function as a protective layer because of its relatively high hardness and high resistance to corrosion. The strong mechanical properties of DLC can be attributed to the highly concentrated SP<sup>3</sup> hybridization of the carbon atoms, which exists in the diamond material.

The storage layer is underneath the DLC overcoat. It is made from magnetic material for storing data. The thickness of the storage layer is about 20 nm. The data is permanently lost if the storage layer is damaged. Current PMR media uses granular continuous materials for the storage layer, such as CoPt alloys. For a HAMR system, a material with higher coercivity will be used as the storage layer to reach the thermal stability. L<sub>10</sub>-FePt alloy is one of the more promising candidates for HAMR systems [22]. In a BPM system, the magnetic storage layer is discrete rather than continuous.



As the fly-height (FH) of the slider drops to less than 5 nm, the surface of the disk should be smooth enough to avoid intermittent contacts between the slider and disk. Currently, the surface RMS roughness of the disk is about 0.1 to 0.2 nm.

On the slider side, the main body of the slider is made from AlTiC and alumina. In order to protect the head from contact and corrosion, a DLC overcoat is deposited on the surface. A TFC heater is embedded at a particular place in the slider to generate a local protrusion towards disk.

The structure of the HDI for HAMR systems is slightly different from that in PMR because of some unique requirements of HAMR systems. A schematic diagram of a typical HAMR HDI structure is illustrated in Figure 1. 16. Many of the components are also commonly used in perpendicular recording media (PMR) technology, such as an embedded TFC heater in the slider, a lubricant layer, a carbon overcoat (COC), a recording layer, a properly designed soft underlayer (SUL), and an interlayer for magnetic property and microstructure control. However, there are many unique aspects of HAMR systems. A laser diode is integrated into the slider. The light is delivered to a near field transducer (NFT) structure by an optical waveguide. The NFT structure is usually made from some metals located at the air bearing surface of the slider. Moreover, a heat sink layer is suggested underneath the storage layer in order to optimize the thermal response of the media and provide a larger thermal gradient [29]. These new functions make the HDI in HAMR systems more complicated than in PMR.

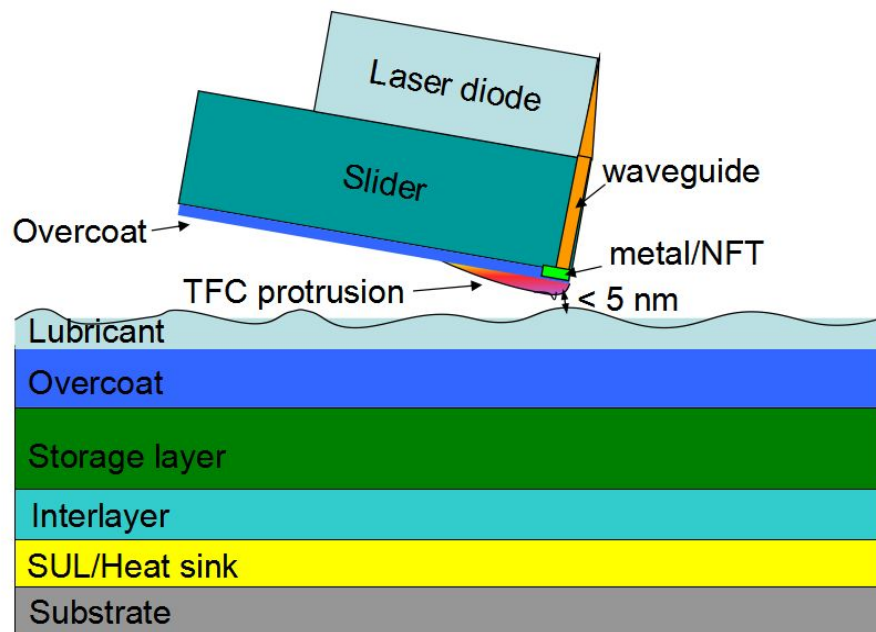


Figure 1. 16 Schematic drawing of HDI for HAMR systems

In HAMR systems, a laser is used to locally heat the disk to the Curie temperature of the magnetic material, which is about 400 to 600 °C. This thermal environment brings

challenges for the stability and reliability of the HDI. A successful HAMR drive has more stringent requirements for the thermal stability of the HDI compared with the current PMR technology. A full evaluation of the HDI thermal stability of the current PMR is necessary when the HDD industry moves to HAMR.

The lubricant changes under the HAMR conditions by various mechanisms, including thermal desorption, decomposition, depletion, evaporation. These processes can cause the lubricant's thickness to change. The failure of the lubricant can cause instability of the air bearing slider's flying and serious wear of the head and disk after the contact.

The carbon overcoat on both the disk and slider can be graphitized and/or oxidized under high temperatures. When the DLC becomes graphitized or oxidized, its mechanical properties degrade as well. Thus, the overcoat loses its ability to protect other layers underneath it. The surface can also become rougher under the high temperature environment, which increases the likelihood of the head-disk contact.

It has been found that the temperature increase of the metal layer for the NFT can be several hundred degrees [25]. A noble metal such as gold is preferred in the NFT because of its good properties in the near field optics. However it has a relatively low melting point, around 1000 °C, which indicates it could be easily changed at the media Curie point after applying the thermal load [34]. And it is very ductile, so that the geometry could be changed during the heating. Moreover, the cyclic thermal condition can make the damage to the NFT metal film more serious due to the material fatigue.

With the exception of material failure or geometry changes of the NFT structure, the mismatch of the coefficient of thermal expansion among different materials around the NFT can cause a local thermal protrusion [35]. The size of the thermal protrusion has been experimentally measured by AFM [36]. It is about a few microns large and 1 nm high. This NFT protrusion superposes on the TFC protrusion, thus reducing the minimum space between the slider and disk. With such a protrusion, the slider has a higher risk of contacting the disk at the tip of the protrusion. The contact can damage both the NFT structure and the disk surface, leading to the failure of a HAMR drive.

The study and analysis of the HDI for HAMR is more complex than in PMR. There are multiple physical couplings among the optical, thermal, mechanical, and magnetic phenomenon in the HDI for HAMR systems. Figure 1. 17 shows some possible couplings among different aspects of the HDI. Thermal energy from a laser diode is delivered to the NFT by an optical waveguide. Some of the light energy is absorbed and dissipated as heat in this process, thus raising the bulk temperature of the slider, behaving as an optical thermal coupling. The light is also focused to a small spot on the disk by the NFT. A large fraction of the energy is dissipated around the NFT because the energy efficiency of the NFT is usually limited to less than 10% [37]. Thermal deformations of the NFT and slider lead to a change of the minimum fly-height, which can be treated as a thermal-mechanical coupling. Furthermore, the thermal deformation of the NFT structure

affects the optical performances of the NFT, such as light transmission efficiency, peak intensity and intensity profile. In this way, there is an optical-mechanical coupling for the NFT. From the disk side, the light energy is finally transmitted to the disk surface and gets absorbed by multi-layers of the disk. Thermal deformation of the disk and depletion of the lubricant occurs as the local temperature of the disk is raised. It is a thermal-mechanical process. Magnetic switching can be achieved by the magnetic transducer when the temperature of the magnetic layer approaches or reaches the Curie point. The thermal-magnetic coupling dominates in this switching process.

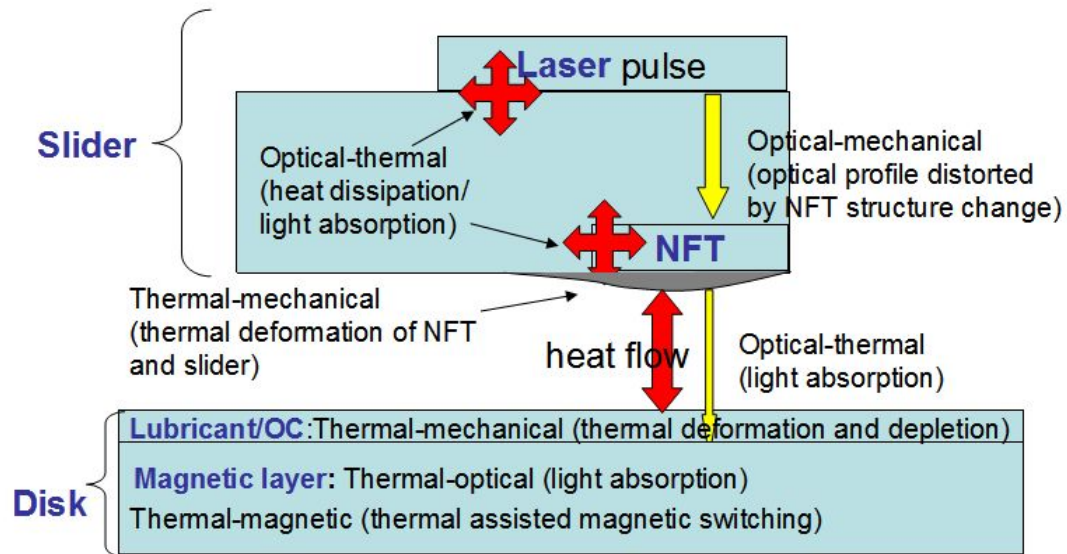


Figure 1. 17 Multiple physical couplings among light, heat, mechanical deformation and magnetics inside the HDI of HAMR systems

In addition to the multi-physics characteristics of the HDI in HAMR, the study of the HDI involves different scales in both length and time, as listed in Table 1.1. The timescale covers more than seven orders of magnitude. The fastest is on the order of a couple of nanoseconds. The length scale covers about 6 orders, while the smallest is around a few nanometers.

Table 1. 1 Length and time scales in HDI for HAMR

Length		Time	
Slider dimension	~1 mm	Life time of HDD	~ 5 years
TFC protrusion	~10 $\mu\text{m}$ by ~ 10 nm	Air bearing resonance	~ 10 $\mu\text{s}$
NFT dimension	~ 0.5 $\mu\text{m}$	TFC response	~ ms
NFT protrusion	~ 1 $\mu\text{m}$ by ~ 1 nm	Laser on for data sector writing	~ 20 $\mu\text{s}$
Heating spot on disk	~ 50 nm	NFT thermal response	~ 10 $\mu\text{s}$
Grain size of magnetic layer	~ 7 nm	Disk heating and cooling	~ 1 ns
Disk protrusion	~ 0.1 nm	Disk deformation	~ ns
Fly-height	< 5nm	Magnetic switching	~ 1 ns

As for the BPM technology, one of the main challenges for its commercial application is the large volume manufacturing of the patterned media disks. The patterned media fabrication has to use available lithography tools. The minimum feature size of the patterned island is about or less than 25 nm for 1 Tb/in<sup>2</sup> [38]. Meanwhile, the conventional optical lithography technology for the semi-conductor industry does not provide an in-time and cheap solution for the BPM. As shown in the international technology roadmap for semiconductors (ITRS, Figure 1. 18) [39], it still will be a couple of years for the semiconductor industry to move to a full production extreme ultraviolet lithography (EUV) which creates a feature size less than 20 nm. But even in 2011, a complete UV lithography machine cost more than 20 million dollars. New cheap alternative lithography approaches with a resolution better than 20 nm are needed for the fabrication of the patterned media.

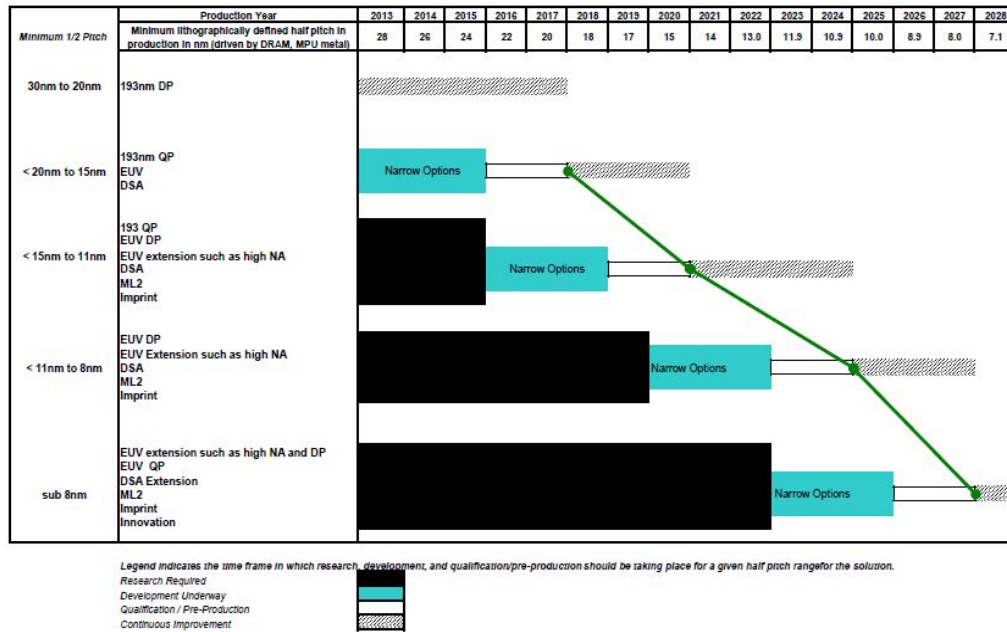


Figure 1. 18 DRAM and MPU Metal Level Potential Solutions for ITRS

## 1.4 Objective

In this dissertation, the changes of the HDI under the HAMR conditions are experimentally investigated with the assistance of a HAMR testbed and numerical models. Different mechanisms of the HDI changes are discussed. The possibility of developing a cheap nanolithography tool for the fabrication of BPM disk is explored as well.

Chapter 2 introduces a method of obtaining the relationship between the temperature increase and distribution and laser power input. It is the first step in studying the HDI in HAMR systems since HAMR writing is very sensitive to the temperature increase of the disk. The data writing can only be achieved when the temperature of the magnetic media approaches or exceeds the Curie point of the magnetic material.

In Chapter 3, the design of the HAMR testbed is introduced. The specifications and functions of this HAMR testbed are also given.

Chapter 4 focuses on the thermal behavior of the lubricant. The lubricant depletion and reflow under various HAMR conditions are investigated experimentally.

Chapter 5 mainly discusses changes in the carbon films under the HAMR conditions. The surface reflectivity and topography changes of the carbon films under various heating methods are discussed.

In Chapter 6, the changes of the NFT under laser heating are discussed. A two-stage heating scheme is proposed to reduce the thermal load to the NFT. With reduced thermal load, the lifetime of the NFT can be extended.

In Chapter 7, the dynamic response to the disk waviness of the HAMR slider with a TFC protrusion and a NFT protrusion is discussed. A new slider design method of combining the TFC and NFT protrusion is proposed for minimizing the flying height modulation (FHM) and reducing the possibility of contact between the NFT and the disk.

In Chapter 8, a plasmonic nanolithography machine is introduced to assist the fabrication of the master disk for BPM. The key specifications and technical details of this lithography machine are also given.

Chapter 9 presents a summary of this dissertation and some suggestions for future studies.

## **Chapter 2 Temperature calibration based on magnetization decay for perpendicular media**

### **2.1 Introduction**

In HAMR systems, a more thermally stable magnetic material than the current PMR media will be used as a recording layer to break the limit of superparamagnetism. However, the coercivity of this material is so high that it is difficult for the magnetic transducers to switch the magnetic orientations at room temperature. For example, one of the HAMR media candidates, a  $L_{10}$ -FePt based magnetic layer, has a coercivity greater than 1.5 Tesla [22], which requires a switching field more than 3 Tesla from the magnetic transducer. However, the high-density perpendicular writing field is limited to about 2 Tesla for the current PMR technology [24]. In order to achieve data writing in HAMR, the temperature of the media should be raised because the coercivity of the magnetic material drops sharply at high enough temperatures. When the temperature is close to the Curie temperature of the magnetic material, the coercivity reduces to almost zero.

In HAMR systems, a laser is proposed as a means to heat the media to the Curie point. Simultaneously, a magnetic field is applied from the magnetic transducer to switch the magnetic bits. The success of the magnetic switching is very sensitive to the media temperature [29]. If the temperature is too low compared with the Curie point, the magnetic transducer will not be able to write any information into the media. Conversely, heating the media over the Curie point requires more energy and may bring a greater challenge for the head-disk interface (HDI). It is therefore very important to understand the local temperature increase during the laser heating and to calibrate the laser power input for HAMR writing. The maximum temperature and the temperature profile are two critical factors for determining the performance of writing. The maximum temperature determines the writeability because the success of writing depends on getting the local media temperature to the Curie point. The size and shape of the magnetic writing bit depends on the temperature profile.

Some studies have been reported that evaluate the temperature increase by use of numerical and experimental methods [40, 41, 42]. Tagawa et.al. [40] observed disk refractive index changes during the laser heating and compared it with the change under conventional oven heating. Their method can be used to get the average temperature during the laser heating. But it has some limitations for getting accurate temperature distributions because of the strong averaging effect for the refractive index measurement by the ellipsometry.

The magnetic Kerr effect combined with optical probing technology [42] has recently been used to study the material's kinetic response under the local laser heating in HAMR systems. The optical measurement of the magnetization by this method is also limited because the size of the laser beam is much larger than the magnetic bits.

Phase change materials can be used to study the relationship between the laser energy input and material temperature [43, 35]. Laser-induced fluorescence has been widely used to measure the instantaneous temperature field [44]. However, the thermal properties of both phase change materials and fluorescent materials are quite different from those of the magnetic layer in HDDs. So the methods based on phase change and fluorescence are not exactly suitable for investigating the thermal behavior of HAMR systems.

In this study, we propose another method to investigate the local temperature increase under the laser heating based on the magnetization decay [45]. This method has the capability of providing the maximum local temperature increase and the temperature history. In Section 2.2, the Arrhenius-Neel (A-N) model is introduced, which is used to simulate the magnetic decay under local laser heating. Section 2.3 provides the experimental conditions and procedure. The experimental results are discussed in Section 2.4. In Section 2.5, a finite element model is built to explain the data. The numerical simulation results are compared with the experimental results. Finally we present our conclusions in Section 2.6.

## 2.2 Numerical model for the magnetic thermal decay

The magnetization decays at high temperatures, as described by the Arrhenius-Neel model [46].

$$\begin{aligned} \frac{dM}{dt} &= -f_0 \exp\left(-\frac{E_b}{K_b T}\right); \\ E_b &= K_u V \end{aligned} \quad (1)$$

where  $dM/dt$  is the time derivative of the magnetization,  $M$ .  $f_0$  is the driving frequency, set to be 1 GHz.  $E_b$  is the energy barrier to switching the orientation of a magnetic grain.  $E_b$  approximately equals  $K_u V$ , where  $K_u$  is the anisotropy and  $V$  is the volume of a grain.  $K_b$  is the Boltzmann constant and  $T$  is the absolute temperature.  $K_u V / K_b T$  normally must be larger than 40 in order to maintain adequate thermal stability of the magnetic bits for several years at room temperature.  $K_u$  also depends on the temperature, dropping as the temperature increases. The relationship between the saturation magnetization, the anisotropy and temperature can be obtained from the mean field theory as determined by the equations [23].

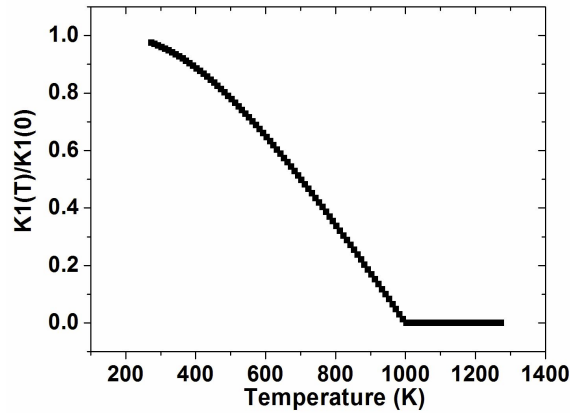


$$\begin{aligned}\frac{K_1(T)}{K_1(0)} &= \tanh(X) \tanh\left(\frac{X}{2}\right) \\ \frac{M_s(T)}{M_s(0)} &= \frac{1}{3} \left[ 2 \tanh(X) + \tanh\left(\frac{X}{2}\right) \right] \\ \frac{M_s(T)}{M_s(0)} &= \frac{5T}{6T_c} X\end{aligned}\quad (2)$$

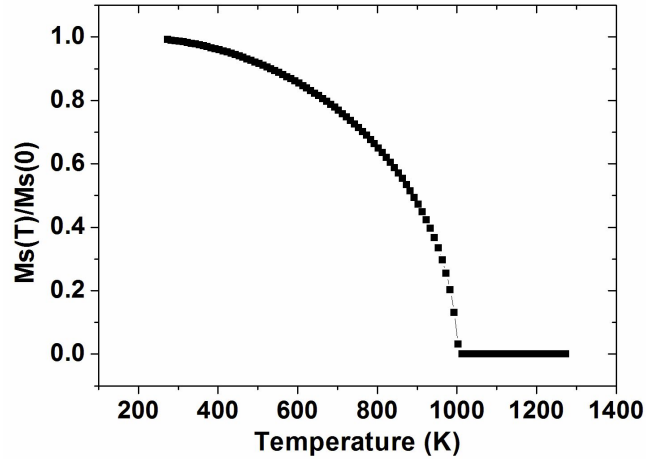
where  $X$  is a dimensionless number, called the Callen-Callen parameter, and it is proportional to the temperature averaged magnetization.  $M_s$  is the saturation magnetization and  $K_1$  is the first order anisotropy constant. The total uniaxial anisotropy  $K_u$  is composed of the first order anisotropy and other higher orders. Typically, the second order anisotropy is 3 to 10 times smaller than the first order, and its reduction due to the temperature increase is sharper. So the second order anisotropy is neglected, and we can set  $K_u = K_1$  to simplify the calculation [47].

$X$  can be obtained from the second and third parts of equation (2) and then  $K_u$  and  $M_s$  can be calculated from the first and second parts of (2). Furthermore, the energy barrier  $E_b$  can be obtained from the  $K_u$  for a fixed volume magnetic grain at a certain temperature. Thus the magnetization decay at a certain temperature can be obtained from equation (1). Finally, the magnetic decay behavior of the magnetic media under laser heating in HAMR systems can be simulated after the temperature history is known.

Figure 2. 1 shows the temperature dependency of the saturation magnetization and the magnetic anisotropy predicted from the Callen-Callen model for the PMR media. The Curie point was set to be 1000 K.



(a) Dependency of anisotropy on temperature from equation 2



(b) Dependency of  $M_s$  on temperature from equation 2

Figure 2. 1 Temperature dependency of the magnetic properties

The magnetization decay was accurately measured by a magnetic force microscopy (MFM) and quantitatively defined from statistical analysis of the MFM images. The thermal response of the media was obtained from a 3D finite element method (FEM) model using the ANSYS thermal solver. The temperature history from the thermal model was used as an input for the calculation of the magnetization decay behavior in the A-N magnetic model.

### 2.3 Experimental procedure

A PMR disk was used in this study because a HAMR disk is not available to us at this time. The PMR disk had an aluminum substrate. In order to quantitatively analyze the magnetization decay, we pre-recorded the magnetic disk with uniform single tone magnetic patterns. The track width was about 80 nm and the track pitch was about 200 nm. The disk was exposed by the laser in the HAMR test stage, shown in Figure 2. 2. The Gaussian radius ( $e^{-2}$ ) of the laser spot was close to 700 nm, and the power was varied from 15 mW to 51 mW in the experiments. The wavelength was 355 nm. Table 2.1 shows the laser power levels and densities for the experiments. The experimental procedure for the laser heating was carried out as follows: the laser beam was focused onto the disk surface, while the disk was rotated at 1500 RPM. The laser beam was moved radially at 0.125 mm/s toward the inner tracks of the disk. Thus, the pitch of the spiral laser heating track was 5  $\mu\text{m}$ , which was much larger than the laser spot size. So the thermal interference between two adjacent exposed tracks could be neglected. Different laser powers were applied at different radii. After exposure, the disk was scanned by a MFM to get the magnetic images.

Table 2. 1 Laser power levels and densities for exposure on the aluminum substrate PMR disk

Power (mW)	20	25	30	36	42	51
Density (mW/ $\mu\text{m}^2$ )	26.0	32.5	39.0	46.8	54.6	66.3

The MFM is a special mode of a scanning probe microscope. It has been widely used to map the magnetic field distribution of samples by detecting the magnetic interaction between the magnetic tip and sample. MFM has two scans in order to get the magnetic field distribution, as shown in Figure 2. 3. The tip scans the sample first with the tapping mode and obtains the surface topography in the first scan. Then the tip is lifted by a constant height with respect to the topography and scans again. At the lifted height, the intermolecular/atomic force interaction is very weak and can be neglected, while the magnetic interaction is the major interaction between the tip and sample. The magnetic information can be obtained from this second lift scan.

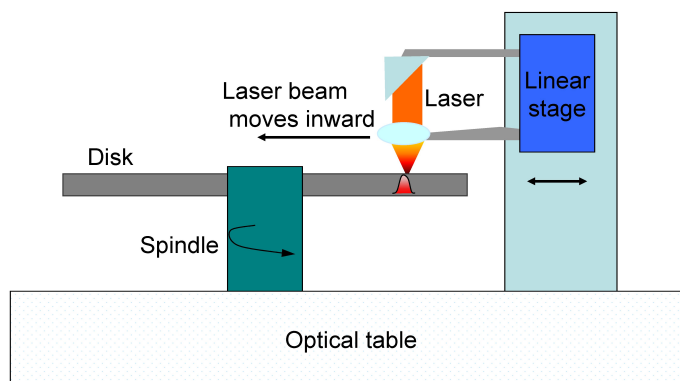


Figure 2. 2 Schematic plot of the experimental setup for HAMR study

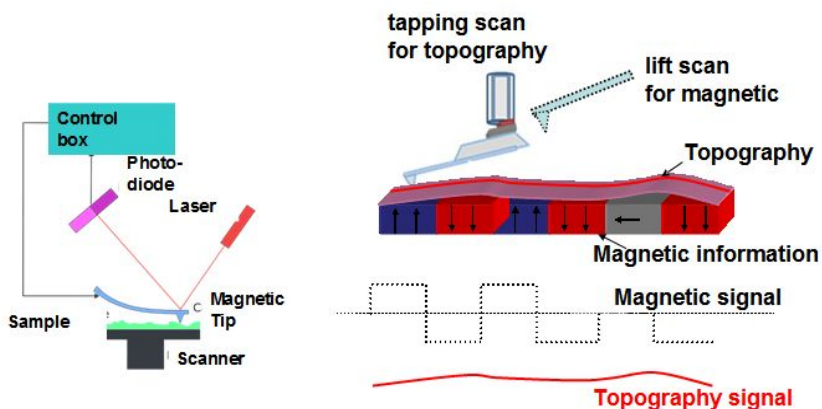
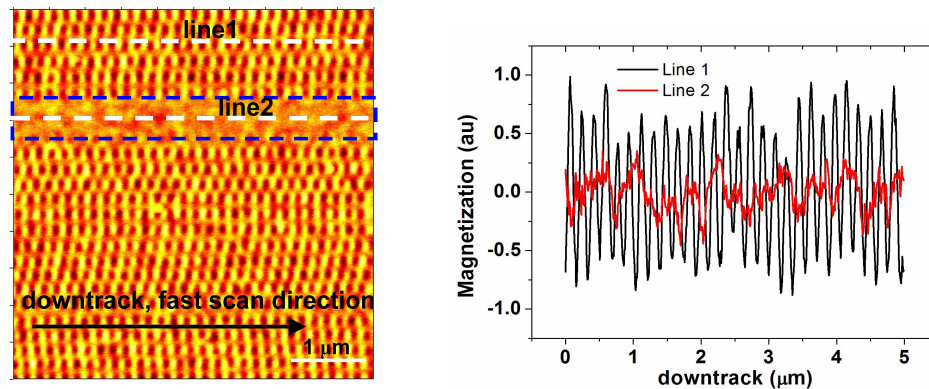


Figure 2. 3 Schematic plot of MFM

## 2.4 Experimental results and discussion

Figure 2. 4a shows a typical MFM image of the magnetic media after laser exposure. The fast scan direction (horizontal) was along the down-track direction. The exposed track is highlighted by the dashed box. Two line profiles were extracted from the magnetic image, as shown in Figure 2. 4b. The first line was from an unexposed area, and the second line was from an exposed area. The first line shows a periodic signal from the pre-recorded magnetic pattern. The amplitude of the second line is smaller than that of the first line, and the second line does not show any periodic characteristic because the magnetic pattern was thermally erased under the laser heating. The statistical analysis of these two profiles indicates that the root mean square (RMS) amplitude of the first profile is 0.49, while that of the second profile is 0.15. The RMS value of the scanning line can be used to represent the magnetic strength of the magnetic pattern and quantitatively define the magnetization decay.



(a) MFM image of the exposed disk

(b) Profiles of the two scanning lines in (a)

Figure 2. 4 A typical MFM image of the magnetic media after laser exposure

Figure 2. 5 shows the surface topography for different laser power densities. At a power density of  $26.0 \text{ mW}/\mu\text{m}^2$ , there was no observable change of the surface topography. But when the power was increased to about  $66.3 \text{ mW}/\mu\text{m}^2$ , an obvious surface change of the exposed track was observed from the topography.

Figure 2. 6 shows the MFM images of the PMR media after laser exposure at different power densities. At the power density of  $26.0 \text{ mW}/\mu\text{m}^2$ , there was no observable change of the magnetic pattern. But if the power was increased to about  $39.0 \text{ mW}/\mu\text{m}^2$ , an erased track was observed from the magnetic image. As the power density increased further, the erased area became larger due to the thermal diffusion, shown in Figure 2. 6d.

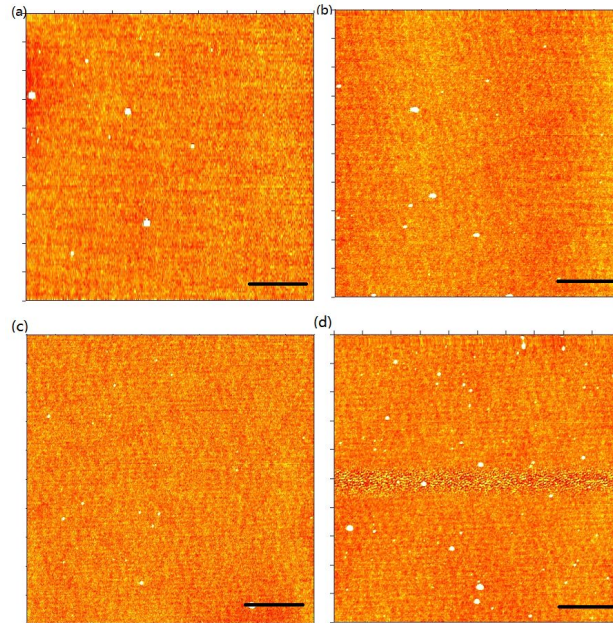


Figure 2. 5 Topography of the perpendicular recording media after laser exposure at different power densities. (a)  $26.0 \text{ mW}/\mu\text{m}^2$  ; (b)  $32.5 \text{ mW}/\mu\text{m}^2$ ; (c)  $39.0 \text{ mW}/\mu\text{m}^2$ ; (d)  $66.3 \text{ mW}/\mu\text{m}^2$ . From image a to d, the scan size is 5 by 5  $\mu\text{m}$  and the scale bar is 1  $\mu\text{m}$ . The down-track direction is horizontal.

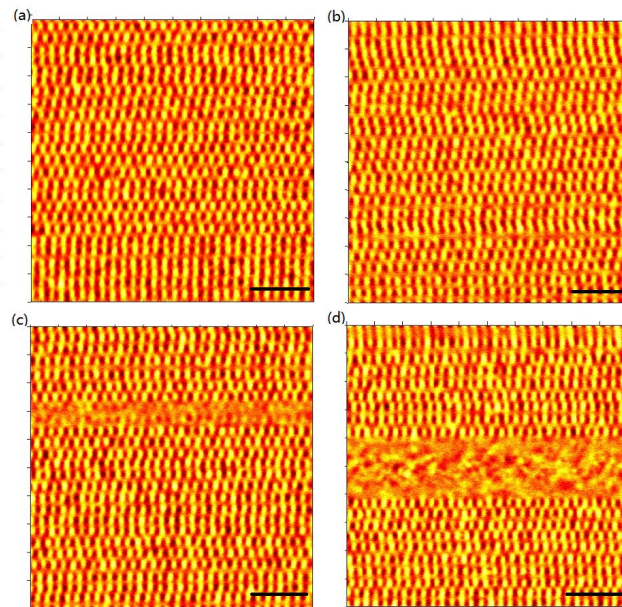


Figure 2. 6 MFM images of the perpendicular recording media after laser exposure at different power densities. (a)  $26.0 \text{ mW}/\mu\text{m}^2$  ; (b)  $32.5 \text{ mW}/\mu\text{m}^2$ ; (c)  $39.0 \text{ mW}/\mu\text{m}^2$ ; (d)  $66.3 \text{ mW}/\mu\text{m}^2$ . From image a to d, the scan size is 5 by 5  $\mu\text{m}$  and the scale bar is 1  $\mu\text{m}$ . The down-track direction is horizontal.

The RMS value of each horizontal scanning line was normalized by the value for the uniform magnetic pattern without laser exposure in the MFM images. The normalized RMS values can describe the magnetization of the magnetic pattern. Figure 2. 7 shows the normalized magnetization for various laser powers. There is no observable magnetization decay at  $26.0 \text{ mW}/\mu\text{m}^2$ . The magnetization decayed about 30% at  $32.5 \text{ mW}/\mu\text{m}^2$ . When the power was increased to  $39.0 \text{ mW}/\mu\text{m}^2$ , the magnetization disappeared around the center of the heating area. For larger powers, the width of the magnetization decay area increased due to the thermal diffusion.

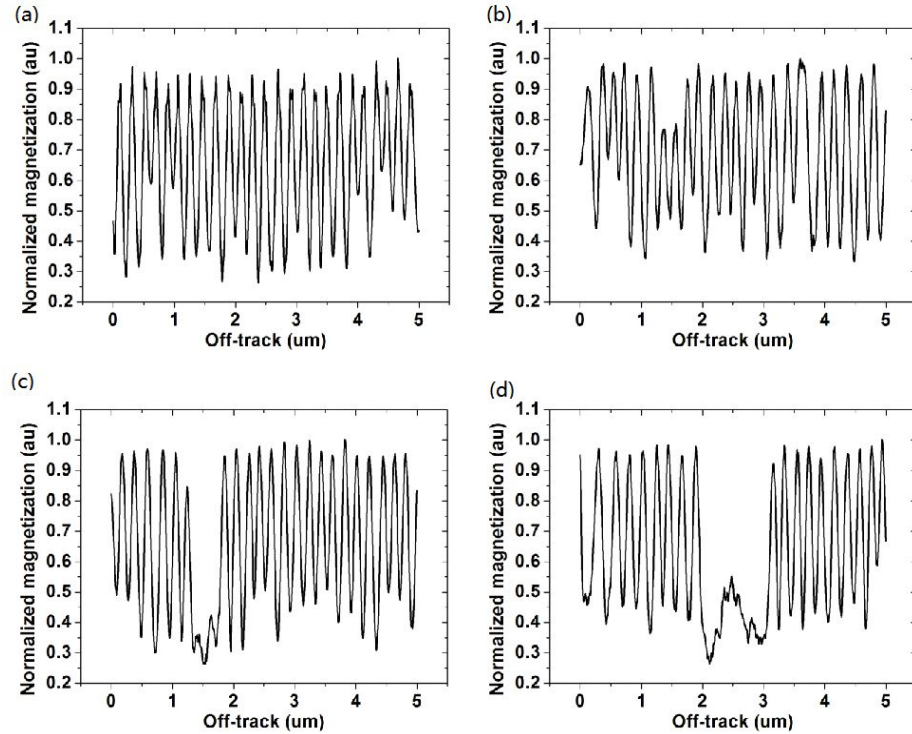


Figure 2. 7 Normalized magnetization along the down-track direction as a function of radial (off-track) displacement for different power exposure. (a)  $26.0 \text{ mW}/\mu\text{m}^2$  ; (b)  $32.5 \text{ mW}/\mu\text{m}^2$ ; (c)  $39.0 \text{ mW}/\mu\text{m}^2$ ; (d)  $66.3 \text{ mW}/\mu\text{m}^2$

## 2.5 Numerical modeling

A numerical model using the FEM was built to simulate the time dependent thermal behavior of the rotating disk during the laser heating in order to interpret the magnetization decay. The 3D model is shown in Figure 2. 8. The multilayer disk was simplified to a two-layer system. The top layer was a 100 nm thick metal layer representing the magnetic layer and soft under-layer. The bottom layer was the  $10 \mu\text{m}$  NiP layer between the Al substrate and magnetic layer. The DLC and lubricant layers were ignored because their thicknesses are much smaller than the other layers. The

laser-supplied heating source was applied to the top surface of the metal layer and treated as a heat flux because most of the optical energy was expected to be absorbed at the very top surface of the metal layer, according to Beer's law. The heat flux was assumed to be a 2-D Gaussian distribution with the functional form given below, and it moved towards the down-track direction at 5 m/s. The Gaussian radius ( $e^{-2}$ ) was set to be 700 nm.

$$H_{flux} = \frac{2P}{\pi w^2} \exp\left(-\frac{2(x(t)^2 + y^2)}{w^2}\right) = P_{den} \exp\left(-\frac{2(x(t)^2 + y^2)}{w^2}\right)$$

$$x(t) = vt$$

Here,  $w$  is the laser Gaussian radius and equals 700 nm in the simulation.  $P$  is the laser power.  $x$  is the down-track direction from the laser beam and  $v$  is the velocity of the disk at the beam spot.  $P_{den}$  is the peak power density.

The mesh size of the top layer was 50 nm by 50 nm by 10 nm and that of the NiP layer was 50 nm by 50 nm by 2  $\mu\text{m}$ . The boundary conditions were set as given below:

(1) The temperature at the bottom surface of the NiP layer, as well as the upstream and downstream surfaces, were set to be room temperature. (2) The moving heat flux was applied on the top surface of the magnetic layer. (3) An adiabatic condition was used at the other boundary surfaces.

The nodal points were all assumed to be at room temperature at the beginning. The temperature increase due to a moving laser heating source was calculated by the thermal transient solver.

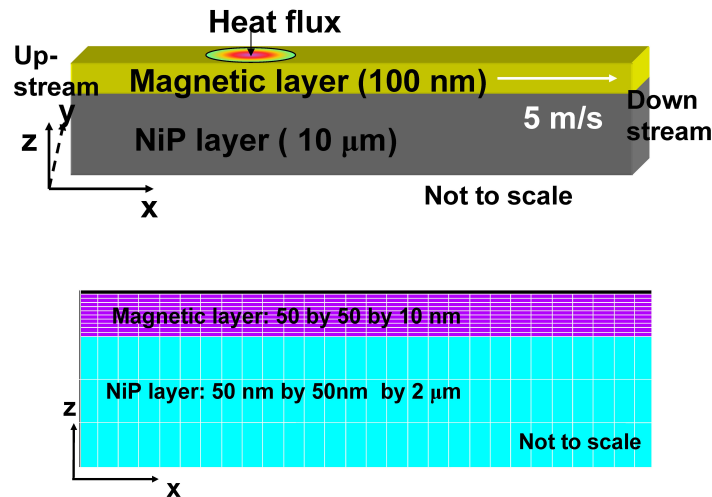


Figure 2. 8 Schematic plot (top) and mesh (bottom) of the 3D FEM model of the thermal behavior simulation for the free laser beam laser heating

Figure 2. 9 shows the numerical simulation result of the temperature distribution for the laser power density of  $39.0 \text{ mW}/\mu\text{m}^2$ . The maximum temperature at the steady state is  $662 \text{ }^\circ\text{C}$  in the center.

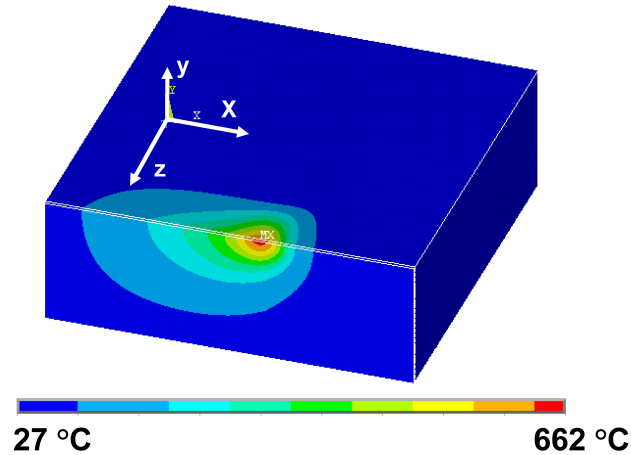


Figure 2. 9 The temperature distribution at the laser power density of  $39.0 \text{ mW}/\mu\text{m}^2$  from the numerical analysis.

The temperature history profile from the thermal analysis was used to calculate the magnetization decay based on the A-N model described in Section II. Three nodes in the laser heating area were chosen to demonstrate the thermal response and the magnetic decay behavior under the laser heating. The first node was located at the center of the heating source. The second and the third nodes were 200 nm and 400 nm, respectively, away from the center of the heating source along the off-track direction. Figure 2. 10 shows the temperature distribution and magnetization decay history of these three nodes when the laser beam approached and moved away from them. The laser power density was  $39.0 \text{ mW}/\mu\text{m}^2$  in this simulation. During the heating period, the laser beam approached these three nodes and the temperature increased. The magnetization started to decay. In the cooling period, the laser left the nodes and the temperature dropped quickly but the magnetization froze at a certain level. Node 1 reached the highest temperature and was demagnetized completely. The temperature of node 2 was somewhat smaller than that of node 1, and it was not totally demagnetized. Node 2 still had some remanent magnetization after the heating. The temperature of node 3 was the lowest, and it was almost not affected by the laser heating. The magnetic simulation also showed that the thermally demagnetized width was close to 400 nm when the power was  $39.0 \text{ mW}/\mu\text{m}^2$ .



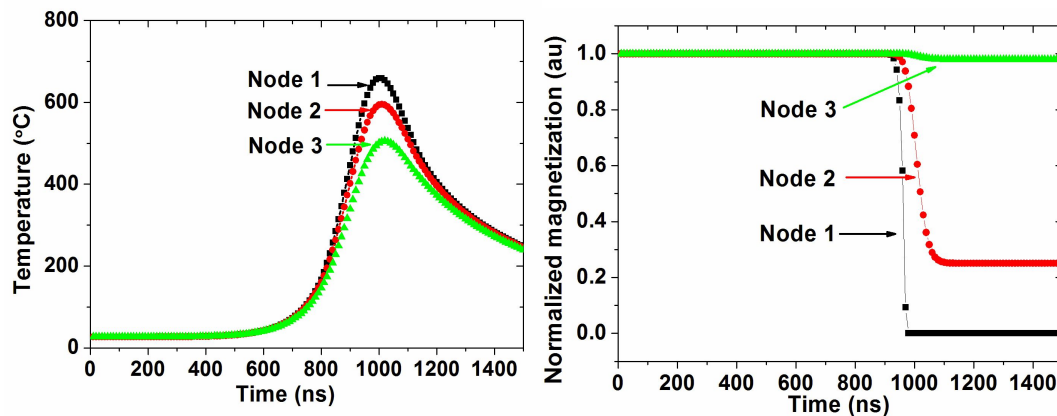


Figure 2. 10 The temperature history (left) and magnetization decay history (right) for the 3 nodes at different locations when the laser passed at a power density of  $39.0 \text{ mW}/\mu\text{m}^2$ .

The magnetization decay behavior was also calculated for other laser power values. The erased area sizes were obtained from these numerical results and compared with the experimental results as shown in the Figure 2. 11. The simulation results agree quite well with the experimental results, and this verifies the feasibility of this temperature calibration procedure for HAMR systems.

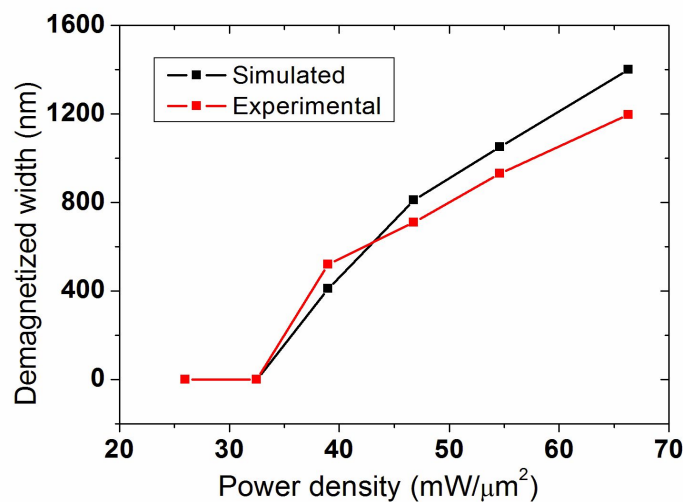


Figure 2. 11 Thermally erased magnetic track width due to the laser heating

## 2.6 Summary

We investigated the temperature increase of a rotating perpendicular magnetic media surface during the laser heating. A method based on the magnetization decay was developed to evaluate the temperature distribution. The magnetization of the media was quantitatively measured by MFM, and the magnetization decay was defined from the statistical analysis of the magnetic image for different laser power exposures. The

relationship between the temperature increase and magnetization decay was obtained from the A-N model. The magnetization decay was calculated from the temperature profile which was generated in a numerical FEM thermal model. The simulation and experimental results were in good agreement. Thus it is confirmed that this method can be used to calibrate the relationship between the laser power and the media temperature increase. Although a PMR disk rather than a HAMR disk was used in this study, this magnetization decay based calibration process can be easily implemented for HAMR systems. This calibration process is a first step toward understanding the thermal behavior of the HDI in HAMR systems.

## Chapter 3 HAMR stage development

A HAMR spin-stand testbed (named “Cal stage”) for the HDI study has been designed and built. Continued improvements and updates of the Cal stage have been achieved to study various aspects of HAMR systems such as the tribological behavior of the head-disk interface (HDI) and the heat transfer mechanism inside a nanometer head-disk gap. Section 3.1 describes the configurations of the Cal stage for tribological study of the HDI in HAMR systems. Section 3.2 describes further improvements of the Cal stage for the study of the nano-scale heat transfer phenomenon in HAMR systems. Section 3.3 summarizes this chapter.

### 3.1 Cal stage for the tribological study of the HDI for HAMR

The Cal stage stands on an optical table, which has the capability to isolate the vibration. Figure 3. 1 shows a schematic design of the Cal stage. It can be divided into five parts: a spindle system, optics, a laser focusing servo system, a linear stage, and a user interface for process control and data acquisition.

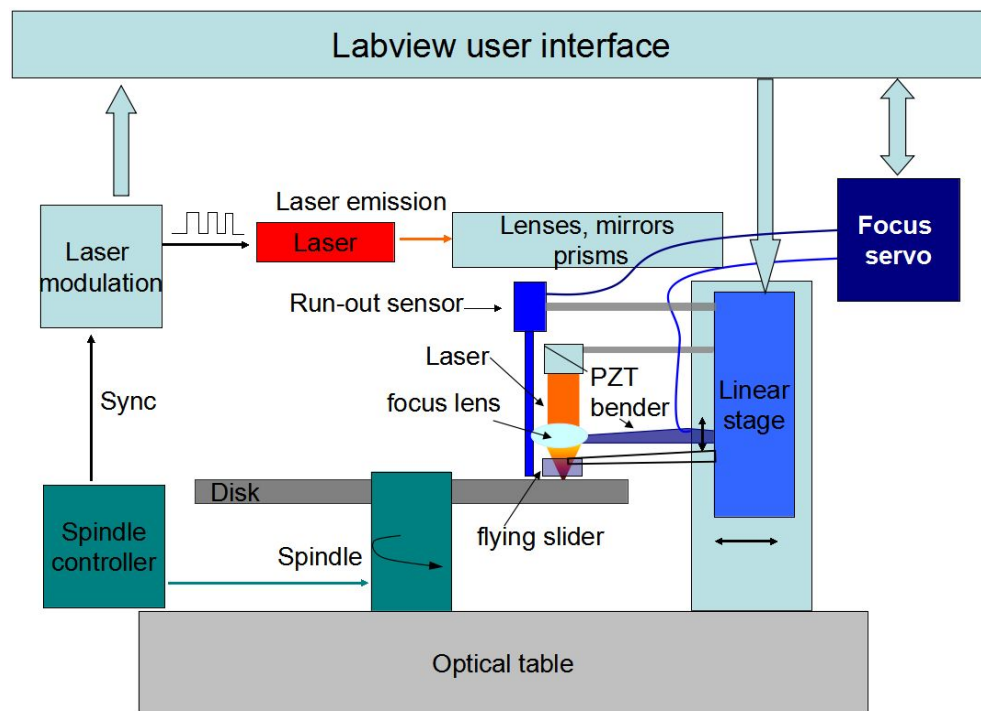


Figure 3. 1 Schematic design of the Cal stage for tribological study of the HDI in HAMR.

#### 3.1.1 Spindle system

An air bearing spindle from Seagull and a spindle controller from DART are used in the Cal stage. The spindle speed can be adjusted from 100 revolutions per minute (RPM)

to over 10000 RPM. The spindle index and encoder can be extracted from an optical encoder. The spindle encoder has 1024 counts per revolution (CPR), providing the angular position of a rotating disk. There is one spindle index pulse for every revolution. Both the spindle index and encoders are accessed by a field programmable gate array (FPGA). Some signal process programs have been implemented in the FPGA in order to synchronize the spindle spinning and other processes in the experiments. A hardware description language VHSIC Hardware Description Language (VHDL) is used for programming of FPGA.

### 3.1.2 Optics

The second part of the Cal stage is the optics. The optics part includes a laser source and some laser delivery components. A continuous wave (cw) solid state infrared laser is used in the Cal stage. The wavelength of the laser is 780 nm, which is also preferred in future HAMR drives. The maximum power output from the laser is 1000 mW.

The laser emission can be modulated by feeding a TTL signal to the laser controller. The modulation feeding signal is provided by the FPGA card. The laser modulation can be synchronized with the spindle index and encoder. The angular location on the disk for laser radiation and the duration of the radiation can be precisely controlled by programming the FPGA. Figure 3. 2 shows an example of the laser modulated signal (red curve), the spindle index signal (black curve) and the laser emission (green curve). The laser emission was detected by a photo-detector. The spindle rotated at 1500 RPM, so one revolution took 40 ms. In this example, the laser was programmed to emit only once for a complete revolution. After one revolution, the modulation signal turned low and the laser stopped emitting. There was an overshoot of the laser emission at the beginning. The overshoot lasted about 4 ms.

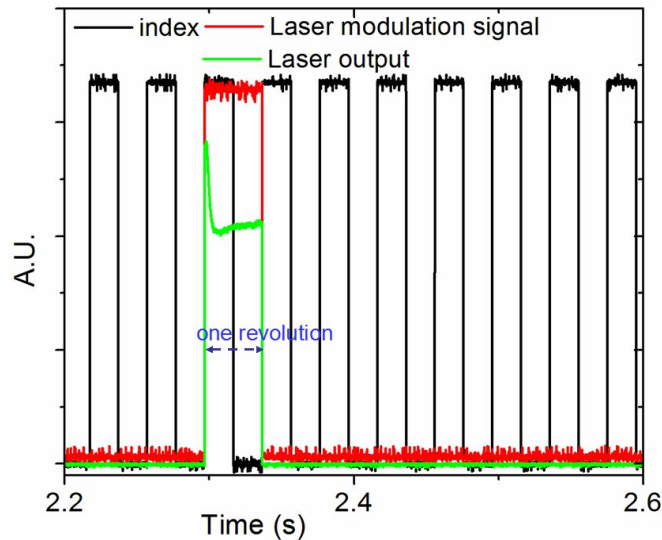


Figure 3. 2 Laser light modulation and synchronization with the spindle index

In general, there is a certain time delay between the laser emission and laser modulation feeding signal because of a limit of the bandwidth of the laser modulation. In other words, the laser cannot respond as fast as the modulation signal if the frequency of the modulation signal exceeds the bandwidth of the laser system. The time delay for our laser system was measured and it was 0.02 ms, as shown in Figure 3. 3. So the highest frequency of modulation is 50 kHz. In HAMR systems, the laser is supposed to be turned on only at the data sectors during the data writing. The time duration for a data sector is approximately 0.02 ms [35] which equals the limit of our laser modulation as well. A faster modulation speed can be achieved by use of an electro-optic modulator (EOM).

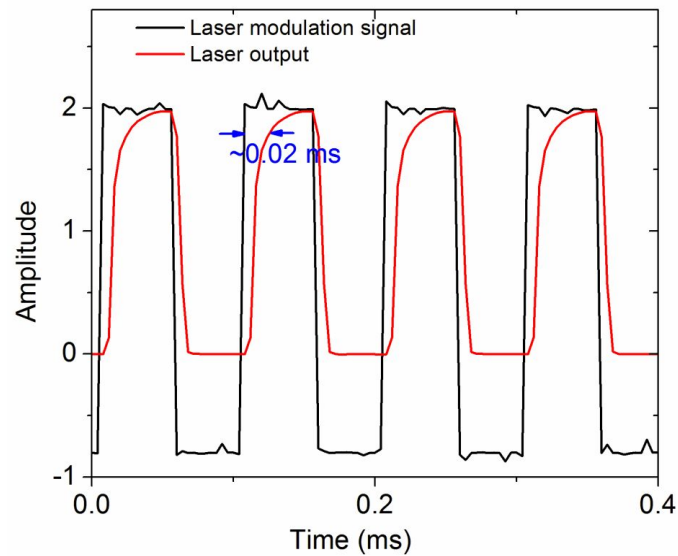


Figure 3. 3 Delay of the laser emission with respect to the modulation signal.

After the laser beam is emitted from the laser, the laser beam is manipulated and delivered to the samples by some optics. Figure 3. 4 shows the beam path. The light is first linearly polarized after the polarizer. Most of the light is p-polarized, while a minor part is s-polarized. The laser power can be changed manually by moving the optical attenuator after the polarizer. After lens 1, the beam is focused to a spatial filter in order to get a better beam quality. The beam shape can be chopped by the spatial filter while losing some of the laser powers. Then the beam enters a polarizing beam splitter, and only the p-polarized light can transmit. The minor s-polarized light is deflected by 90 degree to the left side of the incident beam. This minor s-polarized beam is monitored by a photo detector. The modulation of the s-polarized beam is the same with the incident p-polarized beam. The monitoring of the s-polarized beam gives the modulation information of the incident p-polarized beam. After the beam splitter, there is a quarter-wave plate that converts the p-polarized light to a circular polarized light. Then the beam is elevated by a periscope in order to project the laser energy down towards the disk surface. A prism deflects the beam by 90 degrees without changing the circular

polarization of the incident beam. So the light is illuminated perpendicular to the top surface of the disk. The beam comes to the objective lens and is focused onto the target. In this way, the beam is finally delivered onto the disk surface or the NFT on the slider.

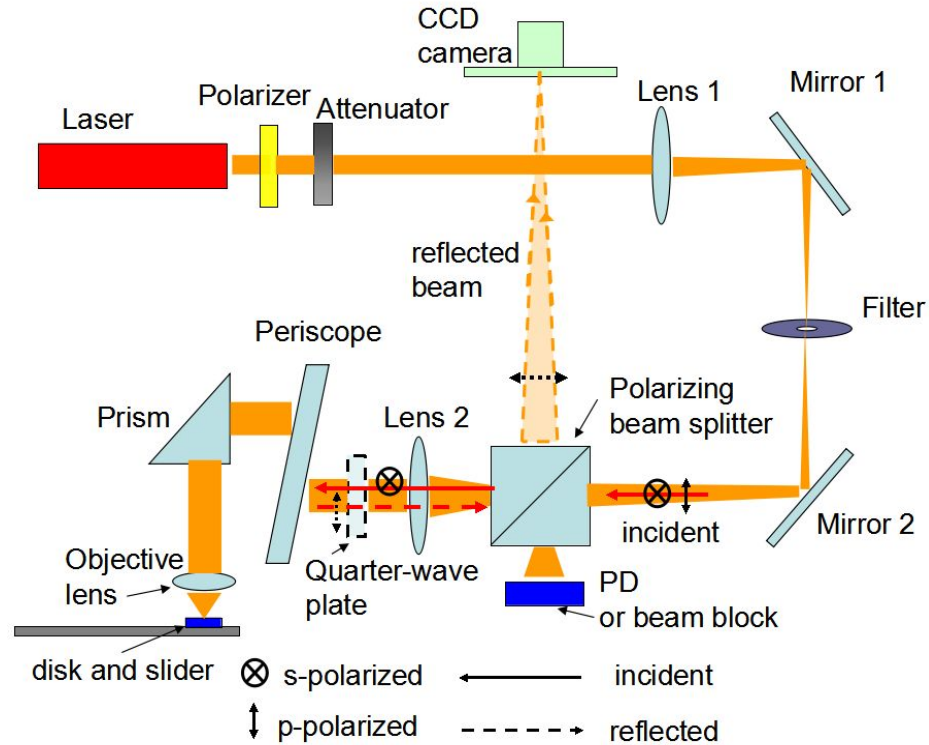


Figure 3. 4 Optical beam path of the Cal stage

There are two experimental modes in the tribological study of the HDI, depending on which surface the laser beam is focused. If the laser is directly focused on a disk surface, it is called the “free laser beam heating mode”. If the laser is focused onto a NFT structure carried by the slider and then the light is further transmitted to the disk by the NFT, it is called the “NFT heating mode”. For both modes, the disk is heated and the temperature of a spot on the disk is raised. A major difference of these two modes is the size of heating area on the disk. In the free laser beam heating mode, the laser heats an area on the order of several microns, while in the NFT heating mode the heated area is at tens of nanometers. The temperature change on the disk depends on the laser power input, thermal properties of the disk, the spinning speed and heating mode.

In the free laser beam heating mode, some of the light is reflected back. The reflected beam is still circular polarized before it re-enters the quarter-wave plate. After the quarter-wave plate, it becomes s-polarized, and it is deflected by 90 degrees when it passes the polarizing beam splitter. In this way the incident beam and the reflected beam are decoupled. The reflected beam is captured by a charge-coupled device (CCD) camera. The place of the CCD camera conjugates with the spatial filter, at which point the laser is

focused by lens 1. When the laser beam is well focused by the objective lens, a clear, reflected image of the laser focused spot can be observed at the location where the CCD is located. So the reflected image can be used to monitor the focus status of the laser beam. A typical reflected image is shown in Figure 3. 5 where the beam was well focused to the disk surface by the objective lens.

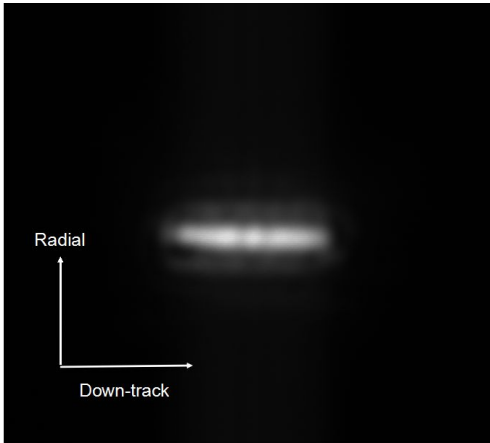


Figure 3. 5 Reflected image of the laser focused spot captured by a CCD camera

The shape of the laser focused spot is elliptic. The profile of the intensity in Figure 3. 6 showed that the Gaussian diameter along the down-track direction is  $5.5 \mu\text{m}$  and is about  $2 \mu\text{m}$  along the radial direction.

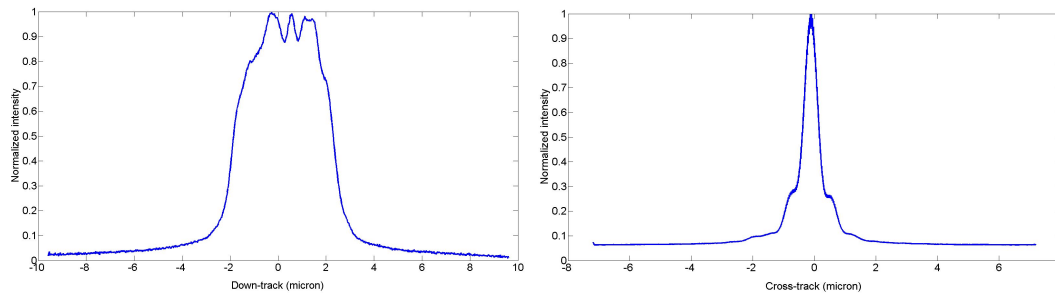


Figure 3. 6 Intensity profiles of the focused laser beam along the down-track (left) and cross-track (right) directions

The NFT heating mode was slightly different from the free laser beam heating mode. A NFT structure was fabricated on the trailing end of the rails of a slider, as shown in Figure 3. 7. The design of the NFT structure is shown in Figure 3. 8. It had a ring structure with a diameter of  $10 \mu\text{m}$  that encircles the NFT structure. This ring and the two horizontal bars were used to help align the laser to the NFT structure.

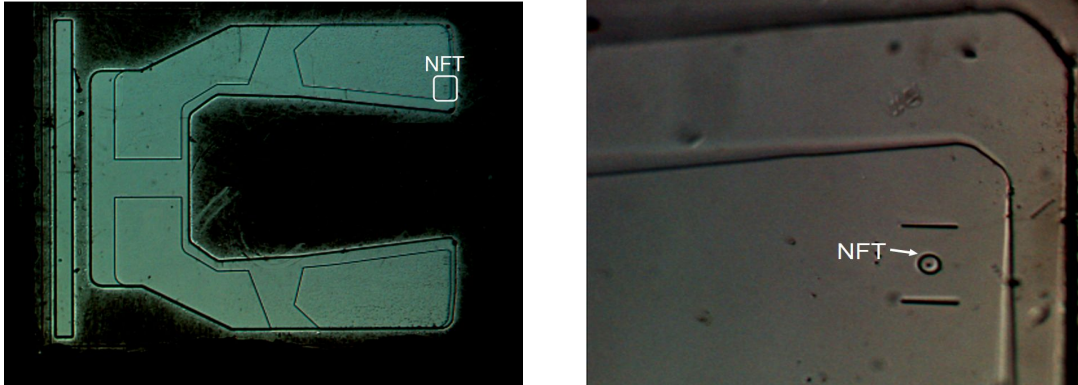
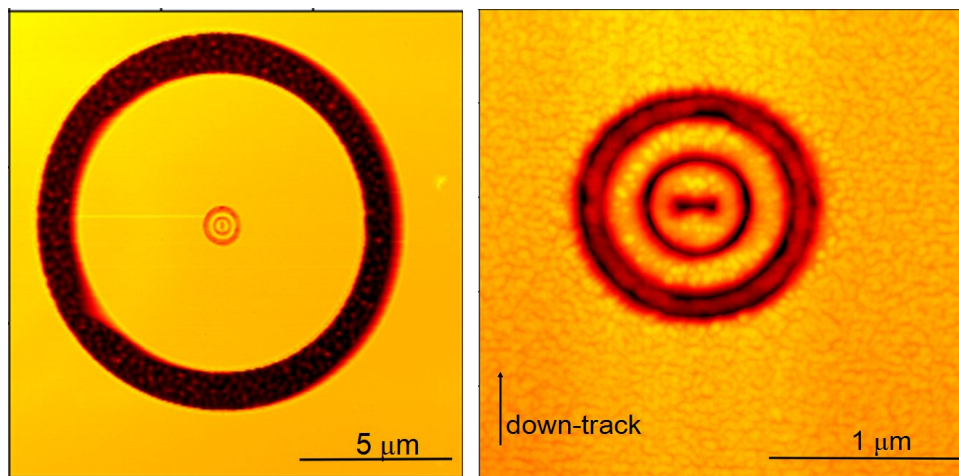


Figure 3. 7 Homemade slider with an NFT; (left) Optical microscope image of a homemade air bearing surface; (right) zoomed NFT structure and alignment structure on the trailing edge



(a) NFT structure and alignment ring      (b) NFT structure

Figure 3. 8 AFM topography of the NFT and alignment mark on the homemade slider surface

In the NFT heating mode, the laser should be aligned to the NFT first by monitoring the reflected image of the NFT at the beginning of laser exposure tests. Usually some alignment marks have to be fabricated together with the NFT structure to assist the alignment because some of the NFT structures are too small to see clearly in the reflected image of the CCD camera, even after hundreds of magnification. Figure 3. 9 shows the reflected image of a NFT and part of an alignment mark.

In the NFT heating mode, after the alignment is done, the quarter-wave plate can be removed, depending on whether a linearly polarized light is needed for the NFT structure to excite the plasmons. For example, if the design of the NFT prefers a polarization along the down-track direction, then the quarter-wave plate should be removed during the laser exposure tests.



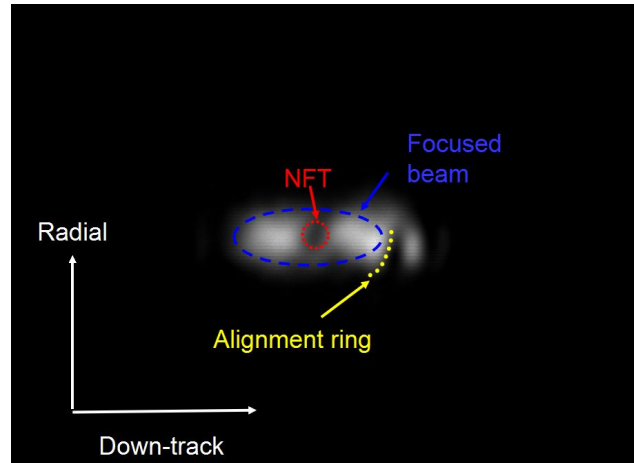


Figure 3. 9 Reflected image of the NFT structure after alignment captured by a CCD camera

When the laser is focused and aligned to a NFT, a large number of collective oscillations of electrons, called surface plasmons, are generated on the metal and dielectric film interface. They are strongly localized to this interface and exponentially decay in amplitude away from the interface. Figure 3. 10 shows the finite difference time domain (FDTD) simulation results of the confinement and enhancement of the light after the NFT at a plane 10 nm away from the NFT. The light wavelength was 780 nm. The tiny focus spot by the NFT is 36 nm (FWHM) along the down track direction and 100 nm (FWHM) along the radial direction as shown in the profile in Figure 3. 11. The maximum enhancement of the intensity is about  $\sim 10$ .

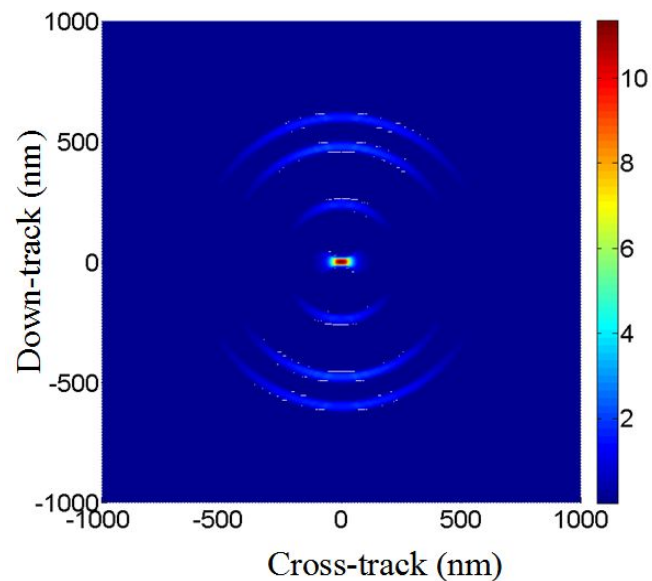


Figure 3. 10 Optical intensity distribution at a plane 10 nm away from the NFT

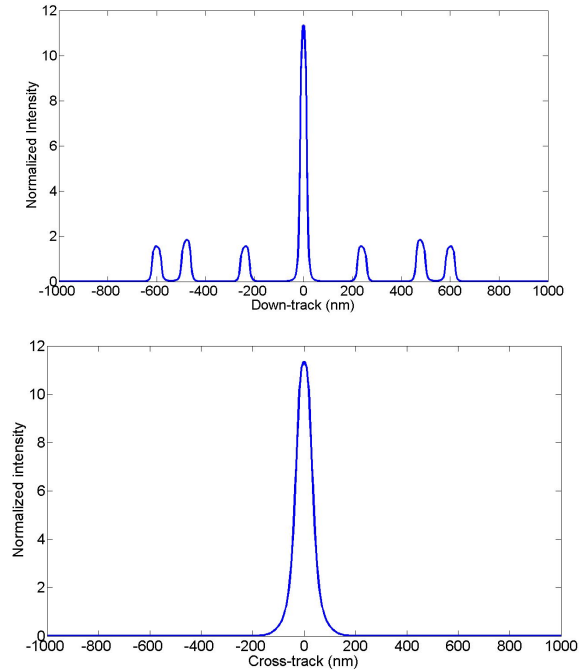


Figure 3. 11 Intensity profile of the transmitted light at a plane 10 nm away from the NFT along the down-track (top) and cross-track (bottom) directions.

### 3.1.3 Laser focusing servo system

The third part of the Cal stage is a laser focusing servo system. An objective focusing lens is used to focus the light to a few microns spot. However, a minimum focused spot and highest intensity can be achieved only in the focal plane when the laser light is focused. The depth of focus for the Cal stage is about 3  $\mu\text{m}$ . Beyond this range, the light is out of focus. When the laser is out of focus, the size of the spot and intensity of the light are quite different from that when laser is in focus. The intensity profile of the beam along the radial direction on the disk surface is compared in Figure 3. 12 for the case when the light was in focus and out of focus. The red curve is the intensity profile when the light was in focus. The black and green curves are the intensity profiles when light was focused below and above the focus plane, respectively. The beam profile became slightly larger and the peak intensity became weaker when the beam was out of focus compared with that when the beam was well focused.

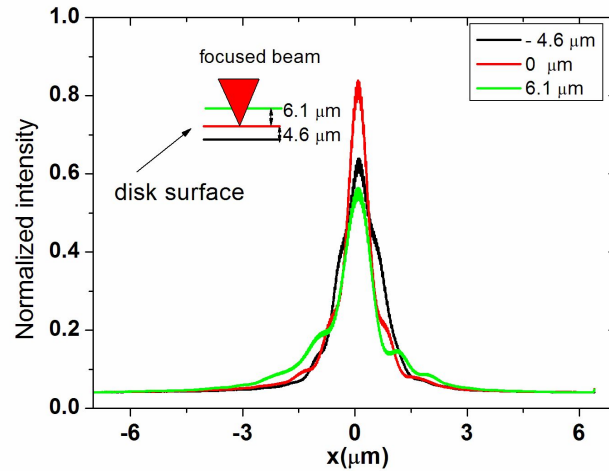


Figure 3. 12 Beam profile along radial direction when the laser was on and out of focus.

The rise in temperature on the disk due to the laser heating is sensitive to the size of the laser heating spot and intensity of the light. In order to have better control of the rise in temperature on the disk, the laser beam should be maintained in focus at all positions of the disk during the whole free laser beam heating process.

However, there always exist run-outs perpendicular to the disk surface because of the unbalanced spindle, disk deformation and clamp distortion. If the disk's vertical run-out exceeds the depth of focus, then the focused light intensity is not at the same level at different circumferential locations. The light intensity at some specific angles is smaller than that at other angles. This run-out depends on the disk installation and type of clamp used in the spindle. The magnitude of the vertical run-out for a 3.5 inch magnetic disk was measured by a displacement sensor. The disk was installed on a 25 mm clamp and rotated at 1500 RPM. Three run-out profiles at the outer, middle and inner radius are plotted in Figure 3. 13. The magnitude of the vertical run-out was larger at the outer radius of the disk than the inner radius. However, the run-out profiles at different radii almost had the same phase.

The run-out of the disk is repeatable once the disk is installed. Repeated measurements of run-out were performed for a 2.5 inch disk installed on a 20 mm clamp. As shown in Figure 3. 14, the red dashed curve is the spindle index. The rising edge of the spindle index indicates the start of a revolution. The other colored solid curves represent the disk run-out measured by the displacement sensor at a fixed radius of the disk. The variation of these run-out profiles were much smaller than the depth of focus. The variation of the run-out at different revolutions can come from the noise of the displacement sensor and mechanical disturbance of the stage. It is noticed that the shape of the run-out profile in Figure 3. 14 is quite different from that shown in Figure 3. 13 because the run-out profile depends on the spindle clamp and every installation of the disk. Different disks and clamps have different run-out profiles.

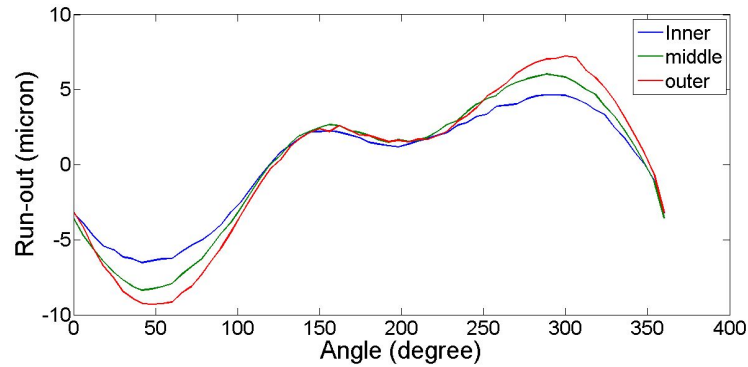


Figure 3. 13 Disk vertical run-out profiles at three different radii for a 3.5 inch disk.

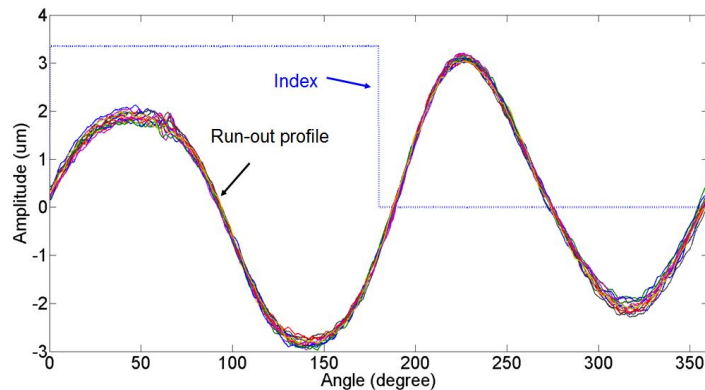


Figure 3. 14 Repetitive disk run-out measurements for a 2.5 inch disk at a fixed radius.

As discussed above, the disk vertical run-out causes the defocus of the laser beam and non-uniform illuminations at different circumferential positions on the disk surface. In order to control the laser focus status, a focusing servo system was developed. The objective lens is attached to a piezoelectric bender. The bender can move the lens up and down, together with the lens. A displacement sensor is placed next to the lens, as shown in Figure 3. 1. The displacement sensor and bender are both mechanically connected to a linear stage and moved together. The relative motion between the disk and objective lens is in-situ measured by the displacement sensor and used as an input for the servo system.

The controller is designed and implemented in a Labview real-time target. The objective lens can follow the vertical run-out motion of the disk and the laser light can remain in focus on any location of the disk when the disk spins.

To design the focusing controller, the characteristic of the bender was studied. The dynamic response of the bender with an attached lens was characterized. A sweep frequency voltage drove the bender's motion, and the response of the bender was captured by the displacement sensor. The transfer function of the bender was later obtained from the spectrum of the bender's response. Figure 3. 15 shows the spectrum of the bender's response. The strongest resonance peak occurred at about 63 Hz. The second

and third resonance peaks were at 72 Hz and 126 Hz, respectively. Those peaks should be attenuated and avoided when designing the control algorithm.

The linearity of the bender's response was studied as well. A single frequency voltage was used to drive the bender. The amplitude of the input was changed from 0.25 v to 1.0 v. The motion of the bender was measured by the displacement sensor. In this way, the relationship between the amplitude of the input signal and amplitude of the bender motion was obtained, as shown in Figure 3. 16. It can be observed that the bender responded linearly to the voltage input.

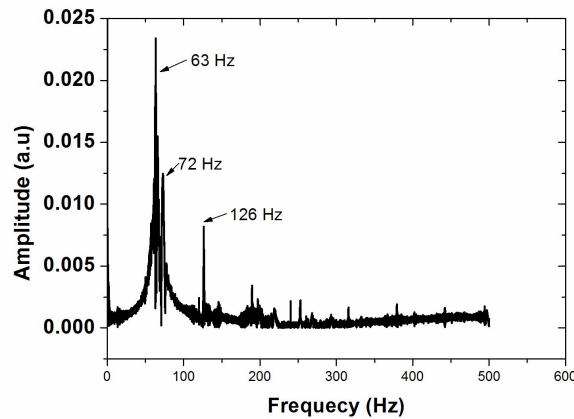


Figure 3. 15 Transfer function of the bender with objective lens attached.

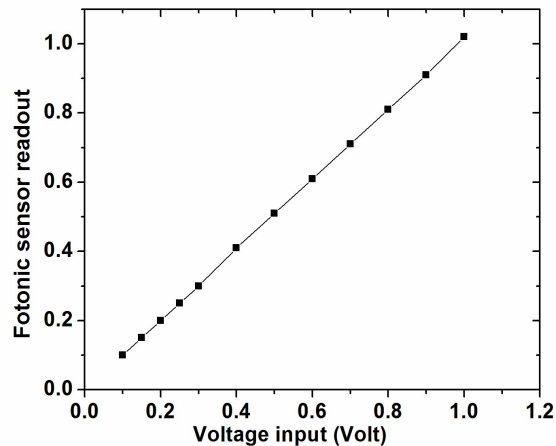


Figure 3. 16 Bender's response to different amplitudes of the driving voltage.

Based on the knowledge we obtained for the bender and spindle system, a simple feed-forward algorithm was designed and implemented in this focusing servo system to make the laser beam remain well focused onto the disk surface. The procedure to start the focus servo system is:

(1) Adjust the Z position of the objective lens to focus the laser beam on the disk surface when the spindle is not spinning.

(2) Adjust the height of the displacement sensor to level the output of the displacement sensor close to zero. A relative motion between the disk and objective lens is then measured by the sensor later.

(3) Turn on the spindle motor, and the disk starts to spin. The displacement sensor gives a periodic output of the disk's vertical run-out.

(4) Start the controller from the Labview interface. The controller gets the input signal from the displacement sensor. Then, the in-situ offset between the objective lens and disk is calculated in the real-time target. The respective control output is further generated by the controller to drive the bender to compensate the offset.

(5) After finishing the exposure tests, turn off the controller.

(6) Stop the spindle, and uninstall the disk from the spindle for further surface inspections by the Candela optical surface analyzer (OSA) or AFM.

(7) The focusing servo system should be restarted from step 1 after the spindle stops or the disk is changed.

The performance of this focusing servo system was verified by comparing focusing status when the focusing servo was on and off. A typical run-out profile is shown in Figure 3. 17. Six different angles on the disk were chosen for evaluating the focusing servo system. At these six positions, the relative distances between the objective lens and disk were different. At some of the locations, the laser beam could be in focus while all others may be out of focus. The reflected images of the focus spots were compared when the controller was off and on at these six different angles, as shown in Figure 3. 18. When the controller was off, the spot size and intensity varied at the different locations. At the angle of 160 and 220 degrees, the laser beam was well focused so a bright, reflected image could be observed. However, blurred and darker reflected images are shown at other angles because the laser was defocused. When the controller was on, the reflected images became uniformly bright at all positions. It was verified that the controller can work effectively to allow uniform illumination at different circumferential positions.

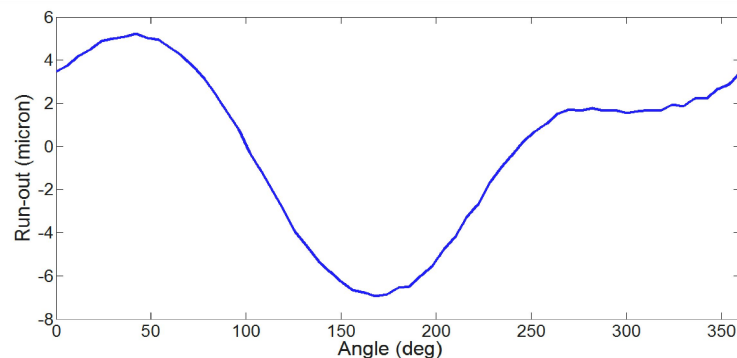


Figure 3. 17 A vertical run-out profile for a 3.5 inch disk

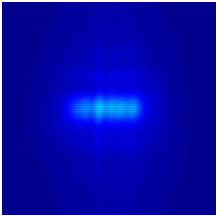
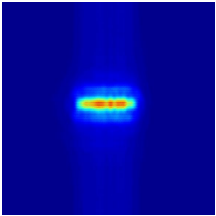
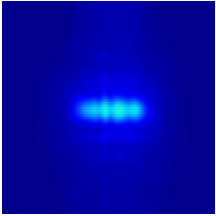
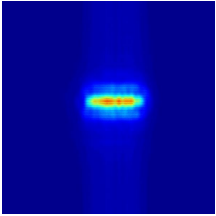
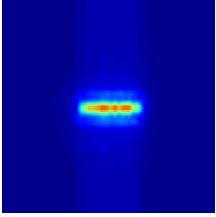
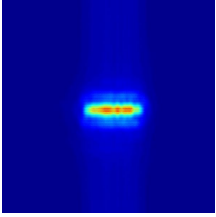
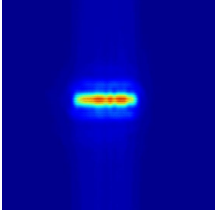
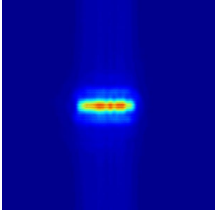
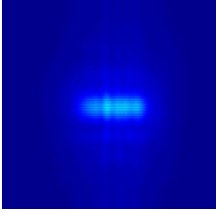
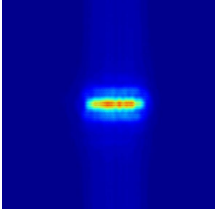
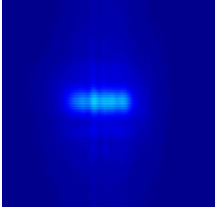
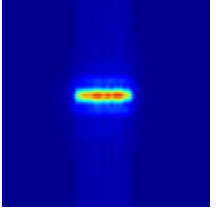
Angle (degree)	Controller off	Controller on
40		
100		
160		
220		
280		
340		

Figure 3. 18 Reflected images of laser focus spots when the focusing servo system was on and off

### 3.1.4 Linear stage

The fourth part of the Cal stage is a motorized linear translation stage from Physik Instrumente. The stage can move in the radial direction. The maximum travel distance is 15 mm. The objective lens, prism and displacement sensor are fixed to the linear stage and they are moved together with the linear stage.

A gearhead is used in this linear stage, and the pitch of the thread is 0.4 mm. The gap between the linear stage with the attached lens and disk surface varies at different radii even when the disk is stationary. There are two main reasons for the variation of the gap, as shown in Figure 3. 19. First, the motion of the motorized linear stage is not perfectly parallel to the disk surface. It has some relative tilt with respect to the surface. This tilt causes a DC drift of the gap. Second, the motion of the gearhead is not entirely smooth because of the thread structure of the gearhead. It produces a periodic change of the gap.

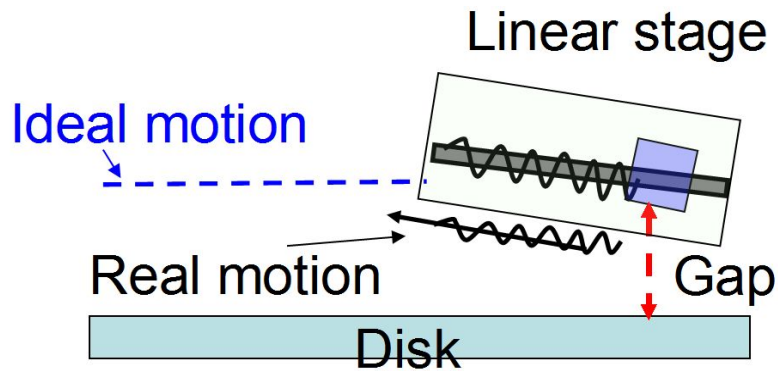


Figure 3. 19 Schematic plot of the relative motion of the linear stage relative to the disk surface

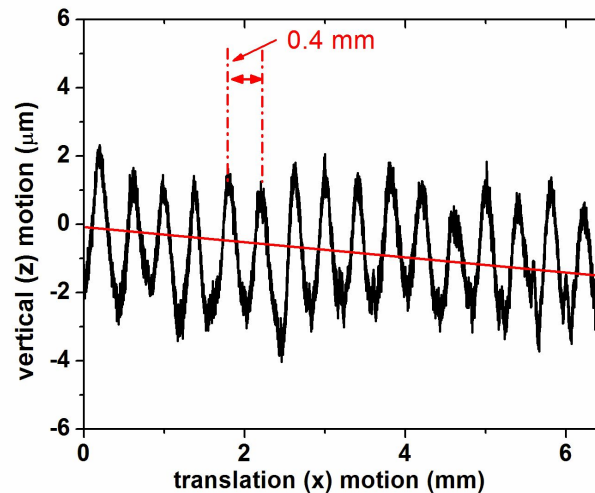


Figure 3. 20 Measured variation of the gap as the linear stage moves radially and the disk was stationary.



The change in the gap between the translation stage and disk surface was experimentally measured, as shown in Figure 3. 20. The change in the gap could be treated as a combination of a linearly increasing DC offset (red line) and a zigzag motion. The zigzag motion had a pitch at 0.4 mm, which is the same as the thread pitch. The DC offset could be minimized by adjusting the relative tilt between the disk and linear stage. After adjusting the tilt, the motion of the linear stage could be very parallel to the disk surface to make the DC offset smaller. The current DC offset is about 2  $\mu\text{m}$  for a 6 mm motion stroke.

### **3.1.5 User graphic interface**

The fifth part of the Cal stage is a Labview user interface, including the data acquisition part and the experimental process control part. The maximum data acquisition rate is 500 kHz for one channel. The Labview real-time target machine can be treated as a platform that has the capability of customization. Different programs can be loaded to the real-time target to control the experimental process for the studies of different phenomena of the HDI in HAMR systems, depending on the design of the experiments.

## **3.2 Cal stage for the study of heat transfer in the HDI**

The current Cal stage has been updated further to study the heat transfer between the flying slider and the disk. It is believed that the near field radiation is enhanced beyond the traditional Planck's law and phonon tunneling occurs in a gap of a few nanometers [48, 49]. This study provides information to understand how the heat is transported inside a nanometer scale gap in HAMR systems. The disk back heating effect can be also studied.

A slider with an embedded contact sensor (ECS) was used for this study. The ECS is a thermal resistance sensor integrated between the magnetic reader and writer [50], as shown in Figure 3. 21. The size of the ECS is about 1 to 2  $\mu\text{m}$ . The resistance of the ECS increases as its temperature rises. Rather than measuring the resistance of the ECS directly, the voltage difference between the positive and negative pins of the ECS is measured when a constant current source is applied to the ECS. The voltage is proportional to the resistance of the ECS. The voltage increases as the temperature of the ECS rises.

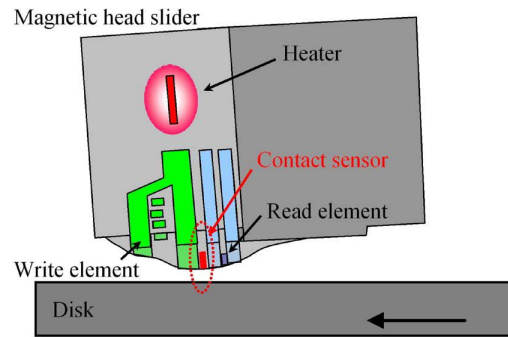


Figure 3. 21 Schematic of a contact sensor embedded into head structure [50]

Some modifications have been made to the Cal stage to make it compatible with the ECS system. The schematic design of the new stage is shown in Figure 3. 22. Figure 3. 23 shows a close up view of the new Cal stage, integrating a function of an ECS.

A slider with the ECS flies up-face on the back side of a special one-side coated glass disk for the study. Only the backside of this special disk has a metal layer and a lubricant layer. The top surface of the disk is transparent which allows the light to transmit through. The laser is delivered through the top side of the disk, and focused onto the coating on the backside of the disk. The backside of the disk is locally heated by the focused laser.

The ECS and laser beam have to be aligned so that the laser heating elevates the temperature of the disk at the location right underneath the ECS. By this way, the HAMR back heating condition can be emulated, in which a slider flies on a heated spot of the disk.

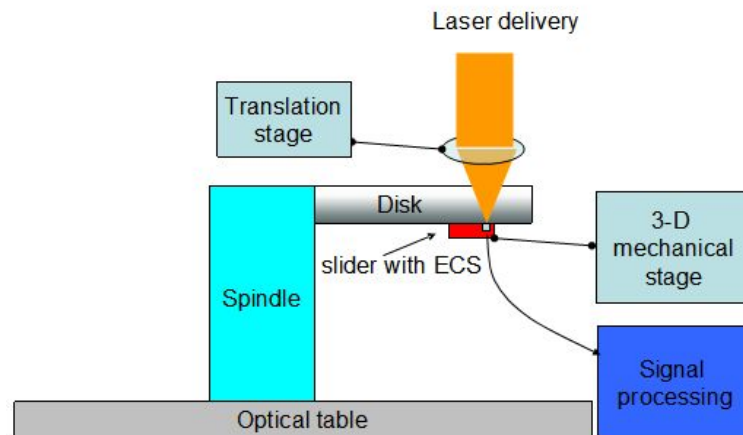


Figure 3. 22 Schematic design of the testbed for study of heat transfer inside the HAMR HDI

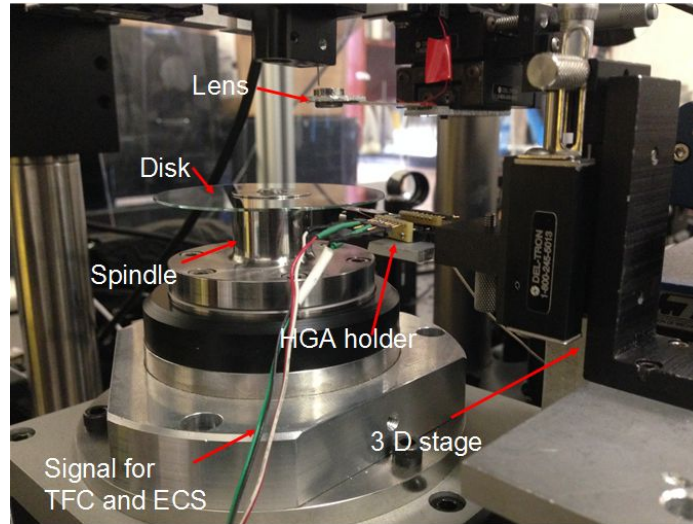


Figure 3. 23 Close up view of the Cal stage integrating a function of an ECS

The alignment between the ECS and laser focus is performed on a transparent disk. A slider with the ECS first flies up-face on the transparent disk. The laser can transmit through this transparent disk and be focused onto the air-bearing surface of the slider. A clear reflected image of the air-bearing surface is captured by the CCD camera. The slider can be moved freely by a 3-D mechanical stage. The position of the laser-focused spot can be also adjusted in-plane by the optics as well. The laser beam is adjusted to align to the magnetic transducer first by checking the reflected image of the magnetic transducer. The ECS is located between the magnetic reader and writer [51]. So once the laser is aligned to the magnetic transducer, only a tiny adjustment is needed to further align the laser to the ECS because the size of the focused spot is relatively larger than the ECS. The finer adjustment is stopped once the ECS gets its maximum signal, which indicates the temperature increase of the ECS is a maximum. Figure 3. 23a shows an optical microscopy image of a magnetic transducer. The reflected image of the magnetic transducer was captured by the CCD camera when the laser was well aligned to the magnetic transducer, as shown in Figure 3. 24b.

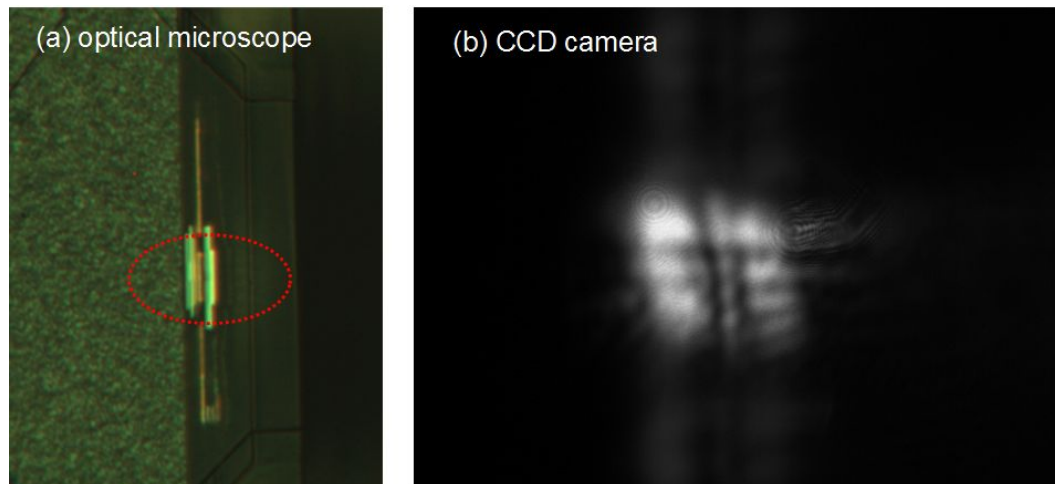


Figure 3. 24 Laser alignment to the magnetic transducer and ECS. (left) Optical image of the magnetic transducer captured by the optical microscope; (right) reflected image of the magnetic transducer captured by the CCD camera.

An acoustic emission (AE) sensor is attached to the suspension base holder and used to detect the head-disk contact, as shown in Figure 3. 25. The amplitude of the AE signal increases when contact happens.

The gap between the ECS and disk can be controlled by the TFC. The Labview real-time target generates a ramp voltage to power the TFC heater. The rate of the TFC voltage ramp can be adjusted in the Labview program. The TFC is powered off when the AE spikes occur, which indicates head-disk contact. This function can help to avoid too much over-push and material wear of the slider and disk. The ECS signal, AE signal, TFC input and spindle index are all recorded by a data acquisition card for further offline data analysis.

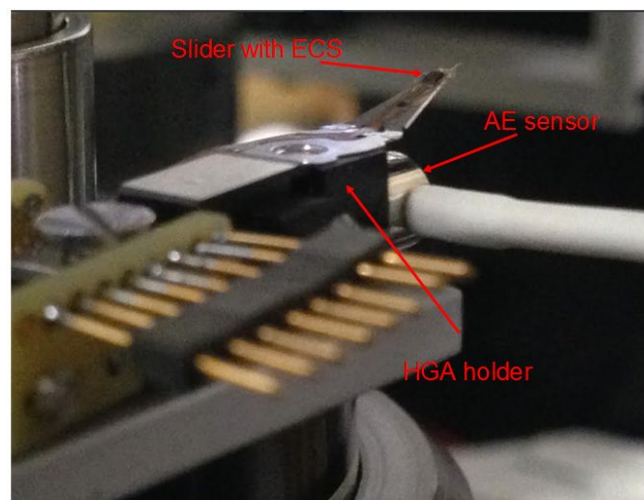


Figure 3. 25 An acoustic emission sensor is attached to the base of a HGA holder

Figure 3. 26 shows a typical ECS signal, AE signal and TFC input when the slider flies on a transparent glass disk. When the laser was turned on, there was a sharp increase of the ECS signal because the ECS was heated by the laser. The signal of the ECS kept increasing as the TFC power went up because the slider was self-heated by the TFC heater.

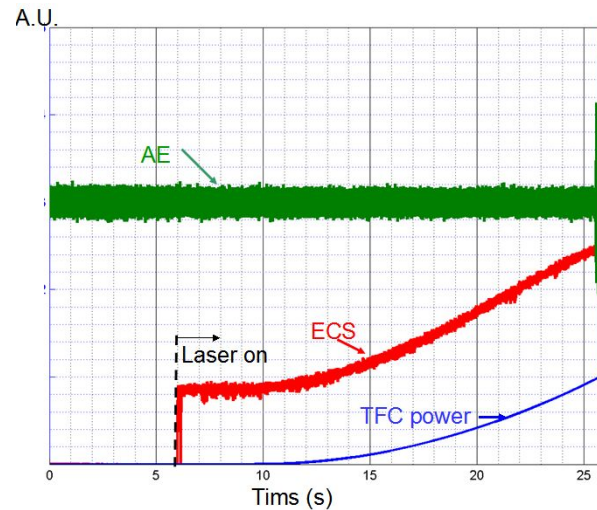


Figure 3. 26 A typical signal from the ECS, TFC and AE sensor in the experiment

### 3.3 Summary

In this chapter, a HAMR spin-stand testbed (Cal stage) for HDI study was introduced. The main functions and configurations of the Cal stage were elucidated. Two major studies on the Cal stage have been performed. One study was conducted to understand the tribological phenomena in the HDI. The other was to investigate the mechanism of heat transfer inside the HDI and the back-heating phenomenon for HAMR systems. The Cal stage is an open platform that can be updated and improved to satisfy the special requirements for different studies.

## Chapter 4 Lubricant changes under laser heating

The structure of the HDI for HAMR is somewhat different from that of the current PMR because of some unique requirements of HAMR systems. A schematic diagram of a typical HAMR HDI structure is illustrated in Figure 4. 1. On the top surface of the disk, there is a lubricant layer with a thickness from 0.8 nm to 1.5 nm. The lubricant is the layer on the disk that is closest to the laser heating source. The use of heat during the recording process requires that the lubricant be thermally stable during the lifetime of HAMR drives. Changes of the lubricant under HAMR conditions may lead to failure of the HDI and eventually damage the magnetic media. The lubricant changes under laser heating are discussed in this chapter.

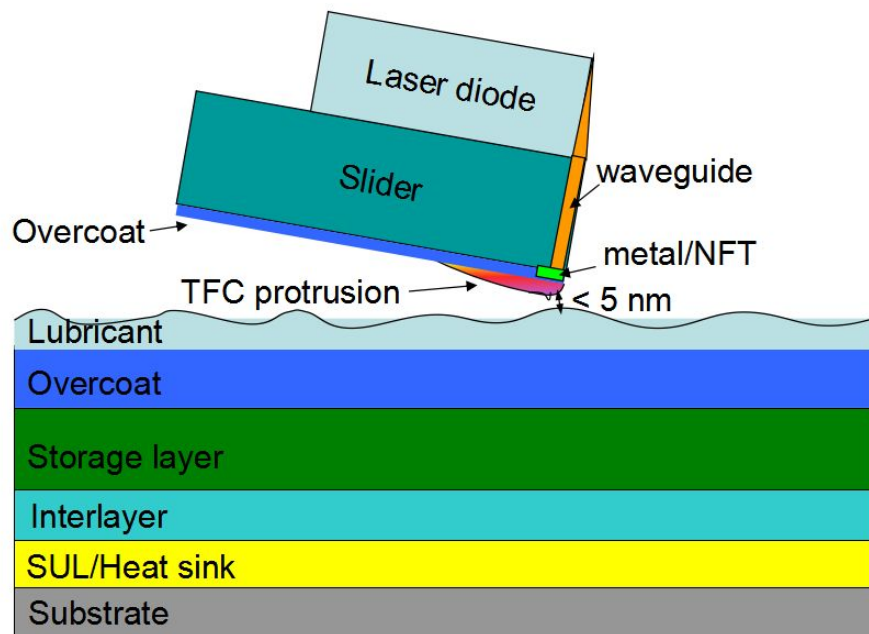


Figure 4. 1 Schematic drawing of HDI for HAMR systems

### 4.1 Introduction

In the current PMR technology, a 0.8 to 1.5 nm thick lubricant film is applied over the carbon overcoat to increase the stability and reliability of the HDI. The lubricant layer considerably reduces friction and wear during head disk contacts, lowers the overall surface energy, adds protection against corrosion, and it passivates the surface against adsorption from organic contaminants [32].

Perfluoropolyether (PFPE) type lubricants are widely used in current HDDs (e.g., Z-dol, Z-tetraol and ZTMD). The lubricant layer can be divided into two parts: bonded

and mobile part. The amount of lubricant that cannot be removed by rinsing in a solution is designated as “bonded”, whereas the lubricant that is removed is viewed as “mobile”. The mobile layer has a viscosity similar to the bulk viscosity of the lubricant, which behaves like a liquid. The bonded layer is more like a solid. As illuminated in Figure 4. 2 [52], the lubricant molecular chains chemically bond to the surface of the carbon overcoat. Some of the lubricant chains tangle together. The bonding ratio is an important characteristic for the lubricant. A typical bonding ratio is about 40-60% for Zdol, 60-80% for Z-tetraol, and 80-90% for ZTMD [32]. Those lubricants are expected to keep their beneficial properties at operational conditions for at least five years.

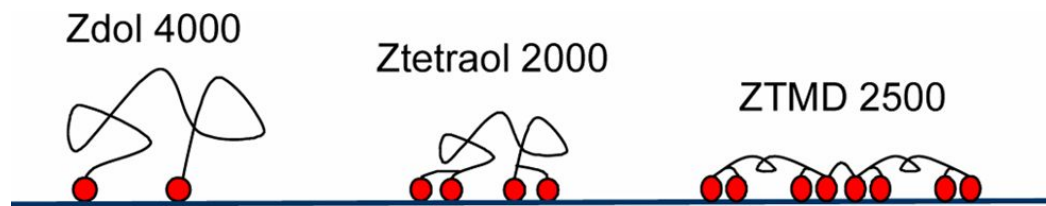


Figure 4. 2 Schematic drawing of lubricant main-chain and end-group progression [52]

In HAMR systems, the laser pulses momentarily raise the temperature of a tiny spot to near the Curie point of the magnetic material, which is in the range of 400 to 600 °C. The lubricant on the disk surface is necessarily heated as well. The thermal excitation only lasts for a few nanoseconds on a point of the disk. This laser heating duration is three orders shorter than the microsecond relaxation time of the lubricant molecule [32]. However, accumulated lubricant evaporation, depletion or decomposition at such a high temperature environment over a lifetime of a drive may be severe [53, 54].

Several research groups have experimentally and numerically studied the thermal behavior of various lubricants. Some new types of lubricants have been proposed for future HAMR drives as well.

In DSI’s work [55, 56, 57, 58], they developed a HAMR test bed that has a function of fast heating by use of a laser. The heating duration can be controlled within several nanoseconds. It was found that the lubricant depletion depth was linearly proportional to the logarithm of the laser heating duration. The lubricant depletion could be alleviated by lowering the laser heating temperature. It was also found that the lubricant accumulated at the edge of the depletion track. The accumulated lubricant at the edge of the track flowed back into the depletion area after a short time. Furthermore, the media cooling time played a significant role in lubricant depletion for media without a heat sink layer and on a glass substrate. DSI’s simulation showed that the evaporation coefficient of lubricant decreased for the temperature range from 406 to 512 K and followed the trend given by the Arrhenius formula.

Professor Togawo’s group in Japan has done several experiments on lubricant evaporation and depletion [59, 60, 61, 62]. In their work, a high heating rate of  $10^8$  °C/s

was achieved by use of a laser. They compared the lubricant depletion under fast heating with that under slow heating by a temperature programmable device (TPD). The heating rate in such a TPD was in the range of 1 to 100 °C/s while the heating duration in the TPD was from seconds to minutes. It was found that the lubricant depletion characteristics could be explained using the experimental TPD results for the tested lubricant films. The depletion mechanism involved desorption or decomposition of the lubricant molecules when the temperature was higher than 350 °C. The monolayer lubricant and multi-layer lubricant showed different thermal behaviors. The critical temperature at which the lubricants started to deplete due to the laser heating was strongly dependent on the lubricant film thickness. A monolayer lubricant with smaller thickness strongly interacted with the diamond-like carbon thin films. Thicker lubricant had more depletion and a higher depletion rate. It was found that lubricant depletion was predominantly due to lubricant evaporation for cases in which the lubricant film thickness was greater than one monolayer. In addition, the lubricant bonding ratio was found to greatly affect the lubricant depletion characteristics. The lubricant depletion depth and width decreased as the bonding ratio increased. The lubricant depletion mechanism also involved the evaporation of mobile lubricant molecules when the maximum temperature was less than 100 °C. Another suggested lubricant depletion mechanism involved the thermocapillary stress effect, which was induced by the disk surface temperature gradient resulting from the non-uniformity of the laser spot intensity distribution.

Wu [63] has proposed a numerical model to study the effects of evaporation, thermo-capillary and thermo-viscosity induced by the laser heating on the lubricant depletion in a HAMR system.

Colleagues from CML at UC Berkeley have systematically studied the lubricant thermal behavior in HAMR conditions by numerical methods [54, 64, 65, 66]. Dahl found that lubricant deformation caused by small thermal spots of 20-nm full-width half-maximum (FWHM) recovered on the order of 100-1000 times faster than larger 1 $\mu$ m FWHM spots. However, the lubricant was unable to recover from sufficiently high writing temperatures. It was also found that in the case of smaller thermal spots with higher temperature gradients, the thermocapillary shear stress was the main driver of lubricant deformation. The thermocapillary stress pulled lubricant away from the thermal spot center to the side ridges, while evaporation was not as important. The lubricant deformation was similar whether the evaporation is considered or not.

Several new lubricant types have been reported to have better thermal stability [67, 68], but it has still not been confirmed how long those lubricants can last under the real HAMR conditions. The heating rate and thermal gradient in HAMR drives is expected to be a few orders larger than that in the conditions when those new lubricants were tested.

To understand the lubricant thermal behaviors under the HAMR conditions will be of great important for the success of the HAMR drive. In this chapter, the lubricant thermal depletion and reflow behaviors under the free laser beam heating and NFT laser



heating are studied using the Cal stage. Section 4.2 describes the experimental process and conditions. The lubricant thermal behaviors, including both depletion and reflow, are discussed in section 4.3. Lubricant changes under the NFT heating are discussed and compared with those under the free laser beam heating in section 4.4. Section 4.5 summarizes this chapter.

## 4.2 Experimental condition and process

### 4.2.1 Free laser beam heating mode

A series of experiments was designed and performed to study the lubricant depletion and reflow behaviors under various free laser beam heating conditions on the Cal stage. Different laser power inputs were applied to get different temperature increases on the disk surface. The lubricant depletions under different heating durations and repetition numbers were also compared to study the accumulated thermal effects, since the lubricant change in real HAMR systems is also a time accumulated process.

Because of the unavailability of a HAMR disk at this time, PMR disks were prepared. 3.5 inch PMR disks with aluminum substrates were used in this study. The lubricant type was z-tetraol with A20H additives in all of the experiments. The bonding ratio was 60%. The total thickness was 9.5 Å.

In the experiments, the free laser beam heating mode with an active focusing servo was applied. With the focusing servo, the illumination was uniform at different positions on a disk. The efficiency of the optical system was about 0.55, indicating that 55% of the total input power was absorbed by the disk.

The power density distribution  $P(x, y)$  was simply modeled as below:

$$P(x, y) = \frac{8P_{absorb}}{\pi d_x d_y} \exp\left(-\frac{8x^2}{d_x^2} - \frac{8y^2}{d_y^2}\right) = P_{density} \exp\left(-\frac{8x^2}{d_x^2} - \frac{8y^2}{d_y^2}\right) \quad (4.1)$$

Here,  $P_{absorb}$  was the actual absorbed power.  $d_x$  and  $d_y$  were the Gaussian diameters along the down-track and off-track directions respectively. When the laser was in focus,  $d_x$  was 5.5 μm and  $d_y$  was 2 μm.  $P_{density}$  was the peak power density.

The disk surface was exposed by the focused laser beam under different conditions, such as duration (repetitions), powers, and spindle speeds. Figure 4. 3 shows the scheme of the laser exposure procedure. Several bands were exposed at different laser power levels and spindle rotating speeds. In each band, seven tracks were exposed under the same power level and spindle speed, but the repetitions for each track were different. The gap between two adjacent tracks in a band was 50 μm. The tracks that were exposed for the higher number of repetitions were exposed first. The free laser beam exposure tests were performed using a procedure described as follow:

(1) The laser was focused well to the disk surface. The first track was exposed by 1000 repetitions.

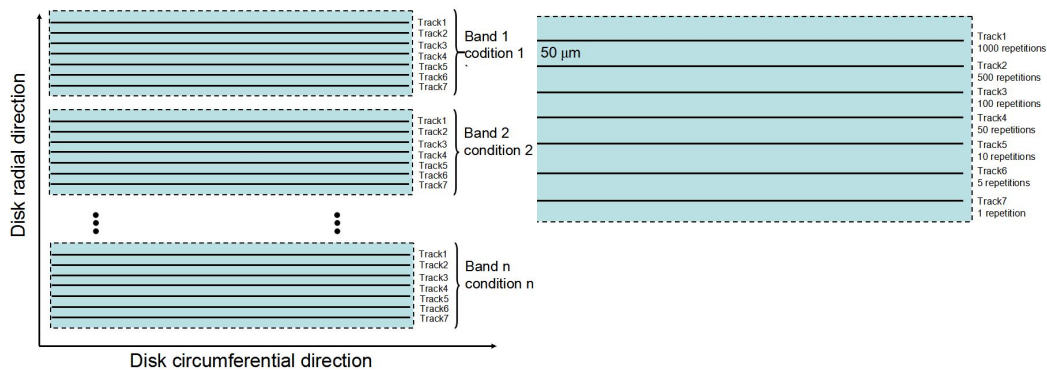
(2) The objective lens was moved 50  $\mu\text{m}$  radially inward after the exposure of the first track was finished and the second track was then exposed by 500 repetitions.

(3) The same process was repeated for the next five tracks, which were exposed for the numbers of repetitions at 100, 50, 10, 5 and 1, respectively. The whole exposure process took less than three minutes.

(4) After all of the seven tracks were exposed, the disk was uninstalled from the spindle and moved to the Candela optical surface analyzer (OSA) for surface inspection within one minute. The first scan was defined as the scan at 0 minutes. The OSA scanned the disk periodically while the disk kept spinning in the OSA at room temperature. Each scan took less than 1 minute and the period between two scans was 1 minute. The scan was stopped after about 22 minutes.

(5) Next we changed the laser power or spindle speed. We repeated steps 1 to 4 to perform the free laser beam exposure for another band with 7 tracks.

(6) After more than 24 hours, the disk was scanned again to determine the permanent steady state change of the disk surface.



(a) Bands exposed under different conditions; (b) tracks exposed for different repetitions in a band

Figure 4. 3 Schematic drawing of the experimental procedure for the free laser beam heating.

Table 4. 1 describes the heating conditions of each band on the sample. The sample was exposed by the focused free laser beam at different absorbed powers and spindle speeds for different bands.

Table 4. 1 Experimental conditions for free laser beam exposure

	Spindle speed (RPM)	Absorbed laser power (mW)	Power density (mW/ $\mu\text{m}^2$ )
3.5 inch, Al substrate, Z-tetraol, 60% bonding ratio, 9.5 Å)	600	110	25.5
	600	137.5	31.8
	600	165	38.2
	600	192.5	44.6
	1500	110	25.5
	1500	137.5	31.8
	1500	165	38.2
	1500	192.5	44.6

#### 4.2.2 NFT heating mode

It was confirmed from the numerical simulation that the size of the NFT focus spot was less than 50 nm along down-track direction as described in chapter 3. The width of an exposed track was much smaller than the lateral spatial resolution limit of the OSA. A single exposed track was not observable by the OSA. So a relatively larger scanning band had to be exposed in a way similar to shingled writing in shingled magnetic recording systems [69], as illuminated in Figure 4. 4. The slider with the NFT was moved in the radial direction at various speeds, while the spindle kept rotating at 1500 RPM. Each exposed track had a spiral shape. The pitch between two adjacent exposed tracks depended on the linear speed of the NFT spot along the radial direction. The slider was moved for 20  $\mu\text{m}$  and then stopped. The laser illumination was stopped together as well. So a 20  $\mu\text{m}$  wide band was exposed. This band was large enough to be detected by the OSA. For example, when the linear speed was 0.1  $\mu\text{m}/\text{s}$ , the pitch between the two exposed tracks was 4 nm. Since the cross-track width of each track was 100 nm, each track could be treated as exposed about 25 times. Because the lifetime of the NFT was limited for our home-made sliders, the sliders could not fly longer than a couple of hours during the laser exposure. So there was some minimum speed limit for the NFT motion in order to shorten the flying time of the slider. The slowest linear speed along the radial direction was 0.1  $\mu\text{m}/\text{s}$  in our tests.

By varying the radial speeds of the NFT, the exposed number of repetition could be controlled to be 25, 12, 4 and 2 in different exposed bands. Right after the NFT exposure, the disk was uninstalled and scanned by the OSA.

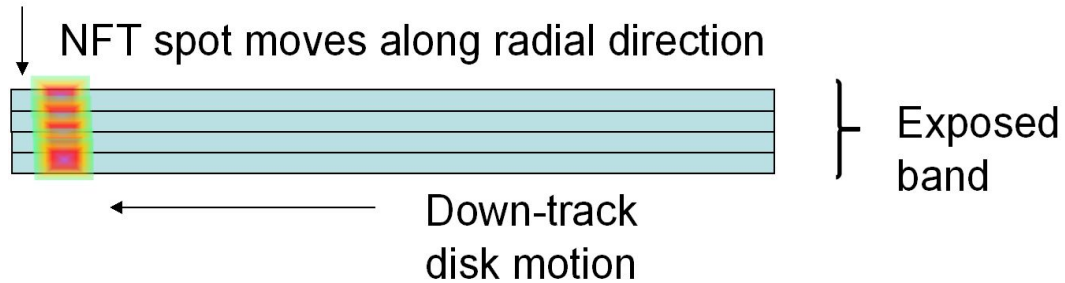


Figure 4. 4 Schematic drawing of NFT heating

### 4.3 Lubricant study under free laser beam heating

#### 4.3.1 Image processing of OSA scans

Figure 4. 5 shows a typical raw OSA Q-phase image of a band right after the free laser beam exposure. All of the tracks in the figure were exposed at 192.5 mW and the spindle speed was 1500 RPM. The exposure repetition numbers of the tracks were 1000, 500, 100, 50, 10, 5 and 1 from top to bottom, respectively. The red color in the figure indicates more lubricant depletion as that the thickness of the lubricant was smaller.

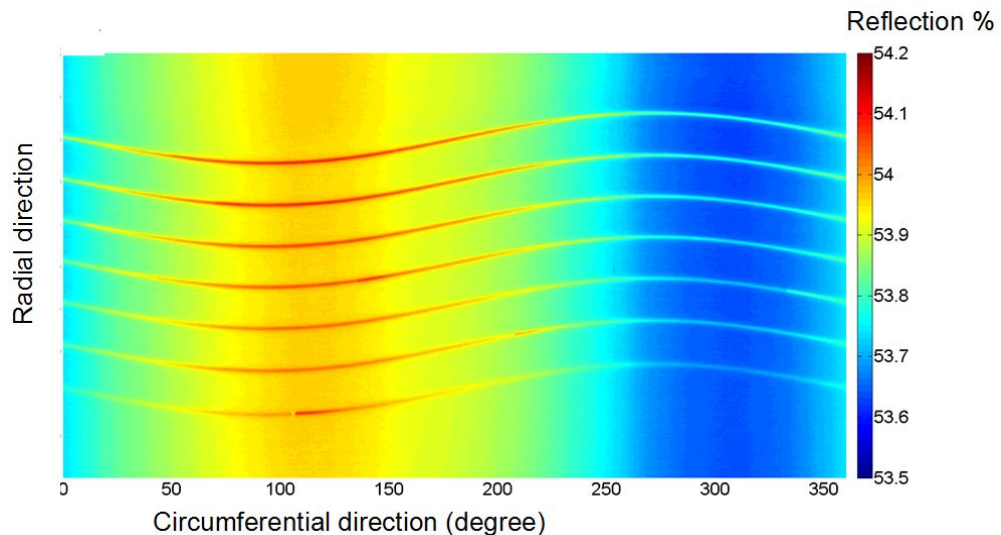


Figure 4. 5 A typical raw OSA Q-phase image of an exposed band

Because of the radial run-out of the OSA spindle and HAMR stage spindle, the exposed tracks in the OSA image showed some curvatures. Meanwhile, the run-out along a perpendicular direction also lead to the non-uniform background in the OSA image. An image processing script was developed to remove these curvatures and backgrounds from the OSA scans. Figure 4. 6 shows the relative reflectivity change of the exposed tracks after removing the non-uniform background and curvatures. After all the image

processing, the final exposed track should be a straight line along the circumferential direction.

The further data analysis, such as the depletion depths and widths of the tracks, was performed based on the finally processed image data.

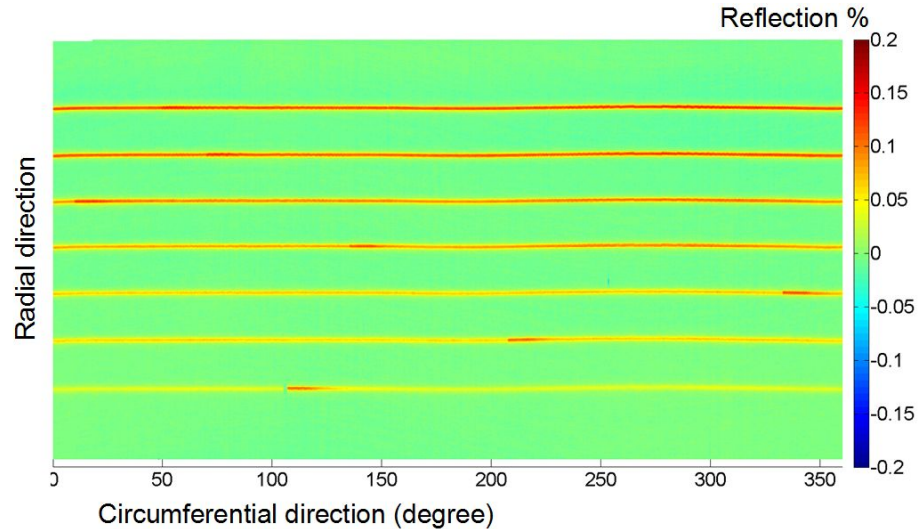


Figure 4. 6 Final OSA Q-phase image after removing the run-out curvature and background.

#### 4.3.2 Lubricant reflow

The lubricant was depleted during the free laser beam heating. However, the lubricant started to reflow back into the depleted region from the adjacent areas as soon as the heating source was removed. A typical exposed track was chosen to study the lubricant reflow behavior at room temperature. This track was exposed for 50 repetitions when the laser power was 192.5 mW and the spindle speed was 1500 RPM. Figure 4. 7 shows the OSA Q-phase image of this exposed track at different times. The red color indicates that the lubricant was thinner and depleted. It can be seen that the contrast of this exposed track became smaller as time elapsed, indicating that the lubricant reflowed back into the depleted area. The depletion was almost totally recovered after 24 hours and there was very subtle change of the disk surface in the permanent state.

The depletion profiles of the exposed track at different times are plotted in Figure 4. 8. The depletion track became shallower with time because the lubricant from the adjacent area of the exposed track flowed back into and filled this depleted track. There was some very small permanent change on the disk surface, probably due to the surface change of the carbon overcoat or substrate [53, 70].

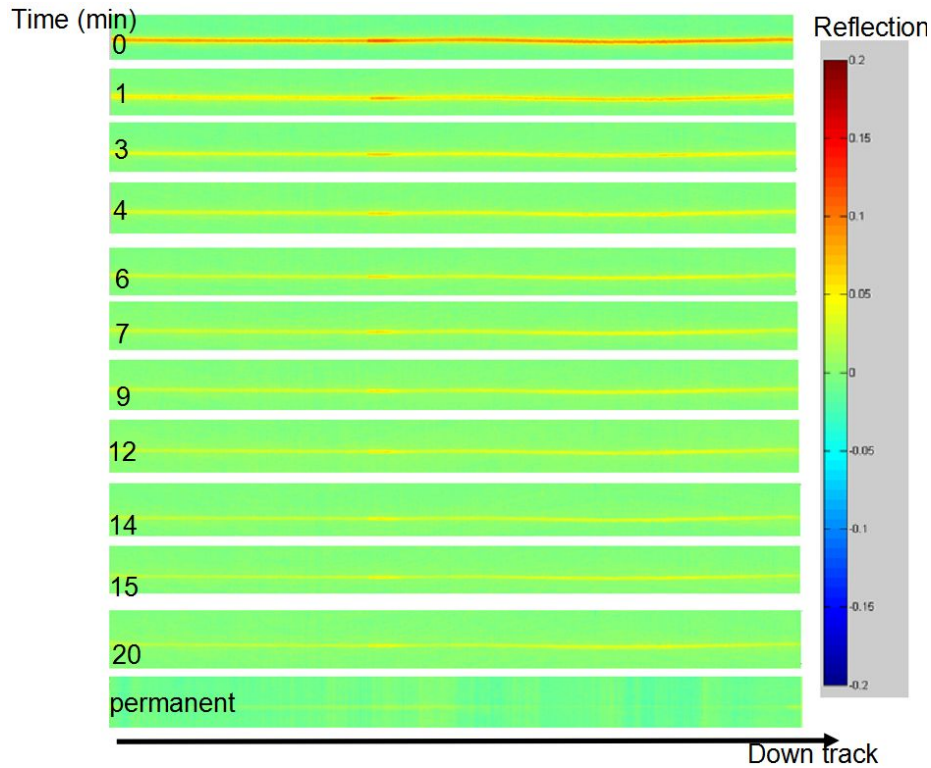


Figure 4. 7 OSA Q-phase image of an exposed track at different time periods when the laser power was 192.5 mW, the spindle speed was 1500 RPM and heating repetition was 50.

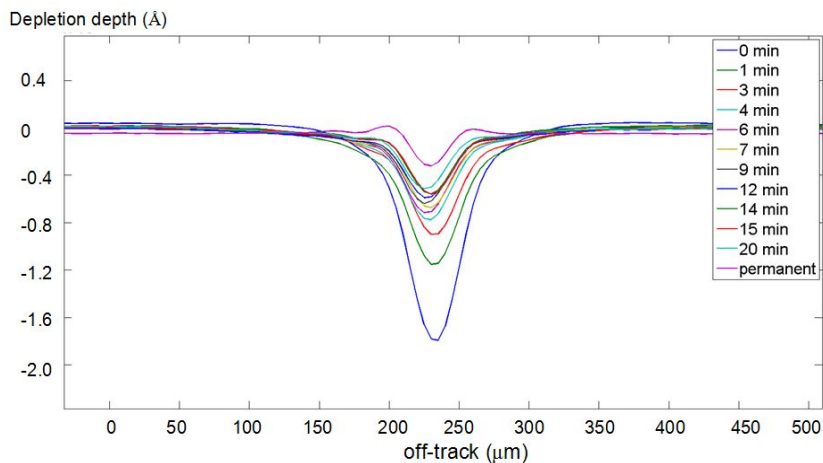


Figure 4. 8 Lubricant depletion profiles of the exposed track at different times. The laser power was 192.5 mW, the spindle speed was 1500 RPM and repetition number was 50.

The real lubricant reflow process was obtained by subtracting the permanent change from the depletion profiles. The relationship between the lubricant depletion depth and time is plotted in Figure 4. 9. The lubricant depletion depth and width both decreased as time elapsed. The lubricant depletion depth decreased with time approximately according

to a power law. The rate of reflow was highest soon after the laser heating source was removed and it later became slower.

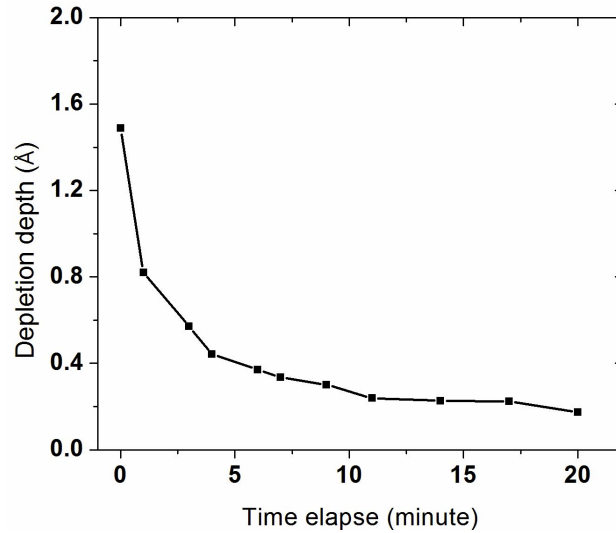


Figure 4. 9 Real lubricant depletion depths vs. time after disk was heated after 50 repetitions. The laser power was 192.5 mW and the spindle speed was 1500 RPM.

The lubricant reflow behavior was analyzed for all other numbers of repetitions when the laser power was 192.5 mW and the spindle speed was 1500 RPM. Under different heating repetitions, the initial lubricant depletion depths (after subtracting the permanent change) were different, as shown in Figure 4. 10. The initial lubricant depletion was higher as the repetitions increased. However, the lubricant reflowed back in a similar power law trend for all the exposed tracks that were exposed for different repetitions.

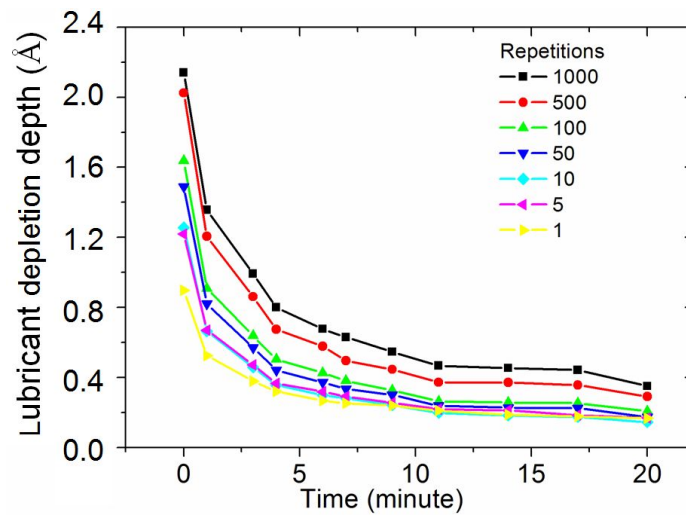


Figure 4. 10 Lubricant depletion depth as time elapses after the tracks were heated at different repetitions. The laser power was 192.5 mW and the spindle speed was 1500 RPM.

The depletion depth was normalized by the initial depletion depth in order to exclude the effect of the initial lubricant depletion. As seen in Figure 4. 11, the reflow processes for those tracks showed the same trends. Almost 80% of the lubricant depletion was recovered after the lubricant relaxed for 20 minutes at room temperature. The lubricant reflow behavior for the exposed track that was heated for 1000 repetitions and 1 repetition slightly deviated from the other tracks. The lubricant reflow of the track exposed for 1 repetition was slightly different probably due to the measurement noise of the OSA. The depletion at repetition 1 was so subtle that the signal to noise ratio was small in the OSA measurements. The track that was exposed for 1000 repetitions was different because the lubricant properties had been changed after the long time heating. For example, if the viscosity increased as the mobile lubricant got evaporated and the bonding ratio increased, the lubricant reflow could become slower [62].

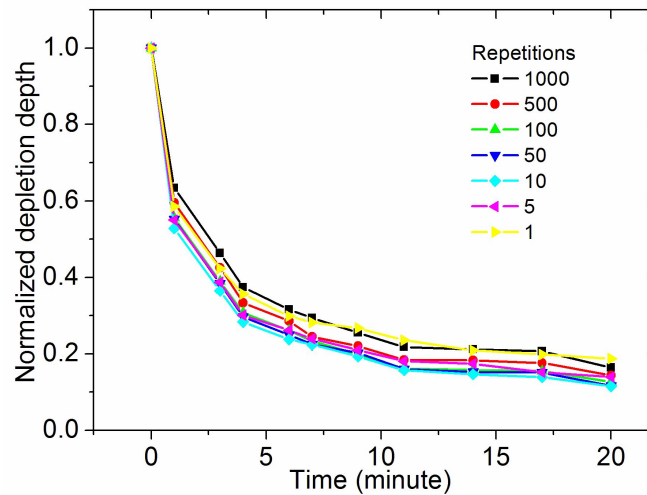


Figure 4. 11 Normalized lubricant depletion depth during the reflow process after the disk was initially heated for the different repetitions. The laser power was 192.5 mW and spindle speed was 1500 RPM.

More data analysis has been performed for the lubricant reflow under other heating conditions, such as different spindle speeds, laser powers and repetitions. The initial lubricant depletion thickness was different under the different heating conditions. But the reflow of lubricant occurred at room temperature for all tests. All lubricant depletion depths in the reflow processes were normalized by the initial values. As summarized, for some of the reflow processes with different heating conditions in Figure 4. 12, the normalized curves almost coincided. After 20 minutes, about 80% of the lubricant depletion was recovered by the reflow. All the lubricant reflow processes followed the same trend and relaxation behavior, regardless of the initial lubricant depletion.



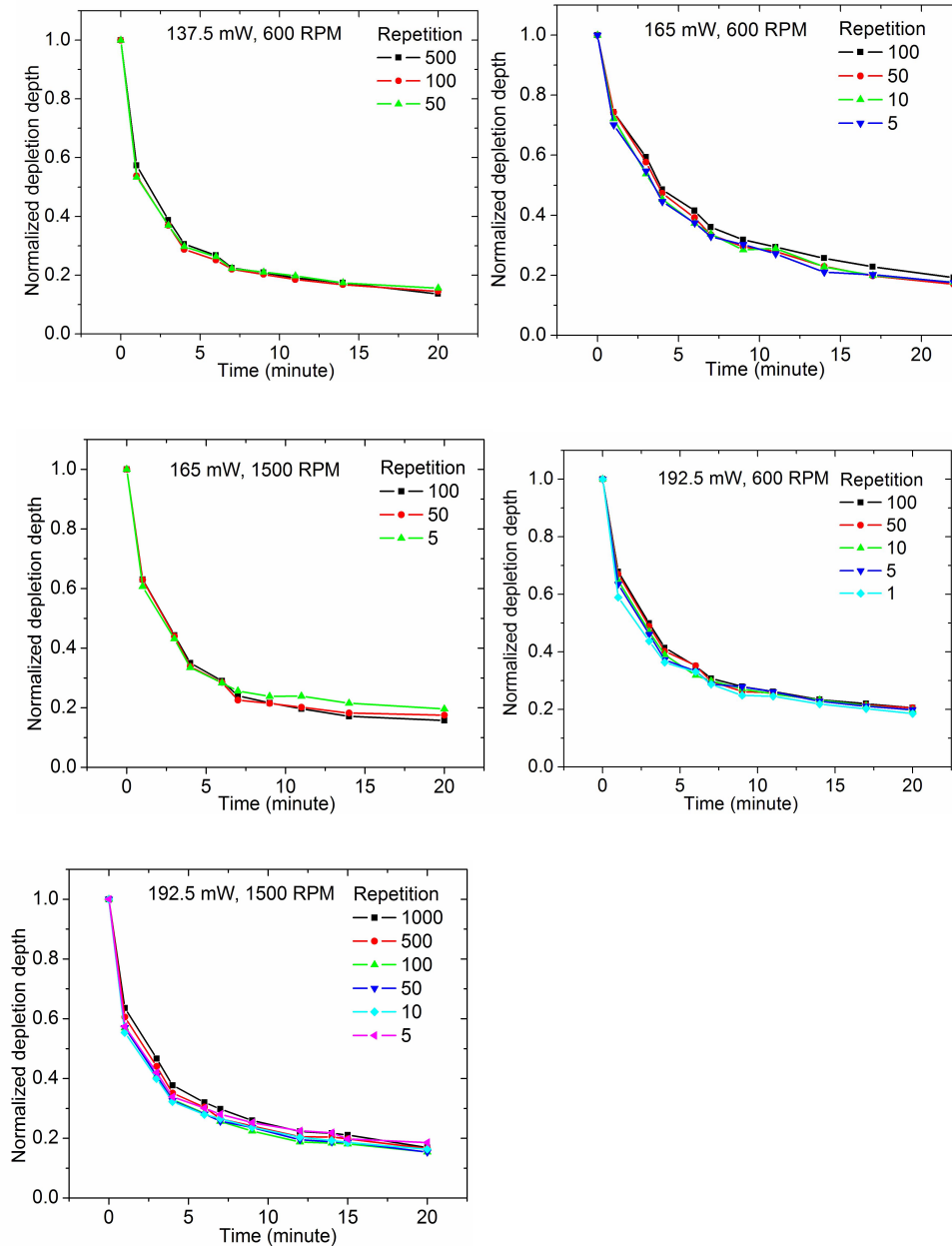


Figure 4. 12 Normalized lubricant depletion depth during the reflow process after the initial heating at various heating conditions.

Five curves with the same number of repetitions were chosen from Figure 4. 12 to show the effect of the heating conditions on lubricant depletion, as shown in Figure 4. 13. Each of those tracks was exposed for 50 and 100 repetitions but at different power levels and different spindle speeds. The temperature increase during the laser exposure was quite different if the laser power and spindle speed was different. So the lubricant depletion was different under the different heating conditions.

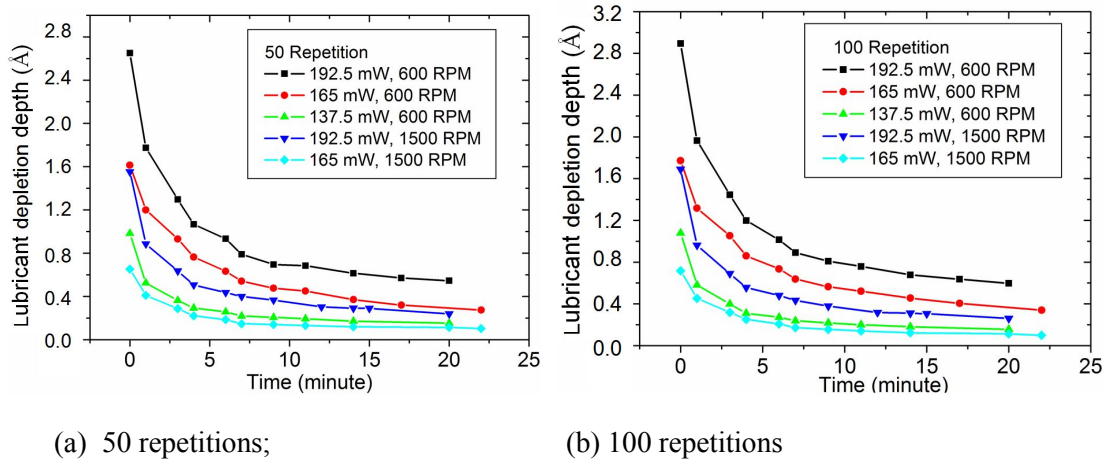


Figure 4. 13 Lubricant depletion after the disk was heated at different power levels and spindle speeds. (a) all of the tracks were exposed by 50 repetitions (b) all the tracks were exposed by 100 repetitions.

The temperature rise and thermal gradient was the largest in the test when the power input was 192.5 mW and the spindle speed was at 600 RPM. The lubricant depletion depth was most in this heating condition, as shown by the black curve in Figure 4. 13. As the power decreased or spindle speed increased, the lubricant depletion depth became less. More details about the lubricant depletion will be discussed in section 4.3.2.

It can be concluded that the lubricant reflows back into the depleted area of an exposed track after the laser heating was removed. After 20 minutes, about 80% of the initial depletion was recovered. The lubricant reflowed back in the same trend, regardless of the initial lubricant depletion.

### 4.3.2 Lubricant depletion under heating by the free laser beam

Lubricant depletion depends on the temperature, temperature gradient, heating duration and air bearing pressure as modeled in [54]. Because there was no slider flying on the disk in the free laser beam heating tests, the pressure on the disk surface was close to atmosphere. So the lubricant depletion in this study mainly focused on the effect of laser power, spindle speed and radiation repetitions.

Figure 4. 14 shows the profiles of the lubricant depletions from the OSA Q-phase image at 0 minutes. These seven tracks were exposed by 1000, 500, 100, 50, 10, 5, 1 repetitions respectively. A higher number of repetitions was equivalent to lubricant exposure for longer durations. The laser power for all seven tracks was 192.5 mW and the spindle speed was 1500 RPM. It can be seen that the lubricant depletion depth of the exposed track increased as the repetitions increased, while the width of the depletion track did not change as the number of repetitions changed.

As described in the experimental procedure (section 4.2.1), the track exposed at the highest repetitions was exposed first and then lower repetition exposures were performed

in sequence. In reality, the track that was exposed earlier had started to reflow during the period for exposing of the other tracks. When these seven tracks were first scanned by the OSA (as defined by 0 minutes), the track exposed for the larger number of repetitions had experienced more time for reflow. So the real initial depletion depth for higher repetition exposure would be slightly higher than the one measured by the OSA at 0 minute.

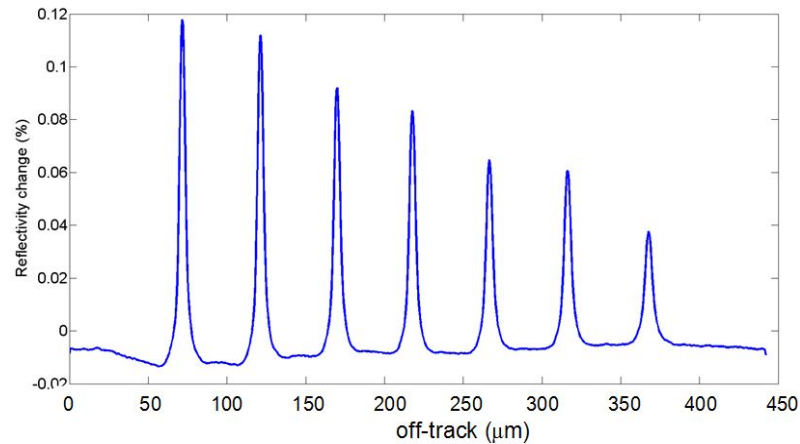


Figure 4. 14 Initial lubricant depletion profile from OSA Q-phase image captured 0 minute (Figure 4. 6). The laser power for all seven tracks was 192.5 mW and spindle speed was 1500 RPM. Repetition was 1000, 500, 100, 50, 10, 5, 1 for the seven tracks from left to right.

The relationship between the initial depletion depth and repetitions is plotted in Figure 4. 15. The effect of permanent change on the initial depletion depth was excluded by subtracting the permanent change from the depletion depth scanned at 0 minutes. The lubricant depletion was a time accumulated process. The lubricant depletion increased as it was exposed for longer times or more repetitions. However, the growth of depletion was faster at the beginning and it became slower as the repetitions increased.

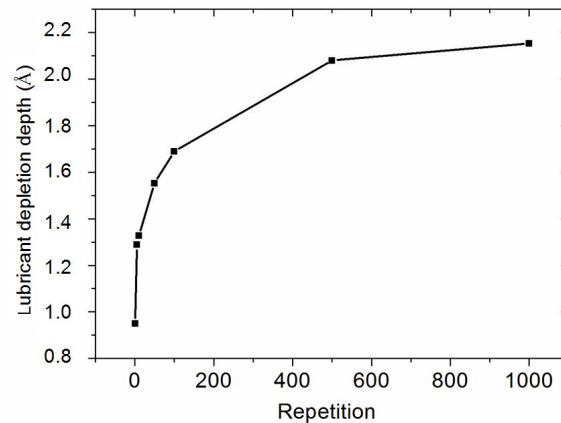


Figure 4. 15 Lubricant depletion at 0 minute vs. number of repetition when laser power was 192.5 mW and spindle speed was 1500 RPM

The lubricant depletion depths with respect to repetitions under different heating conditions were compared in Figure 4. 16. It can be seen that all of the depletion curves showed similar trends in the log scale. The slopes of those curves in the log scale are quite close, although the initial values are different for the different heating conditions.

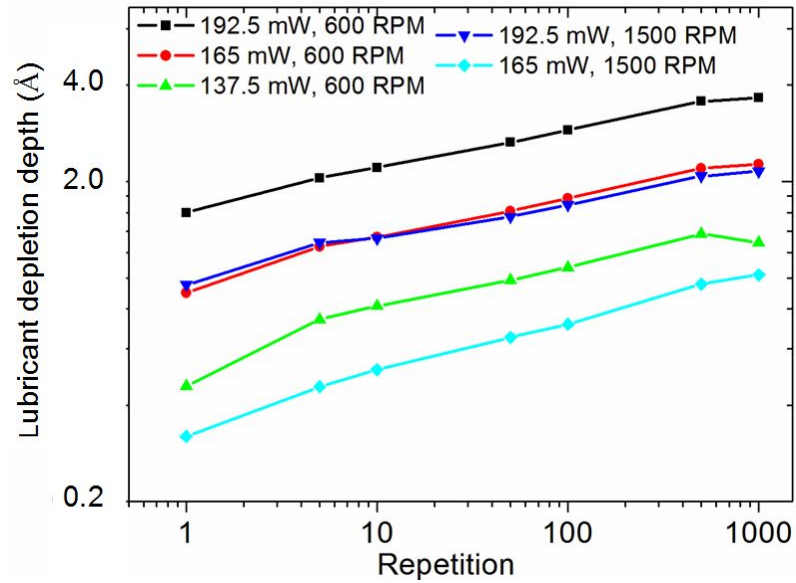


Figure 4. 16 Lubricant depletion vs. repetition under different heating conditions

It was found that the relationship between the lubricant depletion depth and repetitions can be simplified to a power law form as expressed by equation 4.2:

$$\log(d) = a + b \log(t)$$

$$d = 10^a t^b = At^b \quad (4.2)$$

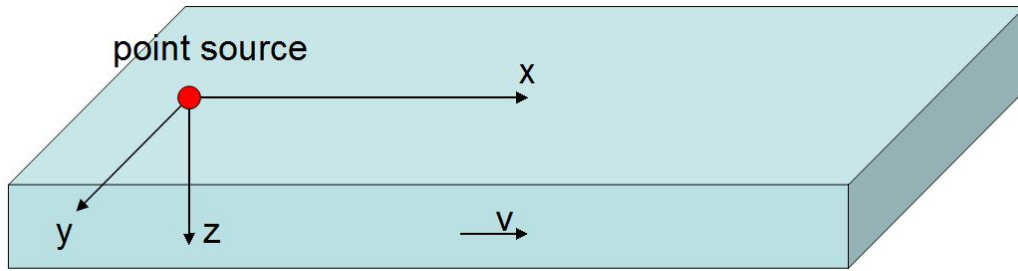
Here  $d$  is the depletion depth measured by the OSA, and  $t$  is the repetition number.  $A$  and  $b$  are two parameters that can be obtained by curve fitting for the 5 curves in Figure 4. 16. The repetition number is equivalent to the heating duration. Larger repetition indicates longer heating time. So equation 4.2 also holds for the relationship between depletion depth and heating duration.

Table 4.2 lists the fitting values of  $A$  and  $b$  for the five different heating conditions. The parameter  $b$  was the same for all of the five heating conditions. Parameter  $A$  was different for the various heating conditions. Larger  $A$  indicates that the rate of depletion was faster. With the same spindle speed, the temperature was higher as the power input increased,  $A$  became larger. With the same laser power input,  $A$  became larger as the spindle speed was reduced. In both situations,  $A$  was larger when the temperature and thermal gradient was higher.

Table 4. 2 Values of parameters A and b for the lubricant depletion model (4.2)

Condition	A (Å)	b
Test 1: 192.5 mW, 600 RPM	1.54	0.132
Test 2: 165 mW, 600 RPM	0.96	0.132
Test 3: 137.5 mW, 600 RPM	0.054	0.132
Test 4: 192.5 mW, 1500 RPM	0.90	0.132
Test 5: 165 mW, 1500 RPM	0.44	0.132

A thermal model was derived to show how the spindle speed and laser power input affected the temperature increase and thermal gradient on the disk. The laser heating was simplified to be a heat flux point source on a semi-infinite moving workpiece, as shown in Figure 4. 17. The plate moves in the  $x$  direction with a constant speed  $v$ . The power of the heating source is  $P$ .

Figure 4. 17 A heating point source on a semi-infinite moving workpiece at speed of  $v$ .

The equation of heat conduction can be described as:

$$-v \frac{\partial T}{\partial x} = \frac{\lambda}{\rho c_p} \nabla^2 T = \kappa \left( \frac{\partial^2 T}{\partial x^2} + \frac{\partial^2 T}{\partial y^2} + \frac{\partial^2 T}{\partial z^2} \right) \quad 4.3$$

Here,  $T$  is the temperature on the workpiece (disk),  $v$  is the workpiece speed,  $\rho$  is density of the workpiece material,  $\lambda$  is the thermal conductivity,  $c_p$  is the specific heat of the material, and  $\kappa$  is called thermal diffusivity.

The boundary conditions are:

$$\frac{\partial T}{\partial x} \rightarrow 0 \text{ for } x \rightarrow \infty; \quad \frac{\partial T}{\partial y} \rightarrow 0 \text{ for } y \rightarrow \infty; \quad \frac{\partial T}{\partial z} \rightarrow 0 \text{ for } z \rightarrow \infty$$

$$T = T_0 \text{ for } x \rightarrow \infty \text{ or } y \rightarrow \infty \text{ or } z \rightarrow \infty$$

The analytical solution for equation 4.3 can be obtained as below:

$$T = T_0 + \frac{P}{4\pi\lambda r} \exp\left(\frac{v}{2\kappa}(x-r)\right)$$

$$r = \sqrt{x^2 + y^2 + z^2}$$
(4.4)

The thermal gradient is given by:

$$\frac{\partial T}{\partial x} = \frac{P}{4\pi\lambda r} \exp\left[\frac{v}{2\kappa}(x-r)\right] \left[\frac{v}{2\kappa} - \frac{vx}{2\kappa r} - \frac{x}{r^2}\right]$$

$$\frac{\partial T}{\partial y} = \frac{P}{4\pi\lambda r} \exp\left[\frac{v}{2\kappa}(x-r)\right] \left[-\frac{vy}{2\kappa r} - \frac{y}{r^2}\right]$$
(4.5)

Figure 4. 18 shows the isotherms of the temperature solution for a moving point source embedded in an infinite medium. They were cylindrically symmetric about the y-axis.

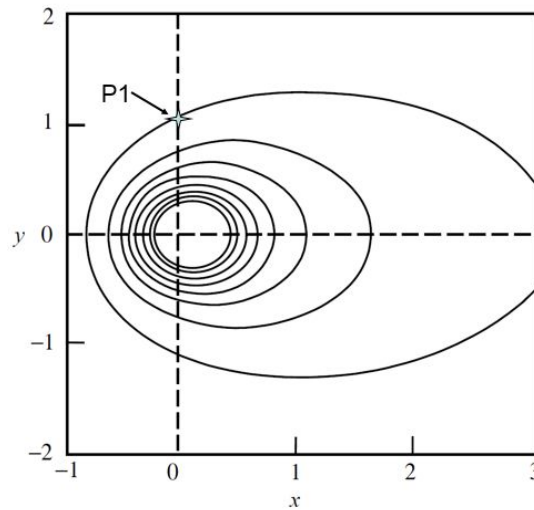


Figure 4. 18 Temperature contours of point source heating [71]

It can be seen from equations 4.4 and 4.5 that, for a fixed speed  $v$ , the temperature rise along the  $x$  and  $y$  directions are both linearly increased with the power. For a fixed power input, the temperature rise decreases as the speed increases because  $x$  is usually less than  $r$ .

It can be seen that the thermal gradient magnitude increases linearly as the power increases for a fixed speed. However, the relationship between the thermal gradient and speed is not so straightforward from equation 4.5.

In the case of the free laser beam heating on a PMR disk, the typical value of  $\lambda$  is 10 W/mK,  $v$  is 10 m/s,  $\kappa$  is  $10^{-5}$  m<sup>2</sup>/s [72]. Considering a point P1 located at (0, 1000 nm, 0),

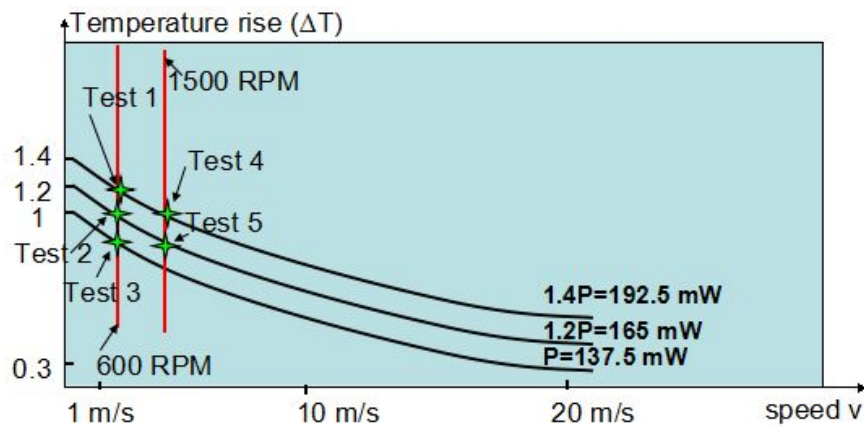
as marked in Figure 4. 18, the temperature and thermal gradient at P1 are obtained as shown in 4.6.

$$T = T_0 + \frac{P}{4 \times 10^{-5} \pi} \exp(-5 \times 10^{-2} v)$$

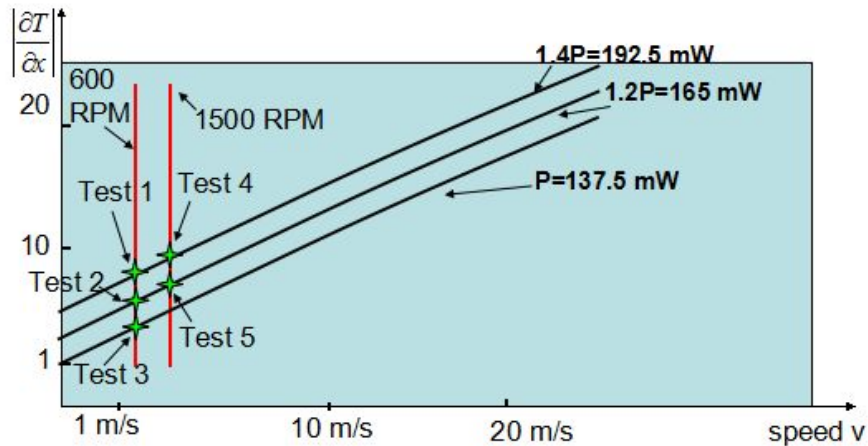
$$\frac{\partial T}{\partial x} = \frac{P}{4 \times 10^{-5} \pi} \exp[-5 \times 10^{-2} v][5 \times 10^4 v] \quad (4.6)$$

$$\frac{\partial T}{\partial y} = \frac{P}{4 \times 10^{-2} \pi} \exp[-5 \times 10^{-2} v][-5 \times 10^4 v - 10^7]$$

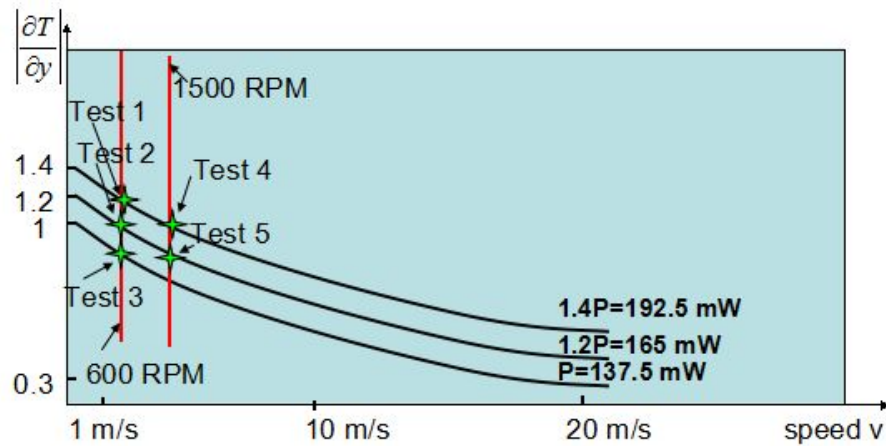
The sketched trends of the temperature and magnitude of the thermal gradient at P1 with respect to the disk speed and laser power are shown in Figure 4. 19. The thermal gradient along the x direction (down-track) almost has a linear relationship with respect to the disk speed when the speed is lower than 20 m/s. As the disk speed increases, the thermal gradient along x finally approaches 0. The temperature rise and thermal gradient along y direction show a similar trend. It can be noticed that the temperature rise and thermal gradient along y (cross-track) is almost the same for test 2 and 4, test 3 and 5. The similar cross-track thermal gradient and temperature caused a similar lubricant depletion under those tests although the laser power and spindle speed were different. This could simply explain why the parameter A for test 2 and test 4, test 3 and test 5 in table II were quite close.



(a) Peak temperature vs. disk speed and laser power



(b) Thermal gradient along down-track direction vs. disk speed and laser power



(c) Thermal gradient along cross-track direction vs. disk speed and laser power

Figure 4. 19 Sketched trends of temperature and magnitude of thermal gradient at P1 with respect to disk speed and laser power.

It is shown in this section that the lubricant depletion behavior of a z-tetraol lubricant can be expressed as a simple power law as  $At^b$ . A is a parameter that mainly depends on temperature and cross-track thermal gradient. A is significantly larger when the temperature and cross-track thermal gradient increases. b is a parameter that does not rely on the heating conditions for the lubricant used in this study.

#### 4.4. Lubricant depletion under NFT heating

The lubricant depletion was scanned by the OSA soon after the NFT heating test. Figure 4. 20 shows the Q-phase image of the lubricant depletion when the total input power to the NFT was 192.5 mW. There were some curvature shapes of the exposed



bands in the Q-phase image due to the spindle lateral run-out for the Cal stage and OSA spindle. The depletion profiles were extracted as shown in Figure 4. 20b.

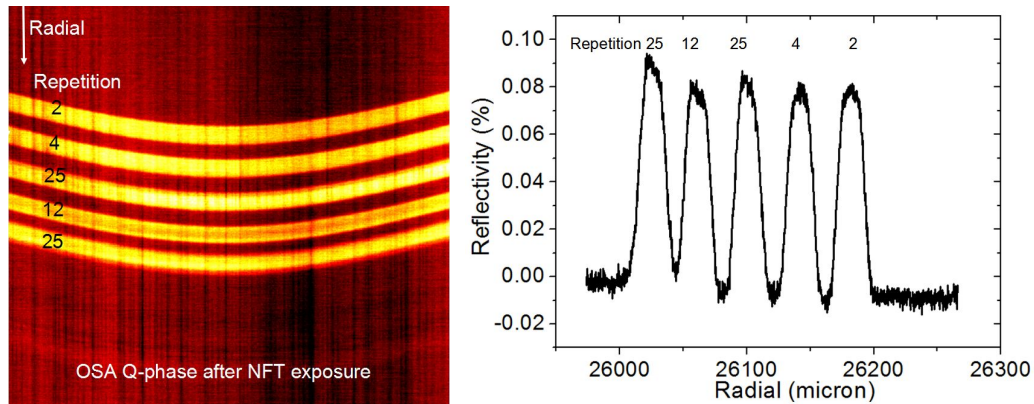


Figure 4. 20 (a) Q-phase image of lubricant depletion after NFT heating (b) surface reflectivity change due to lubricant depletion after NFT heating

There was no significant difference between the different bands that had been exposed by different repetitions. However, comparing the lubricant depletion between the free laser beam heating and the NFT heating mode with similar repetitions, we found that the lubricant depletion under the NFT heating was more severe than that under the free laser beam heating.

The light intensity is enhanced after the light transmits through the NFT. Meanwhile, the size of the NFT heating was about 100 by 36 nm while that of the free laser beam heating was about 2 by 5.5  $\mu\text{m}$ . So the thermal gradient under the NFT heating could be about 2 orders larger than that under the free laser beam heating. From the previous study of the lubricant depletion under the free laser beam heating conditions (section 4.3.3), we have already concluded that the cross-track thermal gradient and temperature rise play a critical role for the lubricant depletion. So it can be inferred that the large thermal gradients during the NFT heating in HAMR systems leads to more significant lubricant change, compared with the case under the free laser beam heating. However, larger thermal gradient in HAMR system is better for the magnetic writing as discussed in chapter 1. A larger thermal gradient in the magnetic layer can equivalently enhance the magnetic flux gradient thus making writing performance better. More optimization can be done to get the balance of the thermal gradient between both lubricant depletion and magnetic writing.

## 4.5 Summary

In this chapter, the lubricant depletions and reflow behaviors were studied under various free laser beam heating and NFT heating conditions. The lubricant reflowed back after it was depleted. The reflow of lubricant after various heating conditions showed similar trends, regardless of the initial lubricant depletion. After 20 minutes, about 80%

of the initial depletion was recovered. The lubricant depletion behavior of a Z-tetraol lubricant could be expressed as a simple power law:  $At^b$ .  $A$  is a parameter mainly depending on the temperature and cross-track thermal gradient.  $A$  is significantly larger when the temperature and cross-track thermal gradient increases.  $b$  is a parameter that does not depend on the heating conditions for the lubricant used in this study.

The lubricant depletion under the NFT heating was compared with that under the free laser beam heating. The comparison showed that NFT heating resulted in more severe lubricant depletion likely due to the larger cross-track thermal gradient. More care should be taken for the HAMR system design because the existence of a trade-off of thermal gradient between the magnetic writing and lubricant thermal stability. Larger thermal gradient favors the magnetic writing while making the lubricant depletion worse.

## Chapter 5 Degradation of carbon overcoat under laser heating

The carbon overcoat is under the lubricant layer on the disk and on the air bearing surface of the slider. The carbon overcoats on both the disk and slider are used as a protective layer to increase the mechanical stability of the HDI. The carbon overcoat is necessarily heated during the HAMR writing. The thermal stability of the carbon overcoat has been another concern for the HDI in HAMR systems. The degradation of the carbon overcoat under various thermal conditions is discussed in this chapter.

### 5.1 Introduction

Presently, amorphous carbon (a-C) is widely used as a protective overcoat for the magnetic disk and the flying slider due to its unique mechanical, physical, and chemical properties [33]. The carbon overcoat is primarily chemically inert and is used to protect the magnetic layer from corrosion. Amorphous carbon does not have grain boundaries and it can be made extremely smooth and continuous. Its excellent topographical conformity allows the slider to fly a couple of nanometers above it. In addition, its hardness can also be tuned to approach that of a diamond so it can act as a wear resistant overcoat. So when contacts occur between the head and disk, the carbon layer can protect the disk and head from wear.

Carbon overcoats on the magnetic disk mainly consist of  $sp^3$  and  $sp^2$  carbon hybridization, as shown in Figure 5. 1. The types of bonding in amorphous carbon give its physical properties (such as hardness, Young's modulus, etc.). Such properties are strongly dependent on the ratio between the  $sp^2$  and  $sp^3$  bonds [73, 74]. The  $sp^2$  component makes a-C like graphite while  $sp^3$  makes it like diamond. In general, it is possible to have a mixture of  $sp^3$ ,  $sp^2$ , and some  $sp^1$  sites in a-C films. Because of the high concentration of  $sp^3$ , the a-C is also known as diamond-like carbon (DLC). In addition, hydrogen and nitrogen atoms are inevitably incorporated during the deposition process of a-C films. Tuning the composition of a-C helps to prevent corrosion of the magnetic layer, enhance the mechanical hardness of the overcoat, and improve the adhesion of the lubricant to the disk overcoat.

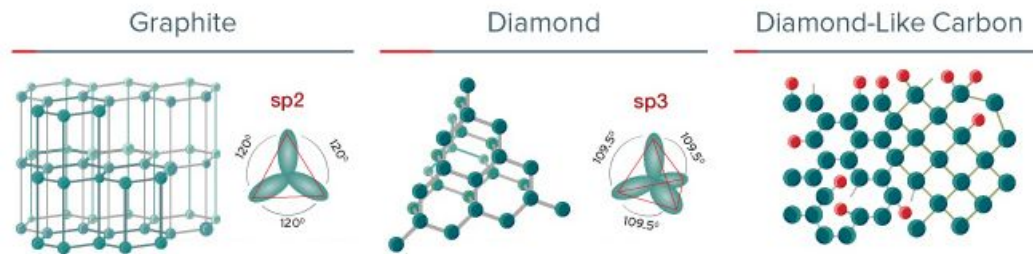


Figure 5. 1 Sp<sup>3</sup> and sp<sup>2</sup> carbon hybridization in diamond like carbon overcoat [75].

However in HAMR systems, the micro-structure of the carbon overcoat can be changed during the writing process if the temperature of the overcoat reaches some temperature for some period of time. Many experiments have reported the carbon overcoat degradation under various heating conditions. The film can lose its mechanical hardness and its function to protect the underlayers after it is degraded. Moreover, the surface roughness can be changed, resulting in problems for flying slider stably.

In Wang's work [76], the laser heating at a power of 150 mW induced significant roughening of the carbon film, which was prepared by chemical vapor deposition (CVD). It suggested that carbon films synthesized by the CVD method would be limited to relatively low laser power heating. However, at the same amount of laser power input, the carbon films produced by the filtered cathodic vacuum arc (FCVA) technique demonstrated superior thermal stability, compared with the CVD films of similar thickness. The thermal stability depended on the film thickness as well. FCVA films demonstrated a decrease in thermal stability for thinner films, which can be attributed to the higher thermal energy absorbed per carbon atom.

Also in Wang's other work [77], rapid heating annealing (RTA) tests for carbon films were performed. It demonstrated significant structural changes in 3.4-nm-thick a-C:H films above a maximum annealing temperature of 400–450 °C in a rapid heating test. The chemical components analysis did not reveal discernible changes in the film thickness or the sp<sup>3</sup> content, indicating that oxidation and graphitization of the a-C:H films were either secondary or negligible under the tested RTA conditions. When the maximum annealing temperature was above 450 °C, it was suggested that the depletion of hydrogen, the increase of the sp<sup>2</sup> cluster size, and the enhancement of the carbon network ordering are the main factors affecting the structural stability of the a-C:H films.

In Togawa's work [60, 78], they found that the surface reflectivity of the DLC film was changed and decreased when the temperature was raised to 365 °C. An asperity was observed along the laser-irradiated track on the disk surface. It was also found that the density of the DLC film was decreased by the laser heating. The decrease of the surface reflectivity was due to the asperity and density change of the DLC film. In a temperature-controlled test by a conventional heater, it was found that the refractive index decreased when the CVD carbon film was heated to a temperature over 300 °C for

600 s. The refractivity of the DLC films continuously decreased with an increase in the heating duration.

In Jone's work in Seagate [79], a pump probe technology was used to measure the transient temperature rise during the laser heating. The heating rate in their test was about  $10^6$  °C/s. It was found that significant structural change (oxidation and graphitization) of the PECVD (plasma-enhanced chemical vapor deposition) carbon overcoat occurred when the temperature was raised to about 480 °C within 500  $\mu$ s. The surface topography of the DLC overcoat also was changed under such a heating condition.

A conventional temperature controlled device (TCD), like an oven or a hot plate, was usually used to heat the carbon film samples because the temperature can be precisely monitored and controlled. Obviously, the time to heat the disk to about 500 °C in an oven was on the order of several seconds. The total heating duration in the TCD was a few orders longer than the HAMR writing, which is on the order of a few nanoseconds. And the heating rate was limited to 10 to 100 °C/s in the TCD. So the heating rate was several orders smaller than the heating rate in HAMR drives, which is about  $10^{11}$  °C/s. So the thermal behavior of the carbon films in TCD may deviate from that in HAMR media.

Quite different from the heating process in TCD, the heating rate of the laser heating can be at almost the same order or slightly smaller than that in HAMR systems. The heating duration was about one order or two orders longer in the focused laser beam heating experiments because the focused beam size was around a couple of microns which was much larger than the heating size generated by the NFT in HAMR systems. However, the accumulated total exposure time for the carbon overcoat on the disk in the lifetime of a HAMR drive can still be emulated by the focused laser beam experiments since a bit on the disk is heated tens of times during a drive's lifetime. The accumulated heating time of a bit on the disk is about 0.1 ms in a HAMR drive [80]. Whereas the carbon overcoat on the slider surface suffers from the laser heating all the time during the data writing. The total heating time of the carbon overcoat on the slider surface is a few orders longer than that of the carbon film on disk surface during a drive's lifetime.

Various chemical component analysis methods, such as X-ray photoelectron spectroscopy (XPS) [81], Raman spectroscopy or Transmission electron microscopy (TEM) [82] have been widely used in the studies of carbon overcoats to understand how the micro-structures evolve after thermal heating. The lack of those tools in CML limited our capability to study the chemical structures of the carbon films. However the surface topography changes and surface reflectivity changes are also figures of merit of the carbon films, because those changes are always caused by micro-structural changes of the carbon films. A conductive AFM (C-AFM) system, which is used to measure the film's conductivity, also has the potential to characterize the micro-structural changes of the carbon films because the  $sp^2$  hybridization component is conductive while  $sp^3$  is not [83, 84]. In CML we modified the scanning probe microscope to a C-AFM system to measure

the perpendicular conductivity of a carbon film. More details of C-AFM measurement are given in section 5.2.

Meanwhile, some studies have been performed in the past several years to investigate the mechanisms of the carbon film degradation by numerical atomic modeling. Sullivan et. al. [85] proposed a model for stress relaxation of amorphous carbon films under thermal annealing. The stress relaxation in carbon film was driven by the conversion of  $sp^3$  into  $sp^2$ . They assumed that the transformation of  $sp^3$  to  $sp^2$  only required thermal activation over a barrier and was governed by the first order reaction rate theory. A model [86] for the conversion of  $sp^3$  to  $sp^2$  in a-C:H vs. temperature and time was developed by refining Sullivan's thermal activation model. Two thermally-activated processes were modeled:  $sp^3$  of carbon hybridization to  $sp^2$  and breaking of carbon-hydrogen bonds.

Molecular dynamics simulation has also been used to study the link between macroscale mechanical properties of carbon films and the microstructure [74]. The graphitization process under friction and thermal heating could be simulated by molecular dynamics as well [87]. It is noticed that graphitization, as quantified by the increase in  $sp^2$  content, happens very quickly in a timescale of  $\sim 20$  ps in the range of the HAMR heating period ( $\sim$  ns). And the graphitization was largely suppressed for the carbon films with high diamond-like characters [88].

Great efforts have been taken to make the carbon films more thermally stable. Some new deposition technologies like FCVA have been proposed to get carbon films with higher  $sp^3$  content. Some additives can also dope into the carbon films to improve the stability as well, as proposed in [89]. Silicon nitride ( $SiN_x$ ) interlayer has been proposed to help in maintaining/improving the  $sp^3$  carbon bonding, enhancing interfacial strength/bonding, improving oxidation/corrosion resistance, and strengthening the tribological properties of FCVA-deposited carbon films, even at ultrathin levels (1.2 nm) [90].  $SiN_x$  has also been investigated as a replacement for the current carbon films [91, 70]. It is still not confirmed that those new hard films can be finally integrated into HAMR systems because other concerns need to be considered as well, like the ability of large volume manufacture, the compatibility with the lubricant, etc.

In general, it is still very important to study and understand how the current carbon film fails under the HAMR conditions. In this chapter, a C-AFM measurement of carbon film conductivity is introduced in section 5.2. Later the study of the carbon film degradation under the various thermal heating conditions, including temperature controlled heater heating, free laser beam heating and NFT heating, is discussed. The experimental procedure is presented in section 5.3. Then the experimental results are discussed in section 5.4. The final section 5.5 summarizes this chapter.

## 5.2 Conductive AFM measurement of carbon films

C-AFM is a secondary imaging mode derived from the contact AFM. C-AFM can be used to characterize conductivity variations of the thin films. A schematic diagram of the C-AFM is shown in Figure 5. 2. A contact mode AFM tip was used in our C-AFM system. The tip was coated by a deposited Pt layer to make it conductive. The carbon films were deposited on the surface of doped silicon wafers which were conductive. The tip contacted the sample and the trace of the tip followed the topography of the sample surface. A constant voltage bias was applied between the tip and substrate. When there was a perpendicular conducting channel in the carbon film, the current through the tip and sample increased [92], as illuminated in Figure 5. 2. The current signal was amplified by a current amplifier and converted into a voltage signal. The voltage signal was further fed into the AFM signal box and captured by the AFM controller. Finally a two-dimensional conductivity image was shown in the AFM control panel together with the topography image. The conductivity measured by the C-AFM was the perpendicular conductivity of the carbon film in this study.

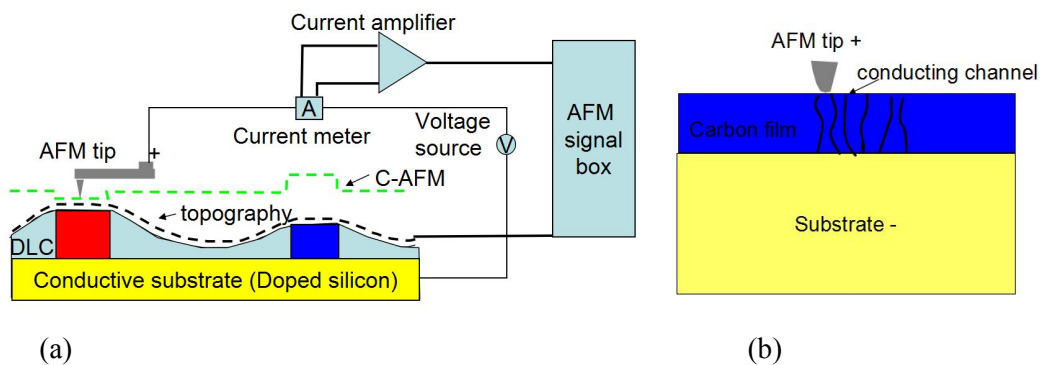


Figure 5. 2 (a) Schematic drawing of C-AFM system for conductivity measurement;

(b) Conducting channels in DLC film

Some experimental measurements of various carbon films by the C-AFM were demonstrated at CML, in cooperation with professor Komvopoulos's group at UC Berkeley and professor Singh Bhatia's group at National University of Singapore. These two groups provided the carbon films and chemical analysis tools.

Fresh a-C films with different thicknesses and  $sp^2/sp^3$  ratios were prepared by a FCVA facility. The film surface roughness and the conductivity distribution in an area of  $1 \text{ by } 1 \mu\text{m}$  were obtained after the samples were scanned by the C-AFM. The thicknesses of those samples were 3.6, 5.4, 9, 18, 27 nm. The fraction of  $sp^3$  component of these samples was measured by the XPS.

Figure 5. 3 shows the typical topography and current image of two different samples. The thicknesses of the samples was 3.6 and 9 nm, respectively. Different voltage bias

between the tip and sample was applied in the measurements of these two samples, in order to get a good image contrast. The thinner film had a relatively higher perpendicular conductance, so a smaller bias was enough to get a good contrast. The amplification of the current was 100 nA/V for the measurements of both samples. As can be seen there were many conducting clusters embedded in the a-C films which were classified as the conductive sp<sup>2</sup> clusters. There was no obvious correlation between the surface topography and current for both samples.

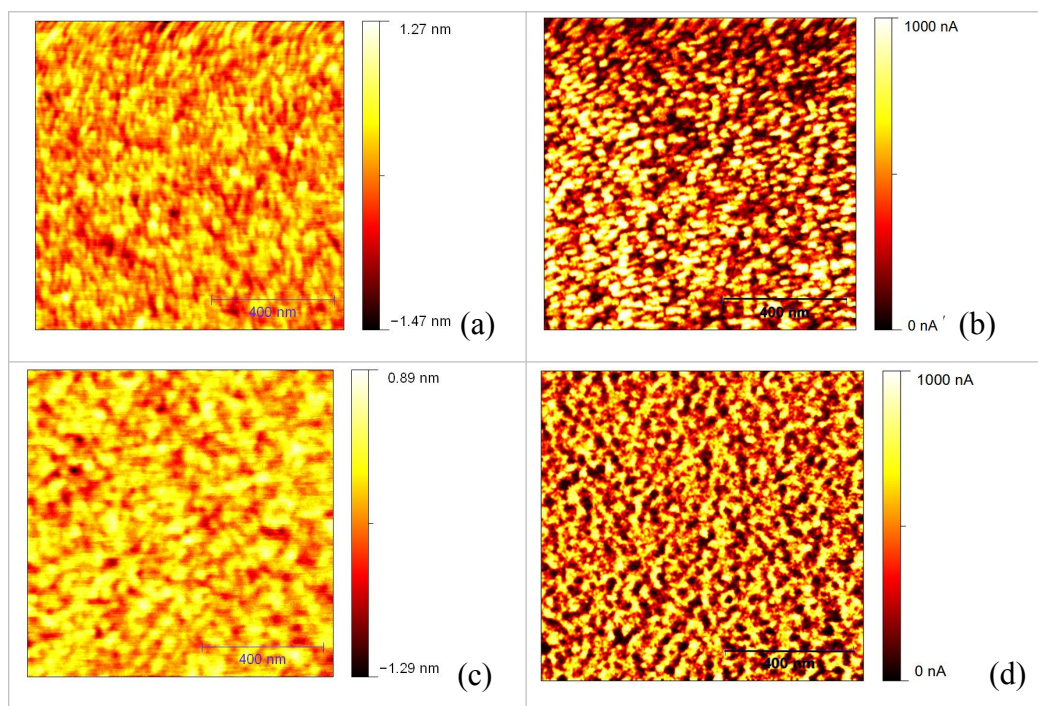


Figure 5.3 (a) Topography of sample 1 (3.6 nm carbon film) (b) Current map of sample 1  
(c) Topography of sample 2 (9 nm carbon film) (d) Current map of sample 2

The perpendicular resistance of the carbon films is the inverse of the conductance. The resistance was calculated from the current images. The RMS values of the perpendicular resistance and surface roughnesses are plotted in Figure 5.4. The film surface became smoother as the thickness increased up to 18 nm. The decrease of the surface roughness with increasing thickness may be related to the increase of the ion fluence, resulting in the increase of the amount of carbon delivered to the surface [93, 95].

The perpendicular RMS resistance increased significantly as the thickness of the carbon film increased, compared with the surface roughness. One reason was that the number of the conducting channels from the top surface to the substrate decreased for thicker a-C films. Meanwhile, the sp<sup>3</sup> fraction also increased as the thickness of the sample increased, as shown in Figure 5.5. There were more non-conductive components inside the a-C films.



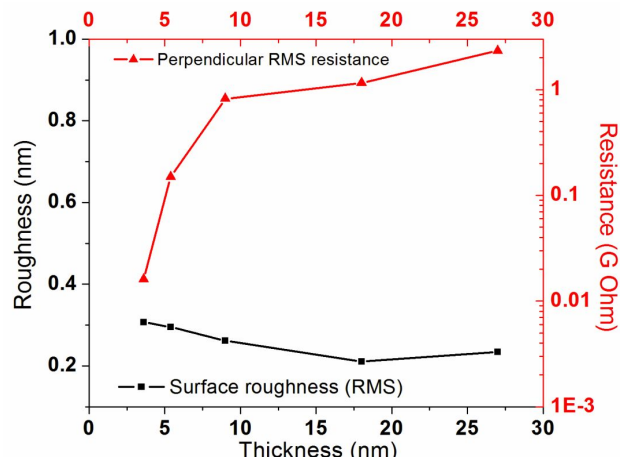


Figure 5. 4 RMS value of the perpendicular resistance and surface roughness for a-C films with different thickness.

To exclude the effects of film thickness on the resistance, the resistivity was used as a figure of merit to characterize their electrical property. The resistivity is an intrinsic property that quantifies how strongly a given material opposes the flow of electric current, and it is independent of film thickness. Resistivity was obtained from the C-AFM measurement, assuming a constant electrical contact area between C-AFM tip and a-C samples of  $100 \text{ nm}^2$ . The average resistivity of the different a-C films is plotted in Figure 5. 5. The resistivity increased as the sp<sup>3</sup> fraction increased, because sp<sup>3</sup> has higher resistivity than other components in a-C films. A sharp increase of the resistivity (7 times larger) occurred when the thickness of the a-C film increased from 3.6 nm to 5.4 nm, most likely due to the existence of a thin sp<sup>2</sup>-rich layer on the top surface of the a-C film [96, 97]. The surface sp<sup>2</sup>-rich layer made the a-C film very conductive. However, when the film thickness exceeded 5.4 nm, a bottom layer with more sp<sup>3</sup> non-conductive components caused a sharp increase in resistivity.

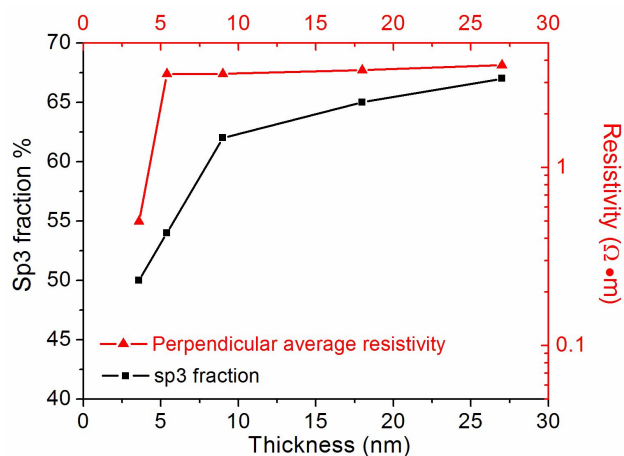
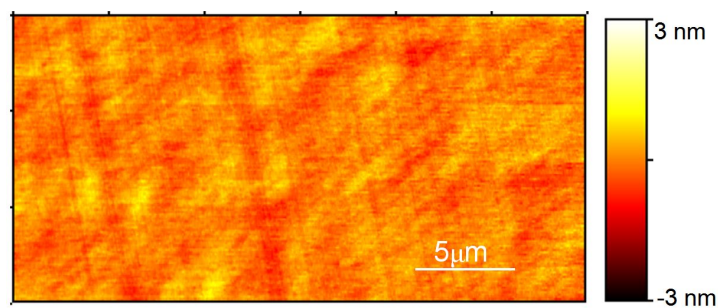


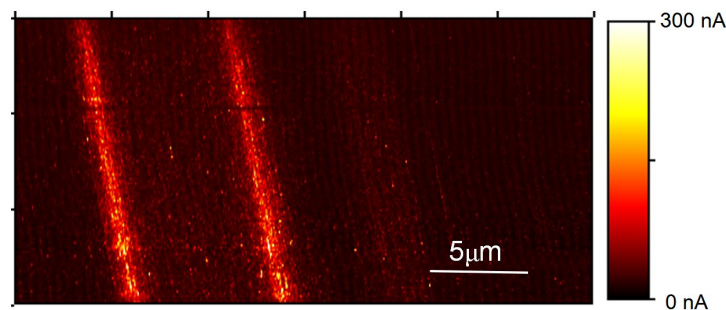
Figure 5. 5 Average resistivity and sp<sup>3</sup> fraction for different thickness samples.

It was observed that the electrical conductivity increased as the a-C film got thermally annealed because of the conversion of sp<sup>3</sup> to sp<sup>2</sup> [85]. The sp<sup>3</sup> to sp<sup>2</sup> conversion or graphitization could also occur when the a-C film is heated by a laser. In this situation, the conductivity of the laser exposed area gets raised. As shown in Figure 5.6, the two brighter lines were the laser-exposed tracks on a commercial PMR disk [70]. The brighter color means that the conductivity of the exposed area had increased, indicating there were more sp<sup>2</sup> components in the exposed area than the unexposed areas due to the sp<sup>3</sup> to sp<sup>2</sup> conversion under thermal annealing.

It is concluded in this section that the C-AFM measurement qualitatively resolved the conductive and non-conductive components for the a-C films. The resistivity of the a-C films showed a dependency on the sp<sup>2</sup>/sp<sup>3</sup> ratio. The existence of a conductive sp<sup>2</sup>-rich surface layer caused the resistivity of a 3.6 nm thick a-C film to be about one order lower than other thicker films.



(a) Topography image



(b) Current image

Figure 5.6 (a) Topography of the PMR disk after laser exposure  
(b) C-AFM conductivity image of the PMR disk after laser exposure [70]

## 5.3 Experimental conditions and procedures for thermal annealing

### 5.3.1 Temperature controlled heating by a temperature controlled electric heater

A simple temperature-control device was built by use of an electric heater, as depicted in Figure 5. 7. The heater had a square shape of width 10 mm, so it could be used to heat locally on the disk rather than heat a whole disk. The position of the heater can be adjusted by a 3D mechanical stage for it to make contact with the bottom surface of the disk. The spindle was turned off so the disk was kept stationary. The disk was heated from the bottom to the top surface when electric power was applied to the heater. A thermal probe was attached to the top surface of the disk to monitor the temperature. By regulating the power to the heater, the temperature can be controlled. The heating rate by this device was about 30 °C/s.

An a-C film with thickness at 26 Å was used in this study. There was no lubricant on the surface. The disk was locally heated to different temperatures at different locations. Every location was heated at the target temperature for about 5 seconds. After that, the heater was removed and the disk cooled down to the room temperature.

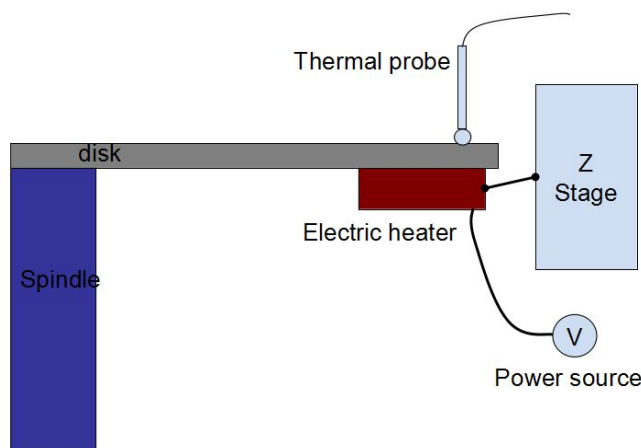


Figure 5. 7 Schematic diagram of a temperature control setup

### 5.3.2 Free laser beam heating procedure

A series of experiments was performed to study the a-C film degradation under a free laser beam heating conditions in the Cal stage. The carbon film's thermal behavior under different laser heating powers and durations were compared.

2.5 inch disks with glass substrates were used in the experiments. The thickness of the a-C film was 26 Å. In all free laser beam exposure tests, there was no lubricant on the top of the a-C films. The laser was directly focused onto the disk surface by an active focusing servo while the disk rotated at 1500 RPM. The laser focused spot size was about 5.5 μm along the down-track direction and 2 μm along the radial direction.

The experimental procedure was the same as the previous lubricant study under the free laser beam heating. A band with 7 tracks was exposed by the focused laser under different repetitions at a fixed power. The repetitions for the different tracks were 5, 10, 50, 100, 500, 1000 and 2000, respectively. The radial distance between two adjacent tracks was 25  $\mu\text{m}$  so that no thermal interaction occurred between two adjacent tracks. Totally seven bands were exposed while the laser power was changed for different bands. The seven power levels in the free laser beam tests are listed in table 5.1

Table 5. 1 Free laser beam heating conditions for the a-C films

	Band 1	Band 2	Band 3	Band 4	Band 5	Band 6	Band 7
Input power (mW)	125	153	176	205	228	257	280
Absorbed power (mW)	68.8	84.1	96.8	112.8	125.4	141.4	154.0
Absorbed power density (mW/ $\mu\text{m}^2$ )	15.9	19.5	22.4	26.1	29.0	32.7	35.7

After all of the bands were exposed, the disk was uninstalled from the spindle and moved to the OSA for surface inspection. The surface reflection image can be obtained from the OSA scan. After the OSA scan, the disk surface was measured by the AFM to investigate the surface topography change.

### 5.3.3 NFT exposure procedure

In order to expose the a-C film by a heating spot on the order of tens of nanometers to emulate the HAMR conditions, we used a home-made NFT structure. The same NFT structure as described in chapter 3 was fabricated by FIB on the home-made sliders. The 2.5 inch glass disk with 26  $\text{\AA}$  a-C film was first dip lubed in a Z-type lubricant solution. The slider was able to fly stably for a while on the disk without showing any acoustic emission contact signal.

The light wavelength in this study was 780 nm. The laser was aligned and focused to the NFT through the slider sapphire body. The NFT was moved in the radial direction over a 20  $\mu\text{m}$  wide band with a constant speed while the disk continued rotating at 1500 RPM. This band was exposed in a manner similar to shingled magnetic recording writing. The radial distance between two exposed spiral tracks was determined by the spindle

rotating speed and NFT radial speed. By changing the radial speed while keeping the spindle rotating at 1500 RPM, the effective exposed repetition for every track inside a band can be tuned, similar to the NFT heating in the lubricant study. Four bands were exposed by repetitions of 25, 12, 4, 2 times in this shingled exposure way.

Right after the NFT exposure, the disk was delubed in a HFE solution to wash away the mobile lubricant. Then the disk was scanned by the OSA and AFM.

## 5.4 Experimental results and discussion

### 5.4.1 Carbon film degradation after thermal annealing using the electric heater

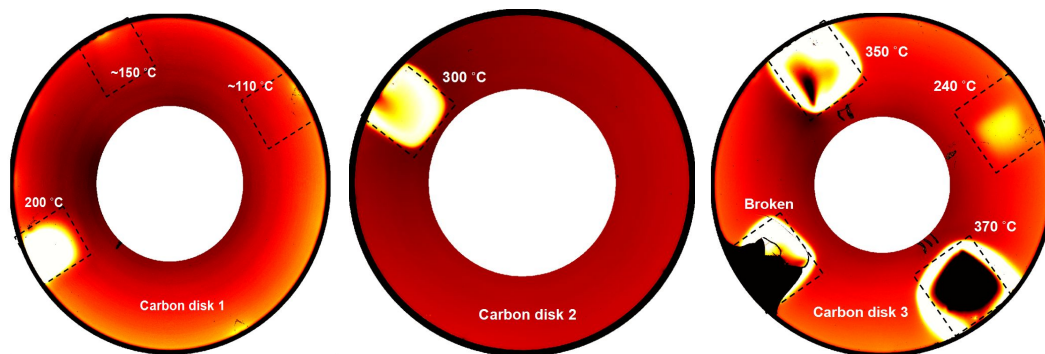


Figure 5. 8 OSA p-sp image of the carbon disks after thermal annealing

Figure 5. 8 shows the p-sp images of the disk scanned by the OSA. The surface reflectivity started to increase when the temperature reached 200 °C. This agrees with Togawa's results that the refractive index started to change when the temperature reached 225 °C [40]. When the temperature was at 150 °C or lower, there was no significant surface reflectivity change. When the temperature was raised to over 350 °C, the surface of the a-C film became darker.

The surface topography was obtained by AFM scans. Three of the surface topography images were shown in Figure 5. 9. The temperatures of these three surfaces were room temperature, 240 °C and 370 °C respectively. It can be seen that the surface was changed after the thermal annealing. The surface RMS roughness obtained from the topography images was plotted in Figure 5. 10. The surface roughness became slightly smaller after the thermal annealing when the temperature was less than 300 °C. The surface became smoother probably due to the stress relief of the thin film [73]. However, as the temperature was raised above 350 °C the surface became rougher again, probably due to the oxidation and graphitization of the carbon film.

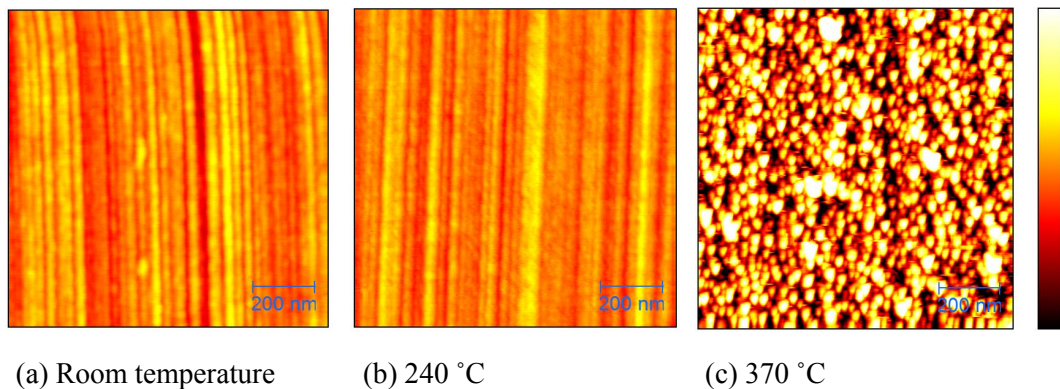


Figure 5. 9 Surface topography of carbon film after thermally annealing at different temperatures. The color bar for all 3 plots is -3 nm to 3 nm.

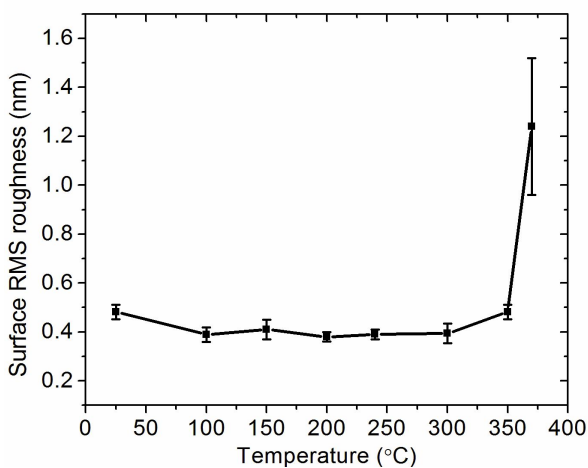


Figure 5. 10 Surface RMS roughness of the carbon film after thermally annealing at different temperatures by a temperature controlled electric heater.

#### 5.4.2 Surface reflectivity change under the free laser beam heating conditions

Three typical p-sp images from the OSA were chosen to study the surface reflectivity change under different repetitions as shown in Figure 5. 11. The tracks in Figure 5. 11a were exposed at  $19.5 \text{ mW}/\mu\text{m}^2$ . The tracks in Figure 5. 11b were exposed at  $29.0 \text{ mW}/\mu\text{m}^2$ . The tracks in Figure 5. 11c were exposed at the higher power density at  $35.7 \text{ mW}/\mu\text{m}^2$ .

It can be seen that when the power density was lower than  $29.0 \text{ mW}/\mu\text{m}^2$ , the surface reflectivity increased as the track was heated for more repetitions. When the power density was at  $35.7 \text{ mW}/\mu\text{m}^2$ , the exposed track got darker, because the surface reflectivity was decreased instead of increased after laser heating. And as the exposure repetitions increased, the exposed track was wider due to the thermal diffusion.

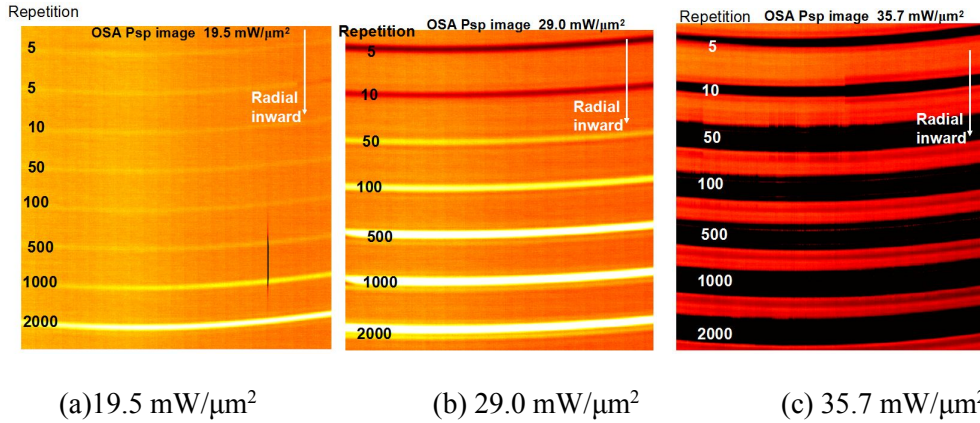


Figure 5. 11 P-sp images of the exposed tracks at different laser power densities

However, when the laser power density was at  $29.0 \text{ mW}/\mu\text{m}^2$ , the trend of the surface reflectivity change was quite different from that in other laser power densities. As the repetitions increased at this intensity, the surface reflectivity first dropped and the exposed tracks became darker at repetitions 5 and 10. Then the surface reflectivity increased as the repetitions were increased to 50. The surface reflectivity was increased further for more repetitions after 50, as shown in Figure 5. 12.

It was found the magnitude of the surface reflectivity was much higher in temperature controlled heating tests, because the heating duration was about three or more orders longer than in the free laser beam heating tests.

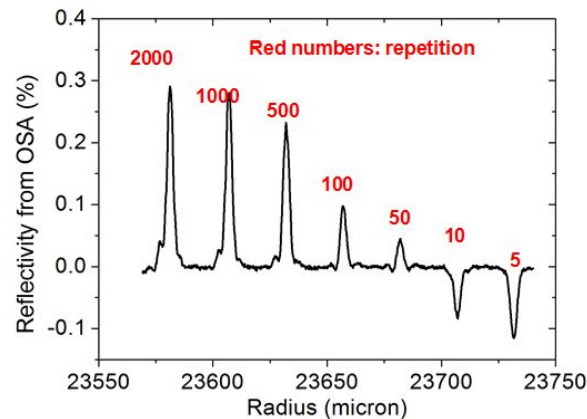


Figure 5. 12 Surface reflectivity profiles of the tracks after exposure at various repetitions at a power density of  $29.0 \text{ mW}/\mu\text{m}^2$ .

### 5.4.3 Surface topography

It has been confirmed that the surface reflectivity of the a-C films mainly depends on the surface topography and the optical refractive index [98, 99]. The optical refractive index can be changed if the material phase is changed or micro-structures are changed. For example, the refractive index of graphite is quite different from that of diamond

although both materials are made from carbon. The surface topography change can be attributed to the change of a few properties of the film, such as micro-structure change [73 ], thermal stress [100] or density [101], etc.

The surface topography of the DLC films under various heating conditions was scanned by the AFM. Six exposed tracks under 6 typical heating conditions were chosen as listed in table 5.2.

Table 5. 2 Exposed tracks under different free laser beam heating conditions

	Track 1	Track 2	Track 3	Track 4	Track 5	Track 6
Power density mW/ $\mu\text{m}^2$	19.5	19.5	29.0	29.0	29.0	35.7
Repetition	100	2000	10	50	500	50

As shown in Figure 5. 13, there was no significant topography change for track 1 when the laser power density was  $19.5 \text{ mW}/\mu\text{m}^2$  and the repetition number was 100, while there was a slight surface reflectivity increase, as shown in the OSA p-sp images (Figure 5. 11). Track 2 was exposed for 2000 repetitions at the same laser power density of  $19.5 \text{ mW}/\mu\text{m}^2$ . The surface of track 2 showed some bump features. The protruded height of the bumps was about 3 nm. The surface reflectivity was also higher than the ambient unexposed areas. Track 3 was exposed by a higher power density of  $29.0 \text{ mW}/\mu\text{m}^2$  for 10 repetitions, and the surface protruded height was close to that in track 2. However in the OSA p-sp image (Figure 5. 11b), the surface reflectivity of track 3 was lower than that in the unexposed area. There was a large difference in the surface reflectivities between tracks 3 and 2, even though their surface topographies were quite close. It is suspected that there was a significant change of the refractive index of both tracks. For track 6, which was exposed at  $35.7 \text{ mW}/\mu\text{m}^2$  for 50 repetitions, a groove with two side ridges was observed rather than a bump. Some material ablation under this level of laser heating caused the groove structure.



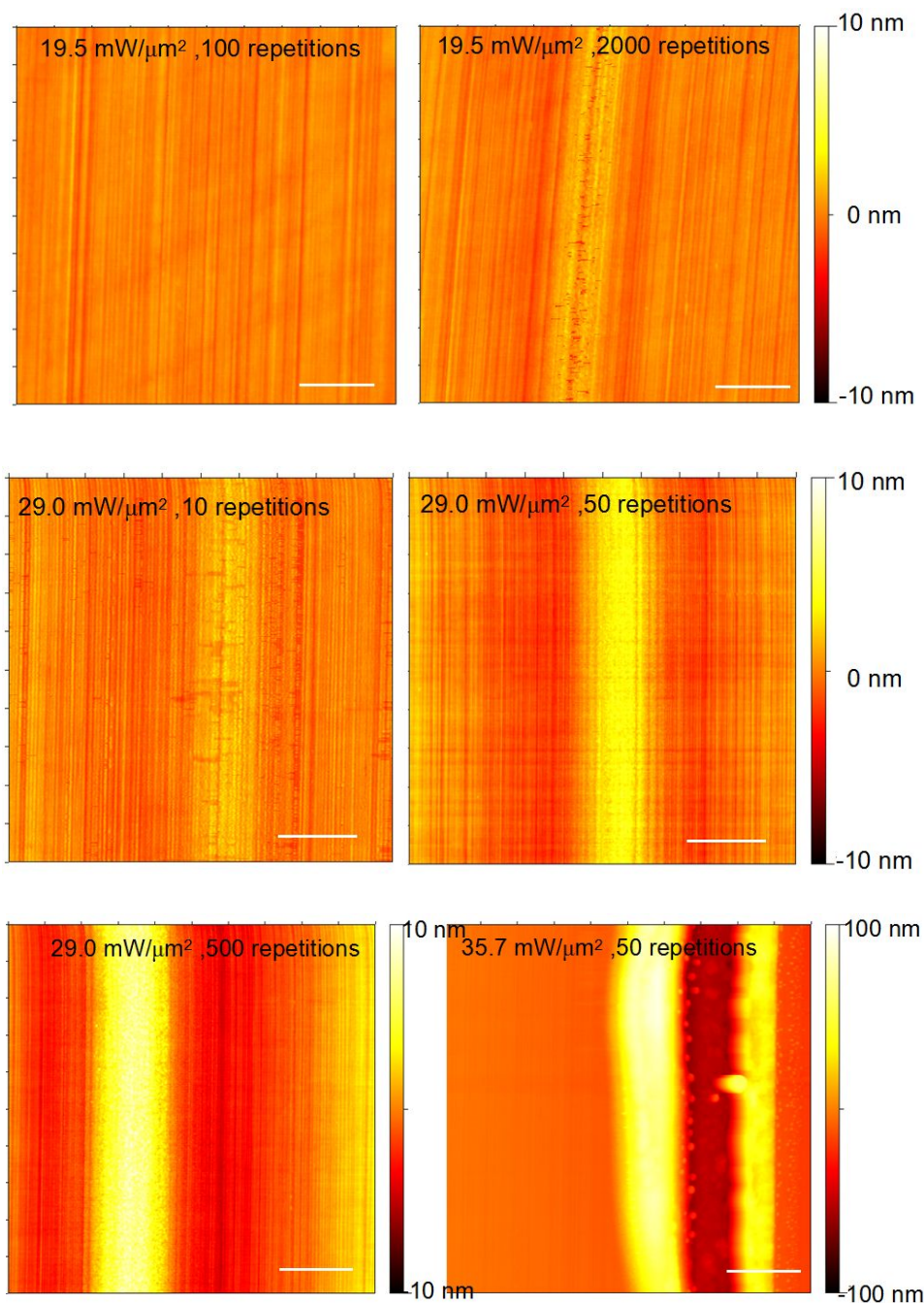


Figure 5. 14 Surface topography for 6 tracks exposed at different conditions. The scale bar in all the figures are 1  $\mu\text{m}$

For a fixed power density, the surface topography change was more severe when the track was exposed for more repetitions, as indicated by tracks 3, 4, 5 in Figure 5. 14. The topography changes of the tracks are compared in Figure 5. 15. Those seven tracks were exposed by different repetitions at the same power density of 29.0  $\text{mW}/\mu\text{m}^2$ . It can be seen that the protrusions increased logarithmically with respect to the repetition.

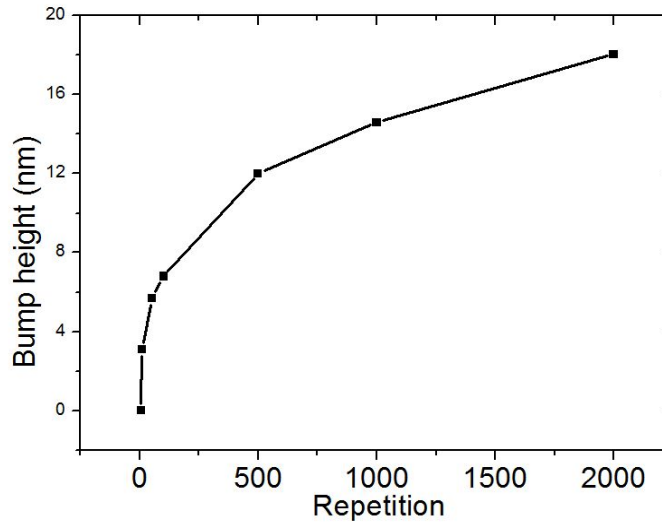


Figure 5. 15 Surface deformation of the tracks exposed at  $29.0 \text{ mW}/\mu\text{m}^2$  under different repetitions.

#### 5.4 Carbon overcoat degradation under NFT heating

After the disk was exposed under the conditions of the NFT heating, the disk was delubed to remove the lubricant. Then the carbon surface was scanned by the OSA. Figure 5. 16 shows the p-sp image of the carbon surface when the input laser power to the NFT was 197 mW. The exposed repetitions for those 4 areas were 25, 12, 4, and 2, respectively. The effective exposed time for a point in those tracks were from  $\sim 200$  to 20 ns.

The magnitude of the surface reflectivity change of an exposed area after 25 repetitions of exposure was close to that in the free laser beam case when the repetition was 10 and the power density was  $19.5 \text{ mW}/\mu\text{m}^2$ . The size of the NFT heating spot was about  $36$  by  $100 \text{ nm}$ , while that of the free laser beam heating spot was about  $5.5$  by  $2 \mu\text{m}$ . The effective accumulated radiation time duration under free laser beam heating was about 60 times larger than that of the NFT heating. However, the power density was enhanced  $\sim 10$  times in the NFT heating. It is very likely that the total energy absorbed by the carbon film in a period of 25 repetitions under the NFT heating was about the same order of that in the free laser beam heating when the repetition was 10 and power density was  $19.5 \text{ mW}/\mu\text{m}^2$ . Thus the reflectivity changes of the carbon films under these two heating conditions were quite close.

Compared with the lubricant depletion discussed in chapter 4, the carbon film degradation did not show strong dependence on the thermal gradient. It can be inferred that laser power and heating duration play a more important role for the carbon degradation than the thermal gradient.

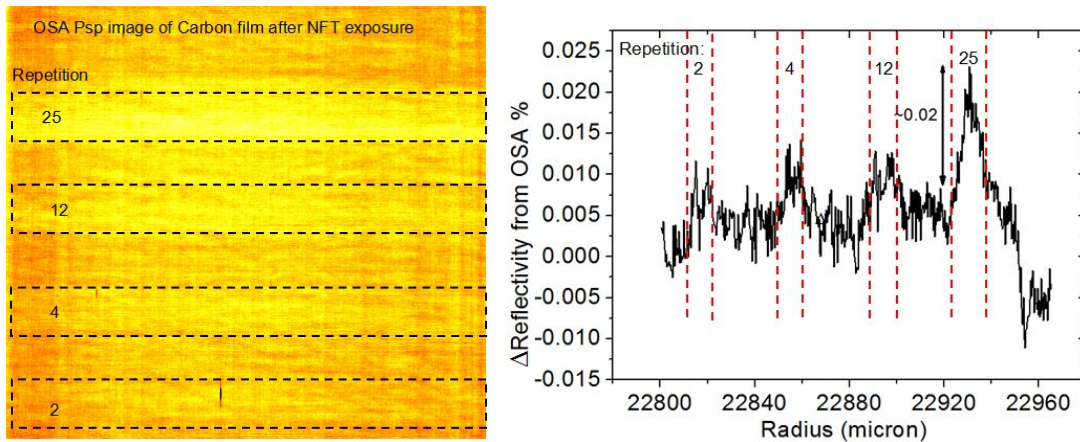


Figure 5. 16 OSA p-sp scan of the disk after the NFT heating for different repetitions.

(Left) P-sp image of the carbon film; (right) profile of the reflectivity change

## 5.5 Summary

In this chapter, a conductive AFM was introduced for the study of the a-C film of HAMR systems. The conductivity image of the carbon film could be used to characterize the sp<sup>2</sup>/sp<sup>3</sup> ratio. A sp<sup>2</sup>-rich layer on the top surface of the ultra-thin a-C film caused a larger conductivity or smaller resistivity. A significant change of the conductivity was observed after the a-C film was heated by the focused laser, due to the conversion of non-conductive sp<sup>3</sup> to conductive sp<sup>2</sup>.

The degradation of the carbon overcoat under the various thermal heating conditions was investigated. Three different heating methods were employed, including temperature controlled heating by use of an electric heater, free laser beam heating and NFT heating. The sizes of the heating areas by these three methods were quite different. An area  $\sim 10 \times 10 \text{ mm}^2$  was heated by the temperature controlled heater; the free laser beam irradiated an area at  $\sim 2 \times 5 \text{ }\mu\text{m}^2$  size while the NFT heated an area at  $\sim 30 \times 100 \text{ nm}^2$ . The heating duration was also different for these three heating methods as well. In the temperature controlled heating, the duration was about a few seconds; in the free laser beam heating, it was from  $\sim 1 \text{ }\mu\text{s}$  to  $\sim 1 \text{ ms}$ ; in the NFT heating, the duration was about  $\sim 20 \text{ ns}$  to  $\sim 200 \text{ ns}$ . The thermal gradients of these three methods were also quite different. The thermal gradient in the NFT heating was the highest because of the tightly focused spot and enhancement of the light density around the NFT.

In the temperature controlled heating tests, it was found that the surface reflectivity started to change when the temperature was higher than  $200 \text{ }^\circ\text{C}$ . The surface reflectivity increased as the temperature increased further beyond  $200 \text{ }^\circ\text{C}$ . However, when the temperature reached about  $370 \text{ }^\circ\text{C}$ , the surface reflectivity began to drop. The surface roughness of the carbon films decreased as the temperature increased up to  $300 \text{ }^\circ\text{C}$ . As the

temperature increased further, to greater than 300 °C, the surface became rougher due to significant surface oxidation or graphitization.

In the free laser beam heating tests, it was found that the surface reflectivity began to change when the laser power density reached 19.5 mW/ $\mu\text{m}^2$ . The surface reflectivity increased as the number of repetitions or heating duration increased. However when the laser power was increased to a higher level at 35.7 mW/ $\mu\text{m}^2$ , the surface reflectivity decreased. It was found that the surface topography was changed by the free laser beam heating. A bump-like deformation was found at a track that was exposed at lower power densities from 19.5 mW/ $\mu\text{m}^2$  to 32.7 mW/ $\mu\text{m}^2$ . The height of the bumps increased in a logarithmic way as the repetitions or heating duration increased for a fixed power input. At higher power densities, like 35.7 mW/ $\mu\text{m}^2$ , the carbon film was removed due to laser ablation.

In the NFT heating tests, it was found that the highest surface reflectivity change was on the same order as that in the free laser beam heating when the power density was 19.5 mW/ $\mu\text{m}^2$  and the repetitions were 10. The surface reflectivity had less change when the repetition number of the NFT heating was reduced.

Comparing the magnitude of the surface reflectivity change under various heating conditions and methods, we found that the heating temperature and duration were the two dominant factors that affected the degradation of the carbon film. It is likely that the carbon film on the disk surface in a HAMR drive can survive when each bit is written only a few times and the heating duration is on the order of  $\sim$  ns during a one time writing process. However, the carbon film on the slider side may suffer from serious thermal degradation because it is continuously heated for much longer duration during the data writing in the lifetime of a HAMR drive.

## Chapter 6 Failure of the NFT under HAMR conditions

The HDI in HDDs is composed of two major parts: head and disk. The degradation of the disk under HAMR conditions has been discussed in chapters 4 and 5. The degradation of the slider could also occur when the laser heat is applied. The degradation of the slider may eventually lead to a failure of the HDI, which is discussed in this chapter.

### 6.1 Introduction

A major unique aspect of the HDI of HAMR systems is the introduction of a laser. The data writing is performed when the heat from the laser is applied to a small area on the media disk. The size of the heating spot should be close to the size of a magnetic bit. The size of a magnetic bit needs to be about 25 nm or less as the areal density increases beyond 1 Tb/in<sup>2</sup>. So the size of the laser focused spot at a scale of about 25 nm is one of the primary requirements for the optical system for HAMR drives. In addition, there should be enough energy from the small focused spot to heat the media to near the Curie point of the magnetic material. In other words, the efficiency of the proposed optical system is of primary importance as well.

However, there are two basic limits of conventional optics that restrict its application in HAMR systems. First, there is a diffraction limit of an optical focus. The size of the focused spot by an optical lens is limited by the wavelength of the light and the numerical aperture of the lens.

$$d = \frac{0.5\lambda}{n \sin \theta} \quad (6.1)$$

where  $d$  is the full-width spot diameter at the half maximum point (FWHM),  $\lambda$  is the light wavelength,  $n$  is the refractive index of the lens. The term  $n \sin \theta$  is called the numerical aperture (NA). In other words, a conventional optical lens is able to focus light to a minimum spot with the size of approximately a half wavelength of the light. For most of the low-cost and high-power semiconductor lasers, the wavelength is in the range of 400 to 830 nm. Obviously, it is not possible to focus the laser light to a spot of 25 nm or even smaller by a conventional optical lens. Second, the far-field transmission of an aperture is also limited when the diameter of the aperture is smaller than the incident light wavelength, as given by the Bethe's law as expressed [102]:

$$T = \frac{64\pi^2 d^4}{27\lambda^4} \quad (6.2)$$

where  $T$  is the ratio of the power per unit area transmitted through an aperture to the power per unit area incident upon the aperture and  $d$  is the diameter of the aperture.  $d$  is smaller than the wavelength. The fourth-power dependence on the diameter causes the transmitted power to fall drastically with the aperture diameter is reduced to tens of nanometers. For example, the efficiency of the light transmission through a near-field tapered optical fiber with a 50-nm aperture is only approximately 0.001%. Most of the incident energy gets dissipated or reflected back.

To overcome these two limits, a near field transducer (NFT) has been proposed to achieve smaller focus spots and higher transmission efficiency, compared with conventional optics. The NFT utilizes localized surface plasmon effects to achieve high field enhancement and the sub-diffraction-limited confinement of light [103]. A large number of collective oscillations of electrons, called surface plasmons, are generated at the metal and dielectric film interface. They are strongly localized to this interface with the field amplitude exponentially decaying away from it.

The NFT has at least three important differences from the conventional optical lens. First, in the near field region, the size of the focused spot can be as small as 1/10 to the light wavelength, which is well below the diffraction limit. Second, there is an enhancement effect of the intensity around the NFT structure. This indicates that the output energy density can be even higher than that of the input although the size of the output is much smaller. The efficiency of current NFTs can reach an order of 10% [104]. Although most of the energy still gets lost, the transmission efficiency of the NFT is a few orders higher than that of the conventional optics. Third, due to the nature of the exponential decay of the evanescent plasmonic waves, the NFT can only work effectively within a distance that is much smaller than the light wavelength, which is around several nm to tens of nm. Fortunately, in HDDs, the recording heads fly within 10 nm above the recording surface, which is within the near field working range of the NFT.

The concept of the HAMR disk drive with a NFT structure has been successfully demonstrated by the major HDD companies: HGST in 2010 [26] and Seagate in 2009 [25]. In both of these works, a focus spot less than 50 nm was achieved by a NFT structure, although very different designs of the NFT structure were implemented.

In HGST's demonstration, the laser light was focused and coupled into a thin film waveguide from the top of the slider as shown in Figure 6. 1. The waveguide was made from a  $Ta_2O_5$  core with  $SiO_2$  cladding. The full width at half maximum (FWHM) of light intensity at the outlet of the waveguide was approximately  $400\text{ nm} \times 250\text{ nm}$ . The laser light was finally delivered to the NFT, which was an E-shape plasmonic antenna attached to the end of the waveguide on the air bearing surface. The light was further focused by the NFT to a near field spot. The FWHM of the final focused spot was  $30\text{ nm} \times 28\text{ nm}$  according to the numerical calculation.

In Seagate's work, a planar solid immersion lens (PSIL) [105] was integrated into a flying slider. Figure 6. 2 shows the schematic diagram of the laser delivery for an integrated HAMR head. The laser beam was first delivered to an optical grating, and then it was coupled to the PSIL. The transverse electric waveguide modes were launched on either side of the PSIL. When these modes are combined at the bottom, the net field is longitudinally polarized, as shown in Figure 6. 3. The NFT was located at the focus of the PSIM, and at resonance the surface charge oscillates along the length of the lollipop peg to generate an electric field at the tip of the peg that couples energy into the medium. The peg provides a lightning rod effect for field confinement. The simulated field intensity on the medium had a rectangular shape, which fitted well with the shape of a magnetic bit.

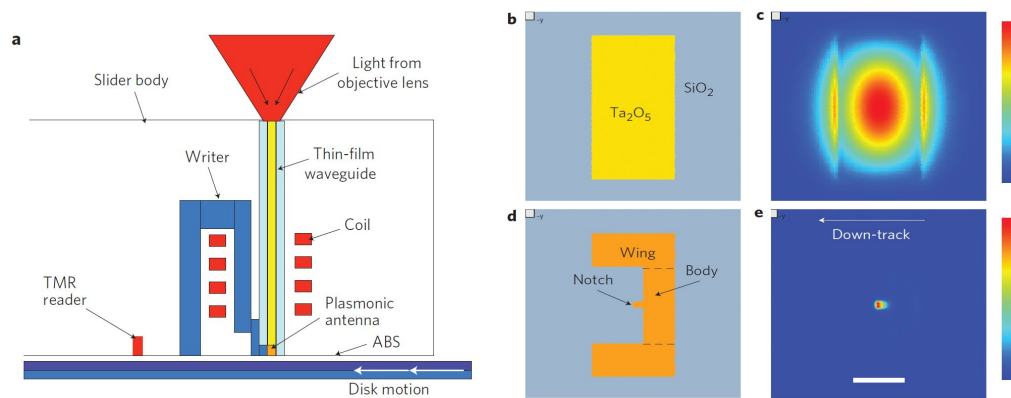


Figure 6. 1 Integrated recording head schematic from HGST. [26]

- a, Schematic diagram showing the HAMR head concept
- b, Cross-section of the waveguide with a  $600 \text{ nm} \times 300 \text{ nm}$   $\text{Ta}_2\text{O}_5$  waveguide core.
- c, Modeled optical intensity in the waveguide for a laser wavelength of  $830 \text{ nm}$ , with  $\text{SiO}_2$  cladding. The FWHM is approximately  $400 \text{ nm} \times 250 \text{ nm}$ .
- d, Cross-section of the E-antenna at the end of the waveguide.
- e, Finite-element modeled absorption profile at the disk surface below the E-antenna. The in-page height of the gold is  $98 \text{ nm}$ , and the antenna is assumed to be separated from a  $50\text{-nm}$ -thick cobalt medium by a  $6\text{-nm}$  air gap. Scale bar,  $200 \text{ nm}$  (b–e).

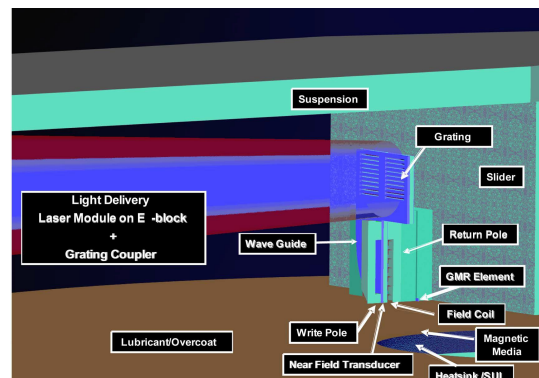


Figure 6. 2 A schematic diagram of an HAMR recording system [29]

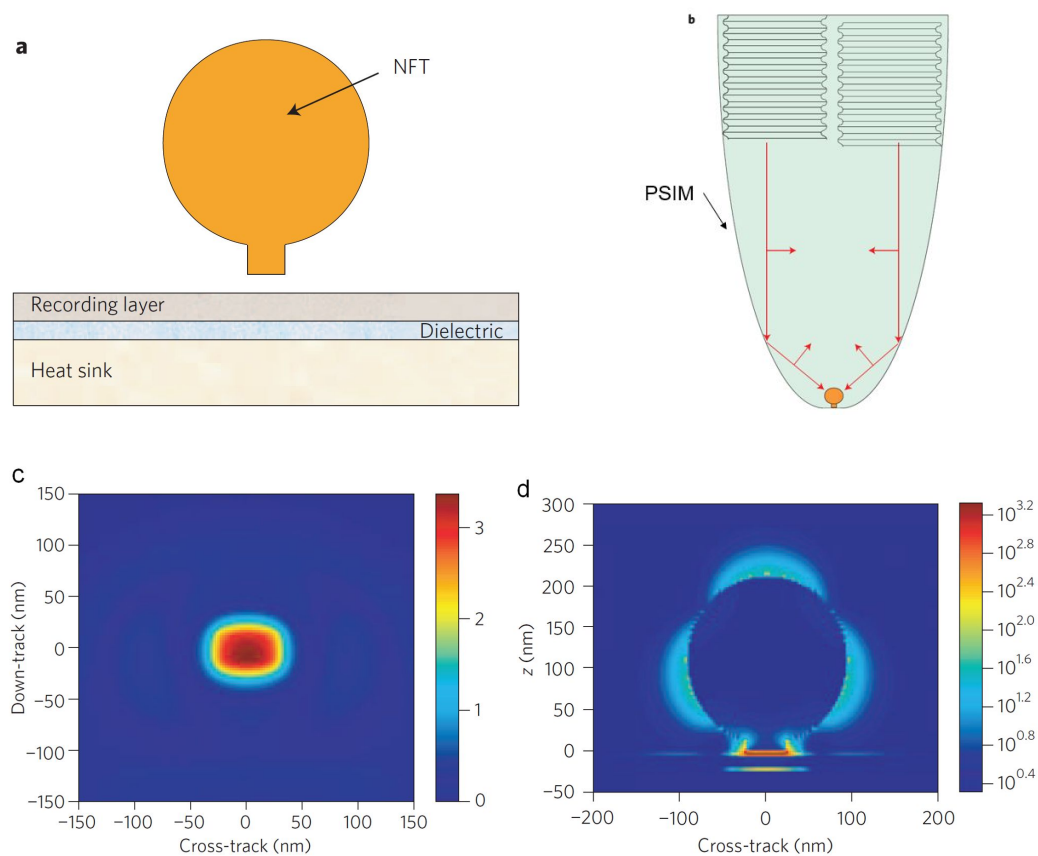


Figure 6. 3 Diagram of the NFT and planar solid immersion mirror (PSIM) for the HAMR system from Seagate. [25]

a, Expanded view of the NFT showing its vertical position with respect to the recording medium.

b, A PSIM) with a dual offset grating used to focus a waveguide mode onto the lollipop NFT. The electric field for the TE mode is shown, which generates a longitudinal (vertical) field at the focus.

c, Profile of the light intensity within the centre of the recording layer at the resonance wavelength.

d, Profile of the light intensity through a cross-section of the NFT

It has been demonstrated that the concept of HAMR can be accomplished by use of the NFT. However, the integrated NFT brings some other new challenges that have prevented the HAMR from commercial application. One major issue is the reliability of the NFT structure [53, 106]. In most of the current published papers for HAMR systems, only a small portion (less than 10 percent) of the total laser energy could be transmitted to the disk from the NFT, although the efficiency of the NFT is a few orders higher than that of conventional optical apertures. Most of the energy is lost around the NFT and waveguide. The temperature increase in the NFT can be several hundred degrees and the



lifetime of a NFT can be limited to several tens of recording tracks based on the report from [25]. A noble metal such as gold is used in the NFT that usually has a relatively low melting point, around 1000 °C, and a low yield point stress at 100 MPa which indicates that the NFT could be very vulnerable to the thermal and stress loads.

Moreover, the NFT's function is intensity enhancement, indicating that the intensity around the NFT is higher than the input intensity. The enhanced energy density could make the thermal load even more pronounced so that the NFT structure is even more vulnerable.

There are at least three mechanisms that finally result in a failure of a NFT structure. The first is its optical function failure due to the geometric structure change of the NFT. The material diffusion/creep is strongly enhanced when the temperature is at the media Curie point, considering that the melting point is only about 1000 °C [107, 108]. The geometry/shape of the NFT structure can be changed after some time and thus the size and shape of the focus spot can be changed [109]. In this situation, the HAMR writing performance could be deteriorated because the thermal profile is changed. The second failure mode is material fatigue. The laser is turned on only during the writing period. So a cyclic heating condition for the NFT is more likely for HAMR systems. However, the cyclic load can cause the thin film to be damaged more seriously due to material fatigue [110]. The third failure mode is the wear of the NFT structure due to the NFT and disk contact. It is believed that the NFT protrudes towards the surface of the disk during recording by a couple of nanometers [35]. This laser induced protrusion superposes on the TFC protrusion and makes the NFT even closer to the disk. So there is more of a chance that the NFT contacts with the disk surface when both the laser and TFC are powered on simultaneously. Material wear around the NFT occurs when the NFT makes contact with the disk. Accumulated material wear could finally lead to the failure of the HDI. What's more, there is no clear evidence that the contacts between the NFT and disk can be detected by current contact detection technology, such as the acoustic emission sensor. Because the size of the laser induced protrusion is on the order of a couple of microns and the height is a couple of nanometers, which are much smaller than the conventional TFC protrusion [35]. All three failure modes can work together to make the NFT fail in a short period and thus reduce significantly the reliability of the HDI.

Several methods have been proposed to improve the reliability of the NFT. Some kind of heat sink layer could be added inside the slider to get better thermal dissipation, so the temperature increase around the NFT could be reduced. Some novel designs of the NFT structure have higher coupling efficiency so the total energy input could be reduced. Furthermore, some new materials with better thermal and mechanical properties are suggested for the NFT fabrication, such as the nitrides or oxides [103, 111, 112]. Those materials are mechanically stronger than currently used noble materials such as gold and silver. The melting points are also higher.

In this work, the damage of a locally designed and fabricated NFT under various heating conditions is investigated. The failure modes of the NFT are discussed for different experimental conditions. Then, a two-stage heating scheme is proposed to reduce the thermal load to the NFT. In this way, the material fatigue and diffusion can be alleviated. In section 6.2, the experimental conditions and procedures are presented. Then the experimental results are discussed. The two-stage heating scheme is introduced in section 6.3. This chapter is summarized in section 6.4.

## 6.2 Experimental study for NFT failure

A 4 by 3 NFT array was fabricated on the trailing end of the rails of an in-house fabricated slider as shown in Figure 6. 4. The design of the NFT structure is shown in Figure 6. 4c. The slider was loaded onto a transparent disk that was rotated at 1500 RPM. The slider could fly stably above the transparent disk without showing any acoustic emission sensor contact signal at a linear speed close to 5 m/s before the laser was focused onto the NFT. When the slider flies, the air bearing cooling could significantly influence the heat conduction between the NFT surface and disk surface. The heat transfer coefficient could be as high as  $10^5$  W/m<sup>2</sup>K [72]. The laser was focused onto different NFTs at different laser power values through the sapphire body of the slider. This laser delivery method was different from that in currently proposed HAMR systems, in which the laser light is delivered to the NFT by an optical waveguide. The laser light in our setup can be largely absorbed by the NFT chromium layer, which can increase the temperature of the NFT. Some of the heat can also be dissipated into the sapphire body by conduction.

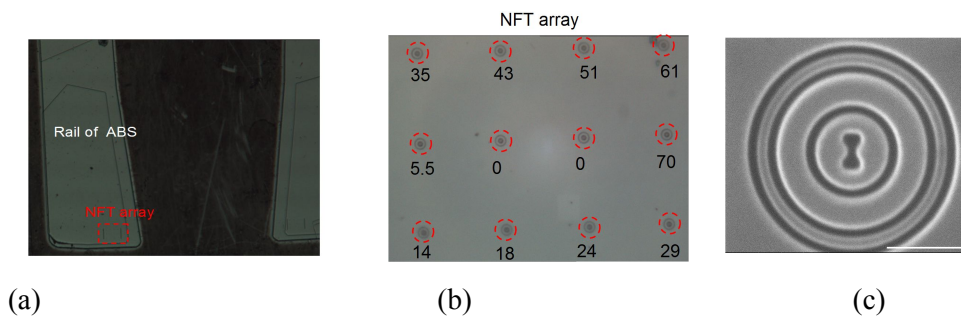


Figure 6. 4 (a) NFT array on the left rail of the air bearing surface. (b) Different laser power values on different NFTs (power unit: mW) (c) SEM image of the NFT, scale bar is 0.5  $\mu$ m.

The laser wavelength was 355 nm in this study. The focused beam spot at the NFT was less than 1.4  $\mu$ m (Gaussian radius ( $e^{-2}$ ) of the laser spot was about 700 nm). The laser power was increased by increments from 0 mW to 70 mW. Each NFT was exposed for 1 minute at a fixed laser power. The amount of laser light energy delivered to the transparent disk through the NFTs could be ignored compared with the energy dissipated in the NFTs.

The far field transmission of each NFT after exposure was first inspected from captured CCD images using a setup shown in Figure 6. 5. When the laser at low power was focused onto the NFT structure, some of the light was transmitted through the aperture of the NFT. The transmission was captured by a commercial CCD camera installed below the transparent disk. The laser power illumination for the far field transmission inspection was fixed at 5.5 mW for all NFTs. The 5.5 mW power was not high enough to cause additional damage to the NFT structure.

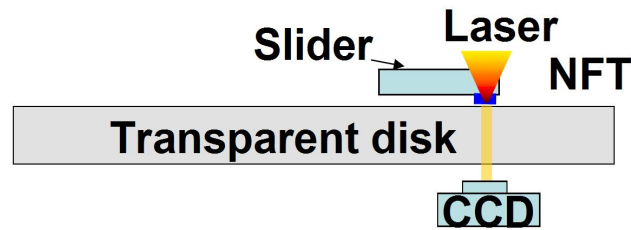


Figure 6. 5 Schematic diagram of the far field transmission measurement setup

The light intensity was enhanced by the NFT structure. This enhancement could make the damage to the metal film even worse. To compare the change of the thin film under laser heating when there is no NFT, a blank area near the trailing edge on the air bearing surface without NFT was exposed by the focused laser beam. The slider was flying at the same condition during this exposure as in the previous NFT exposure tests. Several locations were exposed at different power levels from 0 mW to 70 mW. Each area was exposed for 1 minute as well.

After the laser exposure, the slider was unloaded from the disk. Then the NFT array was inspected by use of an optical microscope. Then the NFT structures and exposed blank areas were further scanned and analyzed by an AFM.

Figure 6. 6 shows the optical images of some NFTs after the laser exposure. The center of the NFT started to change as the laser power exceeded 43 mW. The change area became larger as the exposure power increased to 70 mW.

Figure 6. 7 shows the transmission patterns of two NFT structures after the exposures, marked by the dashed circles. The NFT shown on the left was not exposed, while the NFT shown on the right was exposed at 43 mW for 1 minute during the test. The intensity of transmission from the unexposed NFT was much lower than that from the exposed NFT. Because sapphire is almost transparent and the chromium film is the only layer that can absorb the laser energy significantly, we conclude that the metal (Cr) film was changed under the higher laser power exposure, which commonly occurs in laser material processing.

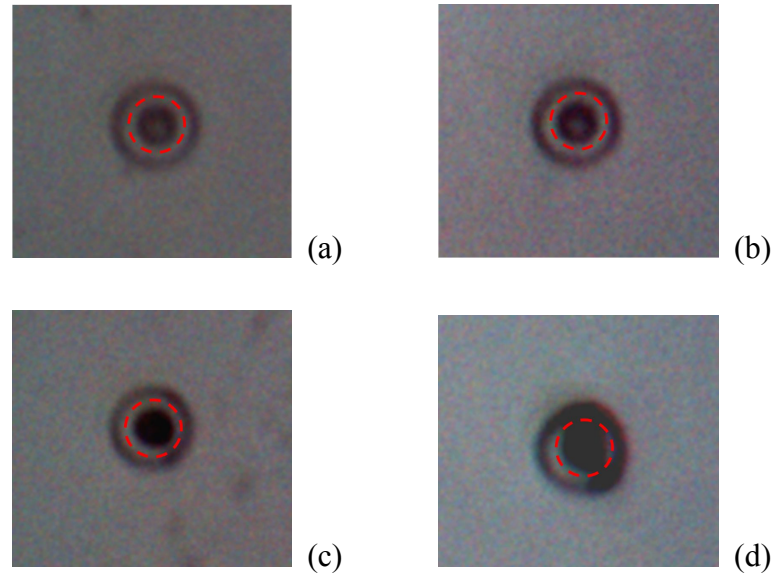


Figure 6. 6 Optical images of the NFTs after laser exposure at different powers. (a) NFT without any exposure; (b) NFT after 35 mW exposure; (c) NFT after 43 mW exposure; (d) NFT after 70 mW exposure.

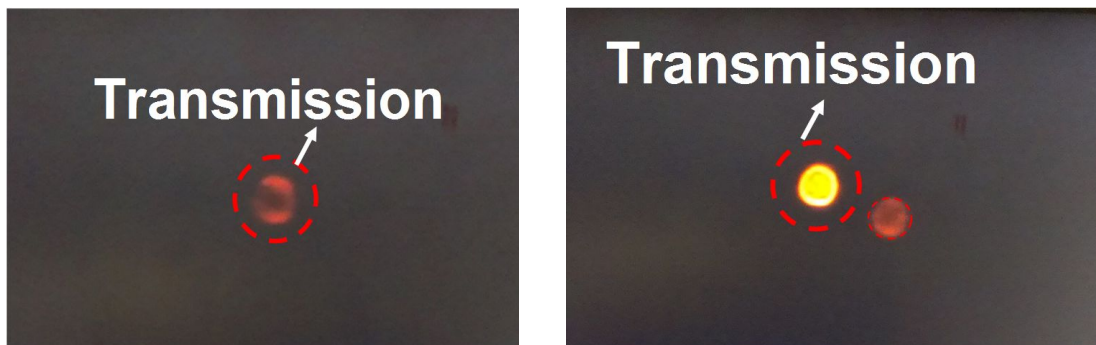


Figure 6. 7 Far field transmission of the NFT after laser exposure. (Left) Transmission of the unexposed NFT; (right) Transmission of the NFT after 43 mW exposure;

The topography scanned by the AFM also confirmed the changes of the NFT structures under high power exposure. Figure 6. 8 shows the topography of 4 NFTs after different exposure conditions. The surface of the NFT was clean if there was no laser exposure. After the laser power was 35 mW, some small particles appeared inside and around the exposed area of the NFT. The sizes of the particles were about 200 to 400 nm, measured by the AFM. After the laser power was 43 mW, larger debris appeared around the laser exposure center. The size of this larger debris was more than 1  $\mu\text{m}$ . In this case, the NFT was no longer functional. Some smaller debris also got trapped inside the NFT structure. When the laser power was increased to 70 mW, the metal material of the NFT disappeared and a hole was generated in the center, and more debris appeared around the

NFT. Those debris and particles could lead to the failure of the HDI, as discussed in our previous work [113].

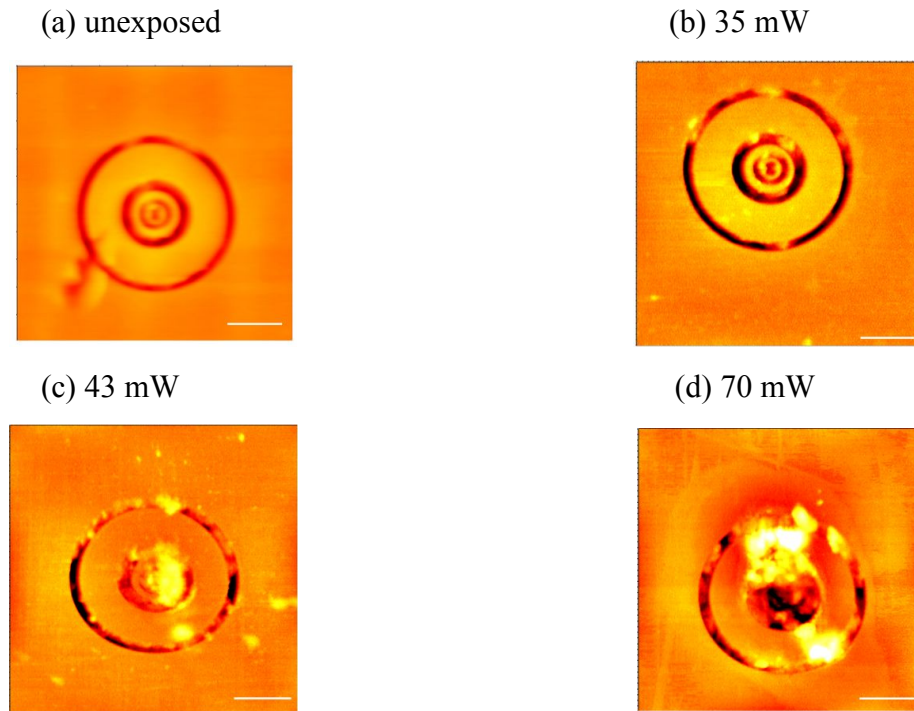


Figure 6. 8 Topography of the NFT structure after different laser exposure conditions. (a) NFT without any exposure; (b) NFT after 35 mW exposure; (c) NFT after 43 mW exposure; (d) NFT after 70 mW exposure. Scale bar is 1  $\mu\text{m}$  for all plots. The outer ring in all plots is not part of the NFT structure, but was used for laser alignment in the experiments.

The topography of the blank area without any NFT structure started to show some change after the laser exposure power was more than 43 mW, as shown in Figure 6. 9. When the laser power was less than 43 mW, there was no obvious surface change and the surface was clean around the exposed area. After the film was exposed by the laser at 43 mW, there was a permanent bump on the film surface. The height of this bump was about 6 nm. The size of this bump was less than 1  $\mu\text{m}$ . Comparing this with Figure 6. 8c, we see that the change of the surface of the NFT was much more severe than of the blank film when they were exposed at the same laser power. The comparison between the exposed NFTs and blank areas indicates that the existence of the NFT can make the change of the HDI more severe.

From the results presented in this section, we can conclude that as the laser power applied to the NFT structure increases, some tiny particles begin to get trapped around the NFT structure. Those accumulated particles could result in a crash of the slider and an instability of the HDI. As the power further increases, the metal film starts to change and some bumps start to appear. In this situation, the geometry of the NFT becomes distorted and its optical performance can be changed. Moreover, the gap between the minimum

point of the slider and disk surface is reduced, so the chance of head-disk contact increases. Finally at high powers, the metal film gets removed due to the laser ablation and the NFT is no longer functional. The existence of the NFT can make the change of the HDI even more severe due to the enhancement effect of the light's intensity by the NFT.

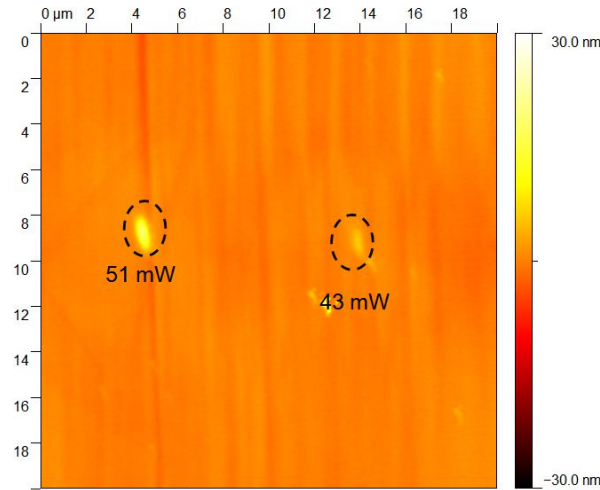


Figure 6. 9 Topography change of the blank metal film of the slider surface after different laser exposure conditions

### 6.3 Dual-stage heating scheme

To make the NFT more reliable in HAMR systems under millions of cycles, it is necessary to reduce the thermal load to the NFT structure while maintaining the amount of the total transmitted energy to the disk for heating or increase the reliability of the NFT materials by other means. In this work, we propose a novel method to reduce the thermal load on the NFT by separating the NFT heating process into two stages [114]. In the first stage, a laser waveguide structure is placed in front of the NFT. This waveguide transmits the laser energy to the disk surface and heats the disk to a peak temperature substantially lower than the Curie temperature of the magnetic material. Then, the NFT works as the second stage to further heat a smaller area ( $25 \times 25 \text{ nm}^2$ ) inside the large waveguide heated area to reach the Curie point. The energy absorbed by the NFT in the second stage is lower than in a single NFT heating scheme proposed in other one stage HAMR systems.

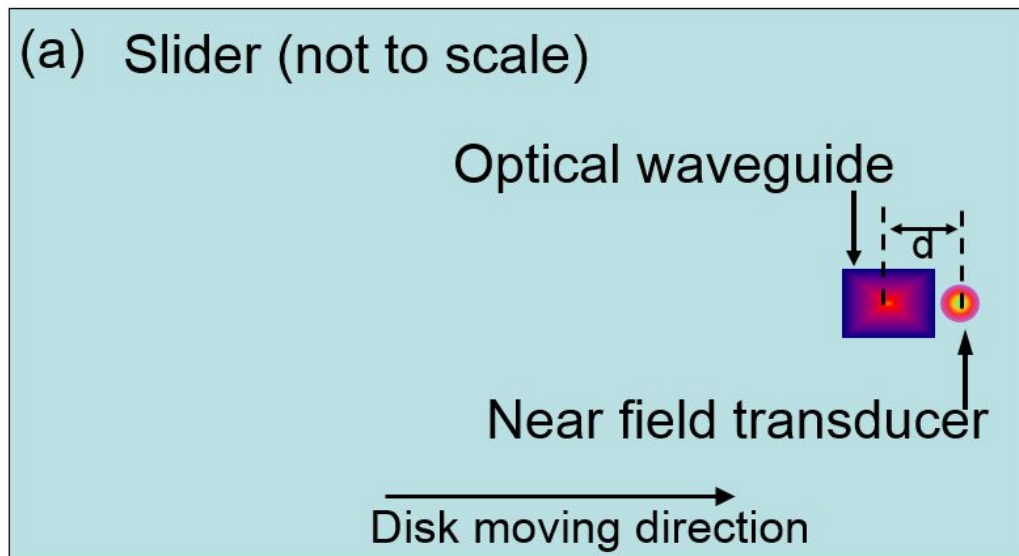
In this work, we designed a bow-tie aperture structure as an NFT to focus light to a spot about 25 nm, using a commercial finite-difference time-domain (FDTD) software (CST microwave studio). A 3D finite element method (FEM) thermal model was developed to calculate the temperature increase of the media under the two heating

sources, using ANSYS. The magnetic switching field of the magnetic layer was obtained from a Callen-Callen model for HAMR systems [23, 45].

### 6.3.1 Modeling

Figure 6. 10 shows a schematic diagram of the two-stage heating scheme. The waveguide is located in front of the NFT structure, with a spacing of  $d$ . Figure 6. 10c shows the typical laser intensity distribution on the disk surface from the waveguide, calculated from CST. The dimension of the intensity profile depends on the size of the  $Ta_2O_5$  core of the waveguide. The profile can be simplified by assuming it to be a 2D Gaussian distribution function. The radius ( $1/e^2$ ) of the laser intensity profile measured at the surface of the disk is  $R_{spot}$ . Figure 6. 10e shows the absorbed power distribution on the surface of the disk from the NFT. In this calculation, a bow-tie aperture structure was used. The calculated intensity profile is close to a rectangular shape. The diameter of the profile ( $1/e^2$ ) along the down track direction is close to 25 nm which satisfies the requirement of initial HAMR systems.

The temperature distribution in the medium was calculated by solving the thermal conduction equation using FEM in ANSYS, as shown in Figure 6. 11. The absorbed power distributions described above were used as heat flux sources in the FEM thermal model. The disk has four layers with different thermal properties. Table 6.1 shows the material properties used in the FEM thermal model.



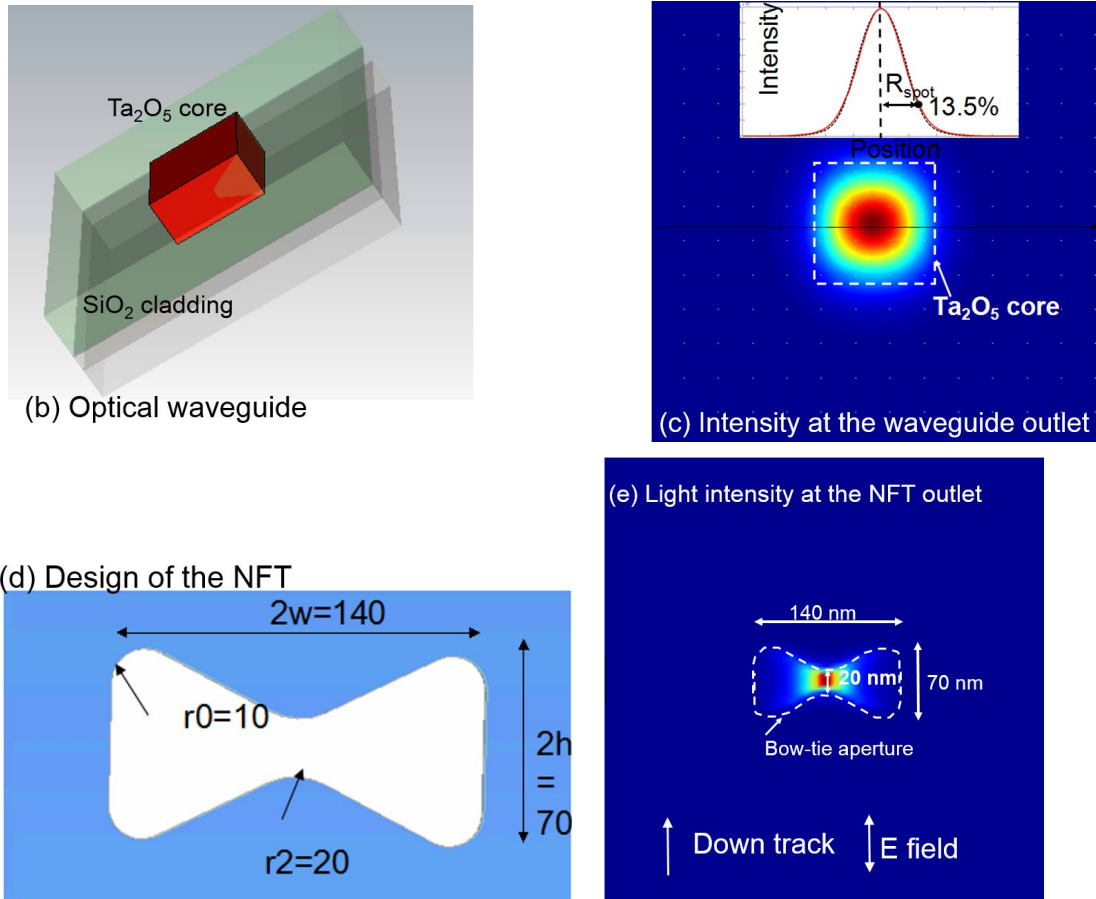


Figure 6. 10 Concept and model of the two-stage heating  
 (a) Schematic diagram of the two-stage heating slider;  
 (b) Design and numerical model for the waveguide  
 (c) Laser intensity distributions for the first stage heating by a waveguide  
 (d) Design and numerical model for a bow-tie NFT  
 (e) Laser intensity distributions of the second stage heating by the NFT

The mesh size is 25 nm by 50 nm in the x-y plane. The boundary conditions were set as below:

1. Ambient temperature at 27 °C (upstream and downstream surfaces, bottom surface)
2. Moving heat flux at the top surface, heat flux had the same distribution as the optical intensity calculated from the optical model.
3. Convection at the top ( $10^5$  W/m<sup>2</sup>K).



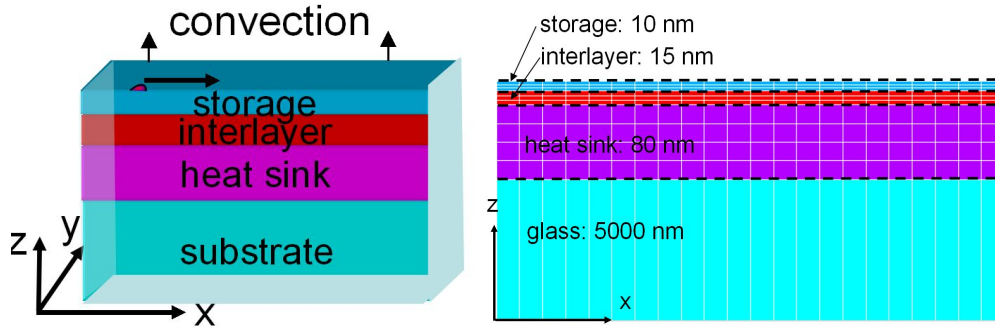


Figure 6. 11 Schematic drawing (left) and mesh (right) of the 3D FEM thermal model for disks multi-layers

Table 6. 1 Thermal properties of 4 layers in the HAMR media [72]

Layer	Thickness (nm)	Vertical Thermal Conductivity (W/mK)	Lateral Thermal Conductivity (W/mK)	Specific Heat (J/m <sup>3</sup> ·K)
Storage	10	50	5	3
Interlayer	15	3	3	2
Heat Sink	80	200	200	3
Substrate	5000	1	1	2

A Callen-Callen model was used to calculate the magnetic switching field. The relationship between the saturation magnetization and temperature can be obtained from the mean field theory as shown in the equations below.

$$\begin{aligned} \frac{M_s(T)}{M_s(0)} &= \frac{5T}{6T_c} X \\ \frac{K_1(T)}{K_1(0)} &= \tanh(X) \tanh\left(\frac{X}{2}\right) \\ \frac{5T}{6T_c} X &= \frac{1}{3} \left[ 2 \tanh(X) + \tanh\left(\frac{X}{2}\right) \right] \end{aligned} \quad (1)$$

Here,  $X$  is the Callen-Callen parameter,  $M_s$  is the saturation magnetization and  $K_1$  is the first order anisotropy constant. We set  $K_u$  to be  $K_1$  for simplification. The switching field  $H_k$  equals to  $2K_u/M_s$ .

### 6.3.2 Results and discussion

The switching field  $H_k$  of the magnetic layer relies on the thermal profile, while the thermal distribution depends on the conditions of the heating sources, including the sizes of the two heating sources and the spacing between them. Figure 6. 12 shows a typical thermal profile for the two-stage heating scheme HAMR. The design goal is to heat a small area of the magnetic layer to the media Curie point after combining the two heating stages. The waveguide heating can raise the disk background to a temperature lower than the Curie point; for example, it can raise the background to 200 °C. At this temperature, the magnetic bits in the adjacent tracks will not be thermally erased by the waveguide heating. The locations of the two peaks of the temperature profile under the two heating sources should be as close as possible. The distance between these two peaks is labeled  $D_p$  as shown in Figure 6. 12. The background temperature ( $T^*$ ) on the disk surface where the NFT heat is applied is always lower than the peak temperature ( $T_{p1}$ ) in the waveguide heating stage. This temperature difference is denoted as  $\Delta T$ , which can be eliminated if  $D_p$  is 0. But  $D_p$  is determined by the sizes of the two heating sources and the physical spacing between them, which is denoted as  $d$  in Figure 6. 10a. The size of the NFT heating source is constrained to be close to 25 nm because of the requirement of the high recording density. So  $D_p$  mainly depends on the size of the waveguide heating source ( $R_{spot}$ ) in the first stage and on  $d$ . The size of  $R_{spot}$  is mainly controlled by the dimension of the waveguide, and it can be calculated using the CST microwave studio software.

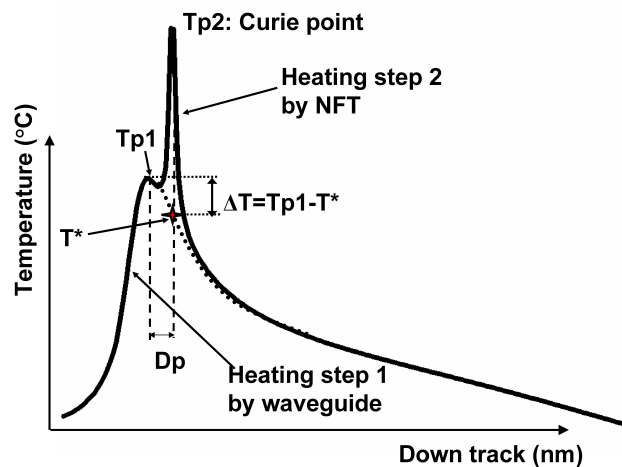


Figure 6. 12 A typical thermal profile on the media surface under the two heating stages

Figure 6. 13 shows the dependence of  $R_{spot}$  on the physical size of the  $Ta_2O_5$  core of the waveguide, calculated from CST. A larger size waveguide can heat a larger area.

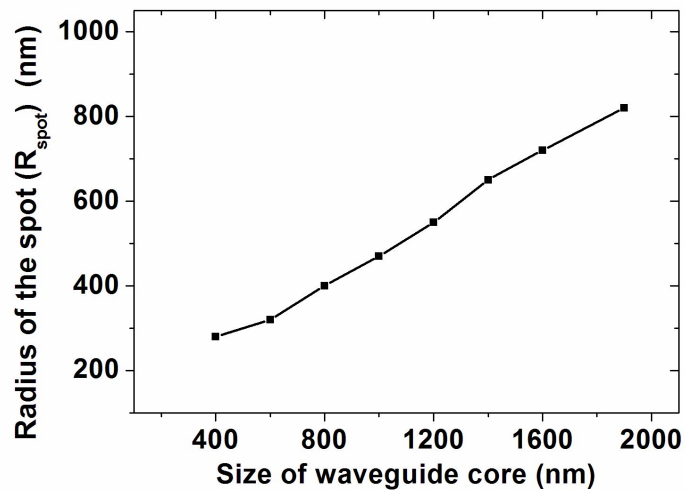


Figure 6. 13 Dependence of the laser radius ( $R_a$ ) on the size of waveguide

The heating sources with different sizes from the waveguide generate different temperature distributions on the disk surface. Figure 6. 14 shows the FWHM of the temperature profile on the magnetic layer and the power needed to heat the disk close to 200 °C when the disk speed is 20 m/s. More energy is consumed to heat a larger area to 200 °C, and the width of the temperature profile is larger. When a larger  $R_{spot}$  is used, more adjacent tracks will be heated and affected.

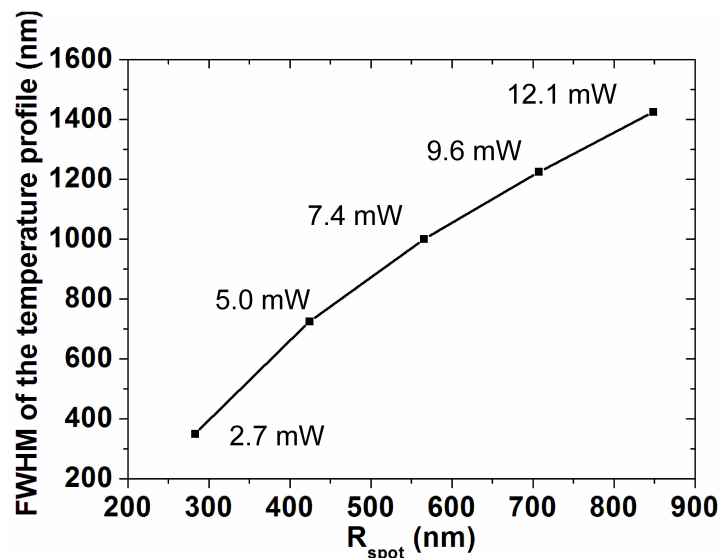


Figure 6. 14 FWHM of the temperature distribution in the waveguide heating stage by different laser radii ( $R_{spot}$ )

There is another trade-off between  $R_{spot}$ ,  $\Delta T$  and  $d$ . A smaller  $R_{spot}$  can provide a sharper thermal gradient which is better for HAMR writing, but it leads to more changes in  $\Delta T$ . It is possible that overheating of the magnetic bits happens at the location of the

temperature peak in the waveguide heating if  $R_{\text{spot}}$  is small and the power input is large. If a larger  $R_{\text{spot}}$  is used, a larger size waveguide structure should also be used. In this case, the physical spacing between the heating sources should be increased to avoid the interference between the two heating sources. Then,  $D_p$  is increased, and  $\Delta T$  becomes larger again. Figure 6. 15 shows the ratio of the background temperature  $T^*$  and  $T_{p1}$  in the waveguide heating as  $R_{\text{spot}}$  changes. It is seen that the ratio decreases as the size of the waveguide heating source becomes larger. A larger ratio of  $T^*$  and  $T_{p1}$  brings benefits for the reduction of the thermal load. The largest ratio is about 0.6 when the radius of the waveguide heating source is 280 nm. The radius of the waveguide heating source cannot be reduced further because of the optical diffraction limits. In the current configuration, the two-stage heating scheme should have its best performance when the radius of the waveguide heating source is 280 nm.

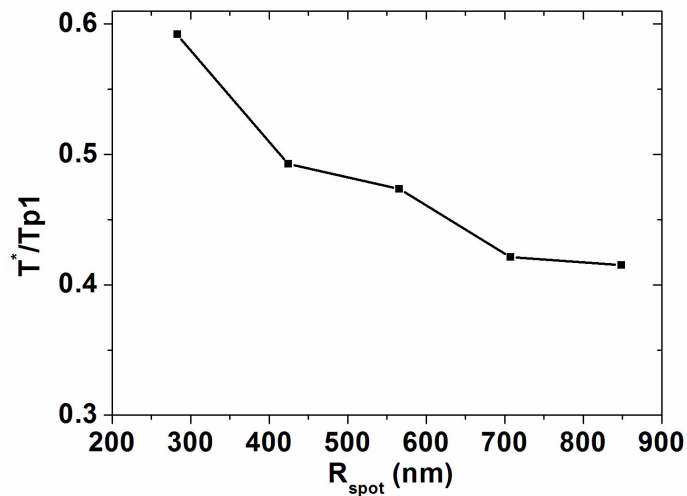


Figure 6. 15 Ratio of the background temperature  $T^*$  and peak temperature  $T_{p1}$  under different  $R_{\text{spot}}$  in the waveguide heating stage

The thermal profile of the two-stage heating scheme is shown in Figure 6. 16. The peak temperature for the two-stage heating can be as high as that in the traditional NFT heating scheme. There is a second smaller peak for the two-stage heating due to the waveguide heating in the first stage. The maximum temperature in the secondary peak is about 200 °C which is about half of the Curie point so the data in the secondary peak will not be erased in the current writing process.

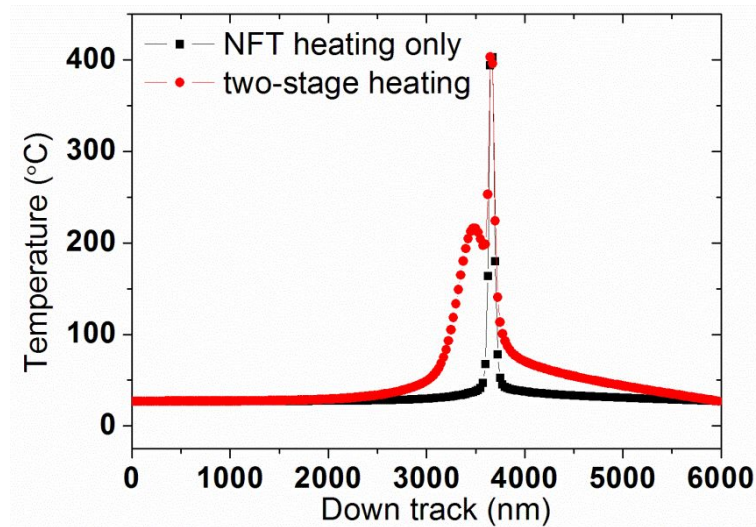


Figure 6. 16 The down-track thermal profile in the two stage heating scheme and single NFT heating scheme.

The Callen-Callen model predicts the magnetic switching field distribution of the magnetic layer for this two-stage heating scheme when  $R_{\text{spot}}$  is 280 nm, as shown in Figure 6. 17. The red curve shows the switching field if only the NFT heating source is applied as in the traditional single stage HAMR systems. The gradients of the switching field at the valley of the two curves are on the same order for both HAMR heating schemes. So the two-stage heating scheme can have similar writing capability as the single NFT scheme.

In this design, the thermal load onto the NFT is reduced by 30% in the two-stage heating scheme compared with the single stage heating system. Thus, it is expected that the temperature of the NFT and thermal stress in the NFT could be reduced as well for this two-stage heating scheme. The total cycle numbers of the metal can be enhanced, according to the S-N curve for metals.

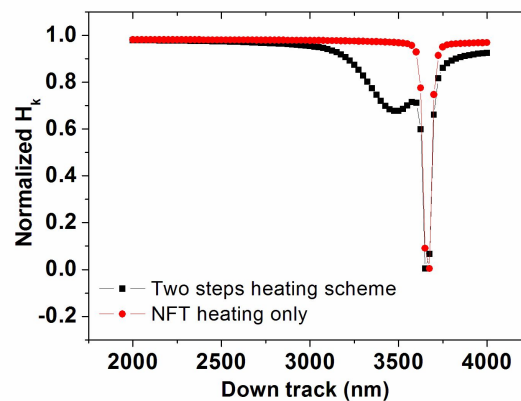


Figure 6. 17 Switching field  $H_k$  distribution on the disk surface for the two-stage heating scheme and single NFT heating scheme.

The FEM thermal analysis of the NFT verifies that the maximum stress and temperature can be reduced if the thermal load is reduced by 30%. The FEM model was built as shown in Figure 6. 18. The metal film with the NFT structure is simplified to a two-layer system. The gold film is 100 nm thick and the substrate is SiO<sub>2</sub> with a thickness of 50  $\mu$ m. The mesh size of the gold film is 100 by 100 by 10 nm. The in-plane mesh size of the substrate is the same as that of the gold film. But the mesh size of the substrate perpendicular to the NFT is 5  $\mu$ m. The laser heating is applied as a heat flux at the interface of the gold and substrate. The boundary conditions were applied as shown in Figure 6. 18. The heat transfer coefficient is set at 10<sup>5</sup> W/m<sup>2</sup>K [72].

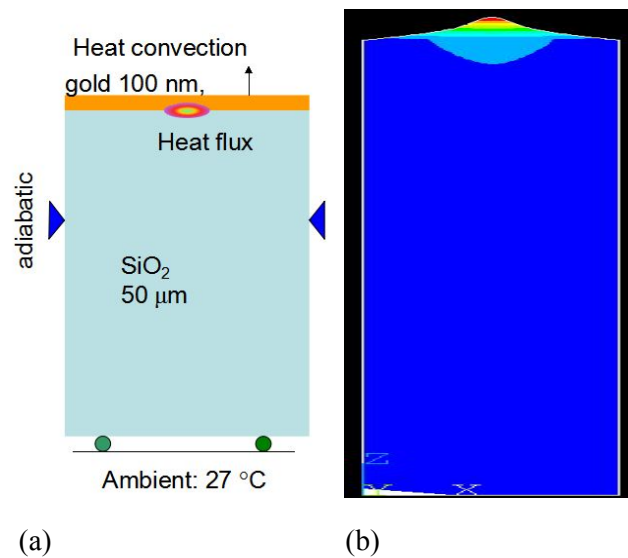


Figure 6. 18 (a) 3D FEM thermal model for the NFT metal layer; (b) Deformation of the NFT under laser heating

The FEM results show a thermal protrusion on the surface of the gold film as shown in Figure 6. 18. Table 6.2 lists the protrusion height and the maximum Von-mises stress inside the thin film. It is shown that the maximum temperature increase and thermal stress are both reduced by about 30 to 20 % with the reduced power.

Table 6. 2 Maximum temperature, mechanical stress and deformation for two-stage heating and single NFT heating.

	NFT only	Two-stage
Maximum temperature	224.6°C	167.2 °C
protrusion	0.84 nm	0.60 nm
stress	308 MPa	219 MPa

It is confirmed that the two-stage heating scheme reduces the thermal load to the NFT so the reliability of the NFT can be enhanced, while the writability is not adversely affected. However, great care should be taken to the two-stage heating scheme because the high background temperature could lead to some adjacent track erasure in the writing process. Further analysis shows that after 10000 adjacent track writes, the magnetization decays by 13%. Further optimization of the magnetic writer design could help to address this problem. At the same time, the two power inputs to the two stages can be controlled and balanced in order to get good reliability and reduce the adjacent track erasure.

In conclusion, a two-stage heating scheme for HAMR systems is proposed in this section. The conventional single NFT heating scheme is replaced by the two-stage heating scheme. The first stage provides an elevated background temperature of about 200 °C by use of an optical waveguide, which is about half of the temperature increase needed to reach the Curie point, while the NFT heats the media further to the Curie point. Numerical simulation shows that the distance between the two heating sources and the size of the waveguide source affect the performance of the two-stage heating scheme. The two-stage heating scheme can provide an effective writing performance for HAMR, while the thermal load to the NFT is reduced compared to a single stage approach. So it is expected that the two-stage heating scheme can extend the lifetime of the NFT under cyclic load conditions.

## 6.4 Summary

In this chapter, the failure mechanisms of the NFT in HAMR systems have been discussed. A NFT array with several NFTs was fabricated on the air bearing surface of a home-made flying slider. The changes of the NFT structure due to laser irradiation at different power levels were inspected by several technologies, such as optical microscopy and AFM. Small debris was found when the laser power to the NFT was around 35 mW. When the laser power was increased to 43 mW or even more, large bumps and significant geometry changes of the NFT were observed. The geometry change of the metal film was more at the surface of the NFT, compared with the case that the film was blank. At very high power, the film around the NFT was removed due to laser ablation.

In order to increase the reliability of the NFT, a two-stage heating scheme was proposed. This two-stage heating scheme reduces the thermal load to the NFT structure by separating the media heating into two steps. A waveguide heating raised a background area ( $\sim 300 \times 300 \text{ nm}^2$ ) to about 200 °C, which was about half of the Curie point. Then the NFT heating raised a small area ( $\sim 25 \times 25 \text{ nm}^2$ ) embedded in the background further to the Curie point. From the numerical simulation results, it was found that the thermal load to the NFT in the two-stage heating scheme can be reduced by about 30%. The thermal stress and temperature increase of the NFT were also reduced. In this way, the lifetime of the NFT structure can be extended.

## **Chapter 7 Fly-height modulation for a two protrusion**

### **(TFC-NFT) HAMR slider**

The fly-height modulation (FHM) is one of main concerns of the head-disk interface. The FHM is induced by the disk run-out, waviness, and slider dynamics. The amount of the FHM in current PMR hard disk drives is less than 1 nm. The FHM is larger when head-disk contact occurs. The FHM should also be considered and minimized for HAMR drives as well in order to get a good reading/writing performance. The FHM of HAMR systems will be different because of the hot working environment. In this chapter, a new design for reducing the FHM in HAMR systems is introduced and discussed.

#### **7.1 Introduction**

The head-disk clearance has been reduced as the areal density increased year-by-year in order to get good magnetic reading and writing performance [14]. Meanwhile, the FHM has also been reduced together with the flying height in order to get stable reading and writing. However, as the fly-height gets further reduced, the chance of contact between the disk and head increases. In HDD products, the head-disk contact should be prevented to reduce the head wear/crash and data loss [115].

During the past ten years there has been a continuous efforts to reduce the magnetic spacing in HDDs from about 12 nm to sub-5 nm in order to get higher recording densities, including continuous improvement of the air bearing surface design, lubricant and DLC thickness reduction, smoother disk surface and TFC.

TFC has been widely implemented as a critical technology to the HDD since 2005, and it has been able to reduce the clearance to less than 5 nm. In this system, a Joule heating element is embedded in the flying slider near the magnetic transducer. The heater is composed of different materials from the surrounding portions of the flying slider on which the magnetic transducer resides. These materials expand and contract more with temperature changes than the body of the slider. The resistive heating is generated when current is supplied to the heater. The heat generated in the heater leads to a local thermal protrusion toward the recording media of the region surrounding the read-write transducers, thus the spacing between the magnetic transducer and media can be controlled by tuning the power applied to the heater. The dynamics of the slider with a single thermal protrusion near the magnetic transducer has been widely investigated both experimentally and theoretically [116, 117]. The thermal response time for the protrusion to reach a steady state temperature and deformation is tens of  $\mu\text{s}$  [118]. This response is slower than the slider's dynamical frequencies, which are usually on the order of a hundred kilo-hertz, so the fly-height is usually only statically controlled in current HDDs



with TFC. Dynamic control of the flying height was presented in [119]. There it was demonstrated that the FHM can be further decreased when a dynamic TFC is applied.

A stable flying state with a lower fly-height is still of great importance in the HAMR system which is supposed to have higher area density than current PMR technology. A small FHM is also necessary for HAMR systems, so it is believed that the TFC should be also implemented for HAMR systems to get lower fly-height and FHM. Any possible contact between the head and disk should be avoided in order to enhance the reliability of the HDI, especially the NFT.

However, the HAMR system is quite different from the traditional PMR as a laser diode is integrated into the flying head, and the light is delivered to a tiny spot on the disk surface by a NFT. All the main components of the HAMR head will be heated during this HAMR writing process. As summarized in Figure 7. 1 [120], the total input electrical power could be on the order of 100 mW while the total output from the NFT to the disk is around 0.5 mW. The total efficiency is less than 1% while most of the energy gets dissipated as a form of heat inside different parts of the head. The dissipated heat inside the head will raise the temperatures of different parts to different levels.

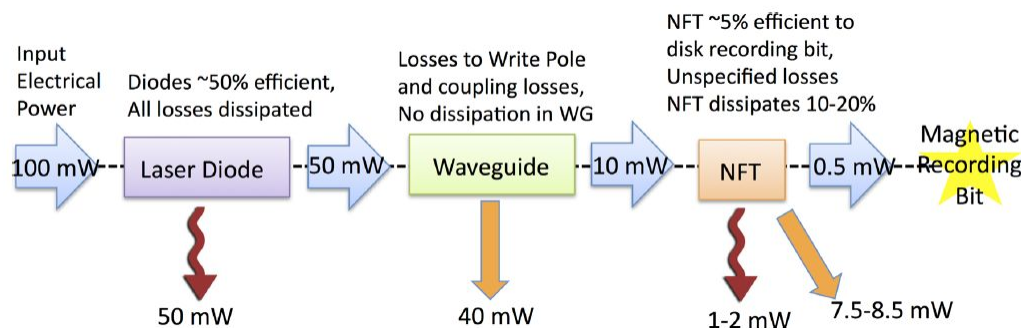


Figure 7. 1 Energy flow in a HAMR drive [120]

Thermal deformation occurs when different parts have different temperatures and coefficients of thermal expansion. It has been mentioned that the temperature increase in the NFT can be several hundred degrees when most of the laser energy gets dissipated as heat around the transducer [121]. In Shreck's work [35], a thin film of phase change material was deposited on the air bearing surface. It had a phase transition temperature at 150 °C. In a flying test, the phase change was founded around the NFT. It indicated that the temperature increase around the NFT could be even higher than 150 °C.

The NFT is usually made of some noble metals, such as gold while the slider body is made of AlTiC and the waveguide is made from SiO<sub>2</sub>. The thermal properties of those materials are quite different, so there is expected to be a thermal protrusion around the NFT structure on the air bearing surface when the laser is on. Some AFM based technology has been developed to measure the size and height of this laser heating induced protrusion, as discussed in [35, 36]. It showed that the height of this laser

induced protrusion is about  $\sim 1$  nm and the lateral size is about  $1 \mu\text{m}$ . It also noted that the current touchdown measurement method using the TFC for this laser induced protrusion during flying is not recommended. Unintentional/unaware head and disk contact could occur when the laser is on during flying and lead to damage of the NFT structure and the HDI. Greater care should be taken for this NFT protrusion because it is hard to detect and also the metallic structure is likely to be damaged.

What's more, this laser heating-induced protrusion is difficult to adjust actively during the data writing process, because the laser power is determined by the requirement of the media temperature needed to write the data.

Inevitably, the HAMR slider will have at least two thermal protrusions: the laser-induced NFT protrusion due to the laser heating, and the TFC protrusion from the conventional Joule heater. There should be some consideration given during the designed location of the TFC and NFT for HAMR systems in order to avoid head-disk contact. Sliders with multi-micron scale protrusions have also been studied numerically by Zheng et al., [122] and experimentally by Juan et al., [123]. The latter showed that the locations and designs of the heater elements have a significant effect on the magnetic spacing.

In this chapter, we introduce a new air bearing surface design with two thermal protrusions. With this scheme, an optimized design allows smaller FHM and also reduces the chance of contact between the NFT and disk.

The air bearing system is simulated by a 2 degree of freedom (DOF) mass-spring-damper model, as described in [124]. The model parameters are identified using an ABS Reynolds equation solver (CML dynamic simulator) [125]. The disk waviness is regarded as a disturbance to the system's equilibrium flying state. The slider can't actively suppress the disturbance and follow the disk waviness because of the phase and magnitude differences between the disturbance and the response of the slider. The protrusions provide additional force and torque excitations to the slider, which can be viewed as a passive feedback loop to compensate the disturbance. The pressure and normal force under the protrusions are obtained for various protrusion heights to calculate the stiffness around the protrusions using the CML dynamical simulator. The gain of the feedback loop is provided by the stiffness. Then the locations and heights of the two protrusions are optimized in order to reduce the FHM due to the disk waviness. The effect of external disturbances on the FH are also discussed.

## **7.2 2-DOF numerical model**

In this paper, a pico-slider (1.25 by 1.0 mm) designed for 10 nm FH is used as an example to show the procedure for the dual-protrusion scheme. The air bearing surface design of this slider and the equivalent 2-DOF mass-spring-damping model are shown in Figure 7. 2. The slider flies at a radius of 30 mm with a disk rotation speed of 7200 RPM

and 0 skew angle. The nominal flying height is 9.5 nm, the pitch is 266.38  $\mu\text{rad}$  and the roll is -2.169  $\mu\text{rad}$ .

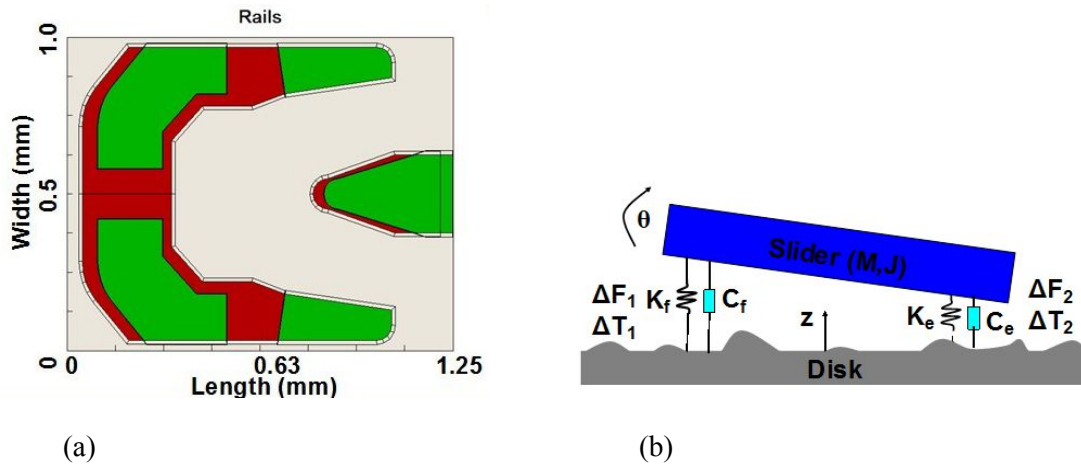


Figure 7. 2 (a) ABS design; (b) 2-DOF mass-spring model

The 2-DOF model can be described by the equation,

$$\begin{bmatrix} M & 0 \\ 0 & J \end{bmatrix} \begin{bmatrix} \ddot{z} \\ \ddot{\theta} \end{bmatrix} + \begin{bmatrix} c_{11} & c_{12} \\ c_{21} & c_{22} \end{bmatrix} \begin{bmatrix} \dot{z} \\ \dot{\theta} \end{bmatrix} + \begin{bmatrix} k_{11} & k_{12} \\ k_{21} & k_{22} \end{bmatrix} \begin{bmatrix} z \\ \theta \end{bmatrix} = \begin{bmatrix} F \\ T \end{bmatrix}$$

where  $z$  is the vertical displacement of the mass center from the mean plane of the roughness surface and  $\theta$  is the slider's pitch.  $M$  is the mass, while  $J$  is the pitch moment of inertia. From the equation we can define  $C$  as the damping matrix and  $K$  as the stiffness matrix.  $F$  is the force excitation and  $T$  is torque.

Figure 7.3 shows the response of the slider to an external impulse excitation, including both a positive force excitation along the  $z$  direction and a positive torque excitation, calculated by the CML dynamic simulator. The 2-DOF transfer function of the air bearing system is obtained by fitting the spectrum of the impulse responses of the force and pitch torque.

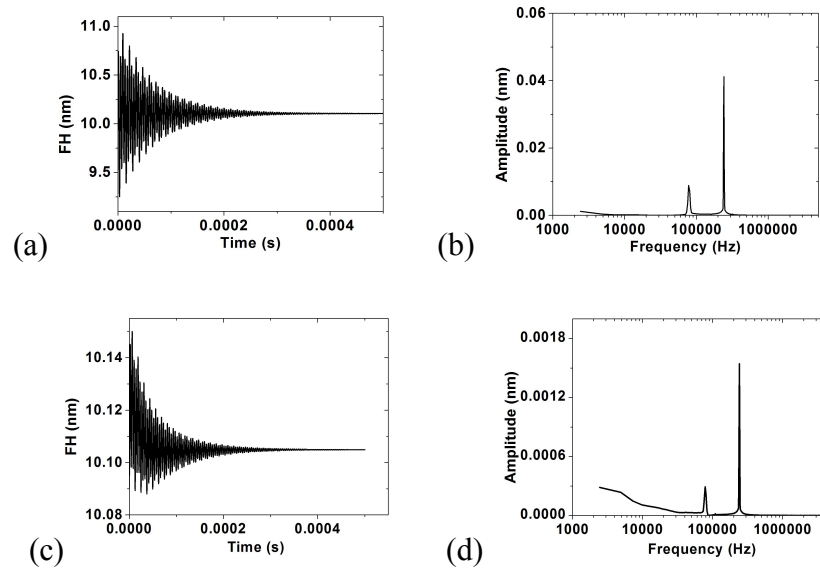


Figure 7.3 The impulse response of the slider and its spectrum. a. Response to the force excitation; b. Spectrum of a; c. Response to the torque excitation; d. Spectrum of c

A feedback control system is designed to represent the air bearing system as shown in Figure 7. 4. This simplified feedback control system helps speed up the optimization process of the dual protrusion design.  $H_1$  is the transfer function from the force excitation to the FH while  $H_2$  is the transfer function from the torque excitation to the FH.  $K_1$  and  $K_1'$  are the force and torque excitations due to the waviness under the laser-induced protrusion.  $K_2$  and  $K_2'$  are the force and torque excitations under the TFC protrusion.  $d$  is the excitation delay distance due to the spacing between the two protrusions. The strength of the feedback excitation, which is defined as the gain of the feedback loop, depends on the air bearing lift forces under the protrusions, which are determined by the protrusion heights and sizes. The delay of the excitation depends on the location of the two protrusions and the velocity of the disk. Since the laser-induced protrusion cannot be adjusted during the writing process in HAMR, the TFC protrusion is the only one to be optimized. So our design goal is to optimize  $K_2$ ,  $K_2'$  and  $d$  to reduce the FHM due to disk waviness and external disturbances. The optimization process is performed as follows: the laser-induced protrusion is fixed next to the writer location and the protrusion shape is obtained from the optical-thermal analysis of the near field transducer. In this way,  $K_1$  and  $K_1'$  can be calculated and fixed. Then some estimated  $K_2$  and  $K_2'$  values are used as trials,  $d$  is tuned to get a smaller FHM for every fixed  $K_2$  and  $K_2'$  set. Once  $d$  is fixed,  $K_2'$  and  $K_2$  are further adjusted to produce the minimum FHM. The following section demonstrates an optimized set of  $K_2$  and  $d$  values.

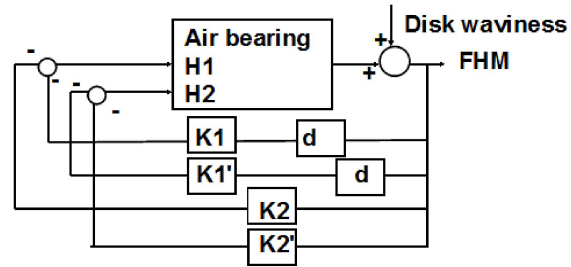


Figure 7. 4 Feedback control loop for the ABS with two thermal protrusions

### 7.3. Dual protrusion design and discussion

Figure 7. 5 shows an optimized arrangement of the TFC protrusion on the rear pad of the slider and the geometry of the two protrusions. The laser-induced protrusion is next to the writer. The TFC protrusion center is set to  $33\ \mu\text{m}$  in front of the laser-induced protrusion. Both the TFC and laser-induced protrusions are assumed to be of Gaussian shape based on the thermal structural analysis of the electrical heater and laser heating. The dimension of the TFC protrusion are  $28\ \mu\text{m}$  along the circumferential direction and  $51\ \mu\text{m}$  along the radial direction based on the data from reference [126]. The peak of the TFC protrusion is  $16\ \text{nm}$  high. The width of the laser-induced protrusion is around  $2\ \mu\text{m}$ , and its height is about  $8\ \text{nm}$ .

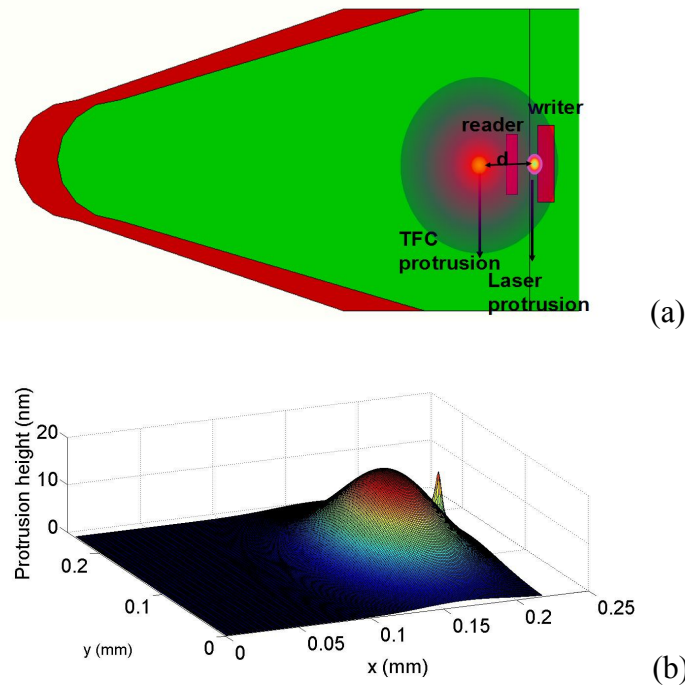


Figure 7. 5 Dual protrusions design. (a) Location of the dual protrusion on the rear pad; (b) geometry of TFC (left bigger one) and laser-induced protrusion (right smaller one)

Figure 7. 6 shows the force provided by the two protrusions with different heights. The feedback loop stiffnesses ( $K_1$  and  $K_2$ ) can be obtained from Figure 7. 6 by calculating the curves' slopes. Since the slider's flying height variation is usually smaller than 1 nm, we can assume that the stiffness is constant once the protrusion heights are fixed.

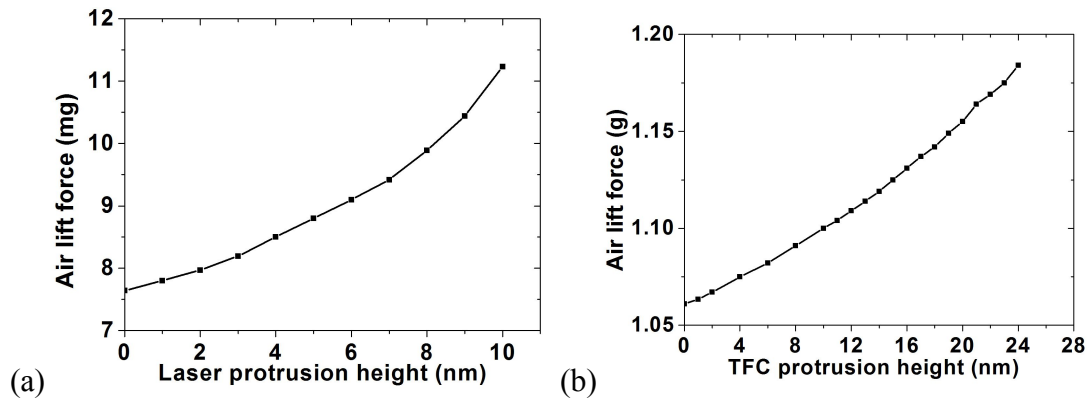


Figure 7. 6 Air lift force under the two protrusions, (a) laser-induced protrusion; (b) TFC protrusion

The slider's FHM due to the disk waviness is calculated using the 2-DOF model, as shown in Figure 7. 7. The standard deviation of the disk waviness is 0.2 nm. The FHM is reduced to 0.07 nm when the two protrusions are used, while it is about 0.2 nm if no protrusions are used, 0.12 nm if only the laser-induced protrusion is used and 0.07 nm if single TFC protrusion is applied. This indicates that the slider can fly stably with less variation for the dual protrusion case, compared with the single laser-induced protrusion case. The suppression of the FHM can be explained in two ways. First, the existence of the TFC protrusion provides additional excitation to the slider and makes the system stiffer. The stronger feedback (larger overall gain) can compensate more disturbances. Second, the TFC protrusion is able to compensate the phase delay of the system because of the location of the TFC protrusion. In other words, the TFC protrusion senses the waviness disturbance before the laser-induced protrusion and provides a larger phase margin for response. From Figure 7. 6, we find that the TFC protrusion provides a lift force 2 orders of magnitude larger than the laser-induced protrusion. The FHM difference between the dual protrusion and the single TFC protrusion cases is very small. Thus, the FHM of single TFC and dual protrusion almost overlap in Figure 7. 7. The TFC protrusion is the dominant factor for the dual protrusion design, and the optimized TFC protrusion makes the air bearing more robust.

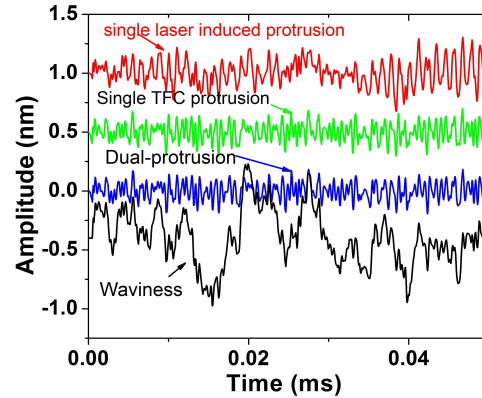


Figure 7. 7 FHM due to the disk waviness when different number of protrusions is applied. The FHM of the single laser -induced protrusion case and TFC protrusion are offset by 1 nm and 0.5 nm, the waviness is offset by -1 nm for a better view

External disturbances result in FHM as well, such as environmental mechanical vibrations and some audio disturbances, which have frequencies of several kilo-Hertz. Figure 7. 8 shows a simulated external force disturbance along the z direction (20 kHz square wave disturbance) and the response of the slider to this disturbance when there is no protrusion, a single protrusion (laser-induced protrusion) and two protrusions, respectively. The FHM is 1.5 nm if there is no protrusion, 1.1 nm for a single laser-induced protrusion while it is only 0.2 nm if dual protrusion is used. It is obvious that the disturbance is suppressed more if two protrusions are applied, compared with the no-protrusion and the single laser-induced protrusion cases.

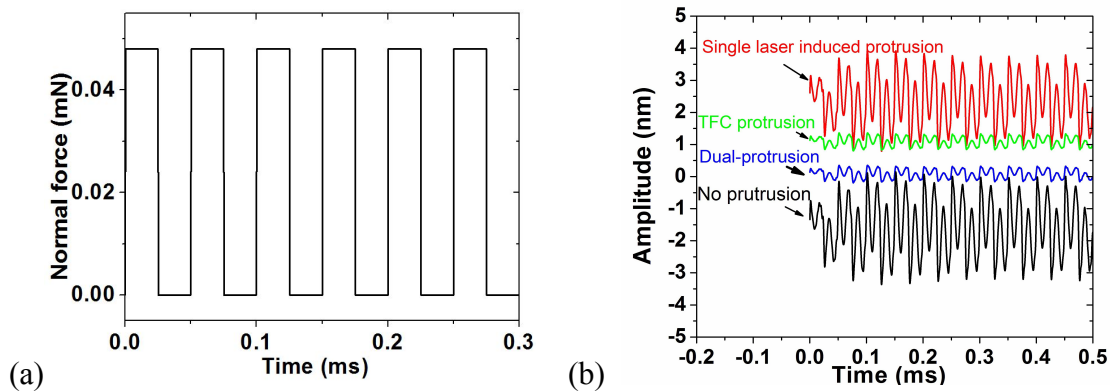


Figure 7. 8 FHM induced by the external disturbance when different number of protrusions are applied. (a) Force disturbance; (b) FHM

In the HAMR dual protrusion system, the TFC protrusion is the only one that can be adjusted by the change of power to the Joule heater in order to make the slider fly stably. Figure 7. 9 shows the FHM change with respect to the TFC protrusion height calculated by the CML dynamic simulator when the separation between the two protrusions is 33  $\mu\text{m}$ . The FHM is normalized to the maximum FHM when there is no TFC protrusion. As

the height of the TFC protrusion increases, the FHM decreases, because the TFC protrusion provides stronger feedback to compensate the disturbance induced by the waviness. However, if the TFC protrusion height becomes larger (18 nm), the FHM increases due to overcompensation. Further increase of the TFC protrusion will lead to slider crash and consume more energy. In this case, the slider crashes when the TFC protrusion height is 34 nm.

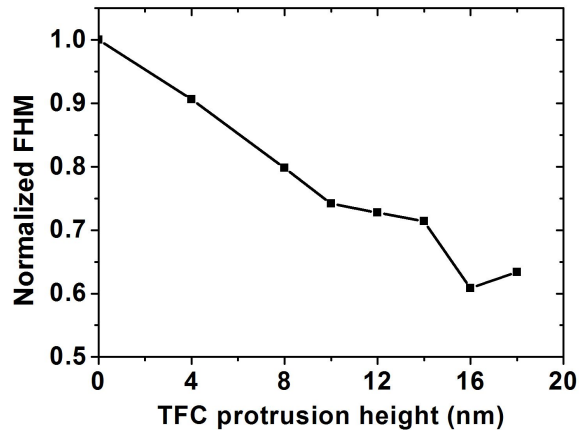


Figure 7. 9 Normalized FHM vs. height of the TFC protrusion by CML dynamic simulator when the dual protrusion separation is 33  $\mu\text{m}$ .

This dual protrusion design has been verified further by changing the location of the TFC protrusion, using the CML dynamic simulator. Figure 7. 10 shows the normalized FHM with respect to the dual protrusion separation and TFC protrusion height. The stars in the figure indicate crashes. When the TFC protrusion is close to the laser protrusion, the slider crashes even when the TFC protrusion is small. For example, when the separation is 0  $\mu\text{m}$ , the laser-induced protrusion is superposed on top of the TFC protrusion, and head-disk contact happens when the TFC protrusion height is 4 nm. When the separation between the two protrusions is increased (if the separation is 40  $\mu\text{m}$ , for example), the suppression of the disturbance is more obvious and the FHM is small. However, more energy is consumed to get a larger TFC protrusion in order to sustain a minimum FHM, and it is possible that the TFC Joule heater will get damaged at higher power. Thus, there are two concerns during the location optimization of the two protrusions. The first is the contact between the laser protrusion and disk, which happens more likely when the separation between the two protrusions is smaller. The second is the TFC heater power or deformation limit when the separation between the two protrusions is larger.



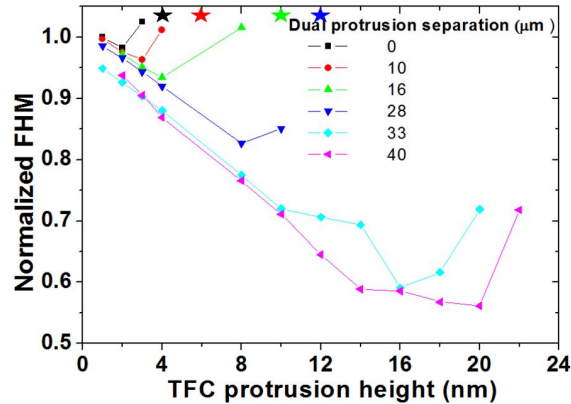


Figure 7. 10 Normalized FHM for different dual protrusion separation and TFC protrusion height. The stars indicate slider and disk contact.

## 7.4 Summary

A 2 DOF mass-spring-damper model is used to simulate the air bearing system, and the disk waviness is regarded as a disturbance to the equilibrium flying state. The two protrusions caused by the TFC and laser provide additional force and torque excitation to the slider due to the disk waviness, which can be viewed as a feedback loop to compensate the disturbance. The gain of the feedback loop depends on the stiffnesses of the protrusions, which are determined by the protrusions' heights and positions. The pressures and normal forces under the protrusions are obtained for various heights of the protrusions to calculate the stiffnesses around the protrusions by the CML dynamical simulator. The optimization process of the dual protrusion design has been discussed based on this simplified feedback system.

There are some trade-offs between the TFC power consumption and protrusion-disk contacts for the dual protrusion design. A more powerful TFC protrusion is necessary to suppress the disturbance effectively if the separation between the two protrusions is larger, while protrusion-disk contacts easily occur if the separation is smaller. The FHM of the dual protrusion slider is reduced significantly when the height and location of the TFC protrusion are optimized. The external disturbance induced FHM can also be suppressed by tuning the height of the TFC protrusion while the laser-induced protrusion remains unchanged. Because the laser-induced protrusion has little effect, there is no need to change the power of the laser in the HAMR slider during the writing process. This scheme of using a passive feedback loop to model dual protrusions for flying height modulation analysis and optimization can help to design the HAMR head with a more consistent flying height and greater ability to compensate the external disturbances.

## Chapter 8 Plasmonic nanolithography system for patterned media

The storage density of magnetic recording keeps increasing every year by shrinking the size of the magnetic bits. The bit size along the down-track direction should be about 25 nm in order to get a storage areal density beyond 1 Tb/in<sup>2</sup> [14]. One magnetic bit in the current perpendicular magnetic recording PMR is composed of about one hundred magnetic grains which maintain the same orientation. As the magnetic bit gets more compact, the size of each magnetic grain drops, and finally the phenomenon called superparamagnetism occurs. In this situation, the magnetic grains are no longer thermally stable and the data bit cannot be stored. In order to overcome the superparamagnetic limit, several approaches have been proposed in the past a few years. Bit-patterned media (BPM) [27] is one of those approaches that has the capability to increase the magnetic storage density beyond 1 Tb/in<sup>2</sup>. In BPM systems, each magnetic bit is composed of a magnetic island, which is physically isolated from other magnetic island on the media surface. The number of grains in a magnetic bit is then much less than one hundred. The volume of each magnetic grain can be larger than that in the current (PMR) media so that the magnetic grain is more thermally stable. In this way, the final size of a magnetic bit can be reduced so the storage density can be enhanced. However, there are still some challenges for BPM technology, such as the large volume fabrication of the patterned media disks [38], the head flying stability on the patterned media [127], the control of defects on the media [128], etc.

Nanoimprint technology has been proposed to achieve the large volume manufacture of the patterned media disks. There are several major steps for the production of a patterned media, as shown in Figure 8. 1 [129]. In order to fabricate the patterned media disks, a master template with the patterned islands must first be prepared. High resolution lithography tools, such as rotary electron beam lithography systems [130], have been used to define the patterns on the master template. Self-assembly of polymers has been proposed to double the patterns and remove some of the defects. Once the solid master templates are accessible, nanoimprint can be used to replicate the template to millions of pattern disks. In nanoimprint technology, a template is “printed” into a liquid resist film on the surfaces to which the pattern is to be copied. After the patterned template is in contact with the liquid resist, the resist is then irradiated with ultraviolet light for a few seconds, which cures the liquid resist and causes it to solidify almost instantly. Then the original patterned template is removed, leaving a copy of the topographic patterns from the surface of the original template on the target surface. More patterned media disks can be fabricated at relatively low cost by use of the nano-imprint technology. Some other post-processes can be performed to make the disk smooth and functional for magnetic recording, such as planarization, lube and burnish.

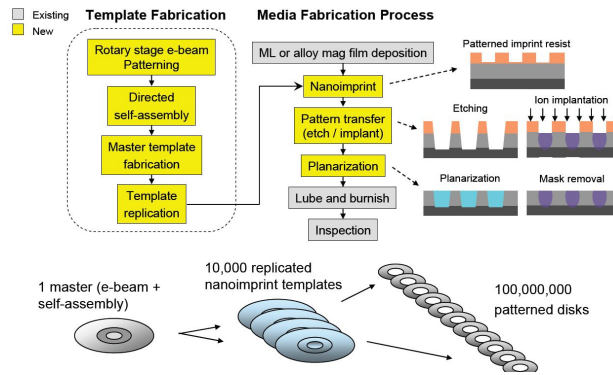


Figure 8. 1 Fabrication process for bit patterned media [128]

The nanoimprint is a template replication process, indicating that the quality of the patterned disk relies on the patterned template. Instead of using expensive and complicated rotary electron beam lithography, a new technology called plasmonic nanolithography [131] can also help to fabricate the pattern template with relative low cost and high throughput. In this chapter, a plasmonic nanolithography machine is introduced, and the specifications of this machine are given as well.

## 8.1 Introduction of plasmonic nanolithography

Traditional optical lithography has been widely implemented in semiconductor industry. However, the minimum feature size (critical dimension, CD) of optical lithography is limited by the optical diffraction limit, as shown in the equation 8.1:

$$CD = k_1 \frac{\lambda}{NA} \quad (8.1)$$

Here, CD is the critical dimension.  $k_1$  factor is a coefficient that encapsulates process-related factors, and typically equals 0.4 for production.  $\lambda$  is the wavelength of light used. NA is the numerical aperture of the lens.

The CD of the optical lithography has now been successfully scaled down to 22 nm by use of a conventional 193 nm ArF excimer laser with the assistance of liquid immersion and double patterning techniques. However, in order to reduce the CD to below 20 nm to achieve higher areal densities for bit patterned media (table 8.1) [38], the laser source will probably have to be changed to extreme ultraviolet with a shorter wavelength at about 13 nm [Figure 8. 2, ITRS 2013]. The cost of the extreme ultraviolet lithography (EUV) system is expected to surpass 120 million dollars, and it has not yet to be delivered for large volume production. The optical lithography is not able to provide an urgent and cheap solution for the fabrication of the patterned media. Other relatively cheaper approaches should be considered for defining and fabricating the patterned media. A plasmonic nanolithography system introduced in this chapter can be a candidate to

break the optical diffraction limit and has some advantages for patterned media template fabrication.

Table 8. 1 Size of a magnetic bit/island and track with respect to areal density [38]

Areal density (Tb/in <sup>2</sup> )	Track pitch (nm)	Bit pitch (nm)	Bit length (nm)
1.0	25	25	13
1.9	18	18	9
5.3	11	11	6
10.3	8	8	4

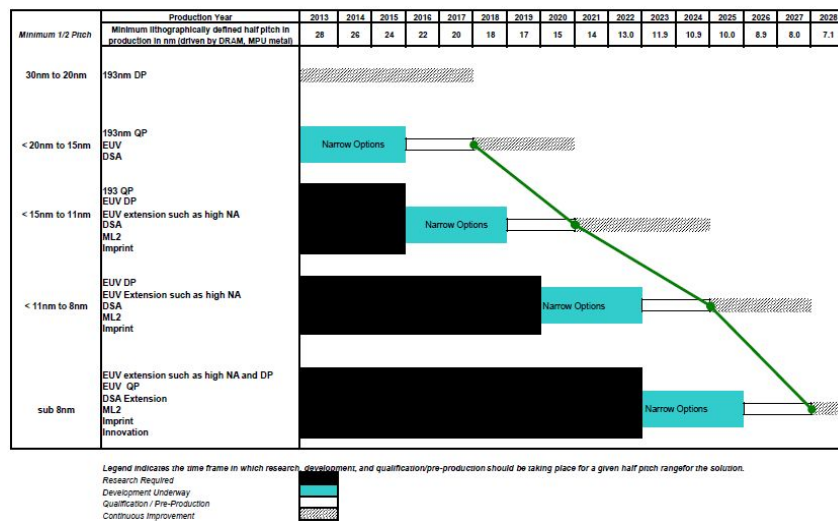


Figure 8. 2 DRAM and MPU Metal Level Potential Solutions for ITRS

A plasmonic lens structure (also called near field transducer) has been proposed for the plasmonic nanolithography [130]. The plasmonic lens is able to focus the light to a spot that is smaller than the optical diffraction limit. However, the laser exposure only works effectively when the gap between the plasmonic lens and the lithography wafer is within several nanometers due to the evanescent decay of the near field intensity. To control the gap within a range of several nanometers, a scanning probe system [132,133] and a flying air bearing surface system were proposed [134]. Such a plasmonic nanolithography system with the flying air bearing surface can scan the wafer at ~10 m/s, which is 3 to 5 order faster than a plasmonic lithography system based on a scanning probe. So the throughput of plasmonic lithography based on a flying air bearing surface could be a few orders higher than that based on a scanning probe.

As demonstrated in [133], the plasmonic nanolithography system was mainly composed of a flying air bearing slider, a UV laser, a lithography wafer with thermal

photoresist, and a spinning spindle. The plasmonic nanolithography system is quite close to the HAMR system which was discussed in detail in the first seven chapters. The main difference of the plasmonic nanolithography system from HAMR systems is that the slider for plasmonic nanolithography does not include the magnetic transducer and the wafer has a thermal photoresist rather than a magnetic layer.

As a lithography tool, the machine should have a friendly user interface for user operations and some system parameters for process control. Also, position control for the lithography machine is a key parameter.

Over the past five years, many efforts have been put into the construction and integration of the plasmonic nanolithography machine, including reducing the width of lithography minimum feature size, improving the high resolution positioning system and improving reliability of the HDI. In 2011, a 22 nm half pitch dot array was demonstrated on the prototype of the plasmonic nanolithography machine [135].

In section 8.2, the configuration of the machine is described. In section 8.3, the positioning control is discussed, including both down-track and radial direction position control. In section 8.4, a high speed pattern generation system is introduced. Section 8.5 presents some experimental results. Section 8.6 summarizes this chapter.

## 8.2 Machine configuration

The plasmonic nanolithography machine has several sub-systems, as shown in Figure 8.3. The lithography machine is composed of an optical system, a spindle system, a linear stage, a rotary magnetic encoder system, a pattern generation system and a central control unit. The machine is built on a vibration isolation table inside a class 100 clean room in order to keep a clean environment.

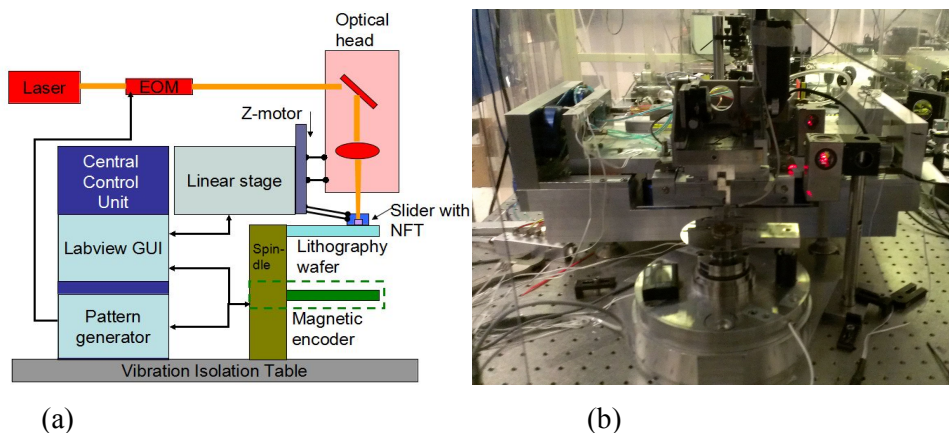


Figure 8. 3 Integrated plasmonic nanolithography machine (a) brief schematic (b) real system

### 8.2.1 Optical system

The optical system includes a picosecond pulsed laser, some mirrors, prisms, an elect-optical modulator (EOM) to modulate the laser pulse, an optical writing head and an air bearing slider with a plasmonic lens.

The laser beam is emitted from the laser and reaches the EOM first. The EOM is able to modulate the laser at 80 MHz. When the modulation signal is high, the laser passes the modulator and exposes the wafer; when the modulation signal is low, the laser is blocked by the EOM and the wafer is not exposed.

By feeding the modulated signal to the EOM from a pattern generator, the exposure to the wafer can be controlled dot-by-dot. Figure 8. 4 shows the dynamic response of the EOM to the input modulation signal. The feeding signal was at 80 MHz. The blue curve is the modulation signal to the EOM. The red curve is the modulated laser output, which is captured by a high speed photo detector. There is a constant time delay of about 3 ns between the input and modulated output.

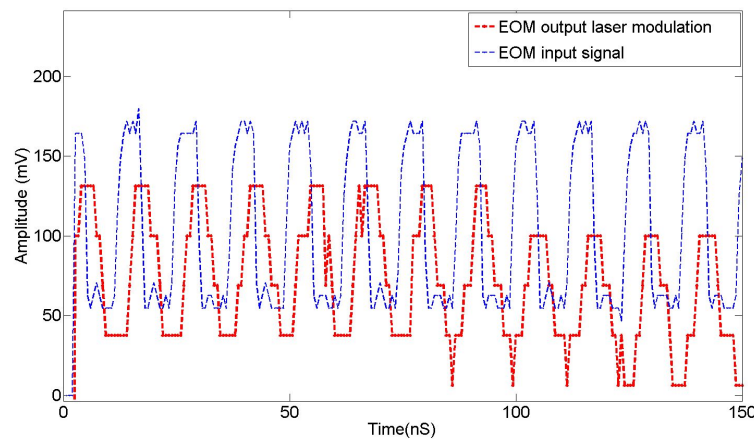


Figure 8. 4 Laser modulation by an EOM. The input and output were both 80 MHz.

The optical writing head is mechanically connected to a motorized linear stage and a carriage. The motorized linear stage (called the z-motor) is installed to adjust the position of the writing head in the direction perpendicular to the disk. Meanwhile, a moving carriage positions the head along radial direction. The main components of the optical head are shown in Figure 8. 5. There is an objective lens inside the optical head to focus light to a plasmonic lens on the air bearing surface of the slider. The objective lens is attached to a high resolution piezo actuator (labeled as the z-actuator) which is widely used for microscope objectives. This z-actuator provides a linear motion perpendicular to the disk surface (z-direction). It is used to compensate the vertical run-out motion of the disk and keep the laser beam well focused onto the plasmonic lens. The z-actuator is mechanically attached to a flexure structure, shown in Figure 8. 6a. Two electrical-piezo actuators are embedded inside the flexure to drive the flexure in the x and y directions. It is able to compensate the drift of the laser beam in both the x and y directions and keeps the beam aligned to the plasmonic lens. The drift of the laser beam usually comes from the misalignment of the optics and thermal expansion of the stage. Two capacity sensors

are installed to monitor the motion of the flexure. The function of the optical writing head is to adjust the objective lens in all x, y and z directions to make the beam well focused and aligned onto the plasmonic lens during the lithography process.

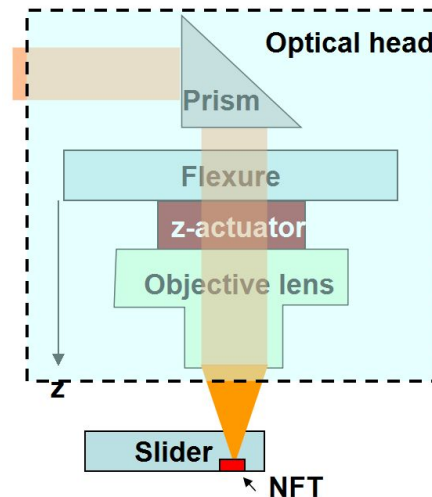


Figure 8. 5 Structure of the optical head

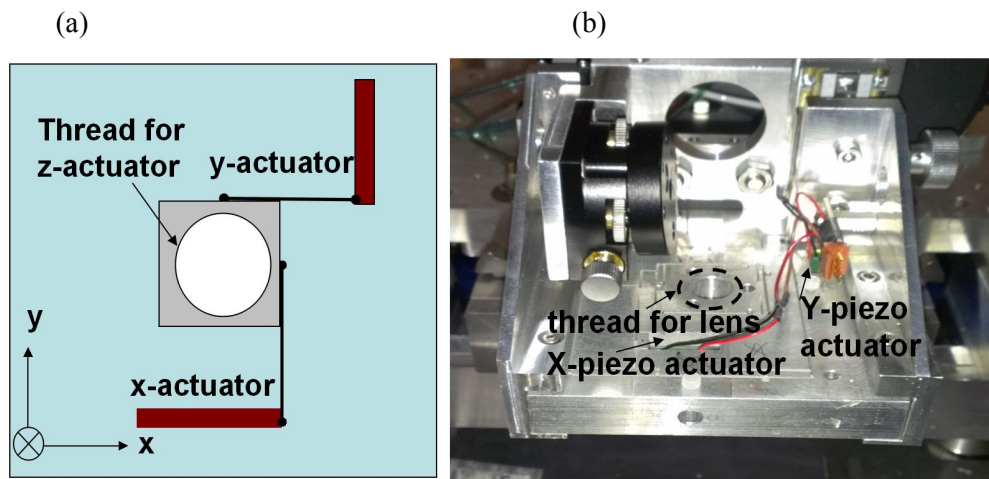


Figure 8. 6 Flexure to assist laser beam alignment to the NFT (a) schematic design of the flexure; (b) photo of the flexure

The air bearing surface design is shown Figure 8. 7 [133]. The numerical simulation showed that the slider flies at around  $20 \pm 2$  nm when the speed is 10 m/s.

Different designs of the plasmonic lens can be fabricated to the surface of the flying slider by some nanolithography technologies, such as a focused ion beam or scanning electron beam lithography. The thermal profile and coupling efficiency depends on the design of the plasmonic lens, as well as the optical and thermal properties of the wafer. A phase change material, which is composed of Te and  $\text{TeO}_x$ , is used as a thermal photoresist. A thin film of the phase change material is deposited onto the glass substrate by use of standard sputtering tools. When the temperature increase of the photoresist film

reaches the threshold temperature, the phase transition occurs. Then the changed material is further selectively etched away, so the lithography pattern is formed. The minimum feature size of the lithography pattern is determined primarily by the thermal profile on the photoresist film. A smaller focus spot from the plasmonic lens is beneficial for reducing the minimum feature size.

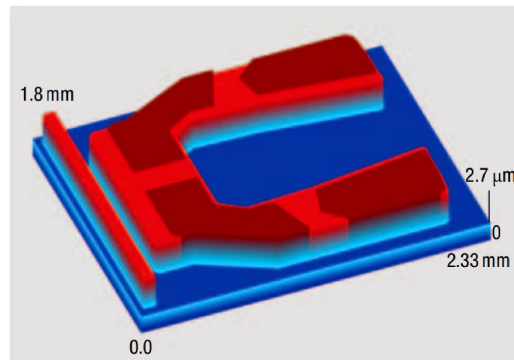


Figure 8. 7 Oblique view of the ABS. The topography is scaled up by a factor of 200 for better illustration

### 8.2.2 Linear stage for radial positioning

A radial positioning carriage is driven by a linear stage to provide a motion of the optical writing head along the radial direction. Combining this with the circumferential motion of the spinning wafer provides a complete two-dimensional lithography writing system.

The linear stage was designed and built at the Center for the Precision Metrology in UNC Charlotte. As shown in Figure 8. 8, the machine is composed of a base that stands on the vibration isolation table, a carriage that is suspended from the base by the air bearings, two vacuum preloaded air bearings that keep the carriage in contact with the shoulder so the motion of the carriage is straight, two electromagnetic motors on both sides of the carriage that can drive the carriage along the radial direction and two Eddy current dampers that are used to make the motion of the carriage smooth.

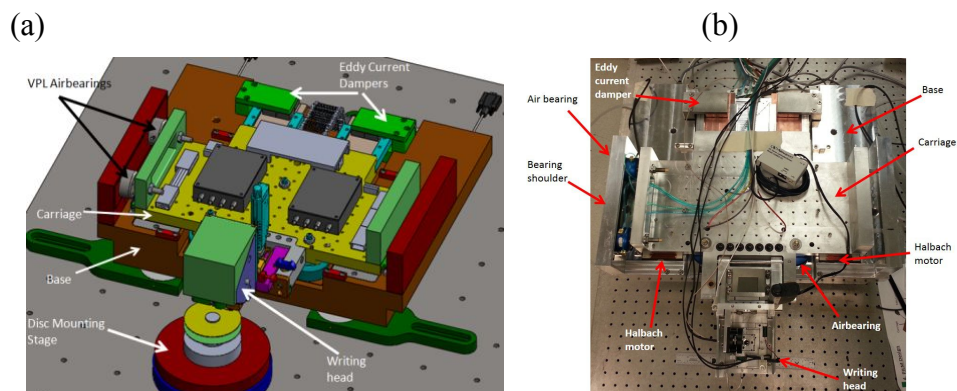


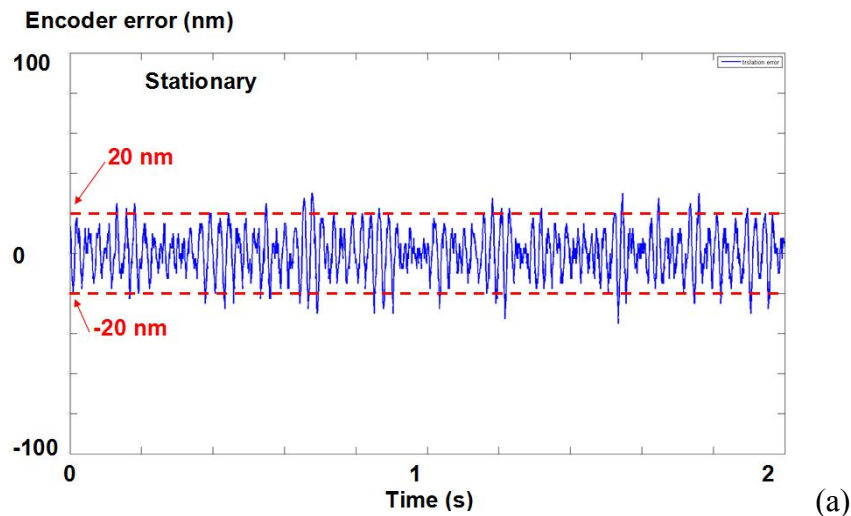
Figure 8. 8 3D design (a) and (b) photo of the linear stage



A high resolution linear encoder scale is embedded in both motors to provide the position information of the carriage. The linear scale has a resolution at 5 nm. The encoder signal is counted by a FPGA real-time target to calculate the position of the carriage. The control algorithm is implemented in the real-time target to give a feedback signal to drive the two motors to follow the desired trajectory.

The position control algorithm was designed by the Mechatronics and Controls Laboratory at the University of California, Los Angeles. There are four basic motion modes for the linear stage. One is the position mode which allows users to move the carriage to any position within the carriage motion stroke at a fixed speed. The second mode is the velocity mode which allows moving the carriage at some constant speed set by the user. The third mode is the trajectory mode. In this mode, the stage follows the trajectory designed by the user. The last mode is the increment mode. A fixed step increment can be performed in this mode. The step size is set by the user.

The position control resolution is determined by the linear encoder resolution and the control algorithm. Figure 8.9 shows the motion of the carriage when the carriage was moved at different speeds for a short period. At a stationary position, the carriage vibrated within 40 nm peak to peak. The shaking of the stage probably came from external disturbances, such as the vibration of the floor and table, acoustic disturbance from the building cooling system, or compressed air fluctuation for the air bearings. When the stage moved at a particular speed, the shaking of the stage became more pronounced than that in a stationary test. The positioning performance was worse when the speed of the stage was higher.



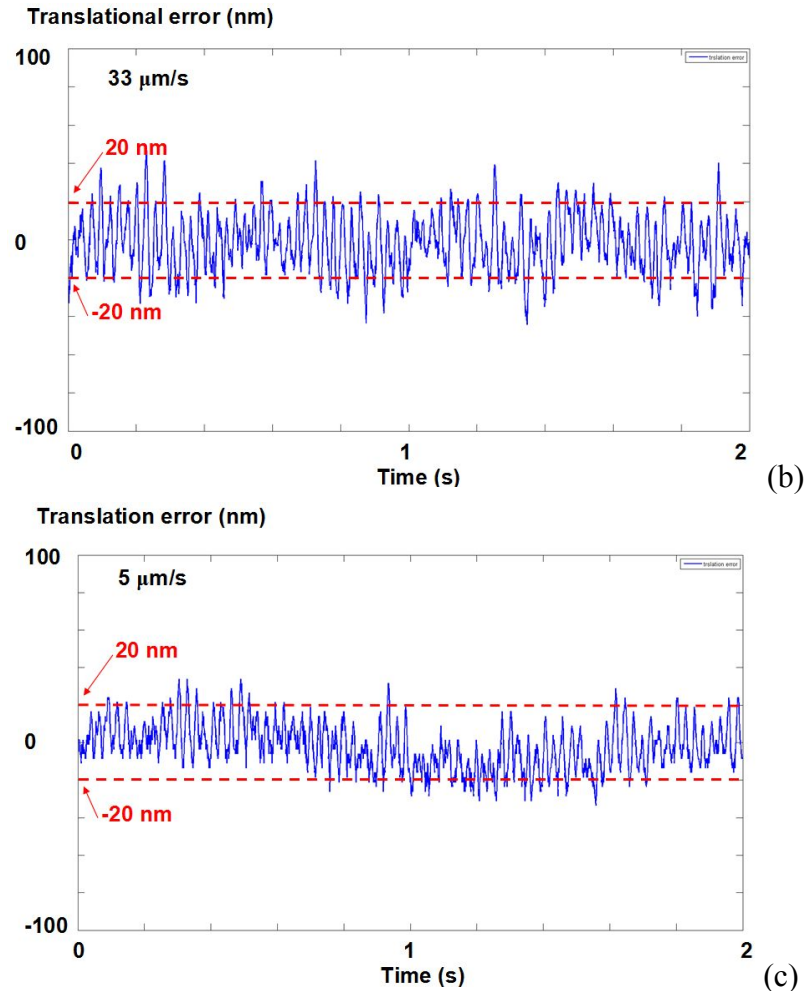


Figure 8.9 Stage positioning error when the stage was moved at different speeds: (a) the stage was stationary; (b) the stage was moved at  $5 \mu\text{m/s}$ ; (c) the stage was moved at  $33 \mu\text{m/s}$ ;

### 8.2.3 Magnetic encoder for circumferential positioning

The circumferential positioning is as important as the radial positioning. A magnetic rotary encoder system was developed at UC Berkeley to provide the high resolution angular position for the rotary spindle [136]. A PMR disk was used as an encoder mask on which the periodic magnetic scales are recorded by a flying magnetic head. The size of the magnetic scale on the magnetic disk can be much smaller than an optical scale. The weak magnetic readback signal from the magnetic scales can be retrieved stably by a magnetic reader which is integrated in the magnetic head. In the current configuration, the resolution of the magnetic encoder is about 2.8 million counts per revolution (CPR), which is higher than that of the usual commercial optical encoder [137] and the magneto-optical technology based rewritable magnetic encoder [138].

This magnetic encoder system has the capability to make in-situ error correction by rewriting the magnetic code disk. It is suitable to assist in the fast patterning of both electron beam lithography and plasmonic lithography machines, which requires high

resolution, high accuracy, high responsiveness and compactness. More details about this magnetic encoder system are given in section 8.3.

### 8.2.4 Pattern generator

A lithography machine should have the capability to convert any user-designed lithography pattern into the real lithography pattern on the wafer. A pattern generator was developed to achieve this pattern conversion. As demonstrated in Figure 8. 10, the logo “CAL” is converted to a binary matrix. This binary matrix is loaded into a pattern generator to generate the modulation signal for the EOM. For example, a gray color “0” means an unexposed pixel on which the laser is turned off, while a highlighted “1” means there is a laser exposure for one pixel. During the writing process, the lithography writing head scans the wafer in the radial direction using the translational motion of the head along the radial direction and in the circumferential direction because of the rotation of the wafer. Based on the writing head position, the pattern generator determines which pixel should be output. By exposing the wafer pixel by pixel, the designed lithography pattern can be finally fabricated on the wafer.

Taking advantage of a field programmable gate array (FPGA), the pattern generator can generate a modulation signal at a rate over 500 MHz based on current capability of the FPGA card. This means that the ideal duration for writing a pixel could be about 2 ns if the bandwidth limit of the EOM is ignored. A faster modulation signal would allow the wafer rotate faster so the throughput could be raised.

In order to enhance the lithography yield, this pattern generator also has the capability to support parallel writing. It is able to generate several laser modulation signals simultaneously and independently. Those modulation signals from the pattern generator can separately control several EOMs and writing heads. More details of the pattern generator are given in the section 8.4.

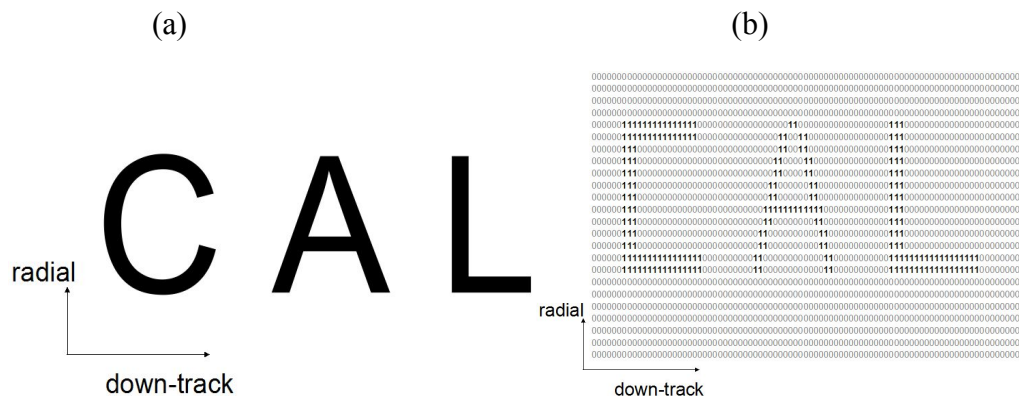


Figure 8. 10 (a) User designed pattern: a “CAL” logo; (b) a binary matrix of the “CAL” logo, used for pattern generator

### 8.2.5 Central control unit (CCU)

The central control unit provides a user graphic interface to help control and monitor the entire lithography process. The CCU is developed based on a labview real-time target.

An operation process flow chart is shown in Figure 8. 11. A homing function should be performed before the lithography starts. The optical head can be loaded by controlling the z-motor in the CCU. Then the slider is load onto the spinning disk. After that, the slider starts to fly at the radius of the home position. The laser alignment can be adjusted to make the beam well aligned and focused to the plasmonic lens by changing the driving voltage for the flexure and z-actuator in the optical writing head. The drift of the alignment during the lithography writing can be compensated by adjusting the flexure as well.

A systematic check is performed to make sure that every component works properly. Then, a trigger signal triggers the pattern generator to initialize the pattern generator. Simultaneously, the linear stage starts to move, and the 2D lithography writing starts. The working status for the linear stage, spindle, and optical writing head is monitored and recorded. If any systematic error occurs, the lithography process will be stopped by blocking the light. Once the lithography writing is finished, the optical writing head is unloaded by controlling the z-motor to move the optical writing head up. Then, the spindle stops and the wafer is unloaded from the spindle for further pattern inspections.

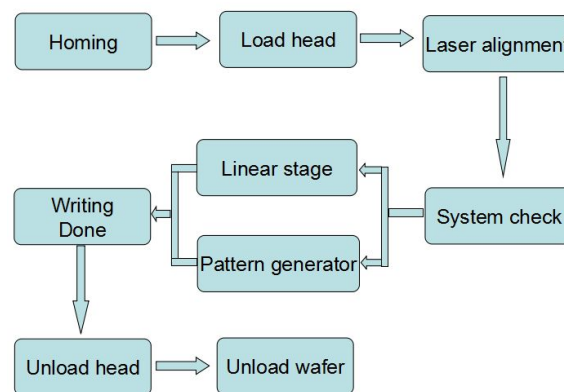


Figure 8. 11 Operation process flow chart for the plasmonic nanolithography machine

## 8.3 Magnetic Rotary Encoder

### 8.3.1 Introduction

In the rotary lithography systems, a rotary encoder for angular positioning is necessary. Two kinds of rotary encoders are widely used. One is an optical encoder that uses an optical code disk and an optical head to get the readback signal. Its resolution relies on the quality of the code disk, disk installation, dynamic response of the optical head and the head detection resolution. An optical encoder is always limited by the

optical diffraction limit. The widely used optical encoder provides a resolution range from hundreds of counts per revolution (CPR) to a couple of million CPR [136]. To implement the optical encoder for the plasmonic nanolithography system, an expensive high resolution optical encoder must be precisely installed.

The second kind of rotary encoder is the magnetic encoder. A magnetic encoder is based on the magnetic readback signal from a magnetic code disk. Some magnetic encoder systems have the capability to also do the magnetic code writing [137]. The magnetic encoder can achieve similar resolution as the optical encoder. The advantage of the magnetic encoder over the optical encoder is that error correction is available for some magnetic encoder systems, in which the code disk can be rewritten.

In this section, a novel high resolution and fast response magnetic rotary encoder system based on a magnetic read/write head and a perpendicular magnetic disk is introduced. The size of the magnetic scale on the magnetic disk can be much smaller than that of the optical scale or the magneto-optical disk. And the weak magnetic readback signal can be retrieved stably by a magnetic reader which is integrated in the magnetic head. In the current configuration, the resolution is about 2.8 million CPR which is higher than the usual commercial optical encoder or the magneto-optical technology based rewritable magnetic encoder. The magnetic encoder system proposed in this work has the capability to do in-situ error correction by rewriting the magnetic code disk. It is suitable to assist in the fast patterning of the electron beam lithography or plasmonic lithography machines, which require high resolution, high accuracy, high responsiveness and compactness.

### 8.3.2 System configuration

A schematic block diagram of the encoder system is shown in Figure 8. 12. An air bearing spindle is used. The rotation speed can be adjusted by the spindle controller. The magnetic encoder disk and lithography sample are both mounted to the main shaft of the spindle and spin together at the same speed.

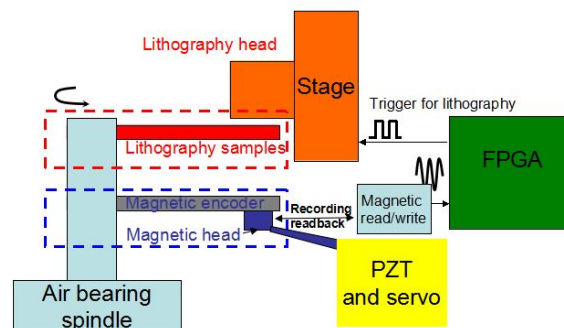


Figure 8. 12 Schematic block diagram of the magnetic encoder system for the plasmonic nanolithography machine

An air bearing spaced magnetic head flies stably over the magnetic encoder disk. A magnetic read/write device is used to write the encoder patterns on the PMR disk and retrieve the readback signal of the encoder patterns. The density of the encoder can be adjusted by tuning the writing frequency by the FPGA (Virtex-5 ML506). Fig 8.13 shows a magnetic force microscope (MFM) image of the magnetic encoders. The bright and dark colors in Figure 8. 13a indicate different polarizations of the magnetic scales. The pitch between two adjacent magnetic scales was about 90 nm, as shown in the profile along a down-track direction. The frequency of the writing signal was 40 MHz. The readback signal had the same frequency at 40 MHz if the spindle speed remained constant.

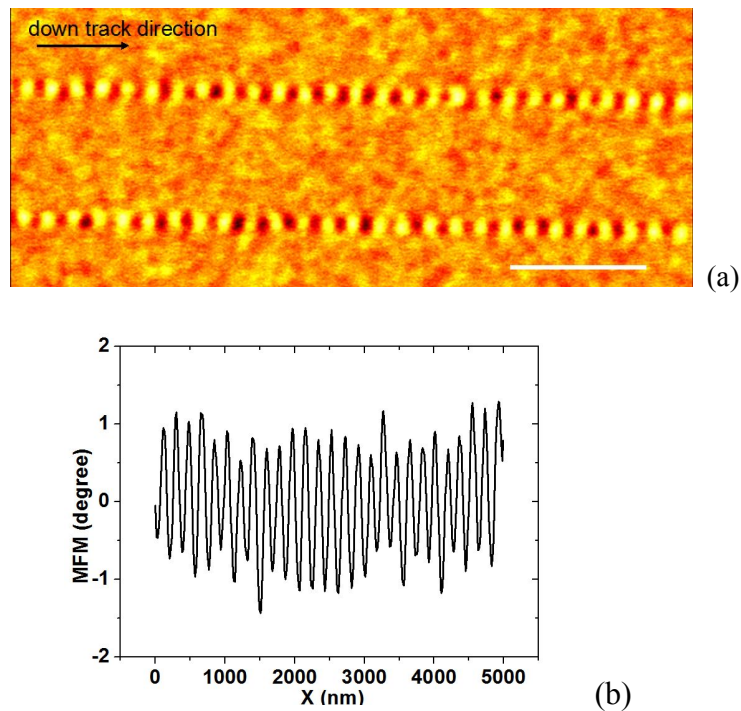


Figure 8. 13 (a) MFM image of two magnetic encoder tracks, the scale bar is 1  $\mu\text{m}$

(b) MFM scanned profile of the bottom magnetic encoder along the down-track direction

However, some encoder measurement errors are introduced if the position of the flying head changes relative to the track center due to the spindle's lateral run-out or other external disturbances. The amplitude of the readback signal becomes too weak if the head flies with a large offset to the track center. In order to make the head fly on the track center and reduce the encoder readback error, a track following servo system was developed.

A structure of interleaved servo sectors and encoder sectors is used for the track following servo system, originated from the servo system in current hard disk drives [140]. Dual-frequency servo bursts are used to code the relative offset of the head to the

center of the track. A FPGA based high speed signal processing module is used to decode the position offset of the head and achieve the in-situ head position control [141, 142].

Figure 8. 14 shows the structure of the interleaved servo sectors and encoder sectors. There are 1024 servo sectors and 1024 encoder sectors for a complete magnetic track on the disk. The length of a servo sector is a few microns, while that of an encoder sector is more than 200 microns. There is a blank zone between every servo and encoder sector. There is no magnetic information in the blank zone so the readback signal on the blank zone is weaker than that of the servo and encoder sectors. When the magnetic head flies over the servo sectors, a trigger signal is generated to begin the calculation of the head offset from the track center from the readback spectrum. Then an electrical piezo stage drives the head back to compensate the offset so that the head can continue to fly along the center of the track when it enters the blank zone and encoder sector. When the servo sector ends and the head enters the blank zone, a counter in the FPGA becomes initialized and waits for the encoder signal. The amplitude of the readback signal on the blank zone is not large enough to trigger the counter in the FPGA. But as the head enters the encoder sector, the pulse of the readback signal from the encoder sector triggers the counter and the angular information is obtained from the counter.

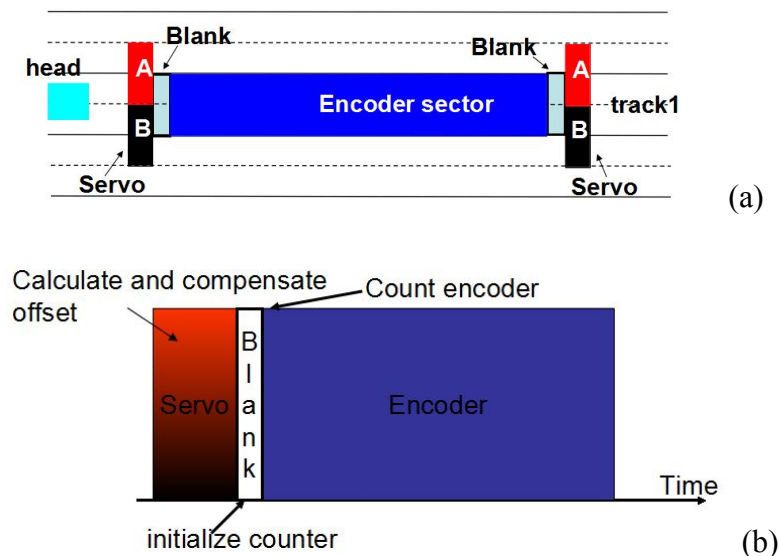


Figure 8. 14 Servo scheme for the magnetic encoder system (a) interleaved structure of dual-frequency servo sector and encoder sector (b) Process sequence of the servo and encoder counter

### 8.3.3 FPGA based servo system for track following

Modern HDDs use an embedded servo format in which the servo information is interleaved with the data sectors on the disk. The head senses the servo signal and extracts the magnetic head position relative to the track center, which is called the position error signal (PES). The position decoding algorithm depends on the position

coding method. Figure 8. 15 shows the typical interleaved servo sectors and the PES bursts pattern used for position encoding. Usually there are a few hundred servo sectors for an entire track which provide a PES sampling rate of about several kHz. The PES bursts consist of 4 or more magnetic blocks, staggered along the down-track direction. The burst pattern, when scanned by the magnetic reader in the magnetic head, gives an analog waveform consisting of a series of voltage pulses with alternating polarity at a specified frequency. The magnitudes of the waveforms for the 4 bursts are determined by the offset between the reader and each burst center, so the position information is encoded into these 4 readback waveforms. When the head has positive, zero or negative offsets, the readback signals of the four bursts are different, as shown in Figure 8. 15b. The length of each burst is about 5  $\mu\text{m}$ , which is necessary to get a good performance considering the speed of the signal processing and device response. The PES servo bursts occupy about 5% of a track in total.

The magnitudes of the bursts' waveforms in the servo sectors are measured quantitatively by using peak detection or area detection methods to calculate the PES. The PES quality is highly sensitive to the quality of the pre-recorded servo pattern during the manufacturing. It requires expensive external systems for positioning the write head to write the staggered servo patterns, and frequent calibrations are required.

Recently, the dual-frequency servo burst method was proposed [143, 144, 145] to replace the traditional servo bursts for the extraction of the PES. As shown in Figure 8. 15c and d, only two servo bursts are used to decode the position. The spectrum of the servo bursts readback signal varies with the offset of the magnetic head reader from the track center. Al-Mamun et. al [141] stated that the dual frequency servo scheme would reduce the servo overhead and relatively increase the PES sampling frequency. Thus, it could improve the performance of the servo controller and finally help increase the track density. However, only theoretical simulations and offline experimental results were shown in that work. Wong et. al [142] built a PC-based servo control system using the dual-frequency servo scheme. Its performance relied on the speed of the PC and the operating system. In their study, the sampling rate was limited to 15 kHz. Guzik et. al [143] used analog devices such as band pass filters and comparators to demodulate the dual frequency servo. Here, a high-speed servo system based on the FPGA is introduced to implement the dual frequency decoding method and track following controller for HDDs.



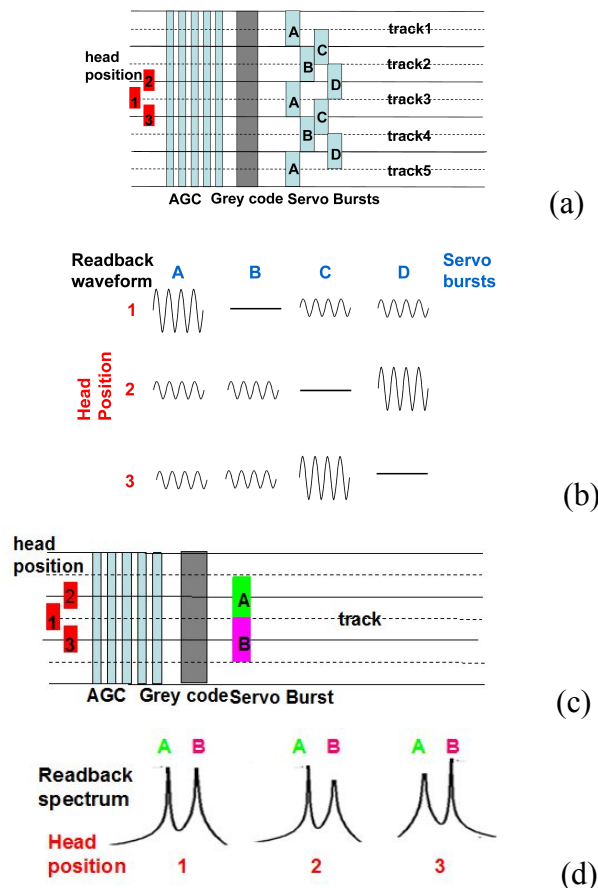


Figure 8. 15 Servo systems in the HDDs showing a typical conventional servo sector; magnetic readback signal of the conventional servo bursts when the head has different offsets from the track center; proposed dual frequency servo bursts; spectrum of the readback signal for dual frequency servo bursts.

The FPGA is an integrated circuit designed to be configured by the user or designer after manufacturing, hence the name "field-programmable". The FPGA shows great potential for real-time hardware computation and emulation [146], real-time control [147], data processing [148], signal synthesis [149], communication [150] and other applications in industrial controllers [151]. The FPGA can be a good choice for the implementation of the position decoding and the control algorithm because of its portability, ability to be reconfigured and rapid parallel processing.

Here we demonstrate a 25.6K samples per second sampling rate for the PES, which is comparable to the PES sampling rate in current HDDs. The maximum sampling rate of the PES can be upgraded to 130 kHz by taking full advantage of the FPGA. The real-time controller is able to compensate the major disturbance induced by spindle run-out using the repetitive control algorithm. The performance of the controller can verify the feasibility of the FPGA based servo system for HDDs.

As shown in Figure 8. 16, the complete system consists of two major parts. The first one is the in-situ PES generation system that gets the real-time position offset of the magnetic head. It includes a spin-stand, a magnetic reading and writing (R/W) device to record and sense the servo sector, a high resolution piezo stage to move the head back on track along the radial direction, a high speed analog-to-digital converter (ADC) from Analog Device (AD9481) to capture the data and transmit it to a FPGA board from Xilinx (Virtex-5 ML506) and a digital-to-analog converter (DAC) to convert the digital PES from the FPGA to an analog format. The digital FPGA board is the core of the in-situ PES generation system, and the decoding algorithm is programmed using very-high-speed integrated circuits (VHSIC) hardware description language (VHDL). Then, the program is downloaded into the FPGA for execution. The DAC and ADC are introduced here to make the digital FPGA board compatible with some other peripheral analog devices. The second part is the real-time control system, which consists of a Labview FPGA card from National Instruments (NI PCI-7833R) and a piezo stage amplifier. The control algorithm can be easily and quickly implemented in the real-time target. The controller output is amplified by the amplifier to drive the piezo stage to do the compensation.

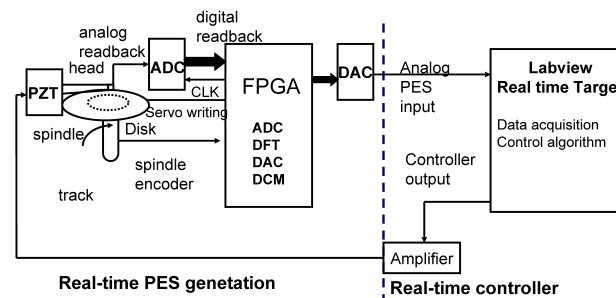


Figure 8. 16 Configuration of the FPGA based servo system for HDDs.

The FPGA outputs the signal to the magnetic R/W device to write the servo tracks on the disk. The readback signal is amplified by the R/W device, and captured by the ADC at a sampling rate of 200MHz. Then, the digitized readback signal is transmitted to the FPGA for spectrum analysis. The 200 MHz clock is used to drive the ADC and process the result in the FPGA, synchronizing them using the digital clock management (DCM) technology in the FPGA. The spectrum is extracted in the FPGA by performing the 540 points DFT. The 8 bits digital PES data is obtained from the DFT spectrum results. Then the digital PES data is converted to an analog format signal by a DAC in the FPGA. In this system, the maximum PES sampling rate is 25.6 kHz if 1024 servo sectors are recorded to the disk and the spindle runs at 1500 RPM. The analog PES is used as the input for the track following controller in the real-time control system. The control output is computed in the real-time control target, and then it is amplified by the voltage amplifier to drive the piezo stage.

Figure 8. 17 shows a schematic plot of the PES generation system as well as the timing of the decoding process. The DCM provides different clock frequencies (CLK) to drive different processes and devices including the DAC, ADC and the R/W device. The data pipelines for the ADC, DFT and DAC are synchronized and initialized by the process management module. The process management module sends out a trigger (data\_input) to the DAC to start acquisition of the data at 200 MHz beginning with the dual frequency servo bursts. The digital data feeds into the pipeline and is stored in a 1024 by 8 bits buffer, which is used to increase the robustness of the program. Once the first data becomes valid in the buffer, the process management initializes the DFT module. Then the whole data frame of 540 data points goes to the DFT module in sequence from the buffer. Right after the whole frame has been transferred to the DFT module, the Fourier transformation starts to calculate the spectrum using radix-2, -3, -4 and -5 butterfly operations. The spectrum results are then ready to be accessed after the transformation is finished. There is a major latency between the first point of the signal data acquisition and the output of the spectrum, represented by d1 in Figure 8. 17b. This delay can be attributed to the data transmission within the buffer, DFT module and the Fourier transformation calculation. Once the magnitudes at about 27 MHz and 33 MHz are obtained from the spectrum, the PES calculation process is enabled by the trigger (DFT\_done) to calculate the PES from these two magnitudes. The PES calculation leads to a second delay, as represented by d2 in the timing diagram. After the calculation process is completed, the PES is stored in another buffer. Then the process management activates the PES conversion process by the trigger designated as “calculation\_done”. The PES conversion process converts the digital PES to an analog signal and outputs the analog PES at the output pins of the DAC board. This conversion process leads to the third delay represented by d3. The “conversion\_done” signal is switched to “high” after the conversion is finished. The current analog PES is then latched until the next servo burst sector comes. The buffers and trigger signals are reset to prepare for the next servo burst and decoding process.

All three delays have been measured by a digitizer card (Innovative Integration X5-GSPS) at 1.5 Giga samples per second, as shown in Figure 8. 17c. d1 took about 6.1  $\mu\text{s}$ , d2 was 0.9  $\mu\text{s}$  and d3 was 0.7  $\mu\text{s}$ . Thus the total delay was about 7.7  $\mu\text{s}$ , indicating that the bandwidth of the PES decoding can be as high as 130 kHz in the current configuration. The bandwidth can be further increased if a clock faster than 200 MHz for data acquisition and transformation is employed.

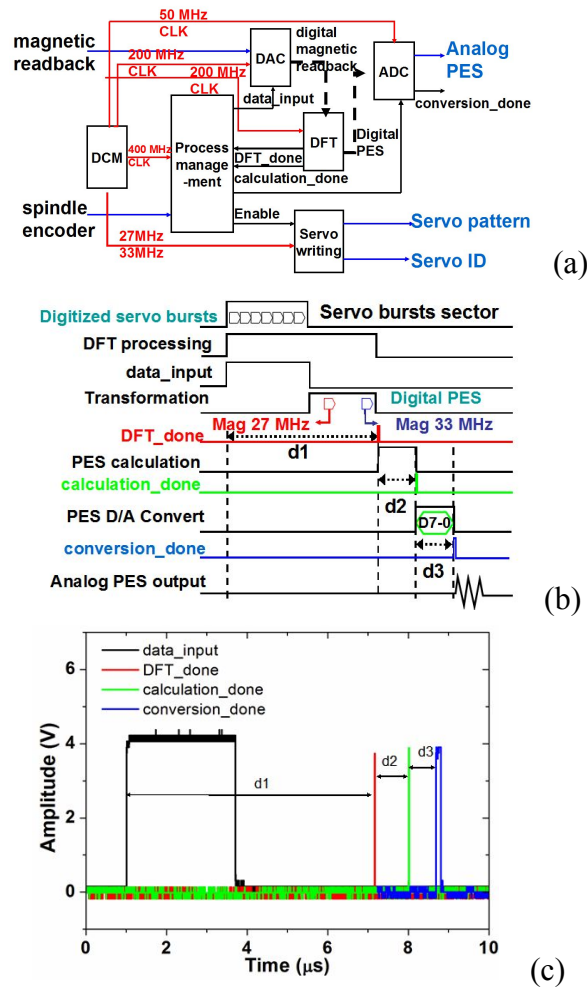


Figure 8.17 (a) Schematic plot of the FPGA; (b) Timing diagram for the decoding process; (c) Delay measurements for the decoding process

### 8.3.4. Servo and encoder writing and reading

The dual frequency servo burst patterns explained in section 8.3.3 were written on a 3.5 inch magnetic disk using the system described above. The second servo track was written adjacent to the first servo track and the distance between the two track centers was about 200 nm. This distance was controlled by the high resolution piezo stage.

Figure 8.18a shows the magnetic readback signal when the head was flying near the middle of the servo and encoder sectors. The readback signal was captured by a high speed data acquisition card (Innovative Integration X5-GSPS) at 1.5 GHz. The readback signal of the servo sector is a convolution of two signals with different frequencies, as shown in Figure 8.18b. The spectrum is shown in Figure 8.18c. Both the 27 MHz and 33 MHz servo burst tracks made contributions to the readback signal so there were two peaks near these two frequencies in the spectrum. The magnitudes of the peaks were slightly different because the magnetic field strengths were different for these two tracks. There were also some subtle peaks at the harmonic frequencies.

The readback signal of the blank zone was much weaker than that of the servo and encoder sectors. The readback signal of the encoder sector was a single tone signal, as indicated by the spectrum of the encoder readback (Figure 8. 18f).

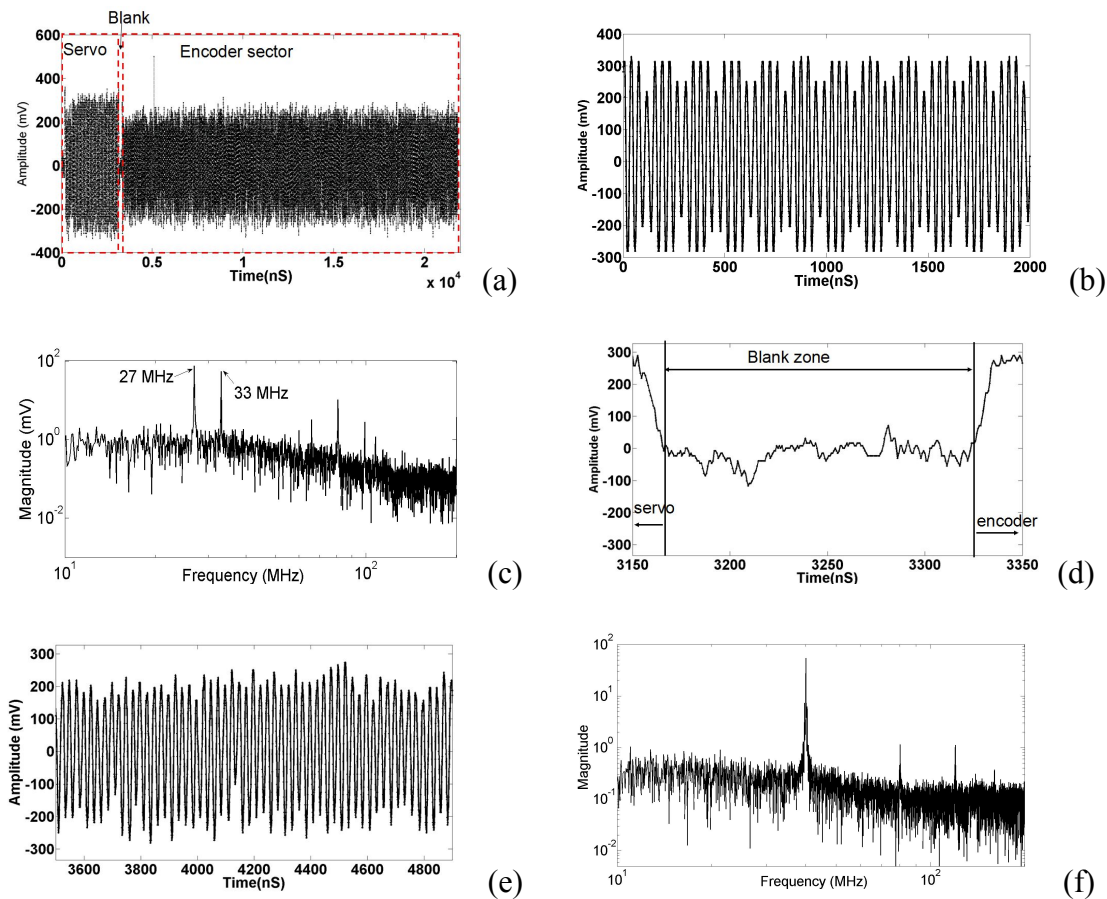


Figure 8. 18 Measured readback signal of the written tracks (a) Readback signal of the interleaved servo, blank and encoder sectors, (b) readback signal of the servo sector, (c) frequency spectrum of the servo sector readback (d) readback signal of the blank zone, (e) readback signal of the encoder sector (f) frequency spectrum of the encoder sector readback

The high resolution piezo stage can precisely move the magnetic head along the off-track direction. The relationships between the piezo stage voltage input, displacement and velocity were calibrated by a laser doppler vibrometer (LDV) and optical displacement sensor before beginning the PES calibration.

The PES calibration and measurements were conducted following the steps outlined below:

(1) Mark one of the servo burst sectors as the calibration sector. The FPGA provides a trigger signal to synchronize the following signal acquisition process when the magnetic head arrives at this sector every revolution.

(2) Move the head along the radial direction with constant speed (125 nm/s) by the high resolution piezo stage. The spindle spins at 1500 RPM. So the head moves 5 nm every revolution when it arrives at the calibration sector.

(3) Capture the raw magnetic readback signal and PES signal of this calibration sector for every revolution. The voltage driving the piezo stage is recorded.

The PES is defined here as the difference between the magnitudes of the two frequency components. The displacement is calculated from the piezo stage voltage input based on the piezo stage calibration results. Then the correlation between the PES and the displacement is calibrated, as shown in Figure 8. 19. When the magnetic head is near the middle of the two servo tracks, the relationship between the PES and the offset is almost linear. The inset linear regression shows that the slope of the PES is 2.62 (-+0.03) mV/nm. However, when the head is close to the center of each servo track, the linearity deteriorated and saturation occurs because the size of the magnetic sensor (reader) is somewhat smaller than that of the track pitch. Great care should be taken when designing the controller to deal with the nonlinearity, such as using composite nonlinear-feedback control [152].

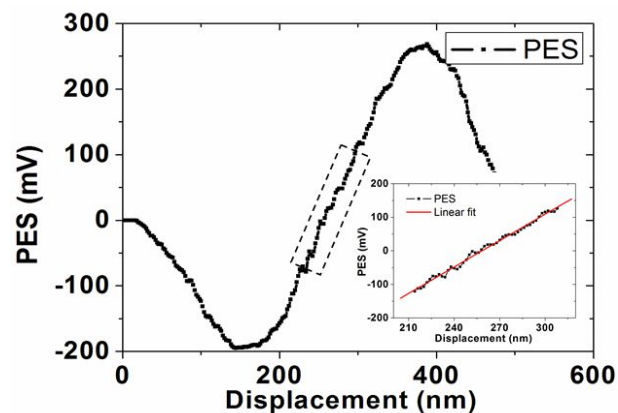


Figure 8. 19 Relationship between PES and the displacement.

### 8.3.5. Track following controller and its implementation

In HDDs the standard deviation of the PES ( $\sigma_{\text{PES}}$ ) is a parameter used to quantify the performance of the track following controller. The design goal of the controller is to reduce the  $\sigma_{\text{PES}}$  to about 10% of the track pitch, which gives a good reading and writing performance in HDDs [153]. In our system, the track pitch is about 200 nm, so a good controller should be able to maintain the  $\sigma$  offset of the magnetic head within 20 nm. The major disturbance in the system is the spindle run-out, which depends on the spindle spin speed. When the spindle rotates at 1500 RPM, the major run-out is 25 Hz, and there are some other significant harmonic components as well.

The frequency response of the piezo stage with the head cartridge plant has been measured by the LDV, as shown in Figure 8. 20. The plant model had 2 weak structural resonances. The first resonance was close to 500 Hz.

Figure 8. 21 shows the structure of the real-time control system. The in-situ PES generation system (FPGA 1) outputs the real-time PES to the real-time controller (Labview FPGA). The control algorithm is designed and implemented in the Labview FPGA card.

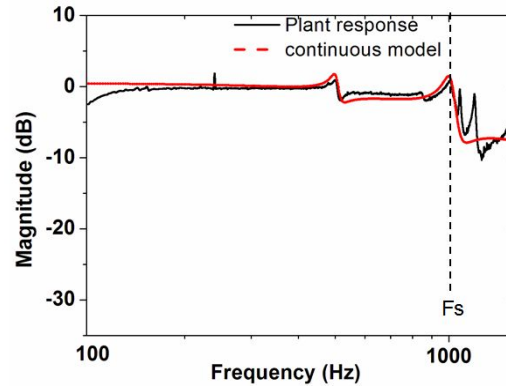


Figure 8. 20 Frequency response and identified model of the piezo stage with head cartridge

Here, a simple PID and repetitive controller [154, 155] was designed and implemented to reject those repeatable spindle run-out components. The well-tuned PID controller is designed to stabilize the closed loop system. It also has appropriate bandwidth to reject the non-repetitive run-out disturbance, such as stage thermal drift. To reject the repeatable spindle run-out, which is the major disturbance in our system, we adopt a repetitive controller. The repetitive controller runs on top of the PID controller to cancel the repeatable run-out. These two control algorithms are chosen because they are relatively easy and fast to implement and tune. Meanwhile the performance can meet our design requirements. The combination of these two controllers can help to verify the feasibility of this FPGA based servo system.

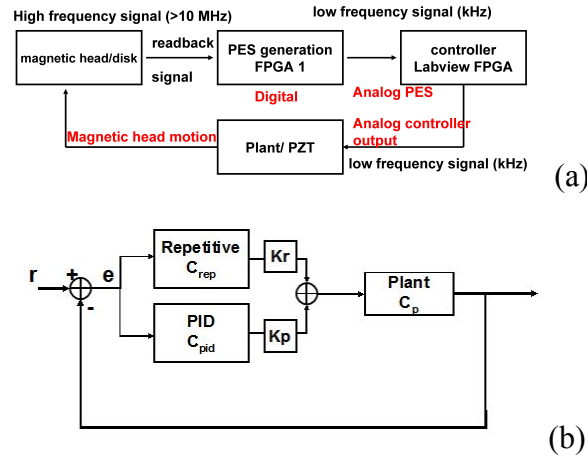


Figure 8. 21 Schematic diagram of the HDD servo controller based on the FPGA. (a) real-time control system structure; (b) combination of PID and repetitive controller in the Labview FPGA.

The bandwidth of the Labview card is limited to 1 kHz, which is lower than the PES generation rate. However, this bandwidth is high enough to deal with the low frequency (25 Hz and its harmonics) spindle run-out. Furthermore, the bandwidth of the controller can be extended to several tens of kHz by using a DSP board.

The identified transfer function of the piezo stage plant model in the Laplace domain was

$$P(s) = \frac{4651 s^4 + 3.99 \times 10^6 s^3 + 2.55 \times 10^{11} s^2 + 7.17 \times 10^{13} s + 2.13 \times 10^{18}}{s^5 + 5663 s^4 + 5.40 \times 10^7 s^3 + 2.67 \times 10^{11} s^2 + 4.67 \times 10^{14} s + 2.06 \times 10^{18}}$$

The plant model is discretized when it is implemented in the Labview FPGA at 1 kHz.

The repetitive controller in this work is described as:

$$C_{rep} = \frac{z^{-N}}{1 - Q(z^{-1})z^{-N}}$$

The delay chain  $N$  in the repetitive controller is determined by the spindle run-out frequency and the controller sampling rate. When the sampling rate is 1 kHz and the basic frequency of the spindle run-out is 25 Hz,  $N$  is set to be 40.  $Q$  is a zero-phase low-pass filter used to enhance the robustness of the repetitive controller. In this work,  $Q$  is selected to be:

$$Q(z^{-1}) = (0.25z + 0.5 + 0.25z^{-1})^2$$



Figure 8. 22 shows the sensitivity function plot. The plot indicates that this controller is able to effectively reject the periodic disturbance at 25 Hz as well as its harmonics. So the PES can be reduced when the loop is closed.

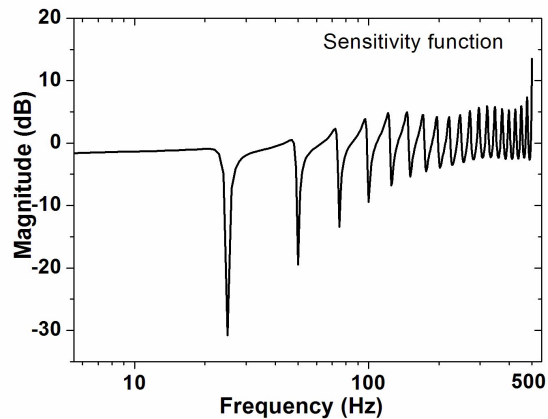


Figure 8. 22 Sensitivity function of the servo system.

Figure 8. 23 shows the PES in the time domain with the controller turned on and off. When the servo controller is activated, the standard deviation of the PES is reduced to 11.5 mV compared to 60 mV when the controller is off. Using the PES calibration results, we can convert the PES to displacement. The standard deviation of the magnetic head motion offset to the reference track center was attenuated from 23 nm to 4.3 nm after the controller was turned on. Obviously, the controller performance was better than the desired requirement, which is to control the offset of the magnetic head within 20 nm. The spectrum of the PES (Figure 8. 23b) illuminates the strong attenuation of the disturbance at the fundamental and harmonic frequencies. The first 4 repeatable run-out components (25 Hz, 50 Hz, 75 Hz and 100 Hz) were reduced by 21 dB, 18 dB, 17 dB and 13 dB, respectively.

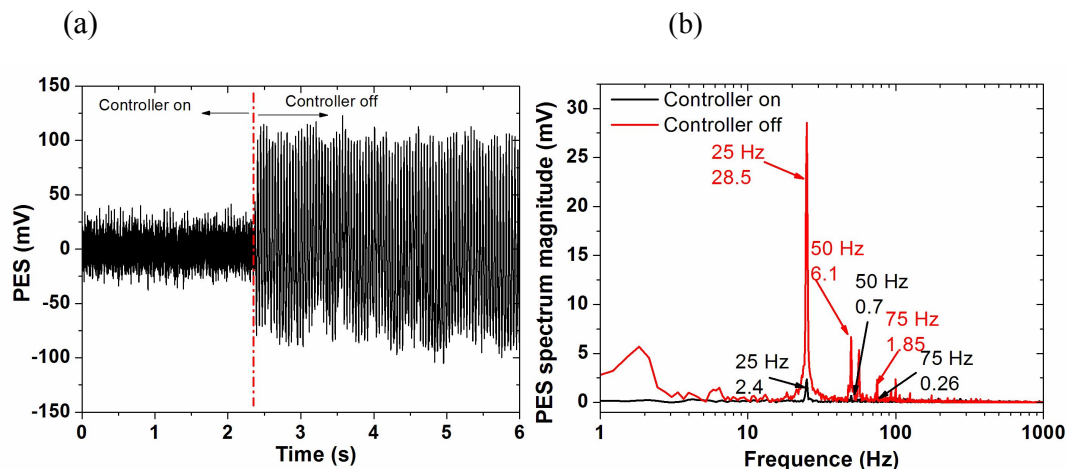


Figure 8. 23 (a) PES history when the controller is switched on and off; (b) spectrum of PES

It has been shown that the track-following servo can work effectively to attenuate the run-out disturbance and make the magnetic head fly above the center of the magnetic track. A stable encoder readback signal can be achieved with this effective track following servo system.

### 8.3.6 Digitized encoder and timing jitter

After a stable analog readback signal of the encoder is obtained with the assistance of the FPGA based track following servo system, this analog readback signal is then further digitized by use of a voltage comparator attached directly to the FPGA card. The digitized encoder signal is transmitted to the FPGA card. The angular information is retrieved by counting the rising or falling edges of the digital encoder signal. Considering that the pitch between two adjacent bits is 90 nm and the radius of the encoder track is 42 mm, the angular resolution of this magnetic rotary encoder can reach about 2  $\mu\text{rad}$ . A delay locked loop (DLL) is implemented in the FPGA to stabilize the encoder trigger and the DLL can also generate a differential encoder signal to achieve even higher resolution. Figure 8. 24 shows the magnetic encoder readback signal (offset by 200 mV) and the locked digital signal from the FPGA. It shows that the FPGA was triggered by every rising edge of the analog readback signal from the encoder sector.

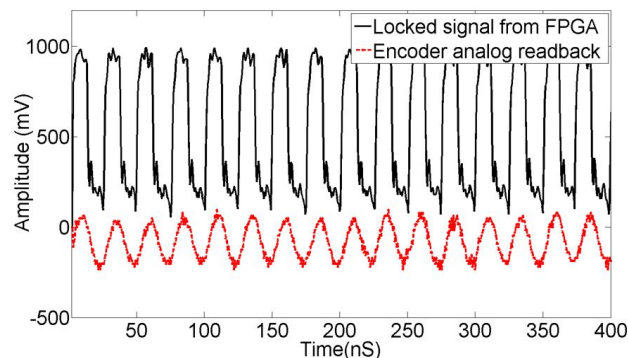


Figure 8. 24 Analog readback signal from the magnetic encoder and digitized signal from the FPGA.

Further signal jitter analysis was performed for the locked signal from the FPGA. The jitter analysis was performed in the procedure described below:

1. Measure the duration (rising edge to rising edge) of one clock cycle
2. Wait a random number of clock cycles
3. Repeat the above steps 10,000 times
4. Compute the mean, standard deviation ( $\sigma$ ), and the peak-to-peak values from the 10,000 samples

The histogram of the period variation is plotted in Figure 8. 25. The mean value of the period between two adjacent rising edges of the digital signal is 25 ns. The standard

deviation of the period jitter is 0.7 ns, which corresponded to about 5 nm root-mean square jitter of the position along the circumferential direction and 0.1  $\mu\text{rad}$  angular jitter.

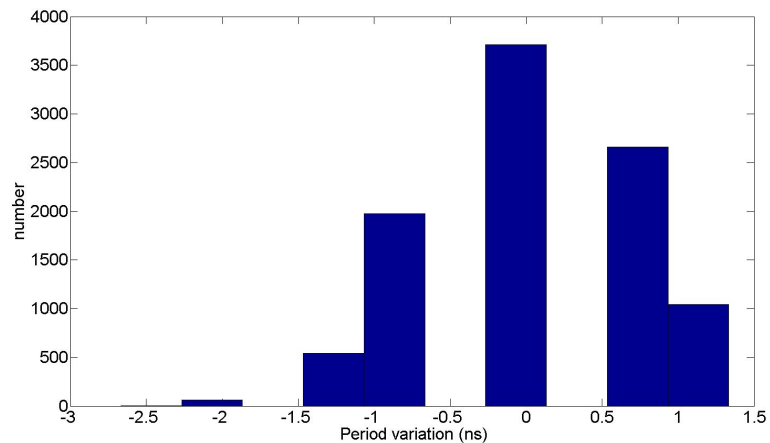


Figure 8. 25 Histogram of the period variation of the magnetic encoder

The performance of the magnetic encoder was compared with the optical encoder. A starting point on the disk was defined in the magnetic encoder and optical encoder. When the slider flew over this start point, the high speed DAQ started to record the magnetic encoder and the optical encoder readback signal simultaneously. This signal acquisition was performed for several revolutions. The relative time delay between the first magnetic encoder pulse and optical encoder pulse was analyzed, as shown in Figure 8. 26. The readback of the magnetic encoder at different revolutions matched, indicating a good repeatability of the magnetic encoder. However, the optical encoder showed a time uncertainty of about 20 ns. This time uncertainty was quite reasonable because the optical encoder edge detection is limited by its diffraction limit. The optical diffraction limit was about  $\sim 100$  nm while the spindle linear speed was about 5 m/s, so the time uncertainty of the optical encoder could be about 20 ns.

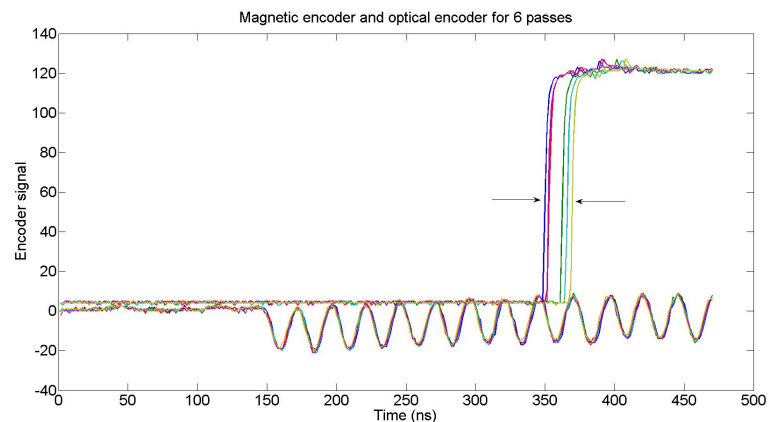


Figure 8. 26 Time uncertainty of the magnetic encoder and optical encoder in 6 revolutions' readback

In summary, an ultra-dense magnetic rotary encoder system is introduced. Interleaved servo and encoder sectors were recorded on a perpendicular magnetic recording disk. A magnetic read/write head flew above the magnetic track to get the readback signal of the magnetic track. The readback signal from the servo sector was used to decode the position offset of the head to the track center. A FPGA based track following servo was developed and implemented to allow the head fly above the encoder track center. The readback signal of the encoder was stable when the track following servo worked effectively. A FPGA was programmed to accomplish the high speed signal processing for the stable encoder signal. The angular position of the spinning disk was obtained by counting the pulse of the encoder signal at a rate of several tens of Mega Hertz.

In the current configuration, this encoder system reaches a resolution at 2.8 million CPR. The pitch between two encoder counts is 90 nm, corresponding to about  $2 \mu\text{rad}$  angular resolution. The standard deviation of the angular jitter is about  $0.1 \mu\text{rad}$ . This magnetic encoder shows less time uncertainty compared to the traditional optical encoder. Higher resolution can be achieved by using a denser magnetic encoder or a delay lock loop to differentiate the phase between two encoder counts.

## **8.4 Pattern generator**

The pattern generator is a critical component for the plasmonic nanolithography machine to be able to convert the user designed lithography pattern to the wafer pattern at high speed. Meanwhile, if multiple NFTs and optical writing heads are used in parallel for one wafer writing, the writing time can be reduced further. However, the high-speed pixel by pixel and multiple head parallel writing style of this lithography machine imposes stringent signal processing requirements for highly accurate pattern placement.

We developed a FPGA-based high speed parallel pattern generator to satisfy the requirements of this plasmonic lithography machine. The FPGA has the capability to process several signals in parallel within a couple of nanoseconds. Also, this FPGA based pattern generator can be easily cloned, integrated, and scaled-up for massive implementations. As shown in Figure 8. 27, several pattern generators can be integrated together to form a pattern generator array. Each pattern generator inside the array can work independently and generate a modulation signal to control each EOM, respectively.

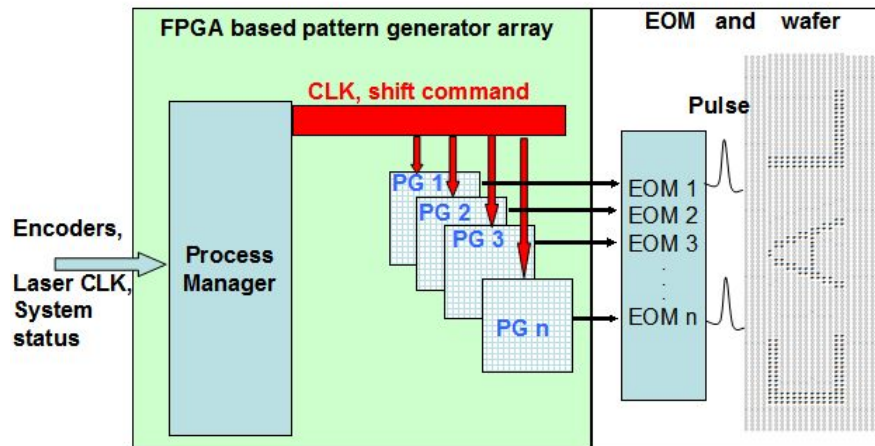


Figure 8. 27 Schematic drawing of a pattern generator array based on a FPGA card

In the current pattern generator, the user designed lithography patterns are converted to a binary matrix, and this matrix is loaded into the memory of a FPGA card. This massive arbitrary pattern matrix could be loaded and stored inside the FPGA if the storage space allows. Dynamically reloading of the matrix is possible by accessing the memory using some third-party software, such as Adept from Digilent [156].

The pattern generator extracts the modulation signals from the binary matrix one by one, according to the position of the lithography head. The row of the matrix indicates the circumferential direction writing on the wafer. Once the spindle finishes a full revolution, a complete row is fully extracted out. Then, the pattern generator shifts to the next row and starts to extract the elements in the next row one by one.

The shift of the elements in the matrix is achieved by a function called a finite-state machine (FSM). The FSM is a robust technology to perform a predetermined sequence of events depending on an order of these events. The FSM is driven by a master clock at 320 MHz in the current configuration. The shift is also synchronized with the magnetic encoder, which corresponds to the circumferential angular position.

Figure 8. 28 shows the FSM flow chart. After the lithography machine CCU finishes the status check, the pattern generator is reset and initialized. The reset and initialization is performed within one driving clock cycle at 320 MHz. Then the FSM enters a state called idle 1 and waits for the index of a revolution and the magnetic encoder. The index signal is high when a new revolution starts. After that, the first rising edge of the magnetic encoder drives the FSM to a state called output. In the output state, the FSM extracts a few elements one by one from the current row of the pattern binary matrix. The number of elements that are extracted can be set by the user. In the current configuration, the default number is 2 when the magnetic encoder is at 40 MHz. The shift and extraction of the elements can be finished in one clock cycle at 320 MHz. The FSM stays in the output state until all of the two elements have been output. After that, the FSM enters idle

2, at which state the FSM waits for the magnetic encoder to become low. Once the falling edge of the magnetic encoder comes, the FSM re-enters the output state to extract another two elements. In a complete revolution, a complete row of the pattern matrix is fully extracted, and then FSM gets into the shift state. In the shift state, the FSM moves to the first element of the next row. After one clock signal, the FSM moves into a wait state. If there are still some rows that have not been extracted from the binary pattern matrix, the FSM moves to the idle 1 state and prepares for a new cycle to extract the elements one by one from the current row for a new revolution. If all the elements of the binary matrix have been extracted, the FSM moves to a stop state. In this case, the whole lithography writing has been completed. During the entire lithography process, if any error occurs, the signal of the status check from the CCU becomes low and the lithography process is stopped. The lithography process can be recovered if the status recovers to normal.

The output from the pattern generator was simulated by a hardware simulator (Modelsim) for the FPGA. As shown in Figure 8. 29, two elements of "10" were extracted for every rising and failing edge of the magnetic encoder. The first element "1" was output after one clock's delay because the shift of the state from idle to output in the FSM took one clock signal. The experimental pattern output and the magnetic encoder signal were captured, as shown in Figure 8. 30. It verifies that two elements "10" were generated after every rising and falling edge of the magnetic encoder.

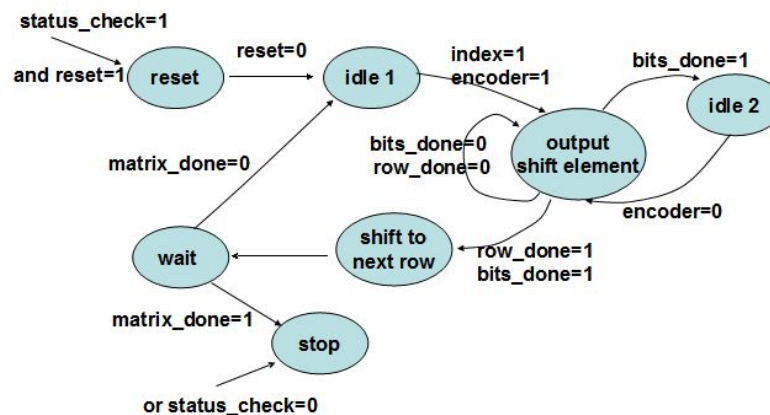


Figure 8. 28 The flow chart of a finite state machine in the FPGA

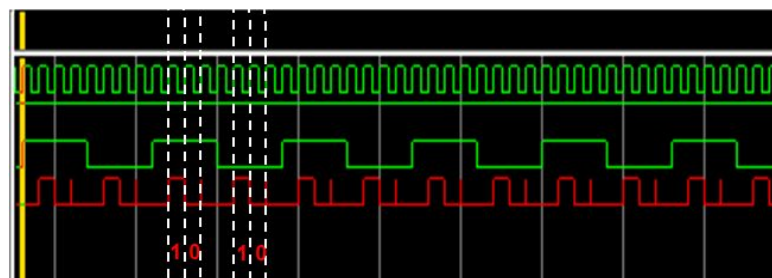


Figure 8. 29 Simulated pattern output from Modelsim.

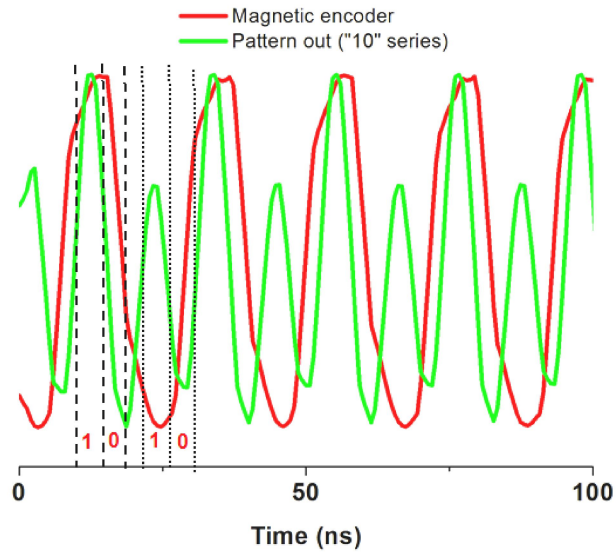


Figure 8. 30 Measured pattern output and magnetic encoder by a high speed DAQ.

It can be seen from Figure 8. 30 that the pattern generation is synchronized with the magnetic encoders. There is some time delay between the pattern output and trigger events due to the shift process of the FSM. These time delays between the pattern output and rising edge or falling edge were not exactly the same. The uncertainty of the time delay could cause an additional stitching error of the lithography patterns. The statistics over 2000 delays show that the average delay was around 3.2 ns which was about one clock cycle when the clock was 320 MHz. The standard deviation of the delay time was 0.5 ns.

The pattern generator has been tested by use of the free laser beam exposure in the lithography machine. Figure 8. 31 shows an optical image of the "CAL" logo. This logo was exposed in the lithography machine. The lithography results verified that the pattern generator can successfully convert the user designed patterns to a real lithography pattern on the wafer.

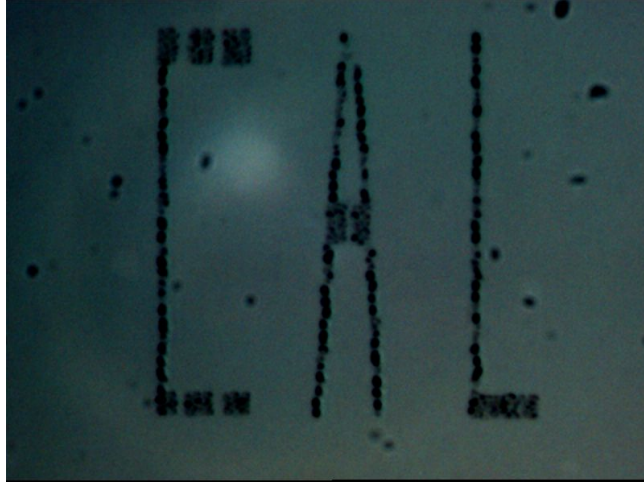


Figure 8. 31 Optical microscope image of the “CAL” logo written by lithography machine for the demonstration of pattern generator.

In this section, a FPGA based pattern generator was introduced for the plasmonic nanolithography machine. The pattern generator can convert any user-designed lithography pattern to a binary matrix stored in the memory of the FPGA. Triggered by the magnetic encoder, the pattern generator produced a signal in a clock period at 320 MHz to modulate the laser pulse based on the binary matrix. The wafer was exposed one pixel by one pixel during the scanning.

Multiple pattern generators can be combined together to form an array to control multiple plasmonic lens in parallel. The parallel writing capability allows this lithography machine to reach a higher throughput.

## 8.5 Summary

In this chapter, a plasmonic nanolithography concept was introduced to assist the master template fabrication for the BPM disks. A plasmonic lens was carried by a flying head. The laser was focused onto the plasmonic lens and further focused to a small area on the wafer. The focused spot size can be much smaller than the optical diffraction limit. A small area of  $\sim 20$  nm on the surface of the wafer was heated by laser illuminated the plasmonic lens. The slider scanned the wafer from the outer to inner radius with a linear circumferential speed at  $\sim 10$  m/s. A high lithography throughput was achieved at such a high scan speed. A further scale down of the minimum feature can be achieved with some optimized design of the plasmonic lens.

A plasmonic nanolithography machine was designed and controlled precisely after the proof of the plasmonic lithography concept. A linear motor with two linear scales was installed in the system to provide an accurate radial motion control for the optical writing head. A rotary magnetic encoder system was implemented in this nanolithography machine to get high angular resolution. To get a stable magnetic encoder readback, a



FPGA based servo system was developed to make the magnetic head fly above the center of the encoders track. In the current configuration, the resolution of the linear scales along the radial direction was 5 nm and the resolution of the rotary magnetic encoder was about 2.8 million CPR. The jitter of the magnetic encoder was about 0.1  $\mu$ rad.

A FPGA based pattern generator was developed and used to convert any user designed lithography patterns to the modulation of laser pulses, thus the pattern can be transferred to the wafer. The lithography results verified the effectiveness of the pattern generator. Multiple pattern generators can be combined together to control several writing heads in parallel for higher throughput.

## Chapter 9 Conclusions and Future Work

### 9.1 Conclusion

The HDI for a HAMR system has been systematically studied, including the degradation of the lubricant layer, the carbon overcoats, the failure of the NFT and fly-height modulation of the HAMR slider. In order to perform the study, a HAMR testbed (named “Cal stage”) was built and implemented. Continuous improvements have been conducted for the Cal stage to study different aspects of HAMR systems, such as HDI failure, heat transfer inside a nanometer scale gap, back-heating effect of the NFT, etc.

Thermal depletion of a Z-tetraol lubricant on 3.5 inch aluminum substrate PMR disks was obtained under various free laser beam heating conditions and also NFT heating conditions. The results can be summarized as follow:

(1) The lubricant depletion depth increased as the number of exposure repetitions increased, following a power law of the form  $At^b$ .  $A$  is a parameter that depends on the heating condition while  $b$  is a constant that is independent of the heating condition.  $A$  is larger at higher exposure powers and lower spindle speeds, which is determined by the thermal gradient and maximum temperature. Larger  $A$  indicates a more severe lubricant depletion.

(2) The lubricant started to reflow back into the depleted region after the heating source was removed. The reflow behaved in a similar way regardless of the initial lubricant depletion. The reflow rate was higher at the beginning and then became slower. 80% of the lubricant depletion was recovered after 20 minutes for the Z-tetraol lubricant used in this study.

(3) The lubricant depletion under the NFT heating was much more severe than under the free laser beam heating due to the larger thermal gradient induced by NFT heating.

(4) The thermal gradient, temperature, and heating duration played important roles for the thermal depletion of the lubricant. The lubricant depletion rate was higher at the beginning of the thermal heating.

(5) The thermal gradient in a HAMR system is several orders higher than that in the free laser beam heating condition. However, the duration of heating in HAMR is several orders shorter. Considering that the fastest lubricant depletion occurs at the very beginning of the laser heating, the thermal depletion in HAMR could still be quite severe.

The thermal degradation of the carbon overcoats was also investigated. A few conclusions were obtained from this study.

(1) A conductive-AFM was used to get the perpendicular conductivity or resistivity of the ultra-thin amorphous carbon (a-C) films and thereby help to characterize the electrical properties of a-C films. The resistance image of the film provided some qualitative information of the sp<sup>2</sup> and sp<sup>3</sup> hybridization inside the a-C film. A surface sp<sup>2</sup>-rich layer existed in the 3.6 nm thick a-C film, leading to a conductivity 7 times larger as compared with other thicker a-C films. The C-AFM could also help to identify the conductivity change of a-C film after laser heating, which was induced by the sp<sup>3</sup> to sp<sup>2</sup> conversion due to thermal annealing.

(2) The surface reflectivity was changed on a 26 Å thick a-C film on a 2.5 inch glass substrate disk when the temperature of the a-C film was raised to over 200 °C for a few seconds by a temperature controlled electric heater. The surface became smoother after the thermal annealing if the temperature was lower than 300 °C due to the stress relief. When the temperature was raised beyond 300 °C, the roughness became larger.

(3) The surface reflectivity started to change when the laser power density was increased to 19.5 mW/μm<sup>2</sup> in the free laser beam tests for a 26 Å thick a-C film on a 2.5 inch glass substrate disk. The reflectivity changed more when the track was exposed for more repetitions. The surface topography started to show change when the power density was increased higher than 19.5 mW/μm<sup>2</sup>. A bump-like deformation was found at the exposed track and the height of the bump increased in a logarithmic way as the repetitions increased. At the highest power density of 35.7 mW/μm<sup>2</sup>, material ablation occurred and the material in the exposed track was removed.

(4) There were only some small changes in the surface reflectivity under the NFT heating because the temperature was not high enough. The carbon film degradation mainly depends on the temperature and heating duration, which was different from lubricant depletion.

(5) It is likely that the carbon film on the disk surface in a HAMR drive can still survive if each bit is written only a few times, because the heating duration will be on the order of ~ ns during a one time writing process. However, the carbon film on the slider side can suffer from serious thermal degradation because it is heated much longer.

The failure of the NFT structure in HAMR-like systems was studied. Three mechanisms of failure were described: geometry change-induced optical failure, material failure, and contact-induced NFT wear failure. A NFT array was fabricated on the ABS of a flying slider. The NFTs were exposed at various laser powers when the slider flew over

a disk. At the power of 35 mW exposure, some tiny particles/debris were found trapped in and around the NFT structure. Those accumulated particles could result in the slider crashing and other instability for the HDI. When the power was at 43 mW, significant thermal deformation around the NFT structure was found. In this situation, the NFT was not able to function well to focus the light to a desired spot. Moreover, the minimum fly-height was reduced, so the chance of head-disk contact increased. At even higher power, the metal film of the NFT was removed due to laser ablation. The existence of the NFT can make the change of the HDI more severe due to the enhancement effect of the light intensity by the NFT.

To increase the reliability of the NFT structure, a two-stage heating scheme was proposed. It separates the traditional NFT heating into two steps. In this scheme, the thermal load to the NFT could be reduced. An optical-thermal-mechanical model was created to verify the feasibility of the two-stage heating scheme. The simulation results showed that the two-stage heating scheme was able to heat an area of a magnetic bit to the Curie point. The magnetic switching field and thermal gradient around this heating area was close to that in a conventional HAMR system with a single NFT heating, indicating that the writing performance in the two-stage heating scheme was comparable to that of the conventional HAMR system.

A plasmonic nanolithography machine was introduced for the fabrication of a master template for the BMP nanoimprint. A plasmonic lens carried by a flying slider was used to focus light to a small area at  $\sim 20$  nm scale on the disk surface, which was coated by a phase change material. The phase was changed by the laser exposure and a lithography pattern was formed after the development. The slider was moved in the radial direction with the optical writing head while the disk was rotated in order to get a complete two-dimensional writing. The radial motion of the slider was controlled precisely by a high resolution linear motor with an embedded linear scale. The angular position was provided by a rotary magnetic encoder system with an angular jitter at about  $0.1 \mu\text{rad}$ . A pattern generator was developed to convert any user-designed lithography pattern to the modulation of the laser pulse and help to generate the pattern on the wafer. This pattern generator can be easily integrated and combined with a pattern generator array to increase the throughput significantly. A lithography logo "CAL" was demonstrated experimentally by use of this pattern generator.

## 9.2 Future work

HAMR has a high potential to continue the increase of data storage areal density for magnetic recording. However, as a new emerging technology, there are still some new physical phenomena that need to be better understood. Some of the conventional designs are expected to be changed and optimized further as well. As discussed in Chapter 1, HAMR is pursuing targets at a length scale of a few nanometers and time scale of a few

nanoseconds. Faster response and the smaller scale provide challenges for most of the current research. In addition, there are some new phenomena occurring at such scales which do not show up in the macro scales. For example, heat transfer can be more pronounced due to the near field radiation and phonon tunneling, as well as the material thermal deformation that occurs in nanoseconds. Actually, the HAMR technology itself provides a very powerful platform for us to study the new physics under those unique scales.

Some more work is being performed or is being suggested in the future for study of the unique aspects of HAMR systems based on our current Cal stage or after some further updates of the stage.

(1) It will be very important to get the temperature distribution and history for both the free laser beam and NFT heating modes. A method based on magnetization decay works effectively for the temperature calibration for the free laser beam heating. However, this has not been demonstrated for the NFT heating mode because the NFT failed before we were able to see the demagnetization. Temperature calibration based on the phase change material could be a better way for the NFT heating as was demonstrated in the plasmonic nanolithography.

(2) Lubricant depletion and degradation of the disk carbon film under the NFT heating can be studied further when a more reliable slider with the NFT structure (HAMR head) becomes available. The current study of the NFT heating in this thesis was limited because of the very short lifetime of the NFT.

(3) The deformation or diffusion of the metal of the NFT structure needs to be further studied. It is important to see how that mechanical change affects the optical performance of the NFT structure. It is also important to see how the material responds to a cyclic thermal load and  $\sim 100$  atm pressure loads.

(4) The local mechanical deformation on the disk is also very important as the fly-height drops to less than 2 nm. It was found from a recent back-heating study that the disk thermal deformation could a reduction in the touch-down power. The deformation height could be a fraction of a nanometer to a couple of nanometers, and it is recoverable. This deformation reduces the fly-height and increases the chance of the head-disk contact.

(5) It has not been confirmed so far whether the current AE contact detection method can work effectively if there is some weak contact between the tiny thermal protrusion around the NFT and disk under a hot environment.

(6) The disk is heated up to near the Curie point. The temperature of the slider is supposed to be lower than that on the disk, and disk back-heating could happen between the NFT and disk. The gap between the minimum point of the slider and disk is lower than 5 nm. At this small gap, the near field radiation and

phonon tunneling could be much more pronounced than that in the macroscale. Therefore, the heat transfer coefficient between the disk and slider could be higher than what is expected from the classic air bearing cooling model [157]. Heat transfer in the head-disk interface and the back-heating effect are extremely important to understand for getting a reliable NFT in HAMR systems. Some studies of the back heating and heat transfer at  $\sim$  nm gap have been performed but not concluded in this thesis. Further updates and reports by other students will present the results regarding this topic.

## Bibliography

---

- [1] Cisco white paper, "The Zettabyte Era: Trends and Analysis", 2014,  
Online: [http://www.cisco.com/c/en/us/solutions/collateral/service-provider/visual-networking-index-vni/VNI\\_Hyperconnectivity\\_WP.html](http://www.cisco.com/c/en/us/solutions/collateral/service-provider/visual-networking-index-vni/VNI_Hyperconnectivity_WP.html)
- [2] Hoyt and T. Coughlin, "iNEMI Mass Storage Roadmap Technology 382 Working Groups Report," Aug. 30, 2013. Online: <http://www.383inemi.org>.
- [3] T. Coughlin and Edward Grochowski, "Years of Destiny: HDD Capital Spending and Technology Developments from 2012-2016," June 2012, IEEE Magnetics Society Santa Clara Valley Chapter Meeting Presentation Summary,  
Online: [http://ewh.ieee.org/r6/scv/mag/MtgSum/Meeting2012\\_06.html](http://ewh.ieee.org/r6/scv/mag/MtgSum/Meeting2012_06.html)
- [4] IBM Archives, "IBM 350 disk storage unit,"  
Online: [http://www-03.ibm.com/ibm/history/exhibits/storage/storage\\_350.html](http://www-03.ibm.com/ibm/history/exhibits/storage/storage_350.html)
- [5] IBM Archives, "IBM 3340 direct access storage facility,"  
Online: [http://www-03.ibm.com/ibm/history/exhibits/storage/storage\\_3340.html](http://www-03.ibm.com/ibm/history/exhibits/storage/storage_3340.html)
- [6] Online resource:  
[http://www.computerhistory.org/groups/storagesig/media/docs/DS\\_Seagate%20ST-506.pdf](http://www.computerhistory.org/groups/storagesig/media/docs/DS_Seagate%20ST-506.pdf)
- [7] Online resources from IBM research:  
<http://www.research.ibm.com/research/gmr.html>
- [8] Wood, Roger, Yimin Hsu, and Marilee Schultz. "Perpendicular magnetic recording technology." Hitachi Global Storage Technologies, Technical Library, White Paper, 27th December (2007).
- [9] S. Iwasaki and K. Takemura, "An analysis for the circular mode of magnetization in short wavelength recording," IEEE Trans. Magn. 11, 1173 (1975).
- [10] S. Iwasaki and Y. Nakamura, "The magnetic field distribution of a perpendicular recording head," IEEE Trans. Magn. 14, 436 (1978)
- [11] Richter, H. J. "The transition from longitudinal to perpendicular recording," Journal of Physics D: Applied Physics 40.9 (2007):
- [12] Inamura, V. Isatake Kaitsu V. Ryosaku, V. Junzo Toda, and V. Toshihiko Morita. "Ultra high density perpendicular magnetic recording technologies." Fujitsu Sci. Tech. J 42.1 (2006): 122-130
- [13] Weller, D.; Moser, Andreas, "Thermal effect limits in ultrahigh-density magnetic recording," Magnetics, IEEE Transactions on, vol.35, no.6, pp.4423,4439, Nov 1999
- [14] Marchon, Bruno, and Terry Olson. "Magnetic spacing trends: from LMR to PMR and beyond." Magnetics, IEEE Transactions on 45.10 (2009): 3608-3611.
- [15] Ambekar, Rohit, Vineet Gupta, and David B. Bogy. "Experimental and numerical investigation of dynamic instability in the head disk interface at proximity." Journal of tribology 127.3 (2005): 530-536.

- 
- [16] "Thermal Fly-height Control (TFC) Technology in HGST Hard Disk Drives." Hitachi Global Storage Technologies, Technical Library, White Paper, Nov. (2007).
- [17] Shiramatsu, Toshiya, Masayuki Kurita, Kouji Miyake, Mike Suk, Satoshi Ohki, Hideaki Tanaka, and Shozo Saegusa. "Drive integration of active flying-height control slider with micro thermal actuator." *Magnetics, IEEE Transactions on* 42, no. 10 (2006): 2513-2515.
- [18] Chen, Yung-Kan, Jinglin Zheng, and David B. Bogy. "Light contact and surfing state dynamics of air bearing sliders in hard disk drives." *Applied Physics Letters* 100.24 (2012): 243104.
- [19] Canchi, Sripathi Vangipuram, and David B. Bogy. "Thermal fly-height control slider instability and dynamics at touchdown: explanations using nonlinear systems theory." *Journal of tribology* 133.2 (2011): 021902.
- [20] PIRAMANAYAGAM, S. N. "Perpendicular recording media for hard disk drives." *Journal of Applied Physics* 102.1 (2007): 011301.
- [21] Kuroda, Atsuko, Yasutaka Nishida, Atsushi Nakamura, Kiwamu Tanahashi, Hisashi Takano, Shinji Narishige, Hajime Aoi, and Yoshihisa Nakamura. "Thermal decay estimation of perpendicular magnetic recording." *Journal of magnetism and magnetic materials* 235, no. 1 (2001): 25-29.
- [22] Thiele, Jan-Ulrich, Kevin R. Coffey, M. F. Toney, J. A. Hedstrom, and A. J. Kellock. "Temperature dependent magnetic properties of highly chemically ordered Fe<sub>55-x</sub>Ni<sub>x</sub>Pt<sub>45</sub>-L<sub>10</sub> films." *Journal of applied physics* 91, no. 10 (2002): 6595-6600.
- [23] Lyberatos, A., and J. Hohlfeld. "Model of thermal erasure in neighboring tracks during thermomagnetic writing." *Journal of applied physics* 95.4 (2004): 1949-1957.
- [24] Batra, Sharat, Jonathan D. Hannay, Hong Zhou, and Jason S. Goldberg. "Investigations of perpendicular write head design for 1 Tb/in<sup>2</sup>." *Magnetics, IEEE Transactions on* 40, no. 1 (2004): 319-325.
- [25] Challener, W. A., Chubing Peng, A. V. Itagi, D. Karns, Wei Peng, Yingguo Peng, XiaoMin Yang et al. "Heat-assisted magnetic recording by a near-field transducer with efficient optical energy transfer." *Nature photonics* 3, no. 4 (2009): 220-224.
- [26] Stipe, Barry C., Timothy C. Strand, Chie C. Poon, Hamid Balamane, Thomas D. Boone, Jordan A. Katine, Jui-Lung Li et al. "Magnetic recording at 1.5 Pb m<sup>2</sup> using an integrated plasmonic antenna." *Nature Photonics* 4, no. 7 (2010): 484-488.
- [27] White, Robert L.; Newt, R.M.H.; Pease, R. Fabian W, "Patterned media: a viable route to 50 Gbit/in<sup>2</sup> and up for magnetic recording?," *Magnetics, IEEE Transactions on* , vol.33, no.1, pp.990,995, Jan 1997
- [28] Terris, B. D., and T. Thomson. "Nanofabricated and self-assembled magnetic structures as data storage media." *Journal of physics D: Applied physics* 38.12 (2005): R199.
- [29] Kryder, Mark H., Edward C. Gage, Terry W. McDaniel, William A. Challener, Robert E. Rottmayer, Ganping Ju, Yiao-Tee Hsia, and M. Fatih Erden. "Heat assisted magnetic recording." *Proceedings of the IEEE* 96, no. 11 (2008): 1810-1835
- [30] "Density Multiplication and Improved Lithography by Directed Block Copolymer Assembly for Patterned Media at 1Tbit/in<sup>2</sup> and Beyond," Hitachi Global Storage Technologies, Technical Library, White Paper, December 2012.



---

[31] McDaniel, Terry W. "Ultimate limits to thermally assisted magnetic recording." *Journal of Physics: Condensed Matter* 17.7 (2005): R315.

[32] Marchon, Bruno. "Thin-Film Media Lubricants: Structure, Characterization, and Performance." *Developments in Data Storage: Materials Perspective*, 144 (2011).

[33] Choong, Allen Poh Wei, S. N. Piramanayagam, and Thomas YF Liew. "Overcoat Materials for Magnetic Recording Media." *Developments in Data Storage: Materials Perspective* (2011): 167.

[34] Marrs, C. D., W. N. Faith, J. H. Dancy, and J. O. Porteus, "Pulsed laser-induced damage of metals at 492 nm." *Applied Optics*, vol. 21, no. 22, pp 4063-4066, Nov. 1982.

[35] Schreck, Erhard, Dongbo Li, Sripathi V. Canchi, Lidu Huang, Gurinder P. Singh, Bruno Marchon, Hans J. Richter, Barry Stipe, and Matteo Staffaroni. "Thermal Aspects and Static/Dynamic Protrusion Behaviors in Heat-Assisted Magnetic Recording." *Magnetics, IEEE Transactions on* 50, no. 3 (2014): 126-131.

[36] Li, Dongbo, Matteo Staffaroni, Erhard Schreck, and Barry Stipe. "A New AFM-Based Technique to Detect the NFT Protrusion on HAMR Head." *Magnetics, IEEE Transactions on* 49, no. 7 (2013): 3576-3579.

[37] Zhou, Nan, Xianfan Xu, Aaron T. Hammack, Barry C. Stipe, Kaizhong Gao, Werner Scholz, and Edward C. Gage. "Plasmonic near-field transducer for heat-assisted magnetic recording." *Nanophotonics* 3, no. 3 (2014): 141-155.

[38] Malloy, Matt, and Lloyd C. Litt. "Technology review and assessment of nanoimprint lithography for semiconductor and patterned media manufacturing." *Journal of Micro/Nanolithography, MEMS, and MOEMS* 10.3 (2011): 032001-032001.

[39] "ITRS Roadmap 2013",

Online available: <http://www.itrs.net/Links/2013ITRS/Home2013.htm>

[40] Tagawa, Norio, Hiroshi Tani, and Kenji Ueda., "Experimental investigation of local temperature increase in disk surfaces of hard disk drives due to laser heating during thermally assisted magnetic recording." *Tribology Letters*, vol. 44, no.1, pp.81-87, Oct. 2011

[41] Lee, Sungae, Shahrukh Niazi, and Chang-Dong Yeo, "The Change in Surface Properties of Magnetic Recording Media Under Pulsed Laser Application." *Tribology Letters*, vol. 47, no. 1, pp.57-65, July 2012.

[42] Paul M. Jones, Julius Hohlfeld, Joachim Ahner, Christopher L. Platt, and Huan Tang. "Carbon Overcoat Loss From the Surface of a Heat Assisted Magnetic Storage Disk due to Laser Irradiation." *ASME 2013 Conference on Information Storage and Processing Systems*, June, 2013, Santa Clara, CA, US.

[43] Yamada, Noboru; Ohno, Eiji; Nishiuchi, Kenichi; Akahira, Nobuo; Takao, Masatoshi, "Rapid - phase transitions of GeTe - Sb<sub>2</sub>Te<sub>3</sub> pseudobinary amorphous thin films for an optical disk memory," *Journal of Applied Physics* , vol.69, no.5, pp.2849,2856, Mar 1991.

[44] Thurber, Mark C., Frédéric Grisch, and Ronald K. Hanson, "Temperature imaging with single-and dual-wavelength acetone planar laser-induced fluorescence." *Optics letters*, vol. 22, no. 4, pp. 251-253 Feb. 1997.

---

[45] Shaomin Xiong; Bogy, D.B., "Investigation of the Local Temperature Increase for Heat Assisted Magnetic Recording (HAMR)," *Magnetics, IEEE Transactions on* , vol.50, no.4, pp.1,6, April 2014

[46] Knight, Brian R., James A. Bain, and T. E. Schlesinger., "Magnetic decay at elevated temperature relevant to heat-assisted magnetic recording." *Magnetics, IEEE Transactions on*, vol. 45, no. 2, pp 883-888, Feb. 2009

[47] Lyberatos, A.; Guslienko, K. Yu, "Thermal stability of the magnetization following thermomagnetic writing in perpendicular media," *Journal of Applied Physics* , vol.94, no.2, pp.1119,1129, Jul 2003

[48] Bair Budaev and David B. Bogy, "On the applications of the Fluctuation-Dissipation theorem to nanoscale radiative heat transfer," CML blue report, January 2013

[49] Narayanaswamy, Arvind, Sheng Shen, Lu Hu, Xiaoyuan Chen, and Gang Chen. "Breakdown of the Planck blackbody radiation law at nanoscale gaps." *Applied Physics A* 96, no. 2 (2009): 357-362.

[50] Shimizu, Yuki, Junguo Xu, Hidekazu Kohira, Masayuki Kurita, Toshiya Shiramatsu, and Masaru Furukawa. "Nano-scale defect mapping on a magnetic disk surface using a contact sensor." *Magnetics, IEEE Transactions on* 47, no. 10 (2011): 3426-3432.

[51] Xu, Junguo, Yuki Shimizu, Masaru Furukawa, Jianhua Li, Yuichiro Sano, Toshiya Shiramatsu, Yuichi Aoki, Hiroyuki Matsumoto, Kenji Kuroki, and Hidekazu Kohira. "Contact/Clearance Sensor for HDI Subnanometer Regime." *Magnetics, IEEE Transactions on* 50, no. 3 (2014): 114-118.

[52] Marchon, Bruno, "Lubricant Design Attributes for Subnanometer Head-Disk Clearance," *Magnetics, IEEE Transactions on*, vol.45, no.2, pp.872,876, Feb. 2009

[53] Shaomin Xiong; Bogy, D.B., "Experimental Study of Head-Disk Interface in Heat-Assisted Magnetic Recording," *Magnetics, IEEE Transactions on* , 50(3), 148-154 (2014)

[54] Dahl, Joanna Bechtel, and David B. Bogy. "Lubricant Flow and Evaporation Model for Heat-Assisted Magnetic Recording Including Functional End-Group Effects and Thin Film Viscosity." *Tribology Letters* 52(1), 27-45 (2013)

[55] Ma, Yansheng, Xiuying Chen, and Bo Liu. "Experimental study of lubricant depletion in heat assisted magnetic recording: effects of laser heating duration and temperature." *Microsystem technologies* 19.2 (2013): 291-297.

[56] Ma, Y. S., X. Y. Chen, J. M. Zhao, S. K. Yu, B. Liu, H. L. Seet, K. K. Ng, J. F. Hu, and J. Z. Shi. "Experimental study of lubricant depletion in heat assisted magnetic recording." *Magnetics, IEEE Transactions on* 48, no. 5 (2012): 1813-1818.

[57] Ma, Yansheng, Xiuying Chen, and Bo Liu. "Experimental study of lubricant depletion in heat assisted magnetic recording over the lifetime of the drive." *Tribology Letters* 47.2 (2012): 175-182.

[58] Zhou, Weidong, Yan Zeng, Bo Liu, Shengkai Yu, and Xiaoyang Huang. "A model for laser induced lubricant depletion in heat-assisted magnetic recording." *Tribology Letters* 45, no. 3 (2012): 411-416.

[59] Tagawa, Norio, Takao Miki, and Hiroshi Tani. "Depletion of monolayer liquid lubricant films induced by laser heating in thermally assisted magnetic recording." *Tribology Letters* 47.1 (2012): 123-129.

- 
- [60] Tagawa, N., and H. Tani. "Lubricant depletion characteristics induced by rapid laser heating in thermally assisted magnetic recording." *Magnetics, IEEE Transactions on* 47.1 (2011): 105-110.
- [61] Tagawa, Norio, Hideki Andoh, and Hiroshi Tani. "Study on lubricant depletion induced by laser heating in thermally assisted magnetic recording systems: effect of lubricant thickness and bonding ratio." *Tribology letters* 37.2 (2010): 411-418.
- [62] Tagawa, Norio, Ryo Kakitani, Hiroshi Tani, Naoyasu Iketani, and Ikuo Nakano. "Study of lubricant depletion induced by laser heating in thermally assisted magnetic recording systems—effect of lubricant film materials." *Magnetics, IEEE Transactions on* 45, no. 2 (2009): 877-882.
- [63] Wu, Lin. "Modelling and simulation of the lubricant depletion process induced by laser heating in heat-assisted magnetic recording system." *Nanotechnology* 18.21 (2007): 215702.
- [64] Dahl, Joanna Bechtel, and David B. Bogy. "Simulation of lubricant recovery after heat-assisted magnetic recording writing." *Tribology Letters* 52.1 (2013): 163-174.
- [65] Shaomin Xiong, Haoyu Wu and David Bogy, "Lubricant Depletion under Various Laser Heating Conditions in Heat Assisted Magnetic Recording (HAMR)," *SPIE Optical Data Storage 2014*, San Diego.
- [66] Wu, Haoyu ; Rodriguez Mendez, Alejandro ; Xiong, Shaomin ; Bogy, David B, "Lubricant Reflow after Laser Heating in Heat Assisted Magnetic Recording (HAMR)", 59<sup>th</sup> MMM Conference.
- [67] Chiba, H.; Oshikubo, Y.; Watanabe, K., "Synthesis of tri-functional PFPE lubricant and its spreading characteristics on a hard disk surface," *Micro-Nanomechatronics and Human Science, 2004 and The Fourth Symposium Micro-Nanomechatronics for Information-Based Society, 2004. Proceedings of the 2004 International Symposium on* , vol., no., pp.261,264, 31 Oct.-3 Nov. 2004
- [68] Zhang, J., R. Ji, J. W. Xu, J. K. P. Ng, B. X. Xu, S. B. Hu, H. X. Yuan, and S. N. Piramanayagam. "Lubrication for heat-assisted magnetic recording media." *Magnetics, IEEE Transactions on* 42, no. 10 (2006): 2546-2548.
- [69] Greaves, S.; Kanai, Y.; Muraoka, H., "Shingled Recording for 2–3 Tbit/in<sup>2</sup>," *Magnetics, IEEE Transactions on* , vol.45, no.10, pp.3823,3829, Oct. 2009
- [70] Abdul Samad, M., S. Xiong, L. Pan, H. Yang, S. K. Sinha, D. B. Bogy, and C. S. Bhatia. "A novel approach of carbon embedding in magnetic media for future head/disk interface." (2012).
- [71] Dowden, John Michael. "The mathematics of thermal modeling: an introduction to the theory of laser material processing." CRC Press, 2001
- [72] ASTC Technical Documents, "ASTC HAMR reference media stack for NFT modeling," (The International Disk Drive Equipment and Materials Association, 2011). [http://idema-cloud.smartsite.net/?page\\_id=2269](http://idema-cloud.smartsite.net/?page_id=2269).
- [73] Li, Hongxuan, Tao Xu, Chengbing Wang, Jianmin Chen, Huidi Zhou, and Huiwen Liu. "Annealing effect on the structure, mechanical and tribological properties of hydrogenated diamond-like carbon films." *Thin Solid Films* 515, no. 4 (2006): 2153-2160.

---

[74] Wang, N., and K. Komvopoulos. "Nanomechanical and Friction Properties of Ultrathin Amorphous Carbon Films Studied by Molecular Dynamics Analysis." STLE/ASME 2010 International Joint Tribology Conference. American Society of Mechanical Engineers, 2010.

[75] Online resource: <http://www.pvdadvancedtech.com/dlc/>

[76] Wang, N., and K. Komvopoulos. "Thermal stability of ultrathin amorphous carbon films for energy-assisted magnetic recording." *Magnetics, IEEE Transactions on* 47.9 (2011): 2277-2282.

[77] Wang, N., K. Komvopoulos, F. Rose, and B. Marchon. "Structural stability of hydrogenated amorphous carbon overcoats used in heat-assisted magnetic recording investigated by rapid thermal annealing." *Journal of Applied Physics* 113, no. 8 (2013): 083517.

[78] Tagawa, Norio, and Hiroshi Tani. "Structural stability of nanometer thick diamond-like carbon films subjected to heating for thermally assisted magnetic recording." *Microsystem Technologies* (2014): 1-7.

[79] Jones, Paul M., Joachim Ahner, Christopher L. Platt, Huan Tang, and Julius Hohlfeld. "Understanding Disk Carbon Loss Kinetics for Heat Assisted Magnetic Recording." *Magnetics, IEEE Transactions on* 50, no. 3 (2014): 144-147.

[80] Ma, Y. S., Y. J. Man, M. Shakerzadeh, H. L. Seet, R. Ji, R. Y. Zheng, H. J. Chung et al. "Laser-Heating-Induced Damage to Ultrathin Carbon Overcoat in Heat-Assisted Magnetic Recording." *Tribology Letters* 53, no. 1 (2014): 303-310.

[81] Pathem, B. K., X-C. Guo, F. Rose, N. Wang, K. Komvopoulos, E. Schreck, and B. Marchon. "Carbon overcoat oxidation in heat-assisted magnetic recording." *Magnetics, IEEE Transactions on* 49, no. 7 (2013): 3721-3724

[82] Wang, N.; Komvopoulos, K., "Incidence Angle Effect of Energetic Carbon Ions on Deposition Rate, Topography, and Structure of Ultrathin Amorphous Carbon Films Deposited by Filtered Cathodic Vacuum Arc," *Magnetics, IEEE Transactions on* , vol.48, no.7, pp.2220,2227, July 2012

[83] Lin, Yu-Hung, Hong-Da Lin, Chun-Kuo Liu, Meng-Wen Huang, Ya-Chi Chen, Jiann-Ruey Chen, and Han C. Shih. "Annealing effect on the structural, mechanical and electrical properties of titanium-doped diamond-like carbon films." *Thin Solid Films* 518, no. 5 (2009): 1503-1507

[84] Umehara, Y., S. Murai, Yasuo Koide, and Masanori Murakami. "Effects of sp<sup>2</sup>/sp<sup>3</sup> bonding ratios on field emission properties of diamond-like carbon films grown by microwave plasma chemical vapor deposition." *Diamond and related materials* 11, no. 7 (2002): 1429-1435.

[85] Sullivan, J. P., T. A. Friedmann, and A. G. Baca. "Stress relaxation and thermal evolution of film properties in amorphous carbon." *Journal of Electronic Materials* 26.9 (1997): 1021-1029.

[86] Mangolini, Filippo, Franck Rose, James Hilbert, and Robert W. Carpick. "Thermally induced evolution of hydrogenated amorphous carbon." *Applied Physics Letters* 103, no. 16 (2013): 161605.

[87] Ma, Tian-Bao, Yuan-Zhong Hu, and Hui Wang. "Molecular dynamics simulation of shear-induced graphitization of amorphous carbon films." *Carbon* 47.8 (2009): 1953-1957.

---

[88] Marchon, Bruno, X-C. Guo, Bala Krishna Pathem, Franck Rose, Qing Dai, Norbert Feliss, Erhard Schreck and Saito, Y. "Head-Disk Interface Materials Issues in Heat-Assisted Magnetic Recording." *Magnetics, IEEE Transactions on* 50, no. 3 (2014): 137-143.

[89] Kadiyala, Krishna C. "Characterization and Tribological Behavior of Diamond-Like Carbon and Nitrogen-Doped Diamond-Like Carbon Thin Films". Diss. Louisiana State University, 2006.

[90] Dwivedi, Neeraj, Ehsan Rismani-Yazdi, Reuben J. Yeo, Partho S. Goohpattader, Nalam Satyanarayana, Narasimhan Srinivasan, Boris Druz, S. Tripathy, and C. S. Bhatia. "Probing the Role of an Atomically Thin SiN<sub>x</sub> Interlayer on the Structure of Ultrathin Carbon Films." *Scientific reports* 4 (2014).

[91] Yen, Bing K., Richard L. White, Robert J. Waltman, C. Mathew Mate, Yoshiaki Sonobe, and Bruno Marchon. "Coverage and properties of a-SiN<sub>x</sub> hard disk overcoat." *Journal of applied physics* 93, no. 10 (2003): 8704-8706.

[92] Liu, Dongping, and Günther Benstetter. "Conducting atomic force microscopy for nanoscale electron emissions from various diamond-like carbon films." *Applied surface science* 249.1 (2005): 315-321.

[93] Zhang, H-S., and K. Komvopoulos. "Surface modification of magnetic recording media by filtered cathodic vacuum arc." *Journal of Applied Physics* 106.9 (2009): 093504.

[95] Zhang, H-S., and K. Komvopoulos. "Synthesis of ultrathin carbon films by direct current filtered cathodic vacuum arc." *Journal of Applied Physics* 105.8 (2009): 083305.

[96] Franta, Daniel, Vilma Buršíková, Ivan Ohlídal, Pavel St'ahel, Miloslav Ohlídal, and David Nečas. "Correlation of thermal stability of the mechanical and optical properties of diamond-like carbon films." *Diamond and related materials* 16, no. 4 (2007): 1331-1335.

[97] Katsuno, Takashi, Christian Godet, Jean-Christophe Orlianges, A. S. Loir, Florence Garrelie, and Alain Catherinot. "Optical properties of high-density amorphous carbon films grown by nanosecond and femtosecond pulsed laser ablation." *Applied Physics A* 81, no. 3 (2005): 471-476.

[98] Fenstermaker, Carl A., and Frank L. McCrackin. "Errors arising from surface roughness in ellipsometric measurement of the refractive index of a surface." *Surface Science* 16 (1969): 85-96.

[99] Smith, Tennyson. "Effect of surface roughness on ellipsometry of aluminum." *Surface Science* 56 (1976): 252-271.

[100] Peng, Wei, Yiao-Tee Hsia, Kursat Sendur, and Terry McDaniel. "Thermo-magneto-mechanical analysis of head-disk interface in heat assisted magnetic recording." *Tribology international* 38, no. 6 (2005): 588-593.

[101] Lucas, C. A., T. D. Nguyen, and J. B. Kortright. "X - ray reflectivity measurements of the expansion of carbon films upon annealing." *Applied physics letters* 59.17 (1991): 2100-2102.

[102] Bethe, H. A. "Theory of diffraction by small holes." *Physical Review* 66.7-8 (1944): 163.

[103] Challener, William A., and Amit V. Itagi. "Near-field optics for heat-assisted magnetic recording (Experiment, Theory, and Modeling)." *Modern Aspects of Electrochemistry* No. 44. Springer New York, 2009. 53-111.

- 
- [104] Challener, William A., and Amit V. Itagi. "Near-field optics for heat-assisted magnetic recording (Experiment, Theory, and Modeling)." In *Modern Aspects of Electrochemistry* No. 44, pp. 53-111. Springer New York, 2009.
- [105] Mansfield, Scott Marshall, and G. S. Kino. "Solid immersion microscope." *Applied physics letters* 57.24 (1990): 2615-2616.
- [106] Biar Budaev and David B. Bogy, On the functional lifetime of near field metallic plasmonic transducers in heat assisted magnetic recording (HAMR), CML blue report, February 2012
- [107] Makin, S. M., A. H. Rowe, and A. D. LeClaire. "Self-diffusion in Gold." *Proceedings of the Physical Society. Section B* 70.6 (1957): 545.
- [108] Harris, K. E., and A. H. King. "Direct observation of diffusional creep via TEM in polycrystalline thin films of gold." *Acta materialia* 46.17 (1998): 6195-6203.
- [109] Challener, William A., Ed Gage, Amit Itagi, and Chubing Peng. "Optical transducers for near field recording." *Japanese journal of applied physics* 45, no. 8S (2006): 6632.
- [110] Lin, I-Kuan, Xin Zhang, and Yanhang Zhang. "Thermomechanical behavior and microstructural evolution of SiNx/Al bimaterial microcantilevers." *Journal of Micromechanics and Microengineering* 19.8 (2009): 085010.
- [111] Naik, Gururaj V., Vladimir M. Shalaev, and Alexandra Boltasseva. "Alternative plasmonic materials: beyond gold and silver." *Advanced Materials* 25.24 (2013): 3264-3294.
- [112] Naik, Gururaj V., Jongbum Kim, and Alexandra Boltasseva. "Oxides and nitrides as alternative plasmonic materials in the optical range." *Optical Materials Express* 1.6 (2011): 1090-1099.
- [113] Zhao, Jia, Shaomin Xiong, David B. Bogy, Kun Sun, and Liang Fang. "Hard-particle-induced physical damage and demagnetization in the head-disk interface." *Microsystem technologies* 19, no. 9-10 (2013): 1313-1317.
- [114] Xiong, Shaomin, Jeongmin Kim, Yuan Wang, Xiang Zhang, and David Bogy. "A two-stage heating scheme for heat assisted magnetic recording." *Journal of Applied Physics* 115, no. 17 (2014): 17B702.
- [115] Liu, Yuliang, et al. "Quantitative relationship between contact stress and magnetic signal strength in perpendicular recording media." *Journal of Applied Physics* 115.17 (2014): 17B725.
- [116] N. Liu , J. Zheng and D. Bogy "Predicting the flying performance of thermal flying-height control sliders in hard disk drives", *J. Appl. Phys.*, vol. 108, no. 1, pp.016102 2010
- [117] T. Shiramatsu "Drive integration of active flying-height control slider with micro thermal actuator", *IEEE Trans. Magn.*, vol. 42, no. 10, pp.2513 -2515 2006
- [118] U. Boettcher and C. A. Lacey "Servo signal processing for flying height control in hard disk drives", *Microsyst. Technol.*, vol. 17, no. 5 "7, pp.937 -944 2011
- [119] T. Shiramatsu , T. Atsumi , M. Kurita , Y. Shimizu and H. Tanaka "Dynamically controlled thermal flying-height control slider", *IEEE Trans. Magn.*, vol. 44, no. 11, pp.3695 -3697 2008

---

[120] Dahl, Joanna Bechtel, and David B. Bogy. "Static and Dynamic Slider Air-Bearing Behavior in Heat-Assisted Magnetic Recording Under Thermal Flying Height Control and Laser System-Induced Protrusion." *Tribology Letters* 54.1 (2014): 35-50.

[121] Xu, Baoxi, Yeow Teck Toh, Cheow Wee Chia, Jianming Li, Jing Zhang, Kaidong Ye, and Chengwu An. "Relationship between near field optical transducer laser absorption and its efficiency." *Magnetics, IEEE Transactions on* 48, no. 5 (2012): 1789-1793.

[122] Hao Zheng; Li, H.; Talke, F.E., "Numerical Simulation of a Thermal Flying Height Control Slider With Dual Heater and Insulator Elements," *Magnetics, IEEE Transactions on* , vol.45, no.10, pp.3628,3631, Oct. 2009

[123] Jia-Yang Juang; Forrest, J.; Fu-Ying Huang, "Magnetic Head Protrusion Profiles and Wear Pattern of Thermal Flying-Height Control Sliders With Different Heater Designs," *Magnetics, IEEE Transactions on* , vol.47, no.10, pp.3437,3440, Oct. 2011

[124] Thornton, B.H.; Bogy, D.B., "Nonlinear aspects of air-bearing modeling and dynamic spacing modulation in sub-5-nm air bearings for hard disk drives," *Magnetics, IEEE Transactions on* , vol.39, no.2, pp.722,728, Mar 2003

[125] Y. Hu, "Head-Disk-Suspension Dynamics," Ph.D. dissertation, Dept. Mechanical Engineering, Univ. California, Berkeley, 1996

[126] J. Zheng and D. Bogy "Investigation of flying-height stability of thermal fly-height control sliders in lubricant or solid contact with roughness" *Tribol. Lett.*, vol. 38, no. 3, pp. 283-289, 2010

[127] Li, Liping, and David B. Bogy. "Air bearing dynamic stability on bit patterned media disks." *Microsystem technologies* 19.9-10 (2013): 1401-1406.

[128] Yang, XiaoMin, et al. "Toward 1Tdot/in<sup>2</sup> nanoimprint lithography for magnetic bit-patterned media: Opportunities and challenges." *Journal of Vacuum Science & Technology B* 26.6 (2008): 2604-2610.

[129] Tom Albrecht, "Generation and Transfer of Large Area Lithographic Patterns in the ~10 nm Feature Size Regime", SPIE Advanced Lithography presentation

[130] Komatsu, Kazunori. "Electron beam lithography method." U.S. Patent No. 7,026,098. 11 Apr. 2006.

[131] Srituravanich, Werayut, Nicholas Fang, Cheng Sun, Qi Luo, and Xiang Zhang. "Plasmonic nanolithography." *Nano letters* 4, no. 6 (2004): 1085-1088

[132] Wang, Yuan, Werayut Srituravanich, Cheng Sun, and Xiang Zhang. "Plasmonic nearfield scanning probe with high transmission." *Nano letters* 8, no. 9 (2008): 3041-3045.

[133] Kim, Yongwoo, Seok Kim, Howon Jung, Eungman Lee, and Jae W. Hahn. "Plasmonic nano lithography with a high scan speed contact probe." *Optics express* 17, no. 22 (2009): 19476-19485

[134] Srituravanich W, Pan L, Wang Y, Sun C, Bogy DB, Zhang X (2008) Flying plasmonic lens in the near field for high-speed nanolithography. *Nat Nanotechnol* 3:733–737

[135] Pan, Liang, Yongshik Park, Yi Xiong, Erick Ulin-Avila, Yuan Wang, Li Zeng, Shaomin Xiong, David Bogy and Xiang Zhang. "Maskless plasmonic lithography at 22 nm resolution." *Scientific reports* 1 (2011).

- 
- [136] Shaomin Xiong, Yuan Wang, Xiang Zhang and David Bogy, "A Magnetic Rotary Encoder for Patterned Media Lithography", ASME ISPS 2014
- [137] Renishaw: Optical rotary (angle) encoders,  
Online: [www.renishaw.com/en/optical-rotary-angle-encoders--6434](http://www.renishaw.com/en/optical-rotary-angle-encoders--6434)
- [138] Tobita, K.; Ohira, T.; Kajitani, M.; Kanamori, C.; Shimojo, M.; Aiguo Ming, "A rotary encoder based on magneto-optical storage," *Mechatronics*, IEEE
- [140] Al Mamun, Abdullah, GuoXiao Guo, and Chao Bi, "Hard disk drive: mechatronics and control," CRC press, 2006
- [141] Xiong, Shaomin, and David Bogy. "Position error signal generation in hard disk drives based on a field programmable gate array (FPGA)." *Microsystem technologies* 19.9-10 (2013): 1307-1311.
- [142] Shaomin Xiong; Bogy, D.B., "Hard Disk Drive Servo System Based on Field-Programmable Gate Arrays," *Industrial Electronics, IEEE Transactions on* , vol.61, no.9, pp.4878,4884, Sept. 2014
- [143] Al Mamun, A.; Guo, G.; Tan, K. C.; Yimei Liu, "Digital processing of dual-frequency servo burst in hard disk drives," *IEEE Trans. Instrum. Meas.*, vol.54, no.4, pp.1354-1360, Aug. 2005.
- [144] Wai-Ee Wong; Lu Feng; Zhimin He; Jun Liu; Cheng Mun Kan; Guoxiao Guo, "PC-based position error signal generation and servo system for a spindrive," *IEEE Trans. Magn.*, vol.41, no.11, pp.4315-4322, Nov. 2005.
- [145] Nahum Guzik, Anatoli B. Stein, Alex Talalai, "Multi-frequency servo bursts in magnetic disc memory system", United States Patent 6785085, Aug. 31, 2004.
- [146] Yuan Chen, V. Dinavahi, " Digital Hardware Emulation of Universal Machine and Universal Line Models for Real-Time Electromagnetic Transient Simulation," *IEEE Trans. Ind. Electron.*, vol. 59, no. 2, pp. 1300-1309, Feb. 2012.
- [147] Idkhajine, L.; Monmasson, E.; Maalouf, A., "Fully FPGA Based Sensorless Control for Synchronous AC Drive Using an Extended Kalman Filter," *IEEE Trans. Ind. Electron.*, vol.59, no.10, pp.3908-3918, Oct. 2012.
- [148] Seunghun Jin; Dongkyun Kim; Thuy Tuong Nguyen; Daijin Kim; Munsang Kim; Jae Wook Jeon, "Design and Implementation of a Pipelined Datapath for High-Speed Face Detection Using FPGA," *IEEE Trans. Ind. Informat.*, vol. 8, no.1, pp. 158-167, Feb 2012.
- [149] Milivojevic, N.; Krishnamurthy, M.; Gurkaynak, Y.; Sathyan, A.; Young-Joo Lee; Emadi, A.; , "Stability Analysis of FPGA Based Control of Brushless DC Motors and Generators Using Digital PWM Technique," *IEEE Trans. Ind. Electron.*, vol.59, no.1, pp.343-351, Jan. 2012.
- [150] Bueno, E.J.; Hernandez, A.; Rodriguez, F.J.; Girón, C.; Mateos, R.; Cobrecas, S., "A DSP- and FPGA-Based Industrial Control With High-Speed Communication Interfaces for Grid Converters Applied to Distributed Power Generation Systems," *IEEE Trans. Ind. Electron.*, vol.56, no.3, pp.654-669, March 2009.
- [151] Rodriguez-Araujo, J.; Rodriguez-Andina, J.J.; Farina, J.; Vidal, F.; Mato, J.L.; Montealegre, M.A., "Industrial Laser Cladding Systems: FPGA-Based Adaptive Control," *IEEE Industrial Electronics Magazine*, vol.6, no.4, pp.35-46, Dec. 2012



---

[152] Guoyang Cheng, Kemao Peng, "Robust Composite Nonlinear Feedback Control With Application to a Servo Positioning System," IEEE Trans. Ind. Electron., vol. 54, no. 2, pp. 1132-1140, April 2007.

[153] Al Mamun, A.; Ge, S.S., "Precision control of hard disk drives," IEEE Control Systems, vol.25, no.4, pp.14-19, Aug. 2005.

[154] Sung-Won Park; Jun Jeong; Hyun-Seok Yang; Young-Pil Park; Park, No-Cheol, "Repetitive controller design for minimum track misregistration in hard disk drives," IEEE Trans. Magn., vol.41, no.9, pp.2522-2528, Sept. 2005

[155] Kim, Byung-Sub, and Tsu-Chin Tsao. "Robust repetitive controller design with improved performance." in Proc. Amer. Control Conf., 2001, pp. 2027-2032.

[156] Online: <http://www.digilentinc.com/Products/Detail.cfm?Prod=ADEPT2>

[157] Juang, Jia-Yang. "Transient Characteristics of Nanoscale Air Bearings Subjected to Joule Heating." Tribology Letters 53.1 (2014): 255-260.